Electron Impact Ionization: Measurements of Absolute Cross-Sections and Cross-Beam Studies

A thesis submitted in partial fulfulment of

the requirements for the degree of

Doctor of Philosophy in Chemistry

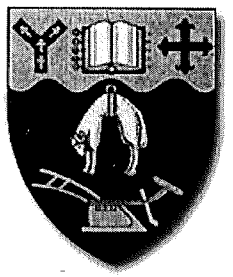

University of Canterbury

Christchurch

New Zealand

Mark Bart

December 2003

To Dad

ABSTRACT

Absolute total electron impact ionization cross-sections have been measured and calculations performed for C_1 to C_4 perfluorocarbons, C_1 to C_5 chlorocarbons and a number of mixed halocarbons and nitriles. Measured and calculated cross-sections using several different models have been analyzed using empirically and theoretically determined functions in terms of fundamental molecular parameters. A series of bond contributions to the total electron impact ionization cross-section have been determined and shown to reproduce total cross-sections for all of the molecules investigated with a high degree of confidence.

An instrument has been constructed for the measurement of pseudo-absolute partial electron impact ionization cross-sections using the NIST standard mass spectrum database as a reference. Measurements were carried out for CF_4, C_2F_6, C_3F_8, C_3F_6, $F_2C{=}CF\text{-}CF{=}CF_2$ and $F_3C\text{-}C{\equiv}C\text{-}CF_3$

Theoretical models of electron impact ionization cross-sections have been critically assessed and a correction factor has been devised and applied to the binary encounter Bethe model of electron impact ionization resulting in a significant improvement in the performance of that model such that it can now be used for molecules comprising of atoms in rows 1 to 4 of the periodic table with a high degree of confidence.

Ion imaging has been applied for the first time to crossed-beam electron impact ionization in an attempt to measure angular scattering patterns and energy disposal in a one step process. The instrument and the ion imaging process are described in detail and preliminary results reported in this thesis.

A feasibility study has been carried out on the use of a capacitance manometer

to measure neutral molecular beam fluxes directly and recommendations made for the future development of a usable device.

ACKNOWLEDGMENTS

I wish to express sincere thanks to my supervisor Professor Peter Harland for all of his perseverance, encouragement and endless enthusiasm for this project. Thank you also to Dr. Brett Cameron and Dr. Todd Clements for their help, encouragement and expert software development, and to Dr. Claire Vallance for her expert electron impact ionization cross-section calculations.

The technical staff have been instrumental in the development of all of the apparatus used in this work. From the mechanical workshop I would like to thank (in alphabetical order) Russel Gillard, Danny Leonard, Wayne Mackay, Nick Oliver and Geoff Spear and from the electronics workshops Sandy Ferguson, Steven Graham, Roger Merryweather and Mike Pearce for providing endless assistance in aid of my elaborate requests. In addition to these core services I would like to thank Dave McDonald and Rob McGregor from the glass shop, John Davis for computer network support and store-men Laurie Anderson and Bruce Whitfield.

My office mates have been great fun and it had been great to get to know all of you; Michelle Hamilton, Ben Perston, Tim Simpson, Nick Weng and of course the infamous Dr. Jim Hudson.

Financial support from the Marsden fund and the Chemistry Department is greatly appreciated.

The biological, emotional and financial support of my family, Fred, Anneke, Suzan, Jessica, Johanna, Julia, Franziska, and Meike has been invaluable especially over the last year. Without all of you things would have been significantly more difficult.

Thanks also to the Keats/Robson family, for your support and Sunday dinners, and the Levick/Harmer family, the Johnson family, the Dunlop family, Paul Heaps and all of my 26 flatmates for your fun and friendship over the years.

Lastly, and most importantly, I would like to thank my friend Jane for her help, perseverance, interesting ideas and exciting adventures.

LIST OF PUBLICATIONS

1. Mark Bart, Peter W. Harland James E. Hudson and Claire Vallance, 'Absolute total electron impact ionization cross-sections for perfluorinated hydrocarbons and small halocarbons', *Phys. Chem. Chem. Phys.*, **3(5)** 800-806 (2001)

2. James E. Hudson, Claire Vallance, Mark Bart and Peter W. Harland, 'Absolute electron impact ionization cross sections for a range of C_1 to C_5 chlorocarbons', *J. Phys. B: At. Mol. and Opt. Phys.*, **34(15)** 3025-3039 (2001)

3. Peter W. Harland, Brett R. Cameron, Mark Bart and Mike O. Pearce, 'Application of ion imaging to the electron impact ionization of oxygen using crossed beams and a custom designed fast multicahnnel pulse generator' *Rev. Sci. Instrum.* **73(6)** 2398-2403 (2002)

CONTENTS

LIST OF FIGURES

LIST OF TABLES

1. INTRODUCTION

Electron impact ionization is employed to produce positive and negative ions in many areas of physics and chemistry. Applications range from analytical mass spectrometry, where electron bombardment is used in high and low pressure ion sources to produce positive and negative ions for separation and analysis by a mass spectrometer or mass filter, plasma studies, fusion modeling, radiation physics and gas discharges to more abstract applications such as astrophysical applications and modeling of planetary atmospheres. As the list of molecules that have been detected in interstellar space continues to grow, the importance of understanding the interactions between these molecules and fundamental charged particles, such as electrons, increases. In addition to these applications, concerns have recently been raised about the potential damage that low energy electrons can inflict on DNA.[1] This has prompted several groups to investigate electron impact ionization of biological molecules: uracil, thymine and cytosine, using low energy electrons, thus opening up new research areas of electron impact in biophysics. An introduction to the electron impact ionization process is included in this chapter with further details at appropriate places throughout this thesis.

When an electron of energy E strikes a molecule, causing it to ionize, the molecule can either retain all of its constituent atoms, giving rise to the parent, or molecular ion, or it can fragment giving daughter ions which may have excess kinetic energy. The fragmentation process for CH_3Cl is schematically represented by Figure 1.1.

In this Figure $\sigma(E)$ represents the total, or gross, ionization cross-section, which is the effective area that a molecule presents to an incoming electron with energy E. $\sigma_i(E)$ represents the partial ionization cross-section, which is the total charge generated

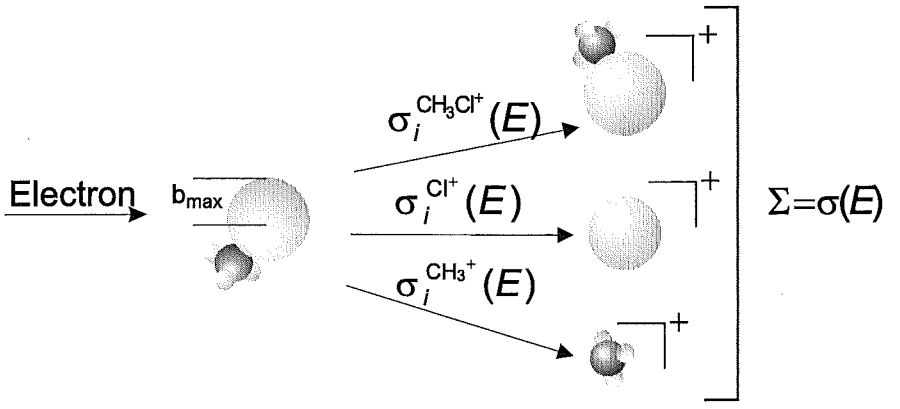

Figure 1.1: Schematic of electron impact ionization and fragmentation processes

per molecule per electron (of energy E) for the formation of an ion with a particular mass-to-charge (m/z) ratio.

In the above example, CH_3Cl^+ is the molecular ion and CH_3^+ and Cl^+ are daughter ions which may possess excess kinetic energy depending on the electronic transitions that the molecule undergoes during the ionization process. If an electron passes a molecule at a distance less than b_{max} the molecule will ionize otherwise it will not. The ionization cross-section is given by the area πb_{max}^2 and varies strongly with electron energy. The maximum cross-section typically corresponds to an electron energy value E of approximately 70 eV, indicating that there is more to electron–molecule collisions than a simple 'hard sphere' collision model predicts.

In a static target gas type experiment, which is the subject of the first part of this thesis, b_{max} is actually the average impact parameter over all molecular orientations. Intuitively, the impact parameter is expected to vary with molecular orientation and a crossed molecular beams experiment with oriented symmetric top molecules, which was the subject of a previous study in this laboratory,[2–5] demonstrated that this is indeed the case.

Experimentally, the measurement of total or gross electron impact ionization cross-sections involves making no distinction between the parent and daughter ions on the basis of their mass-to-charge (m/z) ratio, only the sum total of the positive ion charge is

collected. The measurement of partial electron impact ionization cross-sections on the other hand involves the use of mass dispersion to separate the product ions on the basis of their m/z ratio. Very few absolute partial electron impact ionization cross-sections have been measured. Generally the ion signals are normalized to a previously measured total electron impact ionization cross-section. This is achieved by multiplying the sum of the contributions from the parent ion and all the daughter ions (i.e., the partial cross-sections for each process) by appropriate constants such that the sum is then equal to the total ionization cross-section. Partial cross-sections can be further refined to include state specific cross-sections and angular dependent cross-sections, known as differential cross-sections.

At the molecular level, ionization by electron impact may be considered as a vertical Franck-Condon transition. Because the electron can have energy far in excess of the ionization potential, high electronic states of the molecule are accessible leading to several ionization channels. The molecular ion will have thermal energy and fragment ions may be produced with excess kinetic energy. The measurement of the kinetic energy of the fragment ions gives information about the potential energy surfaces of the target species. Figure 1.2 represents the ionization of a molecule AB, showing three possible transitions, leading to the formation of a thermal ion (a), an ion in an excited state (b), or fragment ion with excess kinetic energy (c). In summary electron, impact ionization may be divided into three broad categories:

1. measurement of total ionization cross-sections σ involving complete ion collection independent of the m/z ratio;

2. measurement of partial ionization cross-sections σ_i involving the collection of ions with a specific m/z ratio;

3. measurement of differential ionization cross-sections involving the collection of ions from a dissociative ionization event with a specific m/z ratio and velocity vector $\mathbf{v}$.

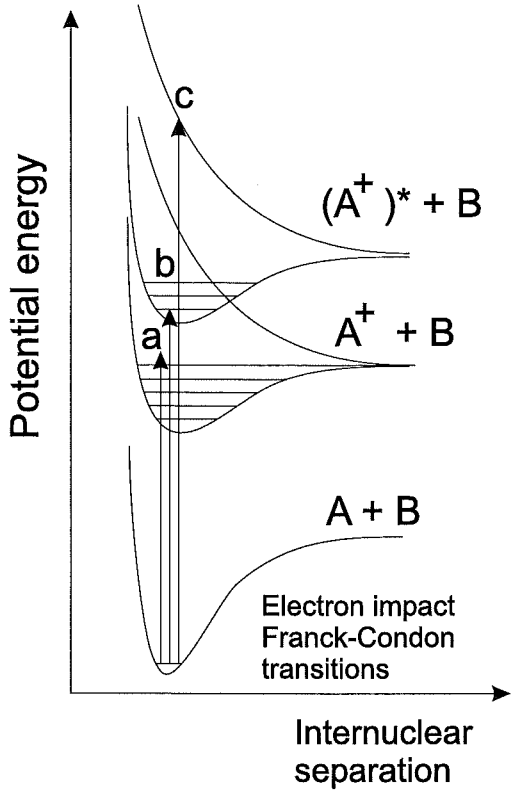

Figure 1.2: Electron impact vertical Franck-Condon transitions.

In all cases, the ionization cross-section is usually measured as a function of electron energy E. In the present work all of the above processes have been investigated.

The Chapters in Part I are structured as follows: Chapter 2 examines experimental methods that have been used for previous measurements of electron impact ionization cross-sections, while Chapter 3 details the measurement of absolute total positive electron impact ionization cross-sections for compounds where no previous data were available. Chapter 4 details the measurement of absolute partial ionization cross-sections using a simple quadrupole mass spectrometer and a normalization procedure that compared the measured data directly to the standard NIST[6] mass spectral data base. Theoretical models for the calculation of electron impact ionization cross-sections and their limitations and deficiencies will be discussed in Chapter 5.

In Part II: Chapter 6 introduces previous applications of molecular beam methods

to electron impact ionization studies. Chapter 7 describes the molecular beam machine used in the present work. Chapters 8 to 12 detail the characterization of the beam machine and the development and application of ion imaging to electron impact ionization processes for the first time in an attempt to measure differential ionization cross-sections directly in a one step process. Although the molecular beam machine is under continual development, preliminary results suggest that this technique is applicable to the study of differential electron impact ionization cross-sections and the dynamics of positive and negative ion-molecule reactions.

In order to measure electron impact ionization and ion–molecule reaction cross-sections directly using crossed molecular beam methods, the density of the electron or ion beam, and of the neutral beam must be known. In the case of charged particle beams this usually involves current measurement using an electrometer. In the case of a neutral beam, this is significantly more difficult. A feasibility study is described in Chapter 13 for the measurement of neutral beam fluxes directly using an MKS Baratron capacitance manometer. Preliminary results from this study indicate that, with a few design modifications, the measurement of neutral beam densities may be directly obtained using this instrument.

Part I

ELECTRON IMPACT IONIZATION: MEASUREMENT OF ABSOLUTE CROSS-SECTIONS

2. MEASUREMENT OF TOTAL IONIZATION CROSS-SECTIONS

While extensive data exist for ionization thresholds, E_0, which are usually measured using an electron impact ionization source coupled to a mass-spectrometer, the number of molecules for which absolute electron impact ionization cross-sections as a function of electron energy are known remains relatively small. In this work a systematic approach to the measurement of electron impact ionization cross-sections with a focus on the effect of the functional group of the target species has been adopted. Over 70 atomic and molecular targets have been studied in the last four years, corresponding to a significant fraction of the ionization cross-section data previously available in the literature.

2.1 Experimental requirements for the measurement of ionization cross-sections

In order to experimentally measure total electron impact ionization cross-sections, a beam of electrons of known current and energy is directed through a thermally equilibrated gas sample at constant pressure. Ions are formed along the electron beam track by collisions of the electrons and the molecules in the gas sample with cross-section σ.

The ion current produced, I^+, is proportional to the number of electrons in the beam, I^-, the electron beam pathlength, l, the number density of the sample, n, and the ionization cross-section, σ, which is an intrinsic property of the sample. The relationship between the measured quantities I^+, I^-, n, l, and σ is given by equation

(2.1):[a]

$$I^+ = \sigma n l I^- \tag{2.1}$$

The number density, n, of the gas is calculated using the ideal gas law, $PV = n'k_BT$:

$$n = \frac{n'}{V} = \frac{P}{k_BT} \tag{2.2}$$

Where P is the pressure in Nm^{-2} and T is the temperature in Kelvin. Combining equations (2.1) and (2.2) gives the equation for σ as

$$\sigma = \frac{I^+ k_B T}{I^- P l} \tag{2.3}$$

It would seem from equation (2.3) that the measurement of σ would be a very straight forward task involving the measurement of five quantities. However, there are strict conditions for these measurements in order to make the measurement of the ionization cross-section, σ, valid.

2.1.1 The measurement of I^+

For an accurate measurement of σ it is of critical importance that either all of the ions that are formed over the length of the electron track are collected and recorded, or, that a known fraction of the ions are collected. The magnitude of the ion current is typically of the order of 0.1 nA to 10 nA for experiments involving a continuous electron beam of $\sim$ 75 nA passing through a static target gas. Single collision conditions must be maintained in order to preclude ion–molecule interactions, multiple ionization events and scattering or reflection of the ion products from the surface of the collector. Current leakage must either be eliminated or properly taken into account and compensated for.

[a] a full derivation of equation (2.1) may be found in Appendix **A**

2.1.2 The measurement of I^-

All of the electrons, or a known fraction of the electrons, that traverse the pathlength, l, through the sample must be collected. The collection of secondary electrons must be minimized. The electron energy must be well defined, and the voltage applied to the electron trap must not affect the energy of the electrons in the beam. It is important that the electron beam current must be sufficiently low to preclude space charge repulsion effects. For the measurement of total ionization cross-sections a longitudinal magnetic field may be applied to constrain the electron beam. If a magnetic field is used the increase in pathlength due to the trochoidal motion of the electrons this must be taken into account. It is also important that the radius of the trochoidal motion of the electrons in the magnetic field is less then the radial dimension of the collision cell, otherwise the electrons will collide with the walls of the collision cell. When an electron undergoes an ionization event the ionizing electron typically loses around 30 eV of its energy,[7] this leads to a change in the electron energy distribution of the ionizing beam. Over a long path length, or when the pressure is high, this can affect the shape of the ionization efficiency curve unless single collision conditions are maintained.

2.1.3 The measurement of n

It is evident from equation (2.2), that the measurement of n requires that the pressure P, and the temperature T, are measured. The pressure must be accurately measured in the collision cell. It is therefore important that the collision cell and the device used to measure the pressure are at equilibrium. This is where most total electron impact ionization cross-sections measured before 1965 incurred large uncertainties. In the past, mercury filled McLeod gauges were used to measure the pressure inside the ionization cell. It has been repeatedly shown that a McLeod gauge can act as a diffusion pump, (the Ishii effect), and can have a serious effect on the pressure measurements, especially for the heavier gases. Rapp and Englander-Golden[8] estimated that the error due to this effect was approximately 1-2% for hydrogen and 20-30% for Ar. These problems have

since been eliminated through the use of capacitance manometers, which have been shown to accurately measure pressure to 10^{-6} Torr.[9] The rate of gas flow through the collision cell should be low enough that the pressure remains constant throughout the collision cell and pressure sensor. The temperature, T, will vary slightly throughout the cell, due to the heating effect from the filament. In the cell used for this research the filament was shielded from the cylindrical collision cell by three stainless steel lens elements and the collision cell was fabricated from brass in order to minimize temperature gradients.

The temperature of the cell should be allowed to equilibrate before any measurements are undertaken, and the temperature should be accurately known. The cell used in the present research required up to an hour to reach thermal equilibrium.

2.1.4 The measurement of l

The pathlength may initially appear to be the simplest variable to measure, but care needs to be taken with the measurement of this quantity also. In experiments where a magnetic field is used the pathlength is affected by the spiraling nature of the electrons in the beam. *Simion*[10] modeling of the collision cell used in this work has shown that this effect is independent of the magnetic field strength and the velocity of the electrons, and depends only on the geometrical constraints placed on the electrons by the electrostatic lens elements. In the case where no magnetic field is used, electron beam divergence must be taken into account. Care must be taken to ensure that no ions formed outside the measured pathlength are detected by the ion collector. In summary the following conditions should be met,

1. The electron beam current should be kept sufficiently low to preclude space charge effects, this is typically $< 10^{-6}$A.

2. The pressure must be kept sufficiently low that there are no collisions between the ion products and the sample gas, and also to eliminate the effects of secondary

electrons.

3. The temperature and pathlength measurements should be carefully considered.

2.2 Literature review - previous experimental methods for the determination of electron impact ionization cross-sections

2.2.1 Introduction

There are five distinct experimental methods that have been developed for the measurement of total electron impact ionization cross-sections.

1. Absolute total independent cross-sections measured by the parallel plate technique.

2. Relative total ionization cross-sections measured in a poorly characterized ion source and normalized to a previously reported result.

3. Normalized total ionization cross-sections measured at one particular electron energy, usually ~70 eV, in a poorly characterized ion source.

4. Absolute or relative partial ionization cross-sections measured by one of the following mass spectrometers: magnetic sector; Neir; cyclotron; quadrupole; double focusing; time-of-flight; Fourier transform. In most cases, cross-sections measured using mass spectrometers are normalized to a previously measured result. The total ionization cross-section is usually reported as the sum of the partial ionization cross-sections.

5. Relative cross-sections using crossed beam methods, which usually involve one of the mass spectrometric techniques above for ion detection. Cross beam techniques are discussed in part II.

2.2.2 The condenser (parallel) plate method

The condenser plate apparatus, and derivatives thereof, is by far the most popular method for measuring total electron impact ionization cross-sections. Some of the earliest measurements of ionization cross-section were by Huges and Klien,[11] and Compton and Van Voorhis[12] who used a variation of the parallel plate technique dating back to the mid 1920's.

Huges and Klien used two parallel plates with a retarding system to determine absolute electron impact ionization cross-sections, as shown in Figure 2.1. An electron beam, produced from a heated filament, was directed through a small aperture normal to the first plate. A retarding voltage was applied to the second plate brought the electrons to a complete stop and then redirected them back to the first plate, where the electrons were collected and the current measured. During the course of this process the molecules sampled the electron energy from zero up to the nominal electron energy value E. The ions were collected on the second plate.

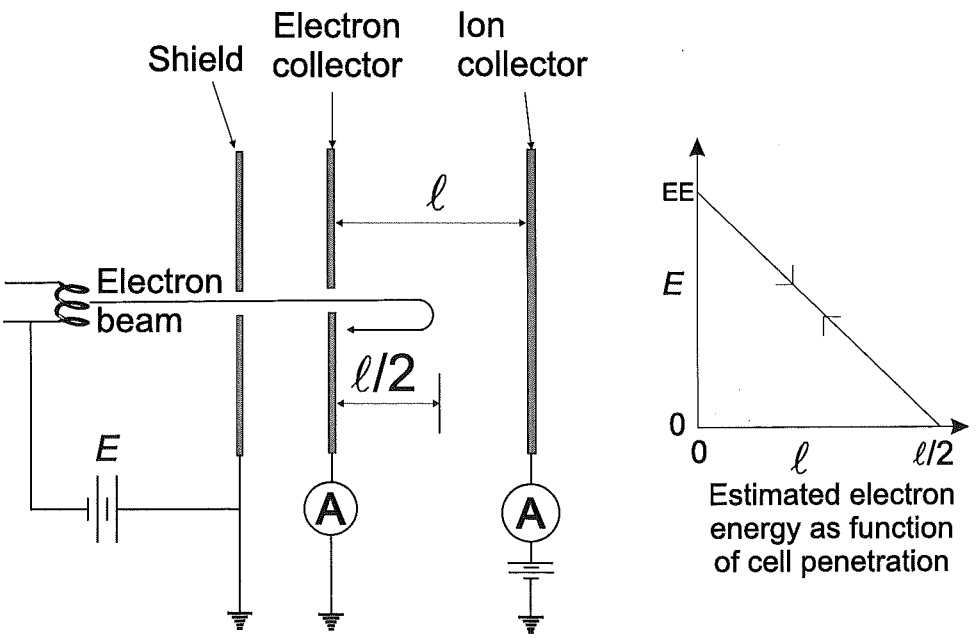

Figure 2.1: Huges and Klein electron impact apparatus.

Huges and Klien measured the ionization cross-section as a function of electron energy for He, Ne, Ar, H_2, N_2 and CH_4.[11] Although both their absolute total ionization cross-sections and their relative values between target gases were over an order of magnitude higher then the currently accepted values,[13–17] they did point out many of the important features of the electron impact ionization curve, including the overall shape and the observation that the maximum occurs between 80 eV and 110 eV electron energy. They also made the important observation that the ionization cross-section is less than the collision rate at all electron energies, suggesting that the electron impact ionization process could not simply be viewed as the hard sphere collision of an electron and a molecule. The fact that they overestimated cross-sections indicates either incomplete electron collection or that the pressure and/or pathlength measurements were incorrect. Judging from the experimental arrangement, it is possible that all of these factors may have contributed, although incomplete electron collection is probably the major factor. The problem of the electrons slowing, stopping and reversing, resulted in all electron energies sampled between 0 eV and E eV with a consequential effect on the values of the ionization cross-section. No mention of temperature corrections or measurements are made.

Compton and Van Voorhis[12] were also working on this problem at the same time. They produced results in better agreement with the currently accepted values.[13–17] The apparatus used was a simple collision cell arrangement where the electron energy was better defined than in the Huges and Klien experiments.[11] Electrons were generated at a molybdenum filament. the ion collector consisted of five 0.5 mm diameter wires in a circular arrangement, supported on a ring of wire at each end. These wires were held at a negative potential $-Vr$. The stated advantages of their wire grid collector compared to a solid plate detector was to: reduce the photo-electric current from the cathode; reduce the collection of primary electrons on the ion detector (which also had the unfortunate side effect of reducing the number of ions collected); and to reduce the electric field from -Vr on the velocity of the electrons. Although Compton and Van Voorhis were very careful in their measurements and checked the calibration of the instrument regularly, the design of the instrument precluded a determination of

accurate values for the ionization cross-section. Initially, there were problems with the confinement of the electron beam, so an axial magnetic field was introduced using an electromagnetic solenoid. Unfortunately, the magnetic field seriously affected the ion trajectories, causing the ions to curve away from the detecting wires. The magnetic field was abandoned in favour of the application of a very high voltage to the electron collector to ensure the complete collection of all electrons. This resulted in a poor energy resolution, hence the shape of the electron impact ionization cross-section curve was 'stretched'. However, the approximate shape and the relative cross-sections for the target gases; Ne, Ar, Kr and H_2 were fairly accurate. The Ishii effect for the pressure measurement may have contributed to the poor results. The measured temperature in the cell was of the order of 324K.

The original Tate and Smith ion source,[18] shown in Figure 2.2, was based on a design by Bleakney[19] originally designed for ion production for subsequent mass analysis. The

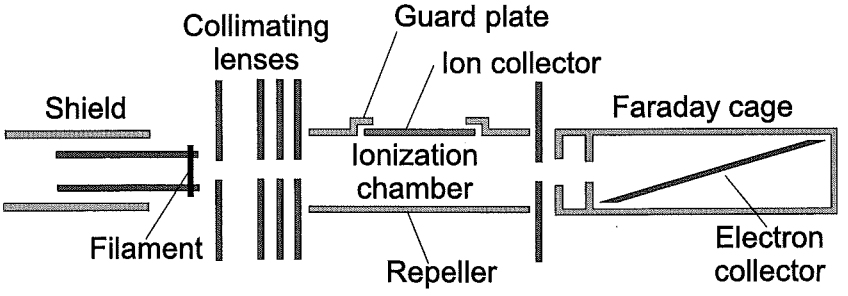

Figure 2.2: Tate and Smith electron impact apparatus.

essential design elements of the source are still used today by several groups for the measurement of electron impact ionization cross-sections. Electrons were emitted from a heated filament and passed through two collimating slits into a collision cell where ions were formed. An electric field of 5 Vcm^{-1} across the collision region directs the ions onto a collection plate. The electrons passed through a further series of three apertures into a Faraday cage. An electromagnetic solenoid was used to generate a magnetic field to constrain the electron beam throughout the collision and detection region. The pressure in the source was measured using a McLeod gauge. Sensitive galvanometers were used to collect the ion and electron currents. The electron collector had a large, 400V,

positive voltage on it with respect to the electron energy to ensure complete collection of all electrons. Field penetration through the apertures was probably detrimental to the electron energy resolution, but the three shields between the ionization chamber and the Faraday cage would have reduced this significantly compared to the Compton and Van Voorhis instrument.[12] A guard plate around the collector was held at the same potential as the repeller plate in order to maintain a homogeneous field in the collision cell. Experiments showed that when the electron current was increased by a large amount, the shape of the curve and the cross-section values changed considerably. This was due to the space charge effects in the electron beam, and as expected this effect decreased with increasing electron energy, due to lower residence time in the collision cell. Initially Smith measured electron impact ionization curves for He, Ne,and Ar,[20] and Hg.[21] Later, with Tate, the source was slightly modified to include differential pumping of the collision cell and the filament region. Molecular targets including N_2, CO, O_2, NO, H_2 and C_2H_2 were measured.[18,22] The cross-sections were normalized against measurements with the pump on the source valved off to eliminate the pressure differential between the source and the McLeod gauge. The Smith[20,21] and Tate and Smith[18,22] results are regarded as the most accurate of the early period, both in terms of the absolute value of the ionization cross-section, the electron energy resolution, and the shape of the curves.[23]

In 1965 Rapp and Englander-Golden published two papers[8,14] on electron impact ionization cross-sections for the inert gases, simple diatomic and triatomic species, CH_4 and SF_6 using a Tate and Smith type ion source in a differentially pumped chamber. The electron beam was generated using an indirectly heated cathode and collimated by a series of lenses. A 600 G magnetic field was used to constrain the electron beam and a field strength of 5 to 25 Vcm^{-1} was used to extract the ions. The cross-section curves were extrapolated back to zero cross-section and the agreement between the measured energy and published appearance potentials were found to be good in all cases. These measurements have since become the *de facto* standard to which all other results are compared.[24,25] The reason that the measurements of Rapp and Englander-Golden are considered to be so much more accurate then all previous measurements is that the

Ishii effect was taken into account for pressure measurements using the relative flow technique. The flow rate for hydrogen out of a reservoir, through a leak valve, into the collision cell was established, while the ionization cross-section for hydrogen was being measured. The leak valve was not adjusted for subsequent measurements of the ion and electron currents which were then compared to the value of σ for hydrogen. The unknown absolute electron impact ionization cross-section σ_U was then calculated using equation (2.4).

$$\sigma_u = \sigma_{H_2} \frac{I_u F_{H_2} K_{H_2}}{I_{H_2} F_u K_u} \sqrt{\frac{m_{H_2}}{m_u}} \tag{2.4}$$

where the subscript u denotes the compound under study. I, F, K and m are the ion current, flow rate, transport coefficient and molar mass of hydrogen and the unknown species. Since the flow through the leak valve was the same as the flow rate out of the collision cell, the steady state pressure in the collision cell was independent of molar mass.[b]

Schram *et al.*[26–29] made a series of electron impact ionization cross-section measurements, including high energy absolute electron impact ionization cross-sections, low energy cross-sections and partial cross-sections. A Tate and Smith type ion source was used to measure electron impact ionization cross-sections for electron energies of 0.6-20 keV for H_2, N_2, O_2, and the inert gases,[26] and hydrocarbons.[27] A commercial electron gun from a television tube was used to produce the electron beam, which was constrained using a 400 G magnetic field generated by an electromagnetic solenoid. The pressure, measured using a McLeod gauge, was in the range of 10^{-4} to 10^{-3} Torr. The ion repeller was typically set to +80 V, the ion collector to +9 V and the electron collector to +400 V. The cross-section was evaluated from a pressure *vs* I^+/I^- plot, with the temperature assumed to be constant throughout the measurements. Since the pathlength of the electron beam was actually much longer then the pathlength over which ions were collected, there was a high chance that electrons formed ions outside the collection region. This would have resulted in the formation of secondary electrons that could have contributed to the measured electron current, giving a measured

[b] Appendix **B** contains further details on this method.

cross-section smaller then the actual value. The uncertainty in these experiments was estimated to be 9%. Because of the high energy of the electrons, x-rays would also have been generated, but because the cross-section for x-ray ionization is relatively low, this may not have been a serious problem. Schram *et al.* were the first authors to report independently absolute electron impact ionization measurements for hydrocarbons as a function of electron energy although the electron energies over which these measurements were carried out did not overlap with the fixed electron energy measurements of Otvos and Stevenson,[30] Lampe, Franklin and Field[31] or Harrison, Nagy and Gupta[32] discussed in Section 2.2.3. Bond contributions to the cross-section for C-H bonds, σ(C-C) bonds and π(C-C) bonds were also deduced. Ionization cross-sections for the inert gases, H_2, N_2 and O_2 were measured for the electron energy range 100-600 eV and the results normalized to the ionization cross-sections for the high energy measurements at the 600 eV energy overlap.[28] The reported values for the ionization cross-sections were 8-20% lower then the values of Rapp and Englander-Golden[8] and 20-35% lower then the values of Asundi and Kerupa[33] for the same electron energies.

The Stebbings group at Rice University, Texas have published 15 papers[15,16,24,34–45] on electron impact ionization using a parallel plate type collision cell. The instrument can be used to measure both absolute total ionization cross-sections and absolute partial ionization cross-sections using a very short pathlength time-of-flight mass spectrometer. The reported FWHM of each mass peak is approximately 20 ns. A diagram of the ion source is shown in Figure 2.3. Errors are claimed to be around 8% for this series of papers. A commercial electron gun is used to generate a pulsed 1 pA beam of electrons in the energy range of 0 - 1 kV, with a pulse width of 20 ns and a repetition rate of 2.5 kHz, giving about 2500 electrons per pulse. The beam then passes through two 760 μm apertures for focusing and collimation. From the diagram in the paper,[15] the total interaction region is approximately 300 mm, but the actual pathlength over which ions are collected is only 19.1 mm. This leads to a small error from secondary electrons and electrons that have lost energy from previous collisions. This is more significant for higher electron energies when the cross-section decreases, because any secondary or scattered electrons that are products from the collision with energy be-

tween 50 eV and 200 eV will contribute to the cross-section near the maximum in the ionization efficiency curve.[c]

The vacuum chamber that accommodates the ion source is pumped down to 2×10^{-7} Torr and the sample gas is admitted to a pressure of $\sim 5\times10^{-6}$ Torr, measured using a capacitance manometer. The ions generated along the electron beam track are repelled out of the interaction region by a 2 kV pulse on the top plate, and are detected using a micro-channel plate coupled to a resistive anode position sensitive detector (PSD). This detector was previously calibrated using an ion beam of known intensity directed at the surface.[15] The position sensitive detector ensures that all ions are collected regardless of their initial kinetic energy since fragments, with high kinetic energy arrive at the outer edges of the detector.

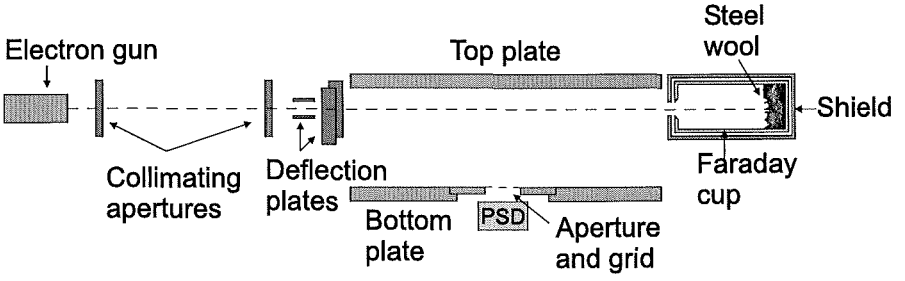

Figure 2.3: Time-of-flight parallel plate apparatus.

Other authors to use the parallel plate type ion source for measurement of electron impact ionization cross-sections include Srinivasan and Rees.[46] They measured electron impact ionization cross-sections for CO and Ar to further examine errors in the previously measured values due to the Ishii effect. Their apparatus was of the same design as Asundi and Kerupa[33] who used a Knudsen orifice to control the gas flow rate, which is linearly dependent on the backing pressure. The results of those authors were in close agreement with the values reported by Rapp and Englander-Golden[14] measured two years earlier. Cowling and Fletcher[47] also used a parallel plate apparatus with a pulsed electron beam to measure total electron impact ionization cross-sections and to explore

[c] For argon the pathlength would have to be of the order of 200 m for every electron to undergo a collision at the pressure used in this experiment

the effect of isotope substitution, for H_2 and D_2. They found that the mean value for the D_2 cross-section was 1% higher than for H_2. Since the reported uncertainty in the measurements was approximately 4% there was no detectable difference between the two isotopes. Chatam *et al.*[48] measured both partial and total electron impact ionization cross-sections for CH_4, C_2H_6, SiH_4 and Si_2H_6, using a quadrupole mass spectrometer and a square box collision cell. The electrons were directed at the wall parallel to the gas flow and the ions were collected on a grid opposite the pumping aperture. The results were normalized to the Rapp and Englander-Golden results with a stated uncertainty of 15%. Recently Nishimura *et al.* have measured absolute electron impact ionization cross-sections for CH_4, C_2H_4, C_2H_6, C_3H_6 (propene and cyclopropane), C_3H_8,[49] and CF_4, C_2F_6 and C_3F_8[50] using a complex parallel plate ion source, with a capacitance manometer for pressure measurement and an electromagnetic solenoid for electron beam confinement.

Winters devised a different method for measuring the total dissociation cross-section and the total electron impact ionization cross-section for CH_4 using a getter pump.[51] The dissociation cross-section was measured by monitoring the pressure change at the getter pump, which does not pump CH_4 but does pump the reaction products from the electron impact ionization of methane. A quadrupole mass spectrometer was used to ensure that no higher and lower molecular mass ions were formed in the ionization cell due to ion–molecule chemistry. This technique is limited to compounds which form molecular ions not pumped by the getter. For methane:

$$CH_4 + e^- \longrightarrow CH_3^+ + H + 2e^-$$

The CH_3^+ and H are absorbed by the getter, resulting in a pressure decrease for CH_4.

$$\frac{dN}{dt} = n_e \frac{N}{V} \sigma l \tag{2.5}$$

$$\Rightarrow \sigma = \frac{1}{n_e l} \frac{V}{P} \frac{dP}{dt} \tag{2.6}$$

The advantage of this particular technique is that the absolute pressure measurement is not important, as long as the change in pressure with time is monitored. If $\ln P$ is monitored as a function of time a linear dependence is observed. A change in the slope is clear when the electron gun is switched on. The disadvantage of the technique was its limitation to a small range of compounds. The numbers worked well and the final results were similar to those of Rapp and Englander-Golden[8] although the uncertainty was estimated at 20%.

A further method for measuring total electron impact ionization cross-sections was the 'gas filled counter' method[25] illustrated in Figure 2.4. This method was first introduced by Graf[52] and later used by Rieke and Prepejchal[53] to measure the electron impact ionization cross-sections for forty molecular species at high (0.1-2.7 MeV) electron energy. By measuring the number of electrons that were involved in an ionization event, and by measuring the number of electrons that are not involved in an ionization event it is possible to determine the probability of an ionization event and hence derive the electron impact ionization cross-section. This technique is particularly applicable to high energy electrons and was used to examine the high energy cross-section expression developed by Hans Bethe, as briefly described in Chapter 5. From Poisson

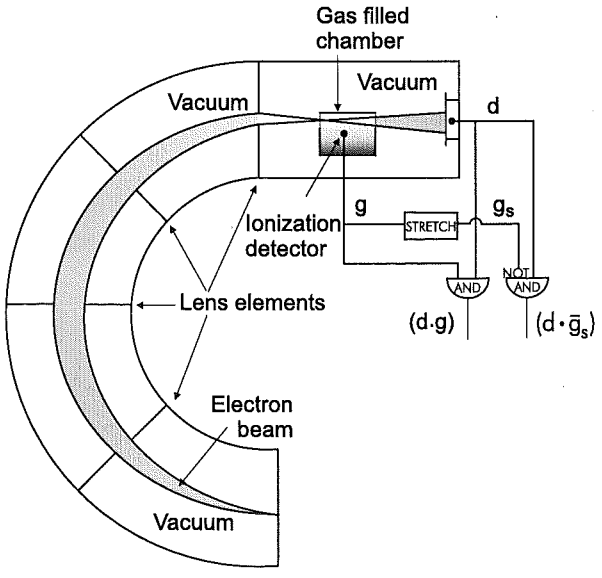

Figure 2.4: Gas filled counter. $d \cdot g$ represents an ionization event and $d \cdot \bar{g}_s$ represents a primary electron that does not cause an ionization event.

statistics, the probability that an electron traverses the chamber without causing an ionization event is given by

$$\frac{(d \cdot \bar{g}_s)}{(d \cdot g) + (d \cdot \bar{g}_s)} = \phi = e^{-nl\sigma_c} \tag{2.7}$$

but because some of the electrons from the ionization event are lost at the gas cell windows a correction must be applied. Assuming that this window effect is independent of pressure, a straight line plot of pressure against $\ln(\phi)$ would yield σ_c from the slope, and the extent of the window effect from the intercept.

2.2.3 Cross-sections at fixed electron energy

Several authors have measured a single cross-section at a fixed electron energy using, for example, a commercial mass spectrometer ion source and normalizing the results to a previously measured absolute value. This technique is prone to error, because changes in temperature or electron current are not detected.

Otvos and Stevenson[30] measured maximum ionization cross-sections for the inert gases, H_2 N_2, O_2, CO, CO_2, N_2O, PH_3, H_2S, HCl, HCN, $(CH)_2$, CS_2, air and a range of C_1 to C_7 hydrocarbons using three different brands of ion source on a magnetic sector mass spectrometer at approximately 75 eV electron energy. They concluded that the total cross-section was given by the sum of the atomic cross-sections, and suggested that more measurements were required. The cross-section was normalized to the Smith cross-section for argon of 3.62Å^2.[20] The danger of this technique is that ions have different transmission coefficients through the ion source and fragments with high kinetic energy are lost. The detection efficiency may also be different for different ions because on examination of the results the relative cross-sections, even for the inert gases are different to those of Smith and of Rapp and Englander-Golden.[14] All three instruments gave slightly different results.

Lampe, Franklin and Field[31] dismissed Otvos and Stevenson's[30] results. They

also used a magnetic sector mass spectrometer to make measurements at an electron energy of approximately 70 eV. Lampe *et al.* used different experimental conditions and a different normalization factor of 3.26Å^2 for argon, as recommended by Massey and Burhop. They also suggested that it was not the atomic contributions that gave the maximum ionization cross-section but the molecular polarizability. Comparisons of cross-sections between experiments was difficult because of the differences between the instruments, normalization factors, voltage calibrations and the methods used to determine cross-section. Lampe *et al.* used a method of plotting ion current *vs* decreasing pressure and determining the relative cross-section from the slope.

Harrison, Nagy and Gupta[32] published one paper extending further the work of Otvos and Stevenson[30] and Lampe *et al.*[31] Total ionization cross-sections were measured at 75 eV electron energy, using an ion source from a commercial mass spectrometer, with a high electron current of 20 μA. Cross-sections were determined by plotting the pressure in the chamber, against the ion current. From the normalized slope of the graph it was possible to determine the cross-section. Harrison *et al.* concluded that the ionization cross-section was related to both individual bond contributions, and polarizability of the target species. They found that a functional group has a contribution to the total ionization cross-section, and as the chain length increases, the ionization cross-section increases by a fixed value for each methylene unit. The increase in cross-section due to the methylene unit was found to be the same for each homologous series of compounds, regardless of the functional group.

None of the above results were entirely conclusive. No effort was made to calibrate the electron energy or the observation that maximum cross-section occurs at a different energy for every target species. No consideration was given to experimental differences and no consideration was given to transmission factors or energetic ions in the mass spectrometer. As the present work shows, in Section 3.2, the ionization cross-section is proportional to both the polarizability and the additive bond contribution of the molecule. The bond contribution model holds particularly well for homologous classes of compounds.

2.2.4 Ionization cross-sections measured with a mass spectrometer – the summation method

The summation method involves measuring the mass spectrum of a target species as a function of the energy of the ionizing electron and then normalizing the sum of the signals as mentioned in the introduction. Special care needs to be taken when making these measurements to ensure that the transmission coefficients through the mass spectrometer and the detector efficiency are the same for each m/z ratio. If the absolute total ionization cross-section for the target species has already been measured, it is possible to normalize the signals to this value. However, if the absolute total electron impact ionization cross-section has not been measured for the target species of interest then the mass spectrometer needs to be calibrated against a known target species, commonly argon. The unnormalized cross-section of target species X is given by:

$$\sigma_u(X) = \sum_n n\sigma_i(X^{n+}) \tag{2.8}$$

If argon is used as a calibrating gas the normalized absolute total electron impact ionization cross-section is then:

$$\sigma_T(X) = \left(\frac{\sigma_T(Ar)}{\sum n\sigma_i(Ar^{n+})}\right)\sigma_u(X) \tag{2.9}$$

Mass discrimination effects are minimal in a time-of-flight mass spectrometer making this the most reliable method for measuring electron impact ionization cross-sections by the summation method. Discrimination effects in quadrupole mass spectrometers, can be significant especially if the range of m/z is large. Detector effects can also be significant as reported by Stephen and Peko,[54,55] who found that the detection efficiency of a microchannel plate detector depends on the history of the micro-channel plate, the operating conditions, the individual plates, and the type of ions detected. For example, protons have a much higher detection efficiency than O^+ ions.

The use of a quadrupole mass spectrometer to determine partial and total ionization

cross-sections was first introduced by Adamczyk *et al.* in 1966[29] and was further developed by Märk and Egger[56,57] who used a double focusing spectrometer to measure electron impact ionization cross-sections. Several other authors have since applied this technique.

Since 1975 Märk *et al.* have measured a number of electron-impact ionization cross-sections: N_2 and O_2,[56] H_2O and D_2O,[57] CO_2,[58] CO,[59] NO_2,[60] NO,[61] N_2O,[62] CF_4,[63] C_{60} and C_{70},[64] CF_2Cl_2,[65] SF_6,[66] C_2H_6,[67] and SiH_4.[68] A Varian MAT double focusing mass spectrometer was used and no discrimination effects were claimed. A schematic of this instrument is shown in Figure 2.5. The pressure was determined using an effusive flow method similar to that of Rapp and Englander-Golden[14] in conjunction with an ion gauge as an extra quality control measure to ensure a constant vacuum chamber pressure, and a capacitance manometer to measure the pressure of gas in the reservoir. An ion beam of known intensity was used to calibrate the particle multiplier. A movable Faraday cup was placed in front of the multiplier and the ion beam current was monitored. The Faraday cup was then removed and the multiplier response was then determined. The electron energy was corrected by extrapolating the argon cross-section to zero and comparing this to the spectroscopic ionization potential for argon The cross-section for the molecule of interest was measured under appropriate pressure and electron current conditions as discussed in Section 2.1 and normalized to the argon data of Rapp and Englander-Golden[14] using equation (2.9). Initially the error was estimated at 10% but this was later revised to 20% because of the low pressure, 10^{-6} Torr, in the chamber and hence the low current on the Faraday cup. In the CF_4 paper,[63] several problems emerged due to discrimination effects from the excess kinetic energy of the light fragment ions. The initial solution to this problem involved integrating the peak area from the mass spectrum, instead of taking the peak heights. In the SF_6 paper,[66] a *Simion*[10] computer simulation was applied to take the mass discrimination due to the kinetic energy of the ions into account. The computer simulation indicated that at an ion energy of 1 eV, $I^+_{1eV}/I^+_{Thermal} = 0.06$ i.e. only 6% of the 1 eV ions were collected compared to the number of thermal ions collected. This casts some doubt on the validity of results reported in their earlier papers, especially

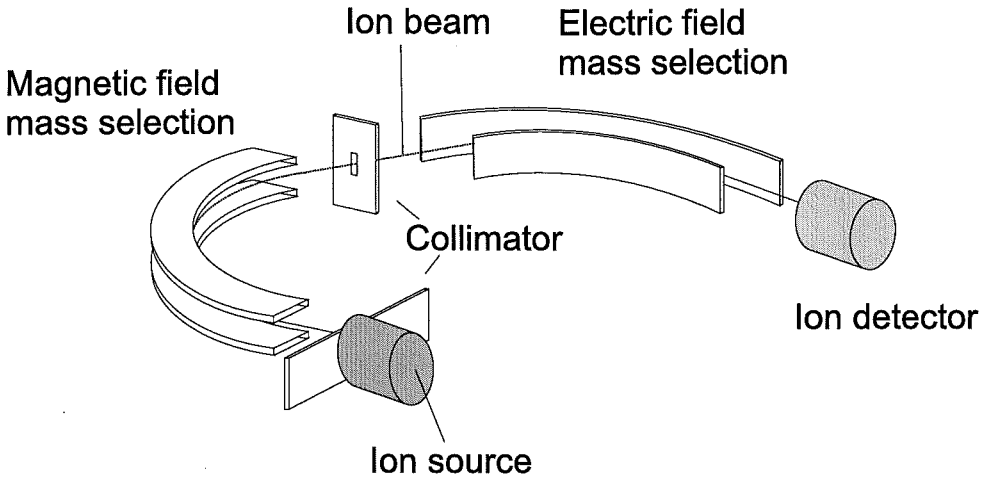

Figure 2.5: Double focusing mass spectrometer.

the partial ionization cross-sections of fragment ions. The Rapp and Englander-Golden SF_6 results were used to normalize the SF_6 data. The computer simulations are then applied to CF_4 data from the previous paper,[63] and the corrections are published in a new paper,[69] these corrections are also applied in the C_2H_6 paper.[67] The ion source was subsequently modified[68] to allow for two *modus operandi*, a high resolution mode and a high extraction efficiency mode where simulations indicated that ions with up to 4 eV of kinetic energy could be collected with the same efficiency as thermal ions.

In a series of papers that are regularly cited in this field, Adamcyzk, Boerbom, Schram and Kistemaker[29] used a newly designed cycloidal mass spectrometer with a claimed 100% transmission efficency for all ions independent of kinetic energy, thus enabling the direct measurement of partial ionization cross-sections for He Ne H_2 and CH_4. Results were normalized to those of Rapp and Englander-Golden.[14] No details were given on how pressure, temperature, or pathlength were measured, or whether the electron current which was approximately 10 μA was regulated. The instrument was not described in detail although a brief paper was published[70] which examined the effect of pressure and extraction potential on the measured ion current. Six years later the instrument was used to measure the partial electron impact ionization cross-sections for CO_2[71] although no further details of the operating conditions were given. O_2^+ was reported as one of the fragment ions from CO_2 at 4% of the base peak; the

United States Department of Commerce standard mass spectrum database[6] does not give O_2^+ as a product ion in the mass spectrum of CO_2. Either ion–molecule chemistry was occurring in their source, implying that the pressure was too high for spatial isolation of the products, or there was a problem background gas interference. The normalization procedure was the same as that used by Crowe and McConkey[72] and so the absolute total electron impact ionization cross-section was reported to be the same. Eight years later, the ionization cross-sections for NH_3 were published,[73] and three years after that cross-sections for SF_6 were reported.[74] Unfortunately further design details and operating conditions were never reported, a serious omission as a simple mass spectrometer with 100% efficiency would be a very powerful tool for measuring partial ionization cross-sections.

Other researchers using the summation method include Center and Mandl[75] who used a quadrupole mass spectrometer to determine the electron impact ionization cross-section for Cl_2 and F_2 from threshold to 100 eV with a claimed 15% uncertanty. Smith and Stevenson[76] also used a quadrupole mass spectrometer to determine ionization cross-sections for SO_2 and SO_3 from threshold to 30 eV. Perrin *et al.*[77] measured the dissociation cross-sections for SiH_4 using a quadrupole mass spectrometer with a reported uncertainty of 25%. The electron impact ionization cross-section for ozone from threshold to 500 eV was first reported by Siegel[78] using a quadrupole mass spectrometer with the cross-sections normalized to unpublished results for He, Ne and Ar. Newson *et al.*,[79] used a time-of-flight mass spectrometer, to measure the ionization cross-section for ozone from 0-500 eV. The results from Newson *et al.* were normalized to those of Seigel.[78]

Poll and Meichsner[80] used a quadrupole mass spectrometer to measure the electron impact ionization cross-sections for CF_4, C_2F_6 and C_3F_8, n-C_4F_{10}, C_2F_4, 1-C_4F_8, SiF_4 COF_2 and CHF_3, all of which are important gases in the semi-conductor industry. Measurements were made from threshold to 135V with an uncertainty of approximately 20%. The results were normalised to those of Rapp and Englander-Golden.[14] Recently Haaland used Fourier transform ion cyclotron resonance mass spectrometry to measure

the electron impact ionization cross-section for SiH_4[81] and C_2F_6[82] from threshold to 200 eV and from threshold to 70 eV, respectively, with an uncertainty of 16%. The results were normalised to those of Wetzel *et al.*[83]

Crowe and McConkey[72,84–86] measured the partial electron impact ionization cross-sections for H_2, N_2, CO_2 and NH_3, using a static target gas, and a rotatable electron gun. This experiment yielded partial differential cross-sections σ_θ^i. The electron impact ion source was well shielded in order to minimize the effect of any stray magnetic or electric fields on the ion trajectories. For angular measurements the pathlength l changed with angle and was normalized by the function $\sin\theta$. It was found that the anisotropy of the differential ionization cross-section decreased with increasing electron energy. These measurements are known as differential electron impact ionization cross-sections and will be discussed further in Chapter 6.

3. EXPERIMENTAL DETERMINATION OF ABSOLUTE ELECTRON IMPACT IONIZATION CROSS-SECTIONS

3.1 Introduction

The electron impact ionization ionization source used in this experiment was designed by Harland and first used by Harris,[87] a previous doctoral student of this research group. The source was then used by Vallance, who measured total ionization cross-sections for CH_4, CH_3F, CH_3Cl, CH_3Br and CH_3I.[88,89] The objective of the present study was to carry out a systematic study of total ionization cross-sections with a view to understanding the effects of functional groups in homologous series, to test the current models of electron impact ionization and to provide data to evaluate the correlations between the maximum ionization cross-section and molecular parameters predicted by a model based on molecular polarizability volumes developed previously by this group. In addition, the design of the ion source was refined and more fully characterized and a computer program, XSECT, was written in Quick-BASIC to automate data collection. XSECT increased the accuracy and speed at which data for electron impact ionization curve could be measured. Now it typically takes 7 minutes to measure an electron impact ionization curve from 15 – 220 eV in 5 eV steps using the automated system.

3.1.1 The vacuum system

This collision cell is housed in a stainless steel vacuum chamber which operates at a background pressure of typically 2-5 $\times 10^{-7}$ Torr. This chamber is pumped by a

4″ Varian diffusion pump, with a pumping speed of 1200 ls^{-1}, backed by an Ulvac 3-phase mechanical pump. The foreline has an Edwards High Vacuum 'Speedivac' electric solenoid for automatic venting of the mechanical pump. There are two Varian model 1251 1 1/B valves to switch the mechanical pump between the diffusion pump and the main vacuum chamber, for rough pumping the chamber to $\sim 10^{-3}$ Torr. Between the diffusion pump and an Airco model 5010-R hand operated rotary gate valve which separates the diffusion pump from the chamber, is a Varian liquid nitrogen trap. Filling of the liquid nitrogen trap is controlled by a custom made solenoid valve controller. The liquid nitrogen sensor consists of two type 4001N diodes. When liquid nitrogen flows over the diodes their resistance drops and the controller closes an electric solenoid valve to interrupt the flow of nitrogen gas used to pressurize a 75 l BOC liquid nitrogen dewar. A second solenoid valve opens which allows the dewar to vent. The liquid nitrogen trap can be set to a 3-hour or 5-hour fill cycle.

The vacuum chamber is a 6-way Varian 6″ cross with 8″ Con-Flat flanges. It is connected to the gate valve through a Varian 6″ elbow. The collision cell is mounted on one port of the cross. The other two ports carry a Dunniway T-100-K ion gauge, and a Swagelok JN type valve, for venting of the vacuum chamber with dry nitrogen. The diffusion pump is protected by a 3-way vacuum protection system. A type 531 thermocouple gauge monitors the foreline pressure, a thermocouple monitors the water temperature and the vacuum chamber pressure is monitored by a Veeco Instruments RG-830 ion gauge controller. If the foreline pressure exceeds 5×10^{-3} Torr, the water temperature exceeds 35 °C or the vacuum chamber pressure exceeds full scale on the ion gauge controller, the diffusion pump switches off.

3.1.2 The collision cell

A Diagram of the collision cell is shown in Figure 3.1. Figure 3.2 shows the collision cell with associated electronics. The electron beam is generated from a heated 0.007″ diameter rhenium filament coated with $BaZrO_3$. The heating current was initially

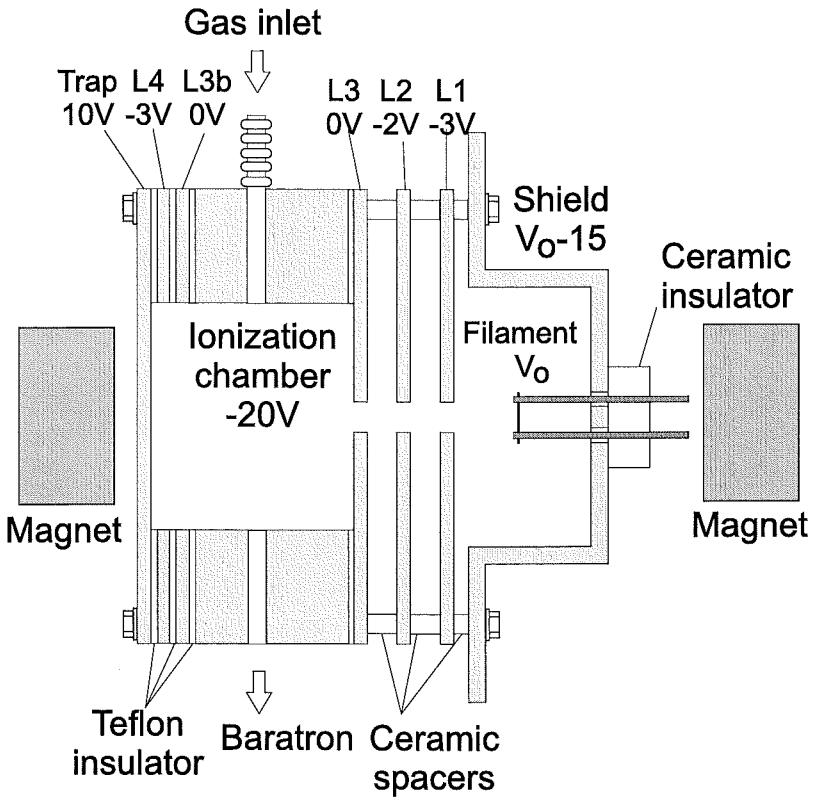

Figure 3.1: Electron impact ionization collision cell used in the present work.

provided by a Goldstar model GP-503 0-5 A, 0-30 V general purpose power supply and later by a custom made regulated power supply. Behind the filament is a top-hat shaped shield held at a potential of -15 V with respect to the filament for directing the electron beam toward three collimating 25 mm × 25 mm × 1 mm stainless steel lenses, with a 2 mm spacing between each element. There is a 1 mm diameter aperture drilled in the center of each of the electrostatic lens elements. The first two lens voltages are regulated by a custom made, 4 channel ±0-300 V, 100 mA power supply, and the final lens is held at ground potential through a central earthing terminal. A Teflon spacer insulates the final lens element from the cylindrical collision cell which is fabricated from brass and is 11 mm long with a radius of 5 mm. The walls of the collision cell are coated in Aquadag colloidal graphite to preclude scattering of the product ions. During an experiment the cell, which was also the ion collector, is maintained at -20 V from ground potential. Low energy electrons that are released in the ionization process

are directed toward the lens elements at each end of the ionization cell and lost to ground. There are two 3 mm apertures drilled in the wall of the cell directly opposing each other. The sample gas is admitted to the cell through one of the apertures *via* a Leybold-Hearaeus Model 283 41 needle valve, (later changed to a Granville-Phillips Co series 203 variable leak valve). The second aperture leads to an MKS Instruments Model 627, 0.05 Torr full scale Baratron capacitance manometer for the measurement of sample gas pressure. The gas lines leading from the cell are fabricated from glass to insulate the cell from the gas feed-throughs in the 8″ flange. These glass gas lines also support the cell on the mounting platform. The product ions are collected on the cell walls and the total ion current is measured using a Keithly Model 486 picoammeter. A small hole drilled partway into the outside wall of the cell houses a thermistor to measure the cell temperature. There are two 25 mm × 25 mm × 1 mm electrostatic lens elements between the collision chamber and the electron trap that are insulated from each other by Teflon spacers with 5 mm apertures drilled in them. The electron beam is collected at a final 25 mm × 25 mm × 1 mm stainless steel lens element that had been coated with Aquadag. The electron beam current is measured with a second Keithly Model 486 picoammeter and is taken as the total current flowing from the third lens element and the electron trap. The electron trap was held at a potential of +10 V relative to ground. Two cylindrical 20 mm diameter by 20 mm long 8000 Gauss cobalt rare earth permanent magnets, connected through a soft iron yoke, are mounted at each end of the electron beam in order to constrain the beam to its axis. The effectiveness of the magnets is demonstrated by examining the electron burn marks on the electron collector which are close to 1 mm diameter.

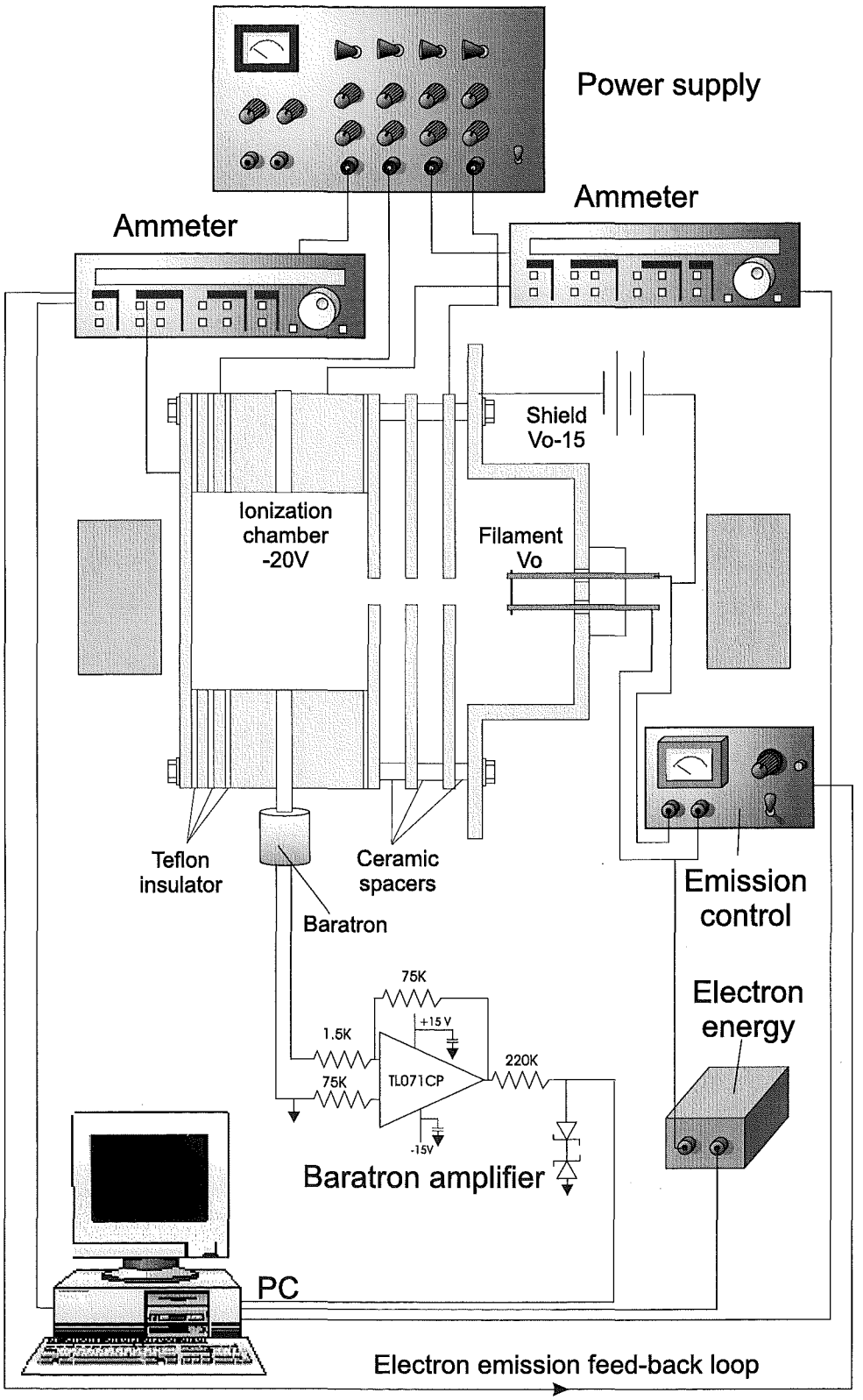

Figure 3.2: Electron impact ionization collision cell and associated electronics.

3.1.3 Computer interfacing

Before the research reported here, experimental data were written down by hand. This was time consuming and required many manual calculations. The first part of the present project involved the interfacing of the experiments using a laboratory PC, IEEE card and a 14 bit commercial I/O card. The computer used was a 66 MHz 486PC running Microsoft DOS 6.0 with 8 MB ram. A flow diagram for the program written to control the experiment is shown in Figure 3.3. EE is the electron energy control and EEinc is the electron enrgy increment between readings. Input values from the previous run were stored in a file called 'defaults.in'. This saves time as most of the inputs were unchanged between runs. If the input data were changed then the new inputs were saved to the file 'defaults.in'. The input file contains the name of the molecule under investigation, the minimum and maximum electron energies, the electron energy increment, the number of averages for the ion and electron current measurements, the wait time between the readings and the number of times that the experiment was to be completely repeated. Next an output file is created with a header file that contains the input file parameters and the time and date for the run. An eight character file name is generated automatically, the first four characters are the date and the next four characters are the time-of-day at which the experiment is run. The electron energy is set and the system pauses for the required wait time. The ion current, electron current, pressure and temperature are then measured. These are converted to SI units and the cross-section, σ, is calculated. The electron energy and the cross-section are written to the output file and the program loops back to the next electron energy. The program is repeated as many times as specified in the input file. There are two industry standard architecture (ISA) cards in the PC: a Lab-Card PCL-812, 0–10 V, 14 bit, analogue-to-digital digital-to-analogue (ADDA) converter with four input channels and two output channels; and a Lab-Card PCL-748, IEEE-488 general purpose interface bus, which controlled and read the picoammeters. The electron energy was controlled by a Spellman MS0.3N12/C 0 to -300 V power supply. This power supply was designed to accept an optically isolated 0 - 10 V input as control,

provided by output channel 1 of the ADDA card, giving a maximum electron energy resolution of 0.018 V.

The temperature is measured by a thermistor inserted into a well drilled into the side of the collision cell. Initially the power requirement for the thermistor to give a sufficient signal level increased the temperature of the thermistor, and led to unreliable results. After the power level was dropped to an acceptable level, the signal required amplification using an LM-10CL-N operational amplifier. The thermistor is calibrated using a water bath, that was slowly heated. The voltage signal from the amplifier is passed into input channel 1 of the ADDA card and converted to a temperature reading. The typical operating temperature of the collision cell is 320 K. The pressure signal from the MKS 627 Baratron is passed into an optically isolated amplifier with a gain of 50 and read by channel 2 of the ADDA card. The voltage signal is then converted to read the pressure in Nm^{-2}. The signal from the Baratron is also read by a Fluke 45 dual display multi-meter to enable the operator to set the pressure prior to an experimental measurement. The IEEE-488 interface allows for complete control of the picoammeters, including setting the trigger rate, and zeroing. The current is returned to the PC as a data string which is converted directly to the numerical value of the current. The ammeters also have a 0-2 V analogue output. The ammeter used to measure the electron current, I^-, is used in a feed-back loop to regulate the filament heating supply in order to maintain a preset trap current, independent of electron energy. This is typically 75-100 nA. The lens potentials, pressure in the cell, and electron trap current are all manually set by the operator prior to the start of each run.

All samples were greater than 99% purity. Gaseous samples were used straight from the cylinder in which they were supplied. Liquid samples were distilled further by several pump-freeze-thaw cycles to ensure complete removal of dissolved gases. The sample line consists of $1/4''$ copper tubing throughout, and sample pressure is monitored with an MKS 122A 0 – 5000 Torr Baratron. The sample line is pumped out to less than 1 Torr prior to the admission of any sample.

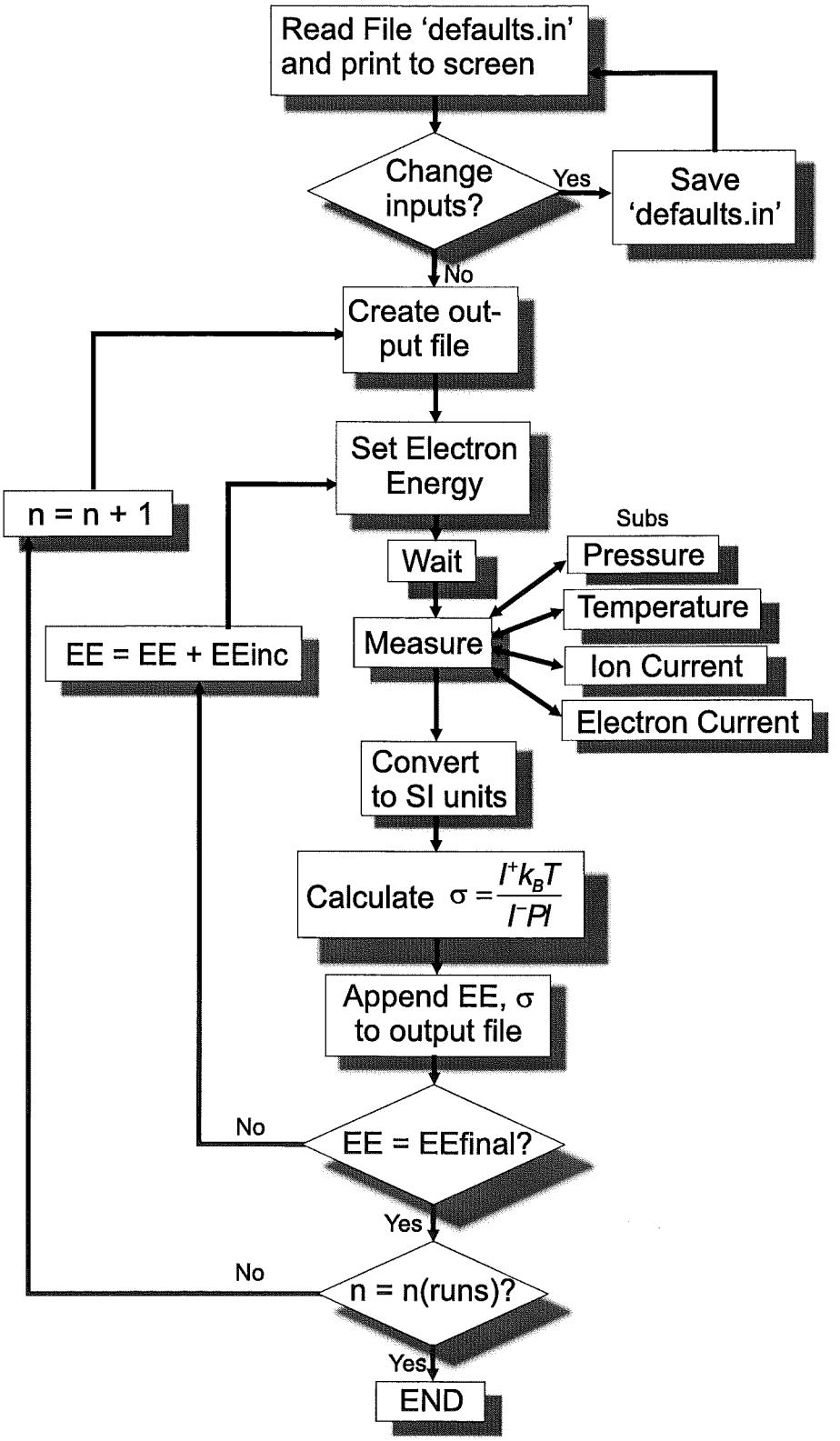

Figure 3.3: Computer interface flow diagram.

3.1.4 Discussion

Simion 6.0 for windows[10] was used to model the cell and to determine the optimum operating conditions. The model simulation was found to reproduce the actual operating conditions fairly well. The typical operating parameters are given in Table 3.1. It is important to show that σ is independent of the operating parameters over the range of cell operating conditions. The measured electron impact ionization cross-section for argon is plotted as a function of chamber voltage and trap voltage at 100 eV electron energy in Figure 3.4, and as a function of pressure in the upper plot of Figure 3.5. When the trap voltage is low, incomplete collection of the electrons leads to a low denominator in equation (2.3), and hence a high value of σ, Figure 3.4 (a). A low cell voltage leads to incomplete collection of the product ions, giving a low numerator in equation (2.3) and hence a low cross-section, Figure 3.4 (b). At very high trap and cell voltages, the electric fields begin to distort the ion and electron trajectories, leading to incorrect values of σ. When the pressure is very low errors in the ion current and pressure measurement are high because of small signals, Figure 3.5 (a). This leads to a large error in σ. As the pressure increases σ becomes constant. Further increases in pressure lead to errors in the cross-section due to scattering of the product ions with the target gas, because at these pressures the experiment is no longer being performed under single collision conditions. As the collision cell becomes contaminated a shoulder begins to develop on the ionization cross-section curve, as shown in the lower plot in Figure 3.5. This became a regular problem during the work on chlorocarbons. To fix this problem the cell had to be disassembled and cleaned thoroughly using petroleum ether (a mixture of hexane isomers), acetone and ethanol. When reassembling the cell it was critical that the filament was correctly aligned with the apertures in the lens assembly otherwise the resulting electron impact curve exhibits large oscillations, particularly at higher energies. Although the purpose of this experiment was not to measure ionization potentials, an extrapolation of the ionization energy from the above graph indicates that the ionization potential for argon is about 12.8 eV; thus the electron energy is within 3 eV of the energy[6] as controlled by the computer.

Table 3.1: Typical operating parameters for electron impact ionization collision cell.

Parameter	Value
Electron Current	100 nA
Filament Current	2 – 2.5 A
L1	-3 V
L2	-2 V
L3	Gnd
Collision Cell	- 20 V
L3b	Gnd
L4	-3 V
Electron Trap	+10 V
Shield	-15 V w.r.t filament.
Pressure	5×10^{-4} Torr
Temperature	320 K
Sample line pressure	200 – 1000 Torr

The electron impact ionization curves are highly reproducible, as illustrated by Figure 3.6, so the statistical uncertainty between the runs is very small. The largest source of random error in this experiment is the measurement of the ion current, since it is the smallest measured variable and therefore the most prone to current leakage through the rest of the circuit. The largest source of systematic error in the experiment is the measurement of the pathlength. The maximum instrument uncertainty may be determined from the sum of the percentage uncertainties and is of the order of 4% as shown on Table 3.2.

Table 3.2: Instrumental uncertainty

Component	Specification	Maximum uncertainty
Keithly 486(I^+)	±0.3% ±500 fA	1.3%
Keithly 486(I^-)	±0.15% ±20 pA	0.2%
MKS 627 Baratron	±0.25%	0.3%
Temperature	320 ±2 K	0.6%
Pathlength	13.3 ±0.2 mm	1.5%
Total		3.9%

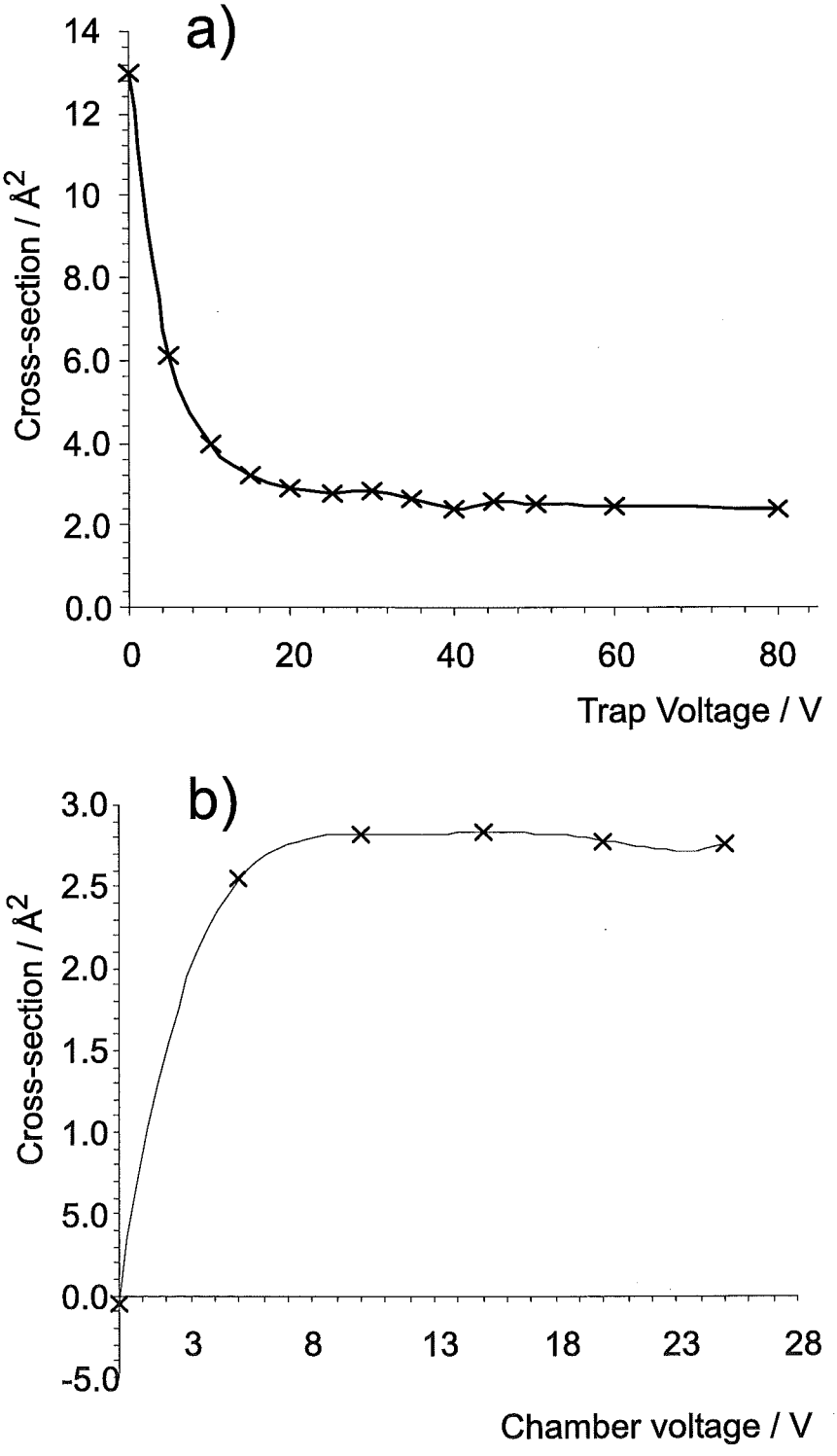

Figure 3.4: The effect of (a) trap voltage and (b) chamber voltage on the measured ionization cross-section.

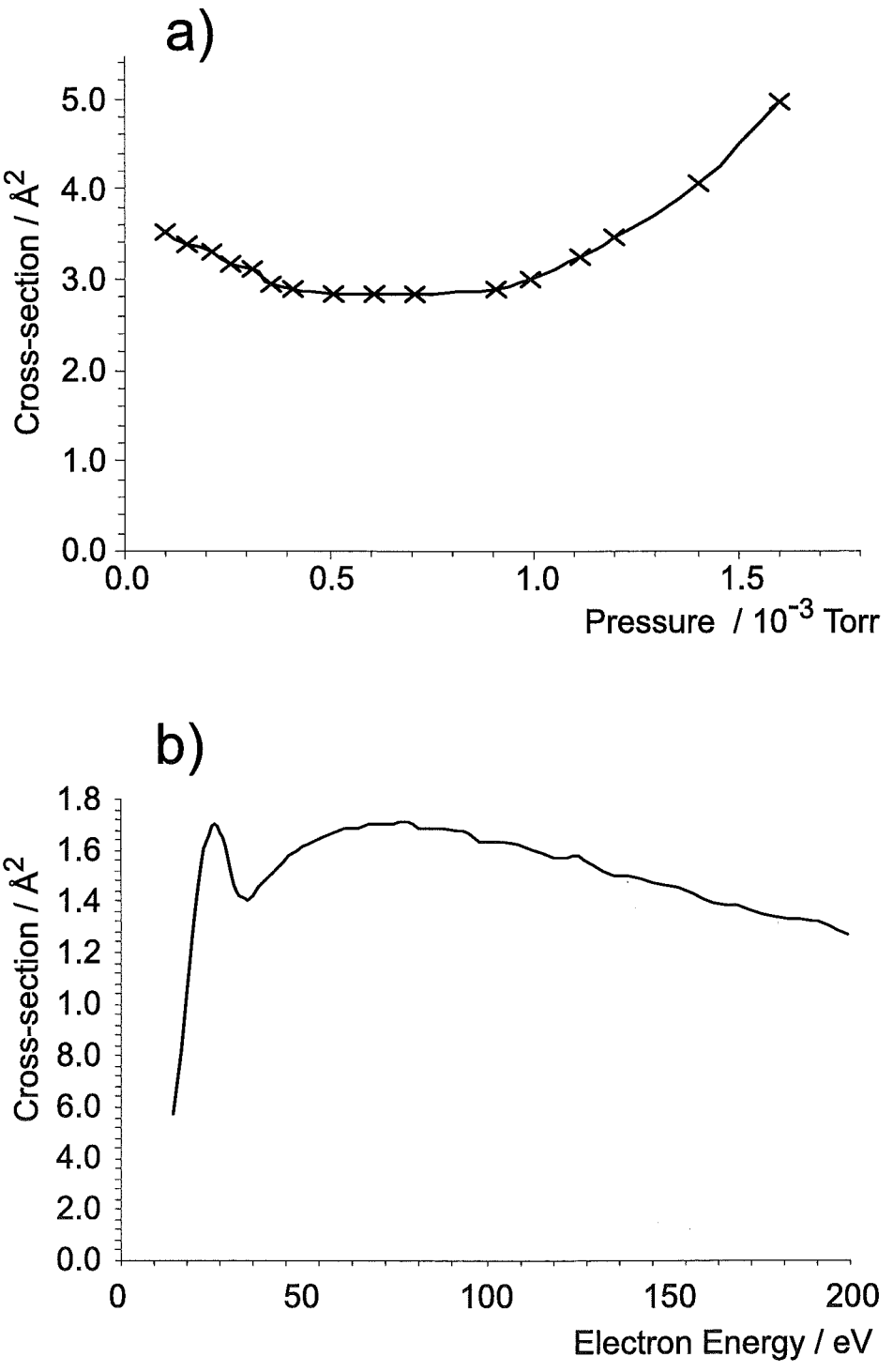

Figure 3.5: (a) The effect of pressure and (b) cell contamination, on the measured ionization cross-section.

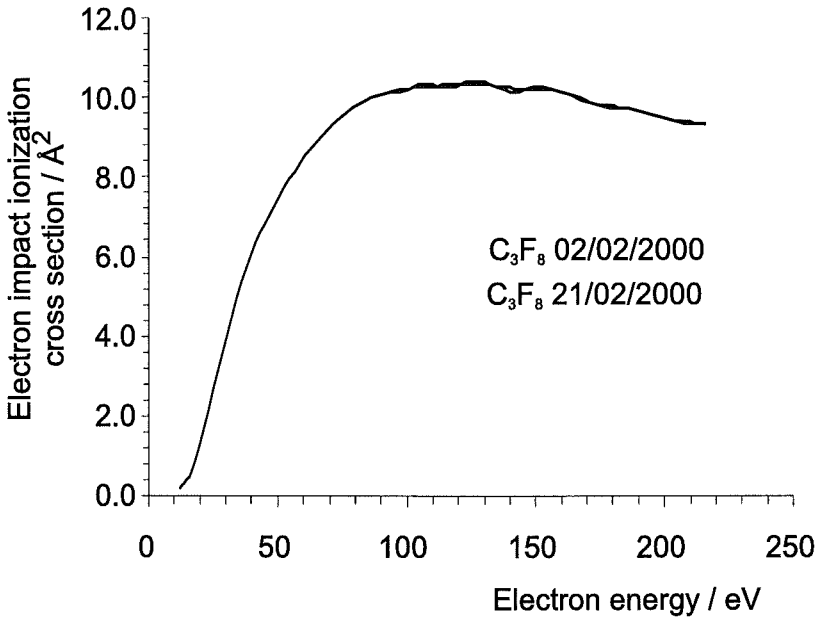

Figure 3.6: Reproducibility of electron impact ionization cross-section curve measured over a three week period.

3.2 Results

3.2.1 The inert gases

The inert gases were measured initially to check that the instrument and control software were functioning correctly, since the inert gases, especially argon, have been determined most frequently by a number of independent groups as indicated in Table 3.3.

The maximum cross-section for argon measured by Otvos and Stevenson,[30] Lampe *et al.*,[31] and and Beran and Kevan[90] have been normalized to the values of Rapp and Englander-Golden. Despite this there are some discrepancies for values for the other inert gases measured to this common reference. The recent results from the group at Rice University[15,16] are lower than the results from all the other groups as indicated on Table 3.3.

Table 3.3: Measured maximum electron impact ionization cross-section values, σ_{max} of the inert gases compared to other values in the literature.

Molecule	σ_{max} Results (Å^2)	σ_{max} (Literature) (Å^2)
He	0.39	0.355[20] 0.21[30] 0.34[31] 0.37[14] 0.291[29] 0.294[90] 0.35[44]
Ne	0.63	1.83[20] 0.46[30] 0.38[31] 0.78[14] 0.575[29] 0.44[90] 0.71[44]
Ar	2.81	3.55[20] 2.86[30] 2.86[31] 2.86[14] 3.025[46] 2.86[90] 2.88[44]

3.2.2 Fluorocarbons

Perfluorinated compounds are of interest in the semi-conductor industry, as plasma etching agents and as cleaning agents for chemical vapor deposition chambers. They also have applications as solvents, refrigerants and are used in fire extinguishers. Although perfluorocarbons are chemically inert, and generally non-toxic, these molecules are potent greenhouse gases that can remain in the troposphere for up to 50,000 years.[91] Absolute electron impact ionization cross-sections have been reported previously for CF_4,[43,50] C_2F_6[50] and C_3F_8[50] in the literature. Beran and Kevan[90] reported relative cross-sections at 70 eV for C_1 - C_7 perfluorocarbons and mixed chlorofluorocarbons at 70 eV electron energy from data obtained using a mass spectrometer ion source. Poll and Meichsner[80] used a quadrupole mass spectrometer to measure the electron impact ionization cross-sections for CF_4, C_2F_6 and C_3F_8, n-C_4F_{10}, C_2F_4, 1-C_4F_8, SiF_4 COF_2 and CHF_3 from threshold to 135 eV. Both of the latter research group results were normalized to the argon cross-section results of Rapp and Englander-Golden. They are not independently absolute.

3.2.3 Chlorocarbons

Chlorocarbons are important as general purpose solvents, cleaning agents and paint strippers, as well as precursors in many chemical processes and as raw materials in the polymer and pharmaceutical industries. C_1 and C_2 chlorocarbons are used in the semi-conductor industry as degreasers in chemical vapor deposition tanks. They are potent greenhouse gases and contribute significantly to the depletion of stratospheric ozone. They have atmospheric photo-dissociation lifetimes of 50 years or more and they are generally toxic and carcinogenic. Very few total electron impact ionization cross-sections have been reported for these compounds in the literature.[13]

Several other simple carbon based compounds, as well as NH_3 and SF_6, have also been measured.

Table 3.2.3 lists the absolute maximum electron impact ionization cross-sections measured using the collision cell described above, as well as the electron energy corresponding to the maximum cross-section. Figures 3.7 to 3.20 show the full electron impact ionization curves from 0 to 220 eV as well as relevant correlations in order to facilitate the determination of specific bond contributions as outlined below.

Table 3.4: Maximum experimental ionization cross-sections.

Molecule	σ_{Max} Å^2	EE_{Max} eV	Molecule	σ_{Max} Å^2	EE_{Max} eV
CF_4	4.77	123	C_2H_4	5.7	90
C_2F_4	5.92	126	E-$C_2H_2Cl_2$	14.49	79
C_2F_6	7.64	120	C_2HCl_3	18.05	82
CF_3CFCF_2	9.89	126	C_2Cl_4	21.74	79
C_3F_8	10.2	126	C_2H_6	7.2	90
CF_3CCCF_3	10.3	123	C_2H_5Cl	10.5	79
$CF_2CFCFCF_2$	10.5	108	1,1-$C_2H_4Cl_2$	14.1	80
$CF_3CFCFCF_3$	11.6	108	1,2-$C_2H_4Cl_2$	14.23	78
CH_3F	3.79	85	1,1,2-$C_2H_3Cl_3$	17.1	82
CF_3H	4.32	120	1,1,1-$C_2H_3Cl_3$	17.6	79
CF_2Cl_2	9.6	82	1,1,2,2-$C_2H_2Cl_4$	19.8	79
CF_3Cl	6.93	105	1,1,1,2-$C_2H_2Cl_4$	21.1	79
CF_3Br	7.87	86	C_2HCl_5	23.61	82
CF_3CN	6.33	105	C_2Cl_6	26.61	90
CH_3CN	6.33	85	1-C_3H_7Cl	14.2	82
CCl_3CN	14.11	86	2-C_3H_7Cl	14.22	82
CH_2Br_2	11.67	78	1-C_4H_9Cl	17.4	80
$CHBr_3$	13.75	80	2-C_4H_9Cl	17.12	80
CBr_4	22.1	86	t-C_4H_9Cl	17.14	86
CH_4	4.23	71	t-$C_5H_{11}Cl$	19.53	86
CH_3Cl	6.63	70	CO_2	3.77	82
CH_2Cl_2	9.35	74	NH_3	2.6	90
$CHCl_3$	12.73	70	SF_6	7.03	126
CCl_4	15.45	71			

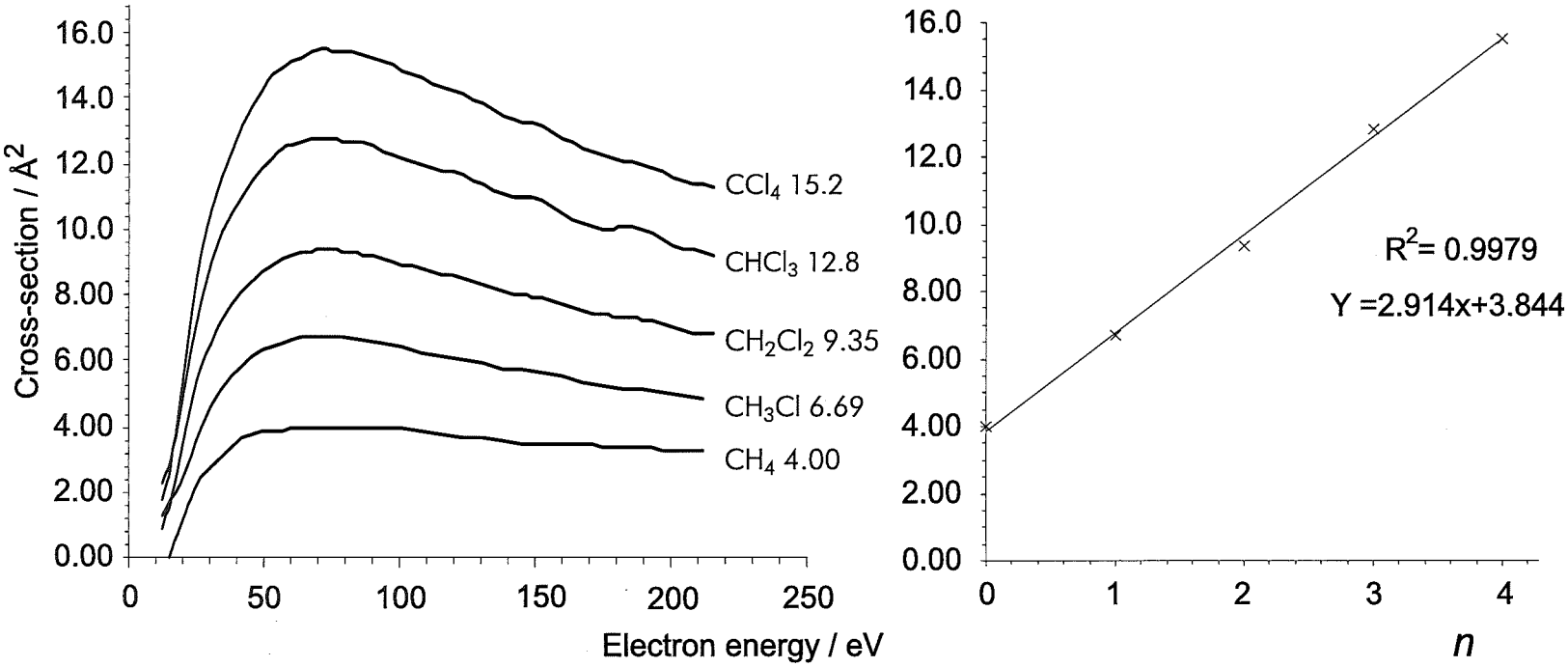

Figure 3.7: Electron impact ionization cross-section curves for methane and chlorine substituted methane. The compounds are indicated on the graph together with the maximum cross-section. The straight line plot is the maximum cross-section against n, the number of chlorine atoms in the target.

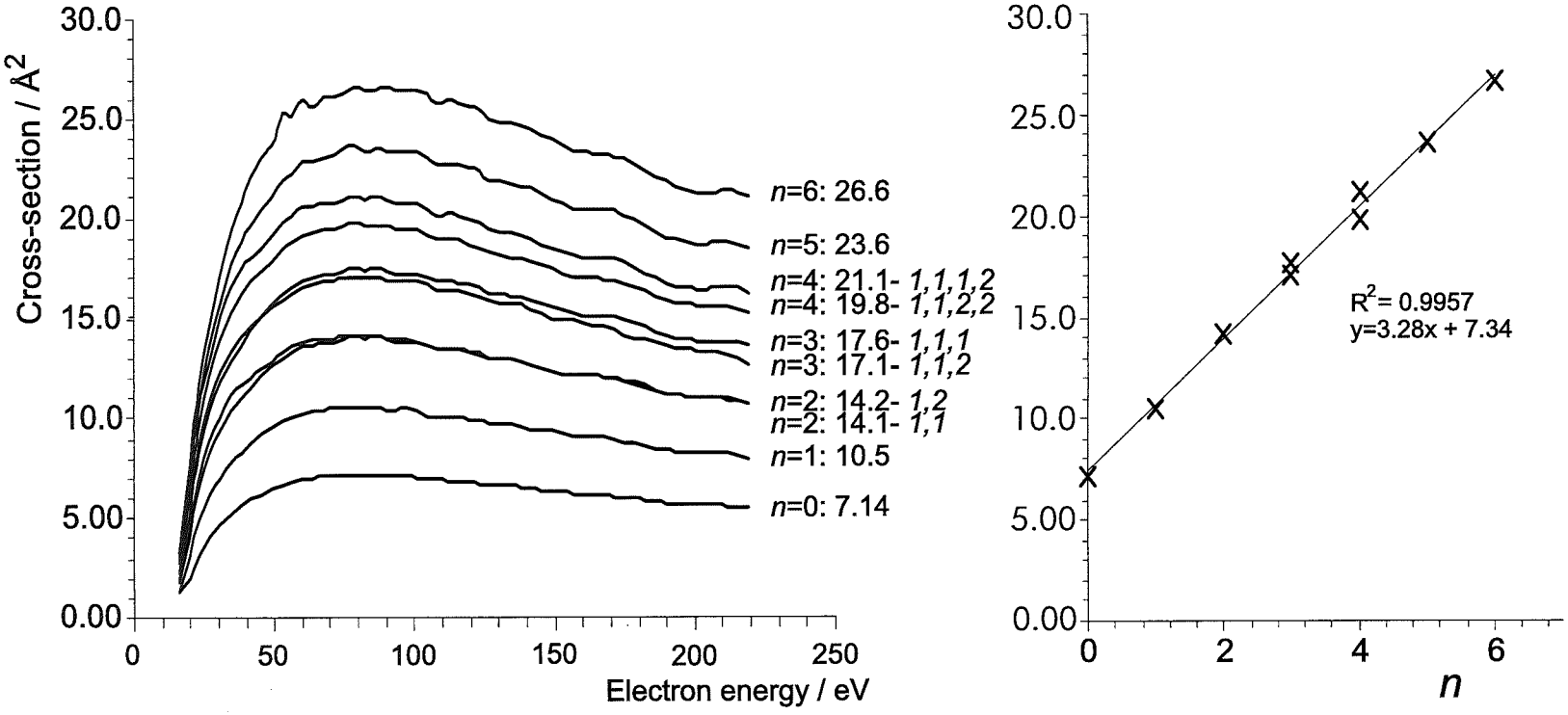

Figure 3.8: Electron impact ionization cross-section curves for ethane and chlorine substituted ethane. The compounds are indicated on the graph, where n is the number of chlorine atoms in the target, together with the maximum cross-section. The isomers are also indicated in italics. The straight line plot is the maximum cross-section against the number of chlorine atoms in the target.

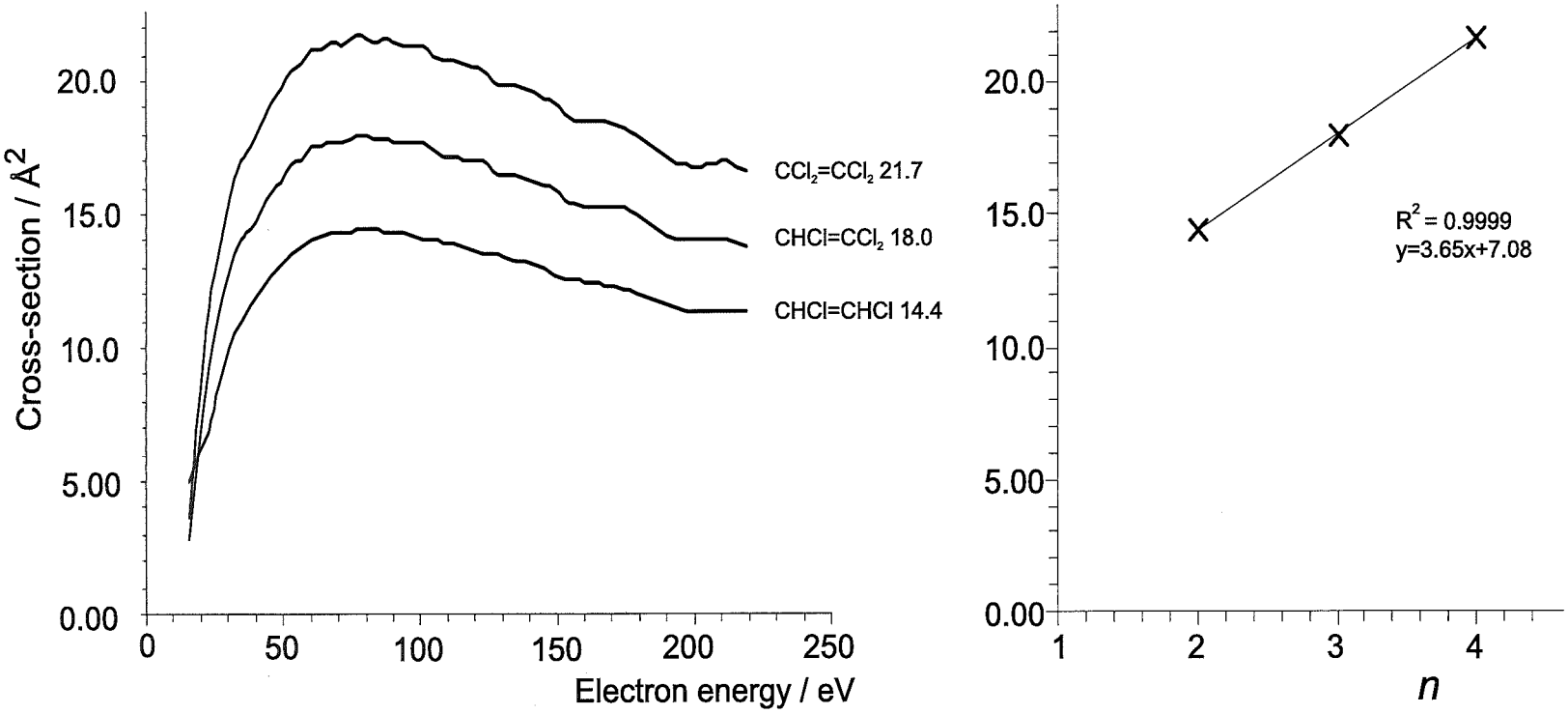

Figure 3.9: Electron impact ionization cross-section curves for chlorine substituted ethene. The compounds are indicated on the graph together with the maximum cross-section. The straight line plot is the maximum cross-section against n, the number of chlorine atoms in the target.

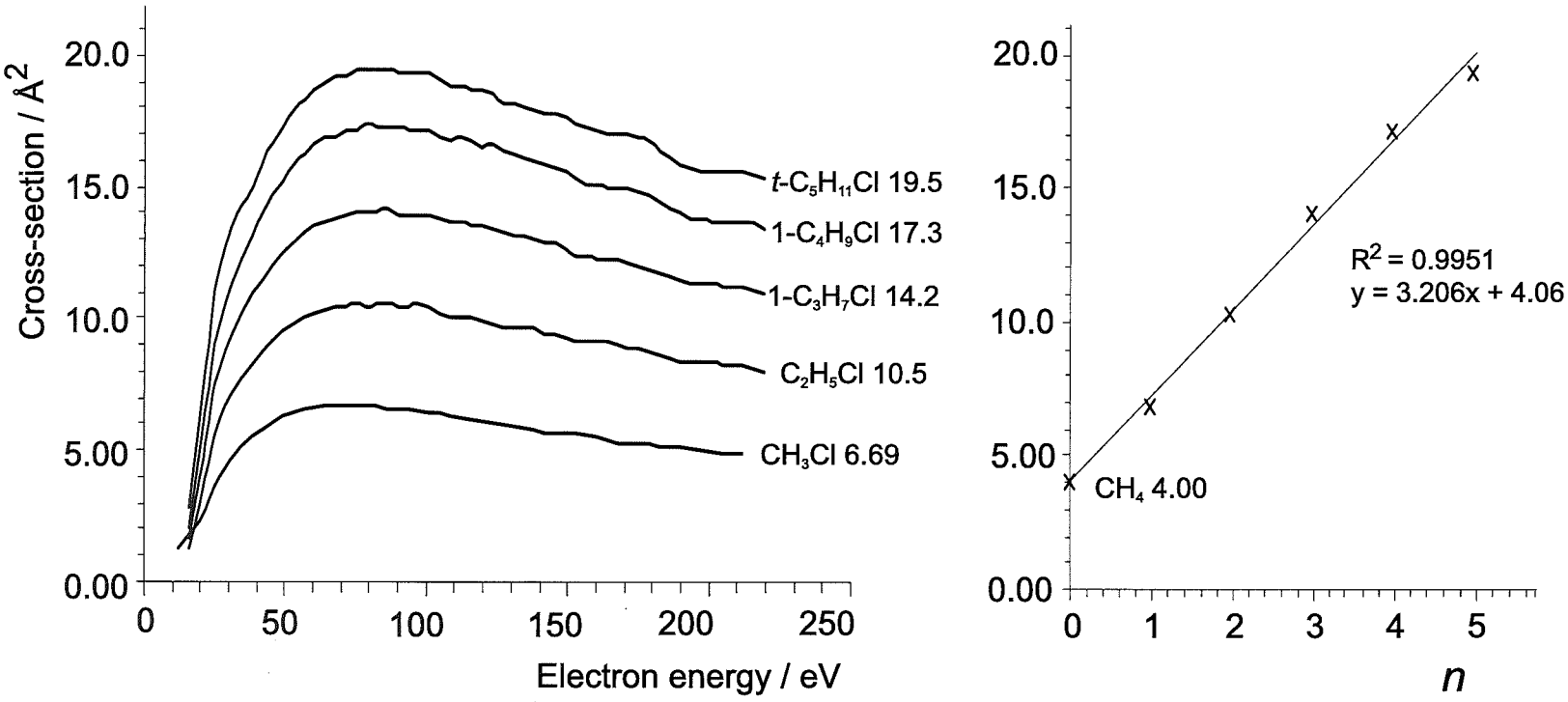

Figure 3.10: Electron impact ionization cross-section curves for monochloro substituted C_1 to C_5 hydrocarbon. The compounds are indicated on the graph together with the maximum cross-section. The straight line plot is the maximum cross-section against n, the number of carbon atoms in the target.

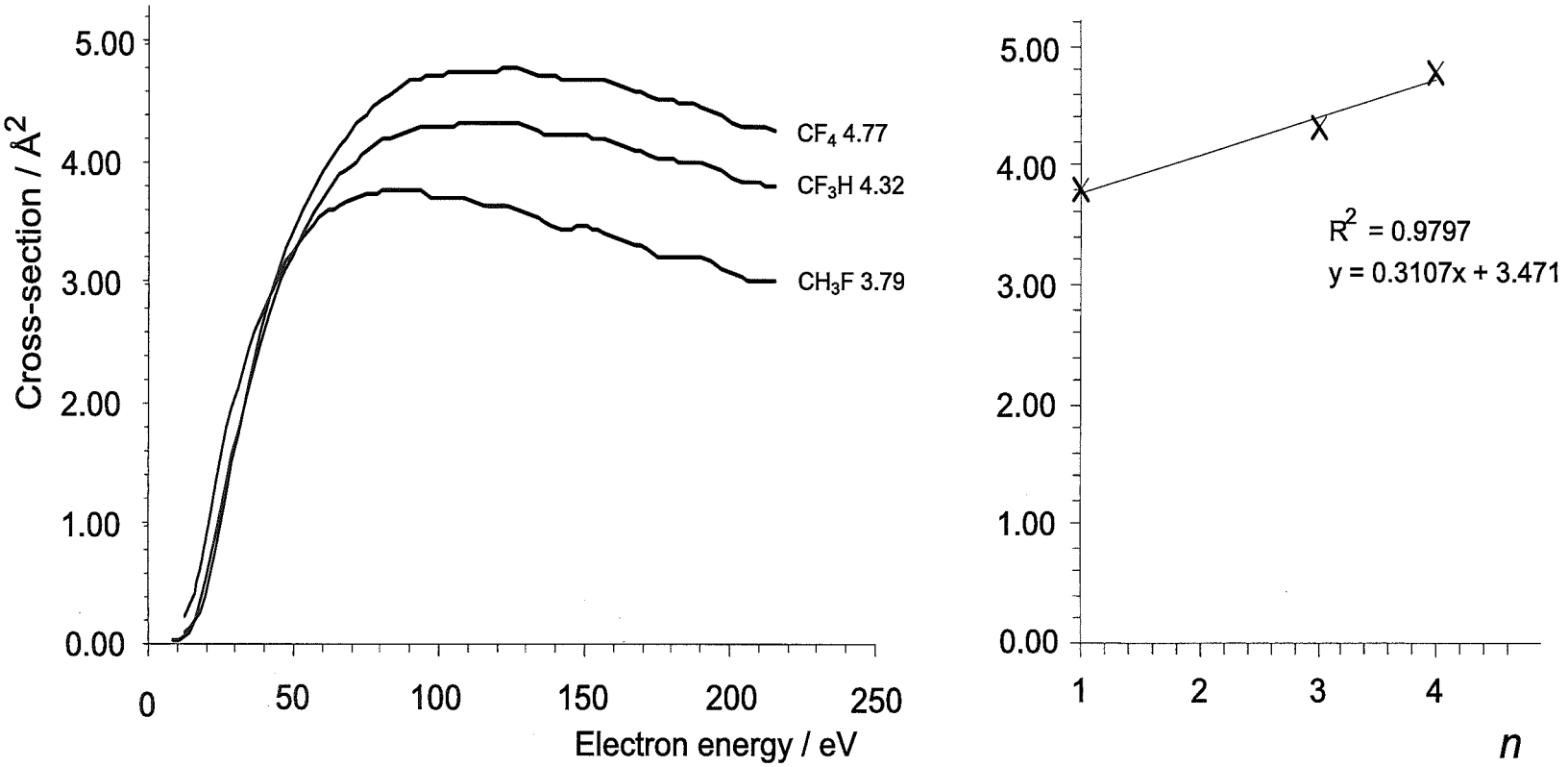

Figure 3.11: Electron impact ionization cross-section curves for fluorine substituted methane. The compounds are indicated on the graph together with the maximum cross-section. The straight line plot is the maximum cross-section against n, the number of fluorine atoms in the target.

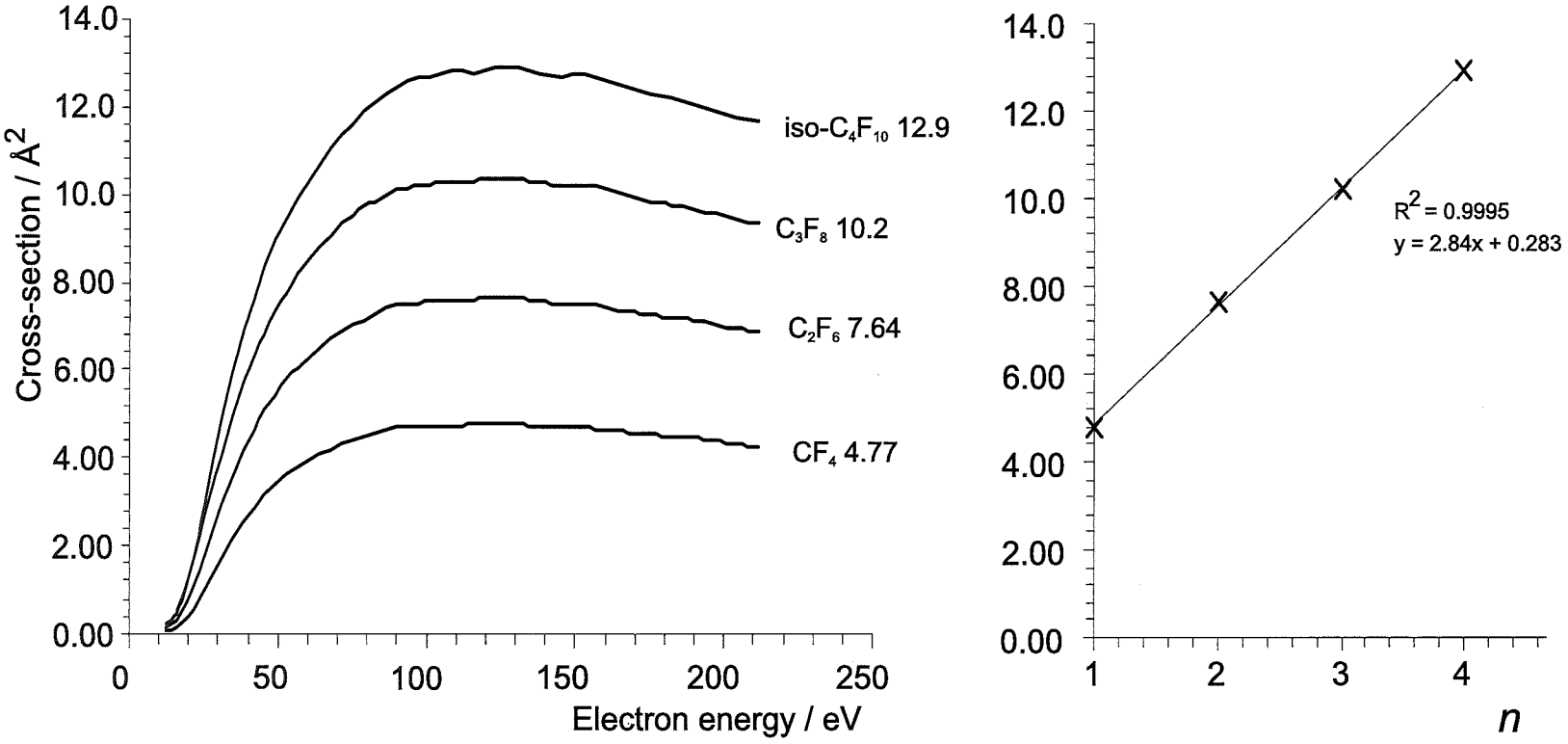

Figure 3.12: Electron impact ionization cross-section curves for C_1 to C_4 perfluorinated alkane. The compounds are indicated on the graph together with the maximum cross-section. The straight line plot is the maximum cross-section against n, the number of carbon atoms in the target.

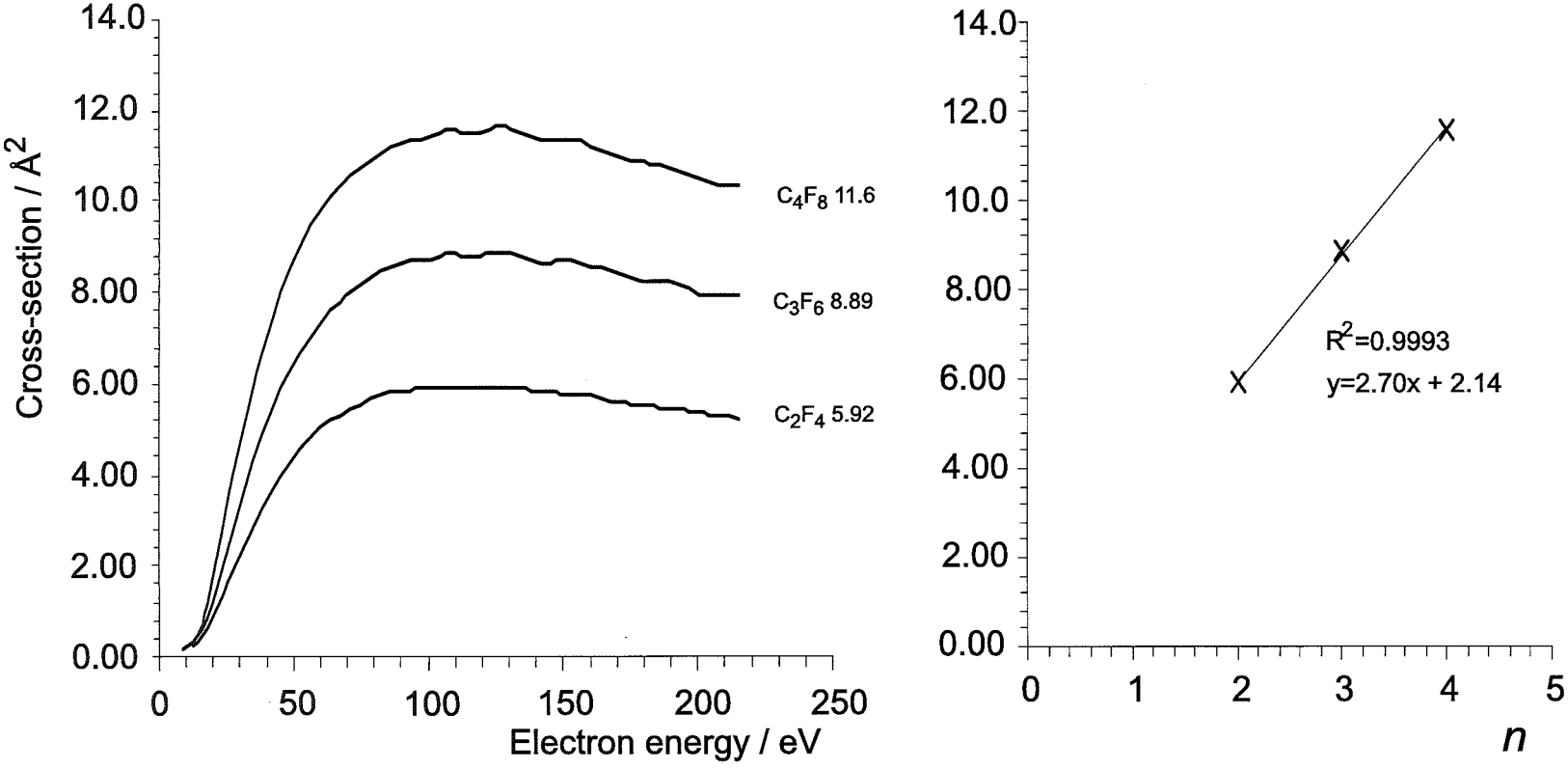

Figure 3.13: Electron impact ionization cross-section curves for C_2 to C_4 perfluorinated alkene. The compounds are indicated on the graph together with the maximum cross-section. The straight line plot is the maximum cross-section against n, the number of carbon atoms in the target.

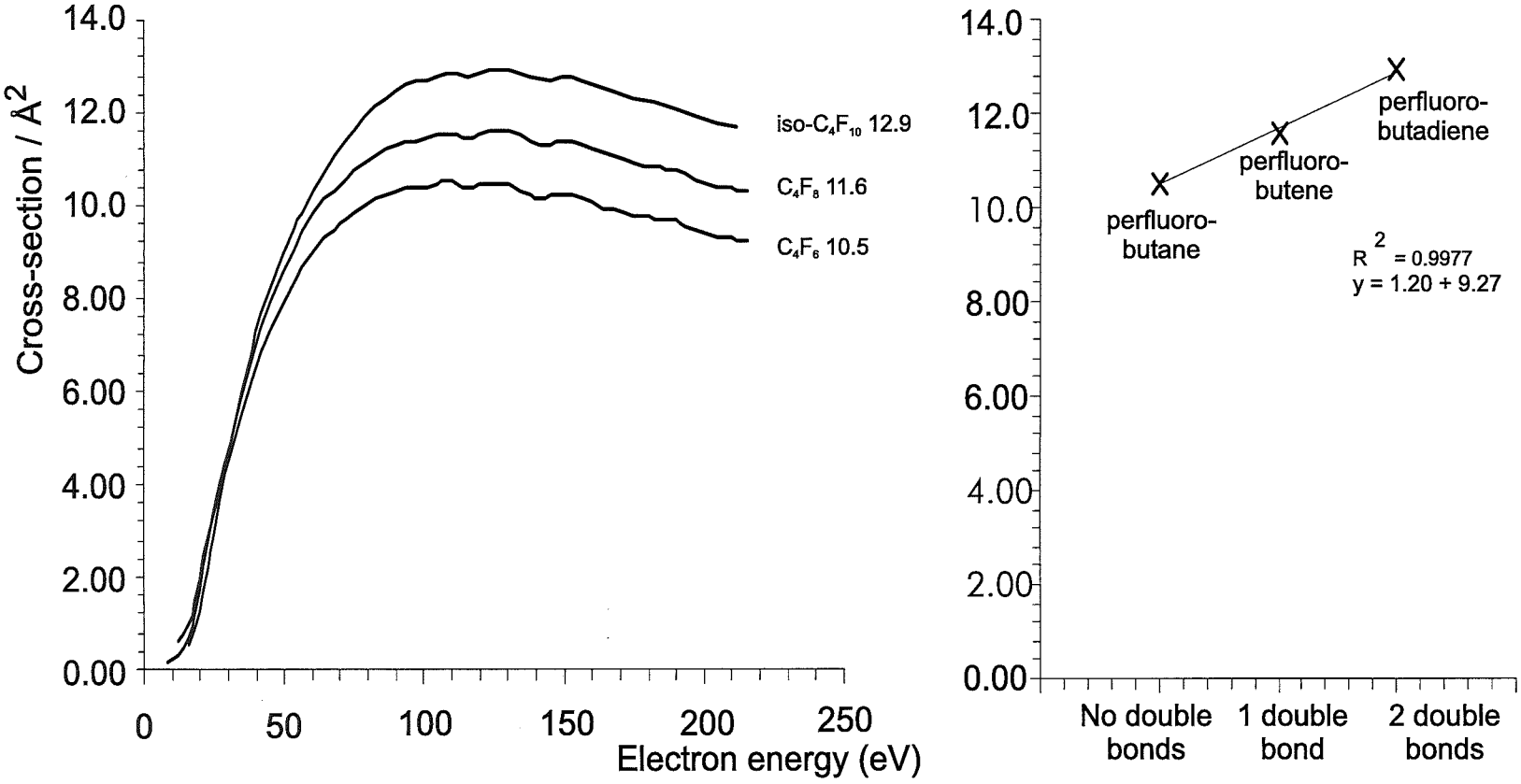

Figure 3.14: Electron impact ionization cross-section curves for perfluorobutane, perfluorobutene and perfluorobutadiene. The compounds are indicated on the graph together with the maximum cross-section. The straight line plot is the maximum cross-section against the number of double bonds in the target.

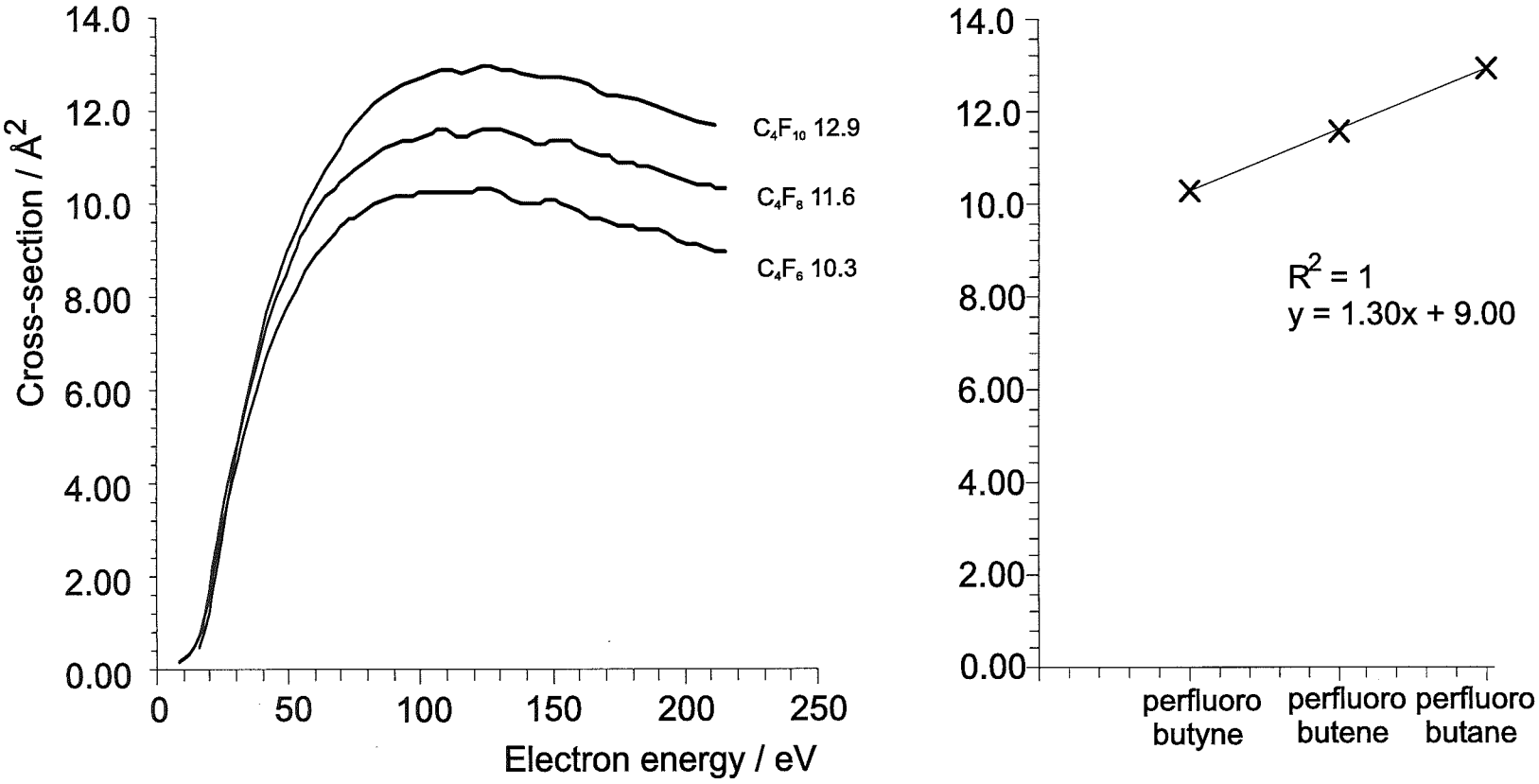

Figure 3.15: Electron impact ionization cross-section curves for perfluorobutane, perfluorobutene and perfluorobutyne. The compounds are indicated on the graph together with the maximum cross-section. The straight line plot is the maximum cross-section against the the indicated compound.

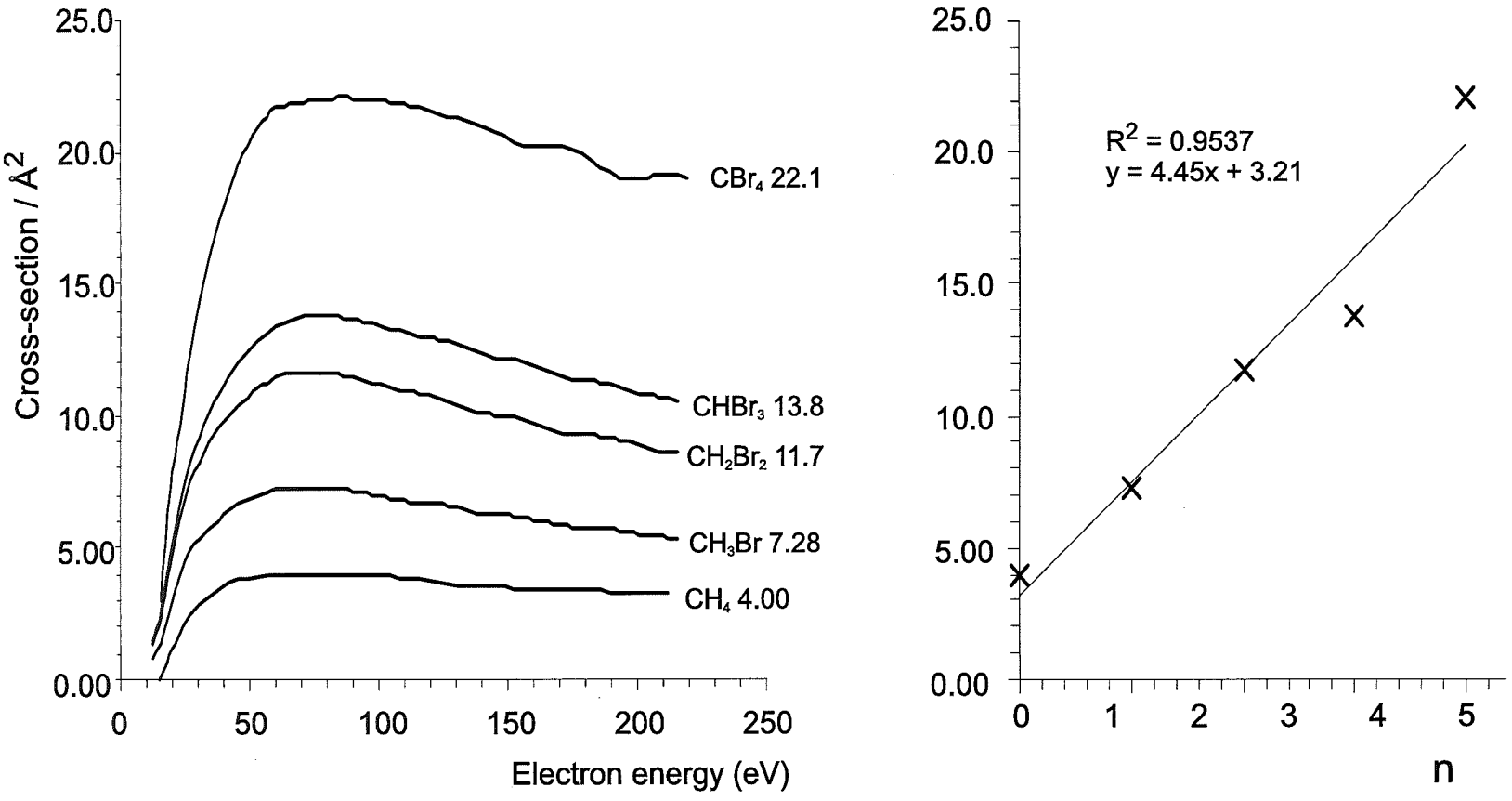

Figure 3.16: Electron impact ionization cross-section curves for bromine substituted methane. The compounds are indicated on the graph together with the maximum cross-section. The straight line plot is the maximum cross-section against n, the number of bromine atoms in the target.

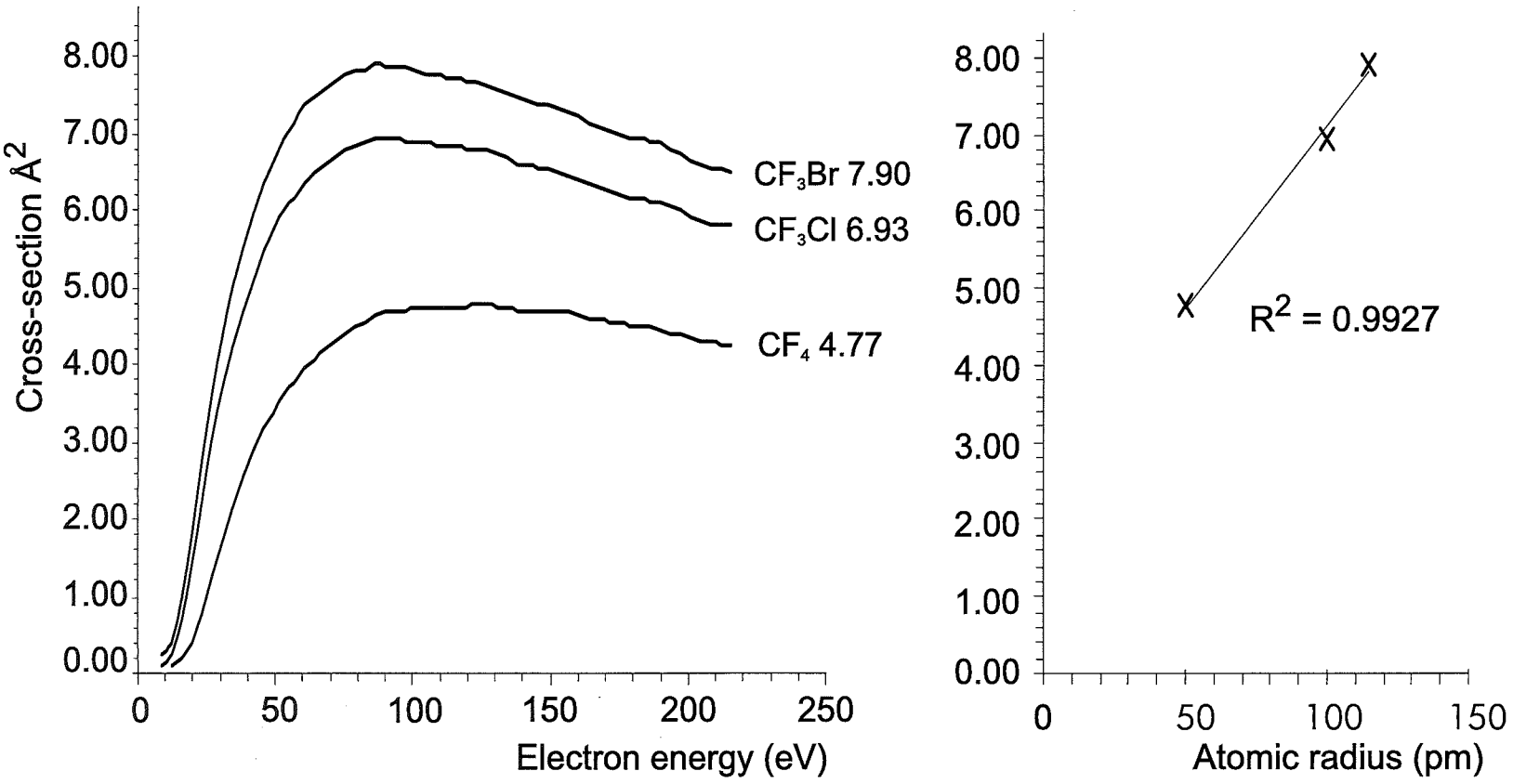

Figure 3.17: Electron impact ionization cross-section curves for perfluorinated methyl halides. The compounds are indicated on the graph together with the maximum cross-section. The straight line plot is the maximum cross-section against the atomic radius of the halide atom.

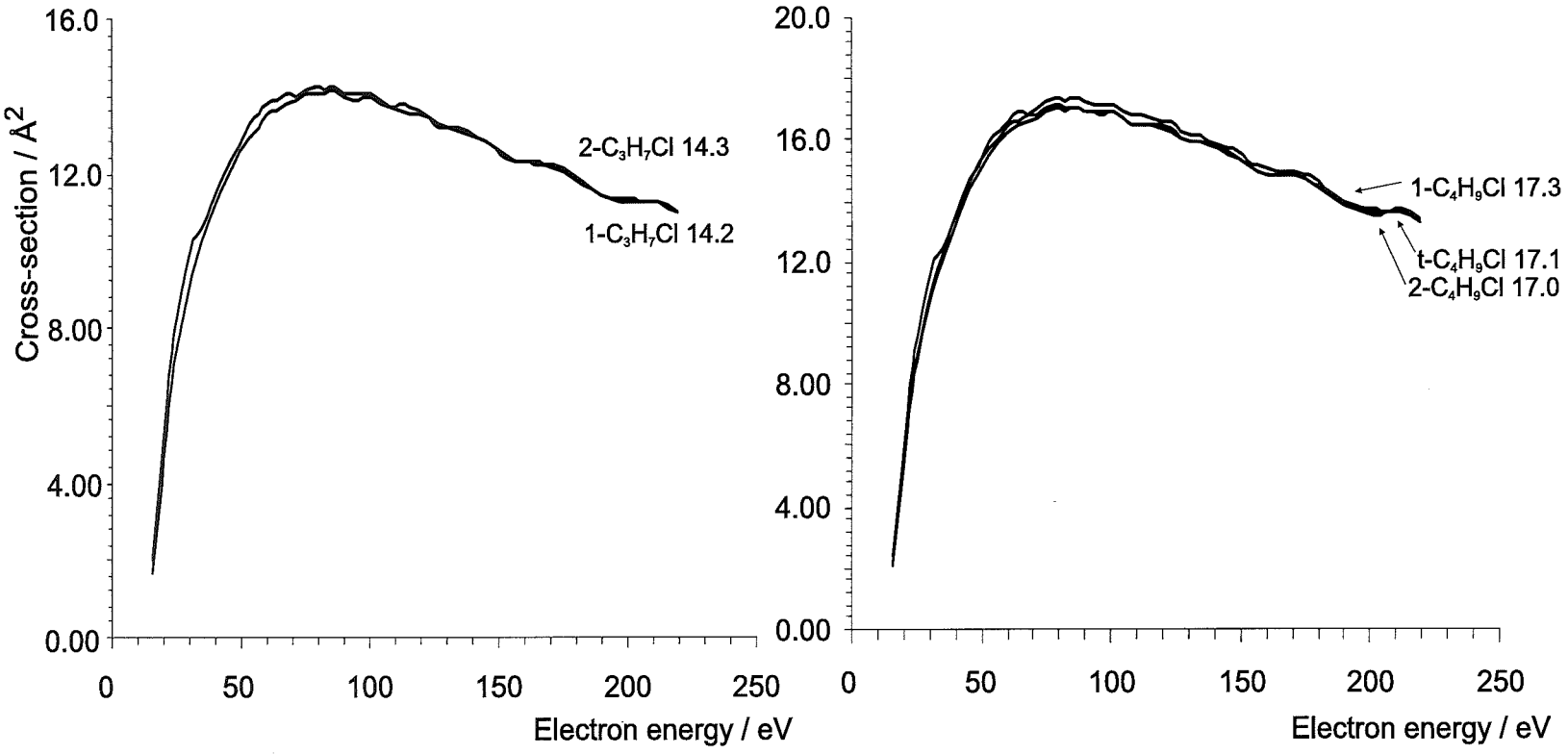

Figure 3.18: Electron impact ionization cross-section curves for monochlorinated propane isomers and monochlorinated butane isomers. The compounds are indicated on the graph together with the maximum cross-section.

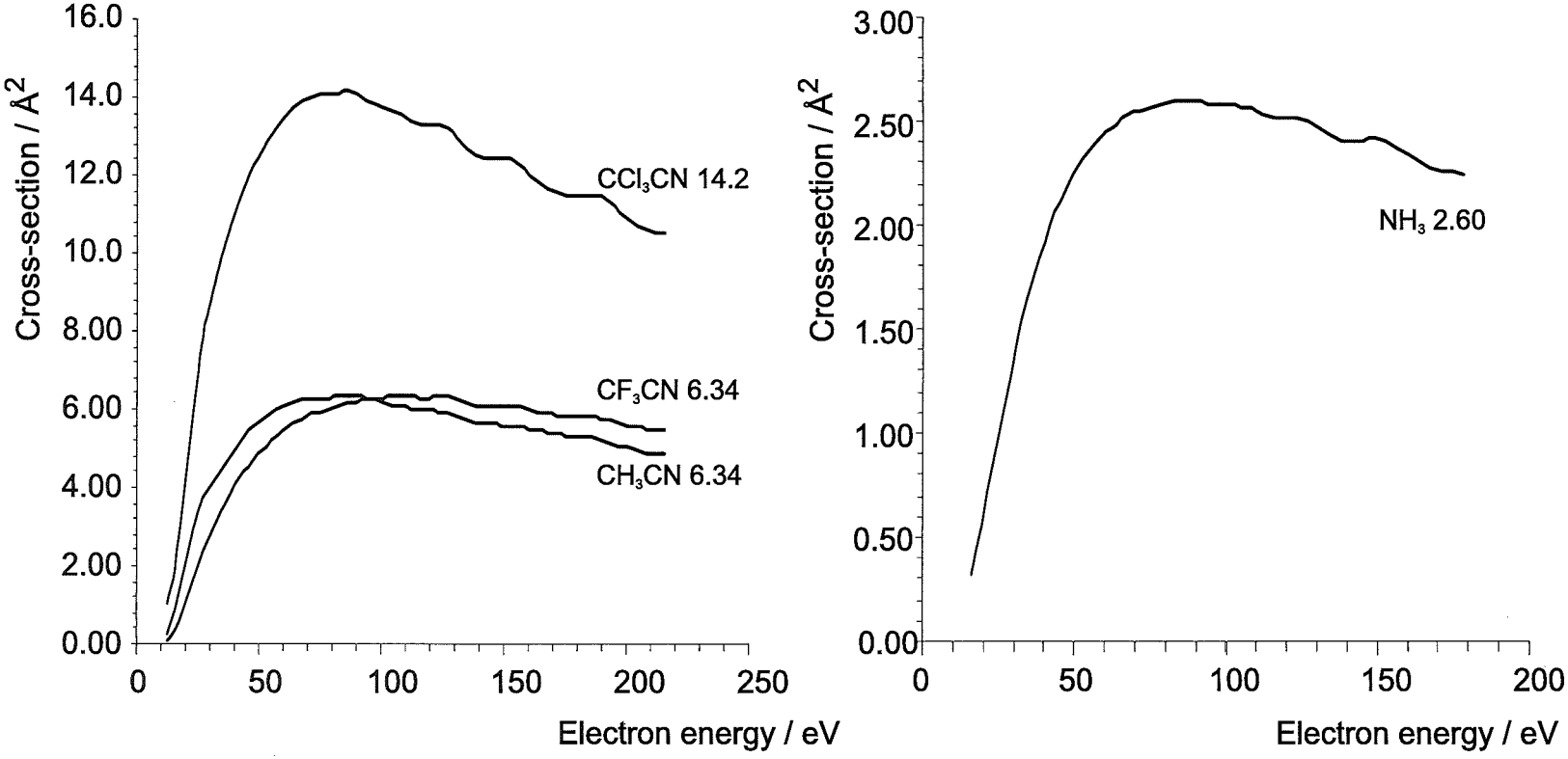

Figure 3.19: Electron impact ionization cross-section curves for acetonitrile. perfluoroacetonitrile and percholoracetonitrile The compounds are indicated on the graph together with the maximum cross-section.

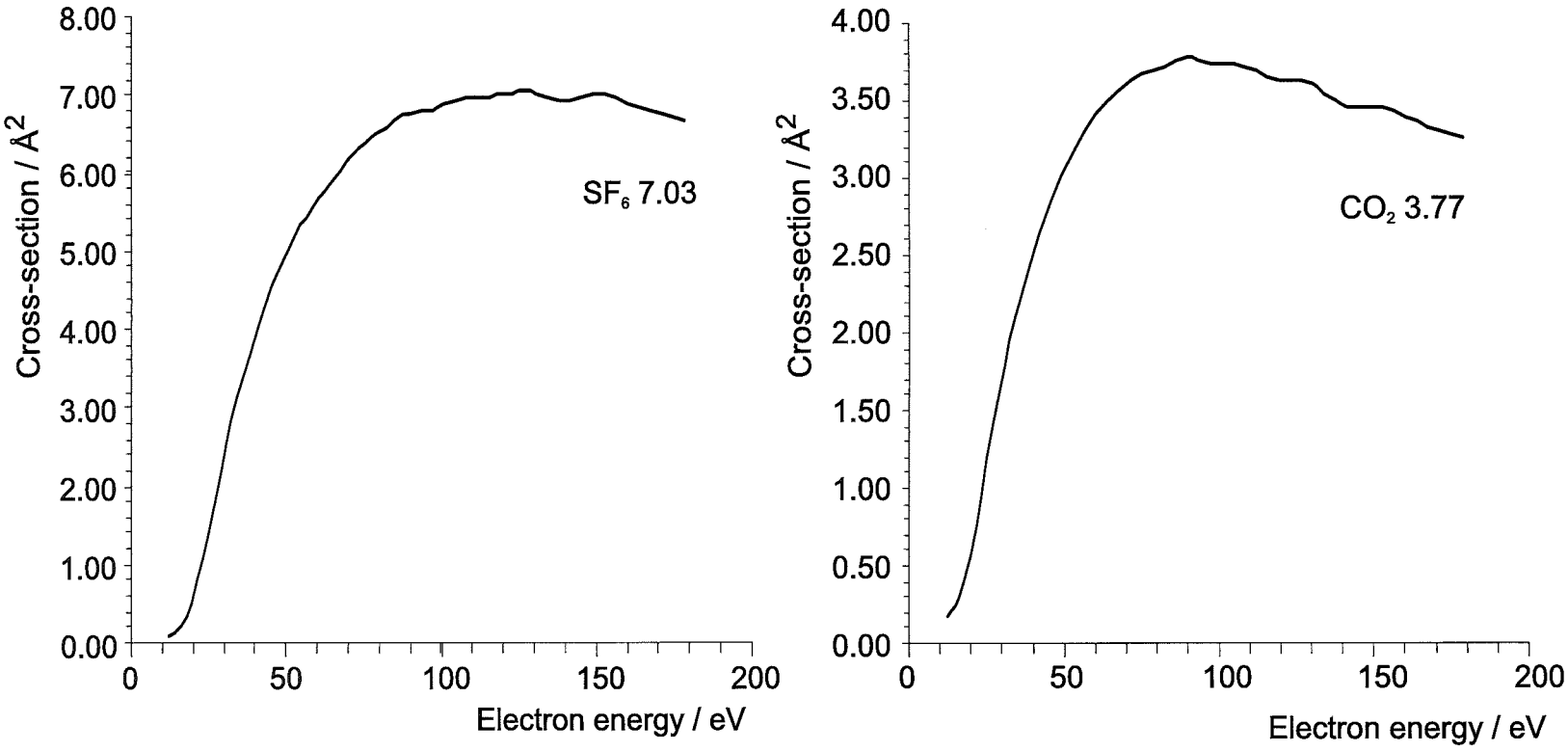

Figure 3.20: Electron impact ionization cross-section curves for carbon dioxide and sulfur hexafluoride. The compounds are indicated on the graph together with the maximum cross-section.

3.3 Correlation of electron impact ionization cross-sections with molecular parameters

There have been several attempts to model electron impact ionization cross-section curves based on molecular parameters. J. J. Thomson[92] used classical mechanics to establish a relationship between σ and the sum over the number of electrons in the nth sub-shell. Bethe[93] observed that the probability of ionization of an atomic target is proportional to the mean square radius of the n, l atomic orbital. Otvos and Stevenson[30] carried out experiments that showed that maximum electron impact ionization cross-sections can be calculated by summing the contributions from the individual atoms in the compound, supporting Bethe's observations. An empirical relationship was suggested by Lampe, Field and Franklin[31] between the maximum electron impact ionization cross-section and the molecular polarizability. These two observations are consistent with each other because of the additive nature of molecular polarizability.

3.3.1 Bond contributions

In the present work it has been found that the relationship between the maximum electron impact ionization cross-section and the sum of the bond contributions, rather than the atomic contributions, works very well for all of the compounds that have been measured. A set of bond contributions to the maximum electron impact ionization cross-section have been determined from the equations of the linear plots in Figures 3.7 to 3.20 and are given on Table 3.5. The maximum electron impact ionization cross-section can thus be predicted for compounds that have not been measured to within 10% of all the target species.

In addition, bond contributions can be used to establish maximum ionization cross-sections for compounds that cannot be readily modeled using either the binary encounter Bethe (BEB) or the Deutsch-Märk (DM) models (to be discussed in Chapter 5). For example, the bond contributions determined experimentally in this work can

Table 3.5: Bond contributions to the maximum electron impact ionization cross-section. † taken from Hudson[94] using the same apparatus.

Bond	Cross-section component (Å^2)
C-H	1.0
C-F	1.1
C-Cl	3.8 for C = 1
	4.4 for C > 1
C-Br	4.5
C-CN	3.0
C-C	1.0
C=C	1.5
C≡C	1.7
C-CH_2	2.8†
C-OH	1.8†

be used to estimate σ_{max} for CCl_3CN: 3(C-Cl) + 1(C-CN) gives an estimated maximum cross-section of 14.4 Å^2, compared with the measured value of 14.2 Å^2. Figure 3.21 shows the measured cross-section plotted against the estimated bond contribution cross-section for all the compounds measured. An adjustment needs to be made to the value of the C-Cl bond depending on the length of the carbon chain, and indications point to steric factors being responsible for this behavior. In the future, this work could be extended to include the bromine substituted hydrocarbons. The effect of substituting a fluorine with a hydrogen for the examination of steric effects would have less of an impact because of the similarity in the bond contribution of the C-H and C-F bonds. Recently, using the apparatus described above, Hudson *et al.*[94] have determined electron impact ionization cross-sections for the C_1 to C_4 alcohols. From these studies bond contributions were determined for the addition of a methylene group and for the C-OH bond contribution. These results reinforced the concept that each bond contributes a characteristic contribution to the maximum ionization cross-section. Each methylene group in the back-bone of the aliphatic alcohols contributed 2.8 Å^2 to the cross-section. This is close to the value determined from the bond contributions shown in Table 3.5: 1 × (C-C) contribution plus 2 × (C-H) contribution gives

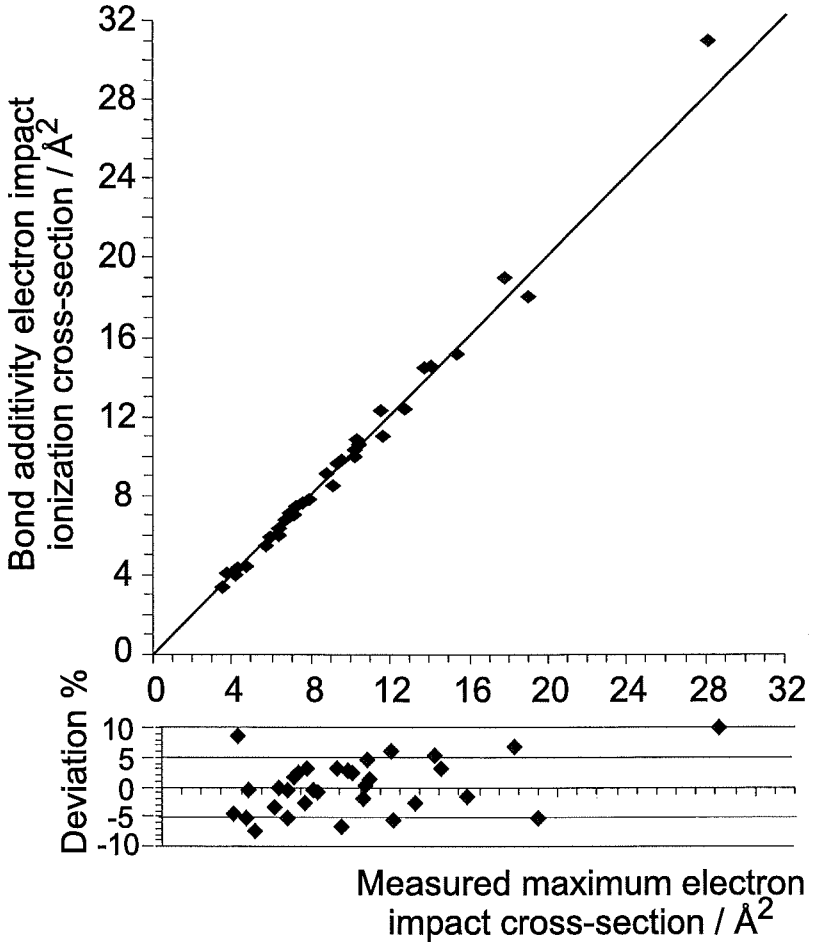

Figure 3.21: Relationship between measured and calculated maximum electron impact ionization cross-sections using the bond additivity model.

a methylene unit contribution of 3.0 Å^2 These values are within 6% of the each other and within the usual experimental uncertainties in the literature. Because of the wide ranging success of the bond contribution model, maximum ionization cross-sections for compounds that have not been measured can now be predicted with a high degree of confidence. A request was received for the experimental cross-section data for the compounds CF_2Br_2 and $(CF_2Br)_2$. Unfortunately, measurements were unable to be made for these compounds.[a] However, using the bond contribution approach it is possible to estimate the maximum cross-sections with a high degree of confidence. Estimating

[a] The New Zealand Government introduced the "Ozone Layer Protection Order 1991" which prohibits the importation of a large number of named halocarbons including CF_2Br_2 and $(CF_2Br)_2$. Most of the compounds studied in this work were purchased before this Order was introduced.

the maximum ionization cross-section for CF_2Br_2: 2 × the (C-F) contribution plus 2 × (C-Br) contribution giving a value of 11.2 Å^2. Using the same method to estimate the maximum cross-section for $(CF_2Br)_2$ gives a value of 14.4 Å^2.

3.3.2 Polarizability

When a molecule is subjected to an electric field, E, a dipole moment is induced in the molecule. The extent of the induced dipole is proportional to the electric field. The constant of proportionality, α, is called the polarizability of the molecule.[b]

$$\mu^* = \alpha E \tag{3.1}$$

α has the units of $C^2m^2J^{-1}$, but this is normally converted into the polarizability volume with units of m^3, by the following:

$$\alpha' = \frac{\alpha}{4\pi\epsilon_0} \tag{3.2}$$

Quantum mechanically, polarizability may be written as:

$$\alpha = \frac{2}{3}\sum_n \frac{|\mu_{0n}|^2}{E_n - E_0} \tag{3.3}$$

with

$$\mu_{0n} = \int \psi_0^* \boldsymbol{\mu} \psi_n d\tau = \langle \psi_0 | \mu_{0n} | \psi_n \rangle \tag{3.4}$$

With $\boldsymbol{\mu}$ as the electric dipole moment operator integrated over the wave functions ψ from quantum states 0 to n. If the transition dipole moment is set to the charge on the electron, q, multiplied by the radius of the molecule, R, then from equation (3.3)

$$\alpha \approx \frac{2q^2R^2}{3\Delta E} \tag{3.5}$$

[b] Polarizability is discussed in more detail in section 5.5.1.

where the excitation energies have been approximated to a mean value ΔE. If ΔE is set to the the approximate ionization energy, $q^2/4\pi\epsilon_0 R$, then the polarizability volume, $\alpha' \approx \frac{2}{3}R^3$ indicating that the polarizability volume is of the same order of magnitude as actual molecular volume; the larger the molecule the larger the polarizability volume, and hence the larger the electron impact ionization cross-section. Strictly, polarizability volumes should be tensors but usually the term polarizability refers to the mean polarizability over all orientations. It has been shown from first principles by Harland and Vallance[89] that the maximum electron impact ionization cross-section is related to the quantity $(\alpha/E_0)^{1/2}$, to a better degree than the actual polarizability volume, where E_0 is the molecular ionization potential. On inspection of equation (3.5) and the subsequent text it is clear why this is the case. The approximate ionization potential has been replaced by the actual ionization potential and by taking the square root the volume is reduced to something closer to cross-sectional area. The following arguments were used to deduce the dependence of the cross-section on $(\alpha/E_0)^{1/2}$.

For an atom with polarizability α, an electron will induce a dipole moment μ proportional to the electric field experienced by the atom due to the electron, given by equation (3.1). This produces a potential, ϕ, due to the dipole:

$$\phi = \frac{\mu \cos\theta}{4\pi\epsilon_0 r^2} \tag{3.6}$$

where θ is the angle between the dipole axis and the vector between the electron and the atom. Because the electron induces the dipole along the vector between the electron and the atom, θ is equal to zero. The potential energy of the electron, charge q, is simply given by:

$$V = -\phi q = \frac{-\alpha q E}{4\pi\epsilon_0 r^2} \tag{3.7}$$

The Coulomb field E produced by the electron is given by Coulombs law:

$$E = -\frac{q}{4\pi\epsilon_0 r^2} \tag{3.8}$$

Combining equations (3.7) and (3.8)

$$V = \frac{\alpha q^2}{(4\pi\epsilon_0 r^2)^2} \tag{3.9}$$

In order to derive a relationship between polarizability and cross-section it is necessary to assume that ionization will occur when the atom absorbs more energy from the potential field then the ionization energy of the target species. This allows the maximum impact parameter, $b_{\max}$, to be related to the ionization potential. When the Coulomb potential is equal to the ionization potential, $r = b_{\max}$,

$$E_0 = \frac{\alpha q^2}{(4\pi\epsilon_0 b_{\max}^2)^2} \tag{3.10}$$

on rearranging,

$$b_{\max}^2 = \frac{q}{4\pi\epsilon_0}\sqrt{\frac{\alpha}{E_0}} \tag{3.11}$$

Combining the numerical constants and setting $\sigma_{\max} = \pi b_{\max}^2$, the maximum cross-section is then given by

$$\sigma_{\max} = 11.92\sqrt{\frac{\alpha}{E_0}} \tag{3.12}$$

for α in Å^3, E_0 in eV and the ionization cross-section in Å^2. This model also works for molecules, even for those with a permanent dipole, because any effect of the dipole interaction with the electron averages to zero in a randomly oriented sample.[88] Figure 3.22 shows plots of the cross-section against polarizability and $(\alpha/E_0)^{1/2}$. It is likely that variations in the reported values of α and E_0 contribute to the spread in these plots. Often several values are quoted for the polarizability values of even small molecules and for larger molecules there are no measurements. This relationship may well prove to be a good source of molecular polarizability volumes.

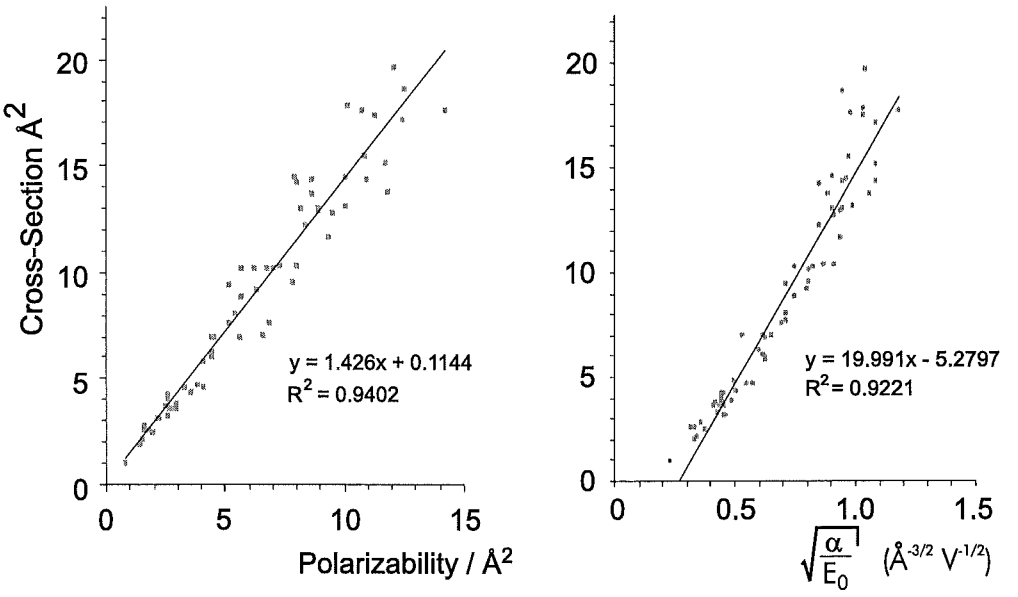

Figure 3.22: Relationship between polarizability and the maximum electron impact ionization cross-section (left) and the relationship between the quantity $(\alpha/E_0)^{1/2}$ and the maximum electron impact ionization cross-section (right).

3.3.3 Steric and isomeric effects

Several isomers of the chlorocarbon compounds were measured as shown in Figure 3.18. In general, the values for $\sigma_{\max}$ and the shape of the curves for the isomers are the same, within experimental uncertainty. Some simple modeling was done using the software package Chem Draw to measure the available surface area for five different projections of 1,1,2,2- and 1,1,1,2- tetrachloroethane and it was found that the 1,1,2,2-tetrachloroethane isomer had a larger projection in all but one of the cases, with the average projection 4.4% larger and the largest difference in the projection being 11%. This is not in agreement with the observed 2% difference between the experimental cross-sections for these isomers, presumably electronic and polarizability effects between the isomers must be the dominant factor. At the present time a series of long carbon chain esters are being synthesized and electron impact ionization cross-sections measured in order to compare the steric effects for a range of isomers.

4. MEASUREMENT OF PARTIAL ELECTRON IMPACT IONIZATION CROSS-SECTIONS

4.1 The method

Partial ionization cross-sections quantify the probability for the formation of an ion with a particular m/z ratio as a function of electron energy, as discussed in the Introduction. The first attempt to measure partial ionization cross-sections using a Spectramass PC200 quadrupole mass spectrometer sampling ions through a 3 mm diameter aperture in the collision cell (Figure 3.1) was abandoned due to low ion signal levels. The entire ionization cell was floated to a positive voltage, equal to the required ion energy for the quadrupole. The failure of this method was unfortunate because the measurement of both partial and total ionization cross-sections simultaneously could have been performed.

Subsequently, an SXP-300 quadrupole mass spectrometer was used independently to measure mass spectra as a function of electron energy as shown in Figure 4.1. Partial ionization cross-sections were extracted using the National Institute of Standards and Technology (NIST)[6] mass spectral data base to account for mass discrimination effects. The sum of the partial ionization efficiency curves was normalized to the absolute ionization cross-sections, Table 3.2.3.

Partial cross-sections were determined by application of the following computer operations.

1. Raw data from the partial electron impact ionization experiment for electron

energy ee was loaded into an array $[ee, I_{i,\text{raw}}]$ for ion i, with intensity I

2. Data in the array were scaled to the NIST mass spectral data, $I_{i,\text{nist}}$ as a percentage of the base peak at ee =70 eV

$$[ee, I_{i,\text{NIST}}\frac{I_{i,\text{raw}}}{I_{i,\text{raw,70eV}}}] = [ee, I_{i,\text{scaled}}] \tag{4.1}$$

3. A cubic spline was fitted using a *Numerical Recipes*[95] algorithm to determine the coefficients a, b, c and d.

$$I_{i,\text{scaled}} = a(ee)^3 + b(ee)^2 + c(ee) + d. \tag{4.2}$$

The electron energy EE from the total cross-section data-set was substituted into equation (4.2). This approach is justified because the dependence of EE and ee on the cross-section is a continuous smooth function and $EE \approx ee$. The new array $[EE, I_{i,\text{scaled}}]$ has intensities that match precisely the electron energy values that were used in the total electron impact ionization cross-section measurements. All of the above steps are repeated for $i = 1$ to n where n is the number of ions for which raw data has been collected.

4. After the above steps were completed it was a trivial task to calculate the pseudo-absolute partial electron impact ionization cross-section for ion i. The data were loaded into a two dimensional array of ion intensities. The normalization factor to calculate the partial cross-section was determined.

$$\kappa = \frac{I_{\text{total}}}{\sum_{i=1}^{n} I_{i,\text{scaled}}} \tag{4.3}$$

The final array contains the data $[EE, \kappa I_{i,\text{scaled}}] = [EE, \sigma_i]$ which were saved to disk and plotted in Figures 4.2 to 4.9.

Using this method pseudo-absolute partial cross-sections were measured for six of the perfluorocoarbon compounds listed in Table 3.2.3.

4.2 Experimental details

The vacuum chamber was pumped by a Varian 4″ 1200 ls^{-1} diffusion pump backed by an Edwards EDM 20 330 $l\text{min}^{-1}$ mechanical pump. The diffusion pump was separated from the main chamber by an Airco 5010-R hand operated rotary gate valve, and a Varian liquid nitrogen trap. The sample was admitted through a 1/8″ stainless steel tube directed toward the back of the ion source. A schematic of the quadrupole mass spectrometer, ion source and associated electronics is shown in Figure 4.1. Ions were formed by electron impact from an open architecture ion source using a computer controlled Spellman MS0.5N12/C 0 – -500V power supply for electron energy control. Mass-tuning of the quadrupole was also computer controlled using an LM-741 operational amplifier. The ion signals were collected from the channeltron particle multiplier and amplified through a Stanford Research Systems SR570 current amplifier. A Stanford Research Systems SR250 box-car integrator was used to collect the amplified ion signals used to average the data. The boxcar was computer interfaced through a Stanford Research Systems SR245 RS-232 serial bus that also controlled mass-tuning. The integrator and serial bus were installed in a Stanford Research Systems CAMAC crate, using a SR280 power supply and digital readout display.

Prior to each run the SXP-300 controller was set to sweep mode in order to monitor the entire mass spectrum, so that tuning of the ion source could be carried out. The SXP-300 controller was then set to computer control mode and the mass was tuned to the first ion specified in the input file. The initial electron energy was then set and the ion signal was collected for a period of 10 seconds. The electron energy was then incremented by an amount specified in the input file. After the ion signal for the maximum electron energy had been been recorded the mass spectrometer was tuned to the next ion and the process was repeated until all the ions had been measured.

4.3 Literature comparison

Partial cross-sections have been published for only three of the six perfluorocarbon compounds measured here. Stephan *et al.* measured CF_4,[63] as described in Section 2.2, using a method that involved *Simion* simulations to estimate and correct for the loss of high energy fragments. Poll and Meichsner[80] used a quadrupole mass spectrometer to measure the electron impact ionization cross-sections for CF_4, C_2F_6 and C_3F_8 but only from threshold to 135 eV electron energy. The results were normalized to those of Rapp and Englander-Golden[14] (using equation (2.9)). Jiao, Garscadden and Haaland[82] measured the partial cross-sections for C_2F_6 with a Fourier transform mass spectrometer from threshold to 70 eV electron energy. Their results were normalized to those measured by Wetzel *et al.*[83] for argon using a cross-beam technique. More recently Basner *et al.*[96] measured partial electron impact ionization curves for C_2F_6 using a reflectron time-of-flight mass spectrometer. The Stebbings group, using the short pathlength mass-spectrometer shown in Figure 2.3, recently measured CF_4 partial cross-sections.[43]

Figure 4.2 shows partial ionization cross-sections for CF_4 compared to the recent values measured by Basner *et al.*,[96] and Sieglaff *et al.*[43] The most notable difference is the much larger contribution to the cross-section from the F^+ ion reported in the literature. The shapes of the literature curves are very similar to the present data. C_2F_6 data are compared to the recent data of Basner *et al.*[96] and Jiao, Garscadden and Haaland[82] in Figure 4.4. Again the shapes are similar but the absolute values are quite different. It is interesting to note that Basner *et al.*[96] did not report a partial ionization cross-section for the CF^+ ion, although this peak was recorded in the present data and, according to the to the standard mass spectrum,[6] this is a significant ion at approximately 18% of the base peak. The method developed here allows for a comparison to be made between the results from different research groups using a range of methods and will provide useful data for the evaluation of future theories on the ionization process and mass spectra.

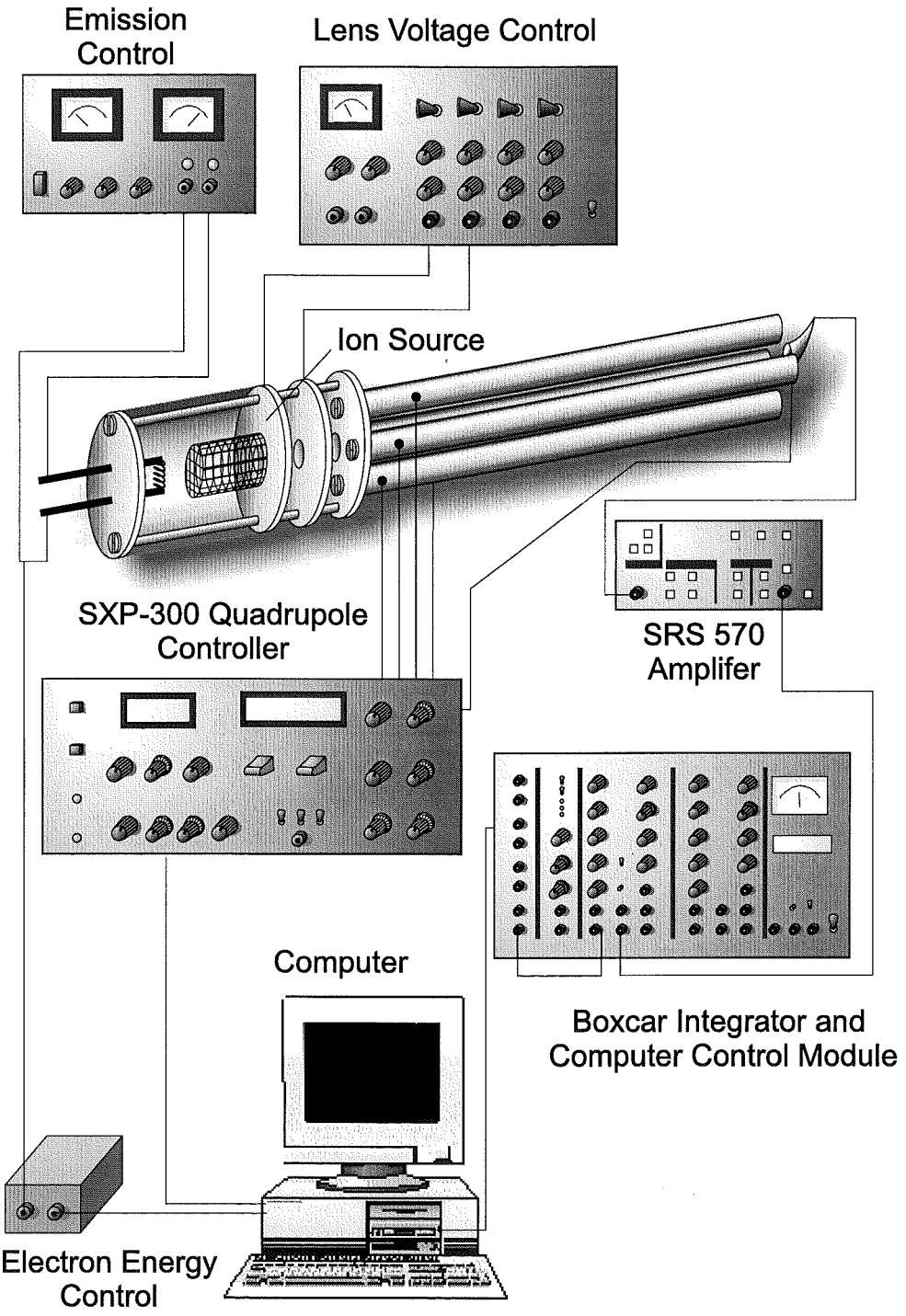

Figure 4.1: Schematic of experimental components for the measurement of absolute partial electron impact ionization cross-sections.

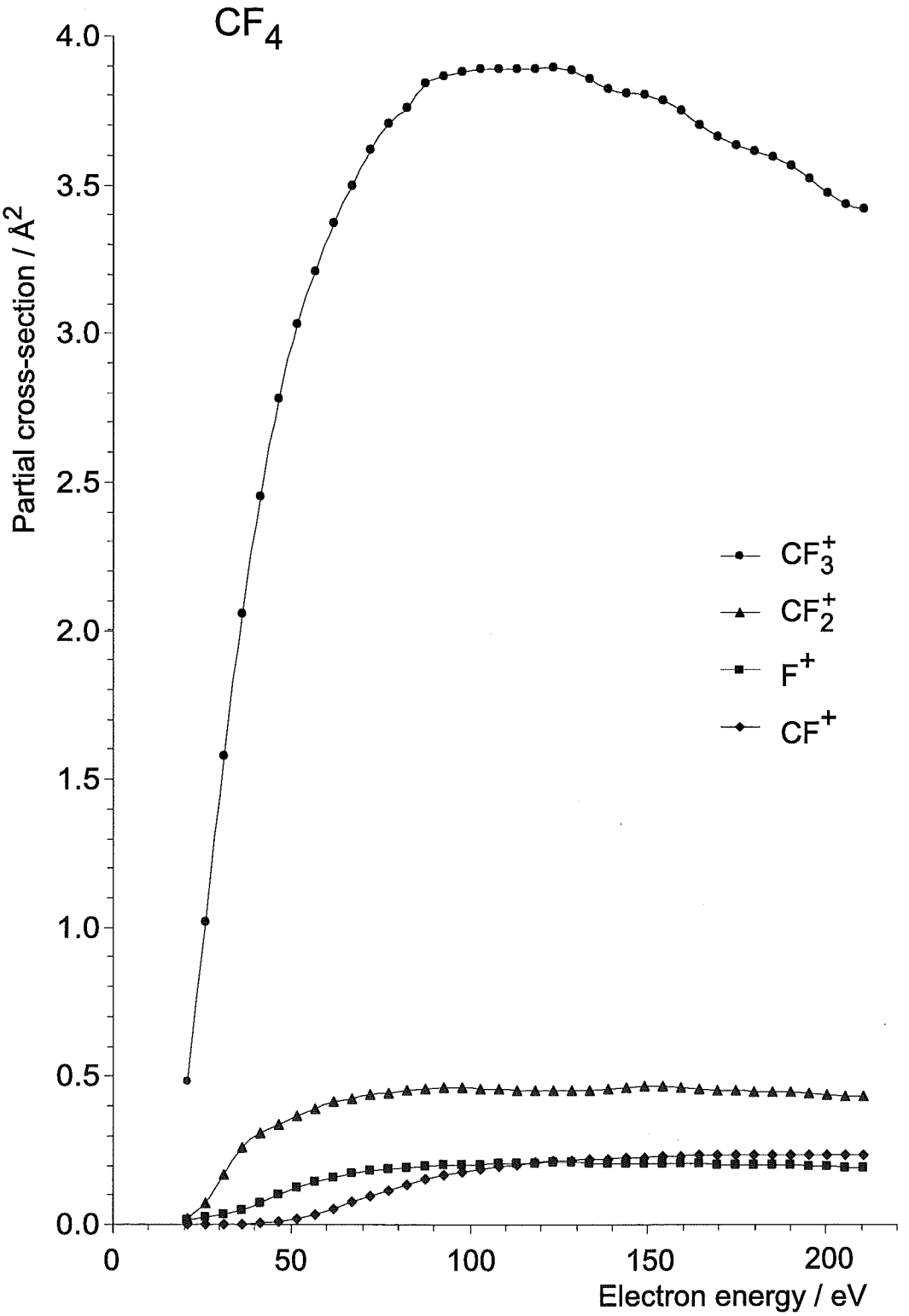

Figure 4.2: Absolute partial electron impact ionization cross-sections for CF_4.

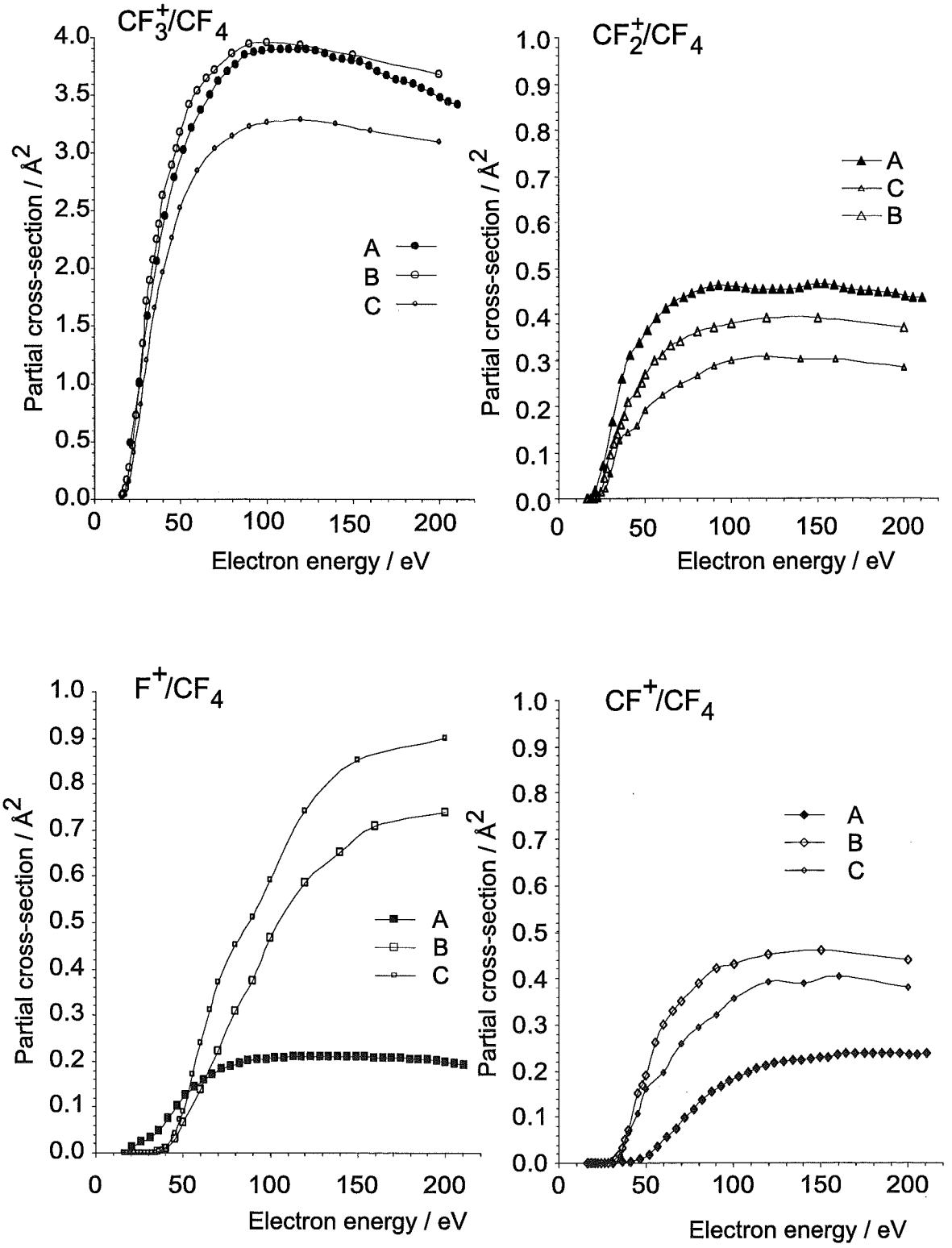

Figure 4.3: Absolute partial ionization cross-sections for CF_4 comparison to literature data: (A) present results; (B) Sieglaff *et al.*;[43] (C) Basner *et al.*[96] Note the change in scale for the minor ions.

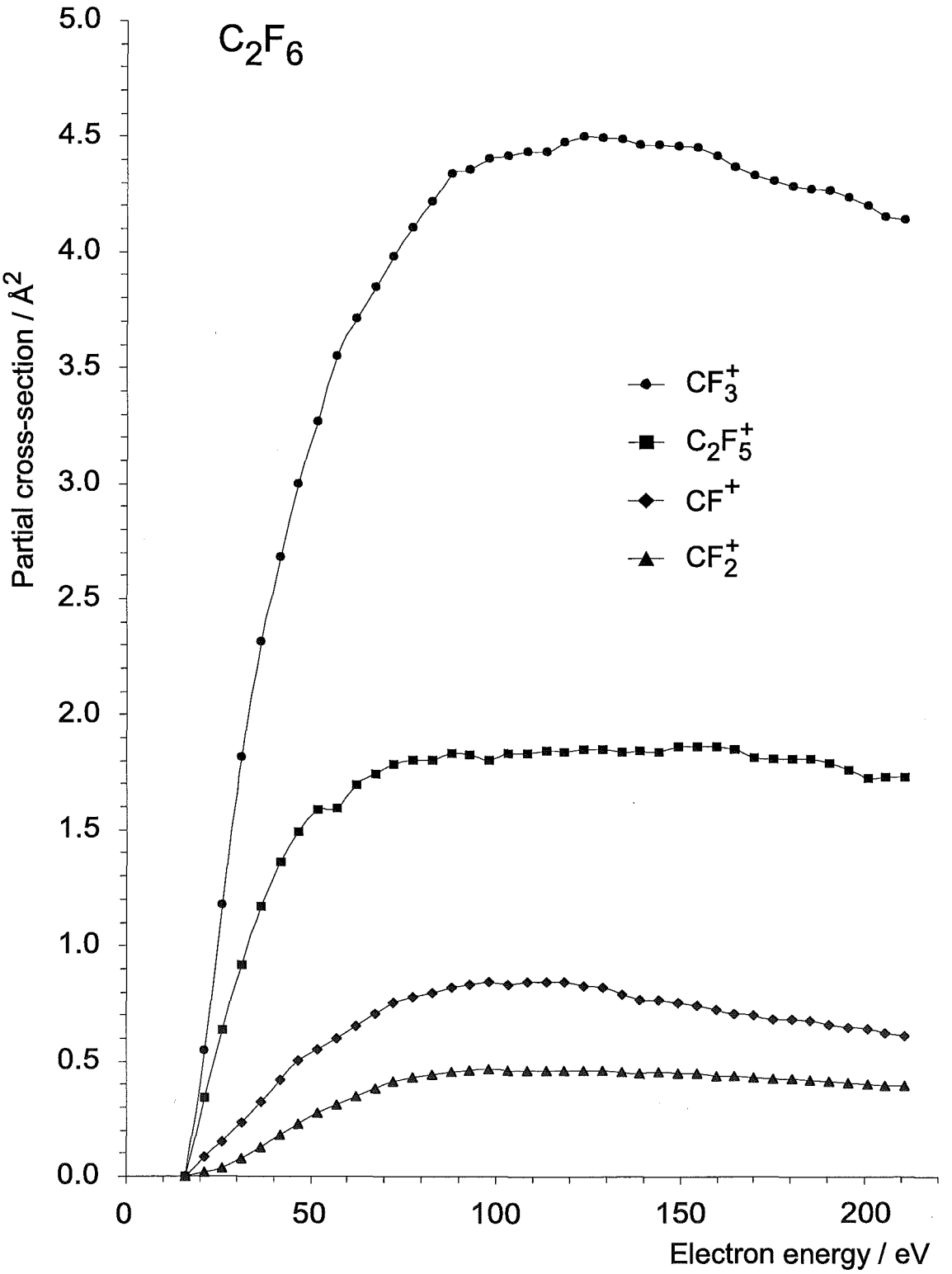

Figure 4.4: Absolute partial electron impact ionization cross-sections for C_2F_6.

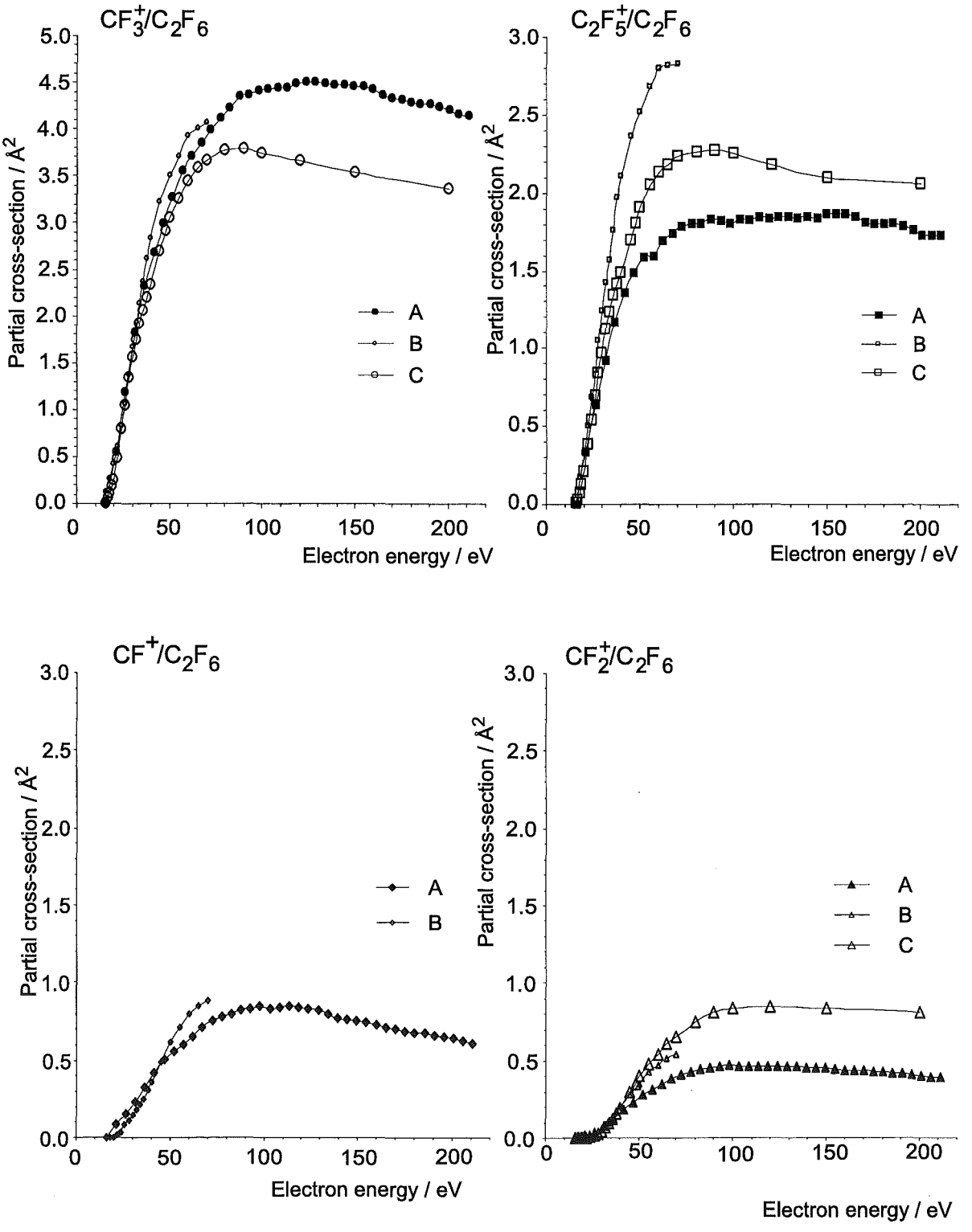

Figure 4.5: Absolute partial ionization cross-sections for C_2F_6 comparison to literature data: (A) present results; (B) Jiao *et al.*;[82] (C) Basner *et al.*[96] Note change in scale for minor ions.

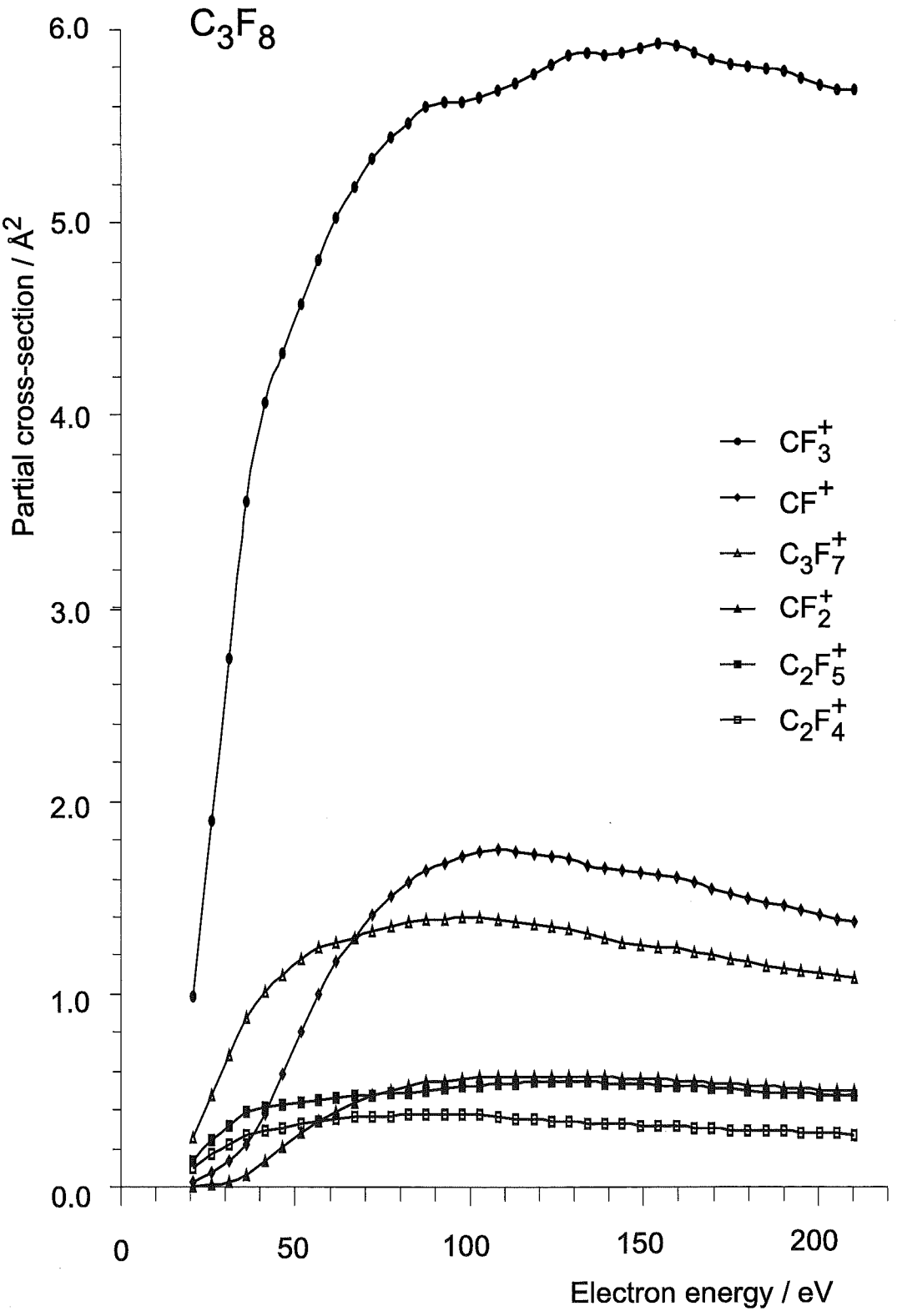

Figure 4.6: Absolute partial ionization cross-sections for C_3F_8.

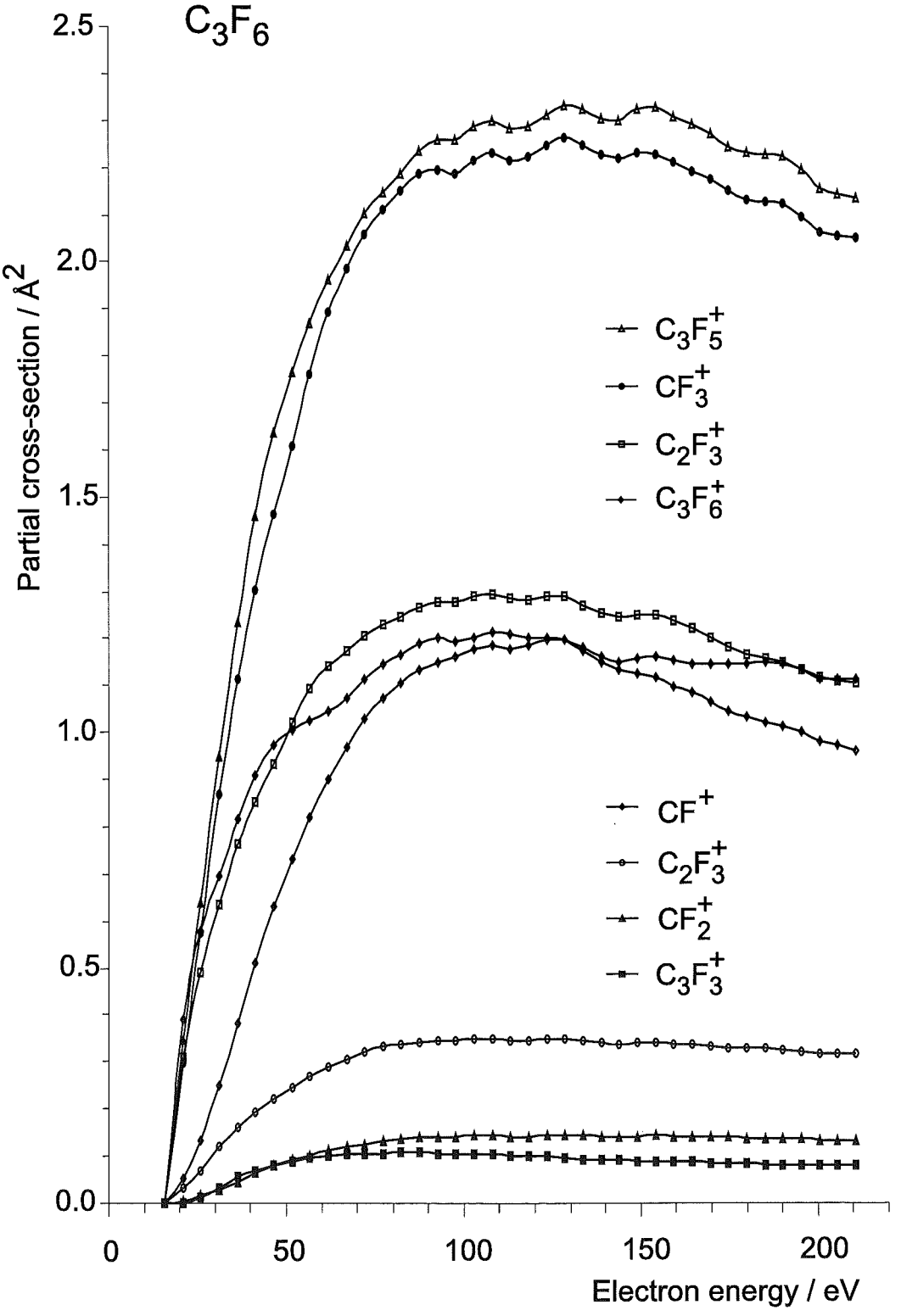

Figure 4.7: Absolute partial ionization cross-sections for CF_3-$CF{=}F_2$.

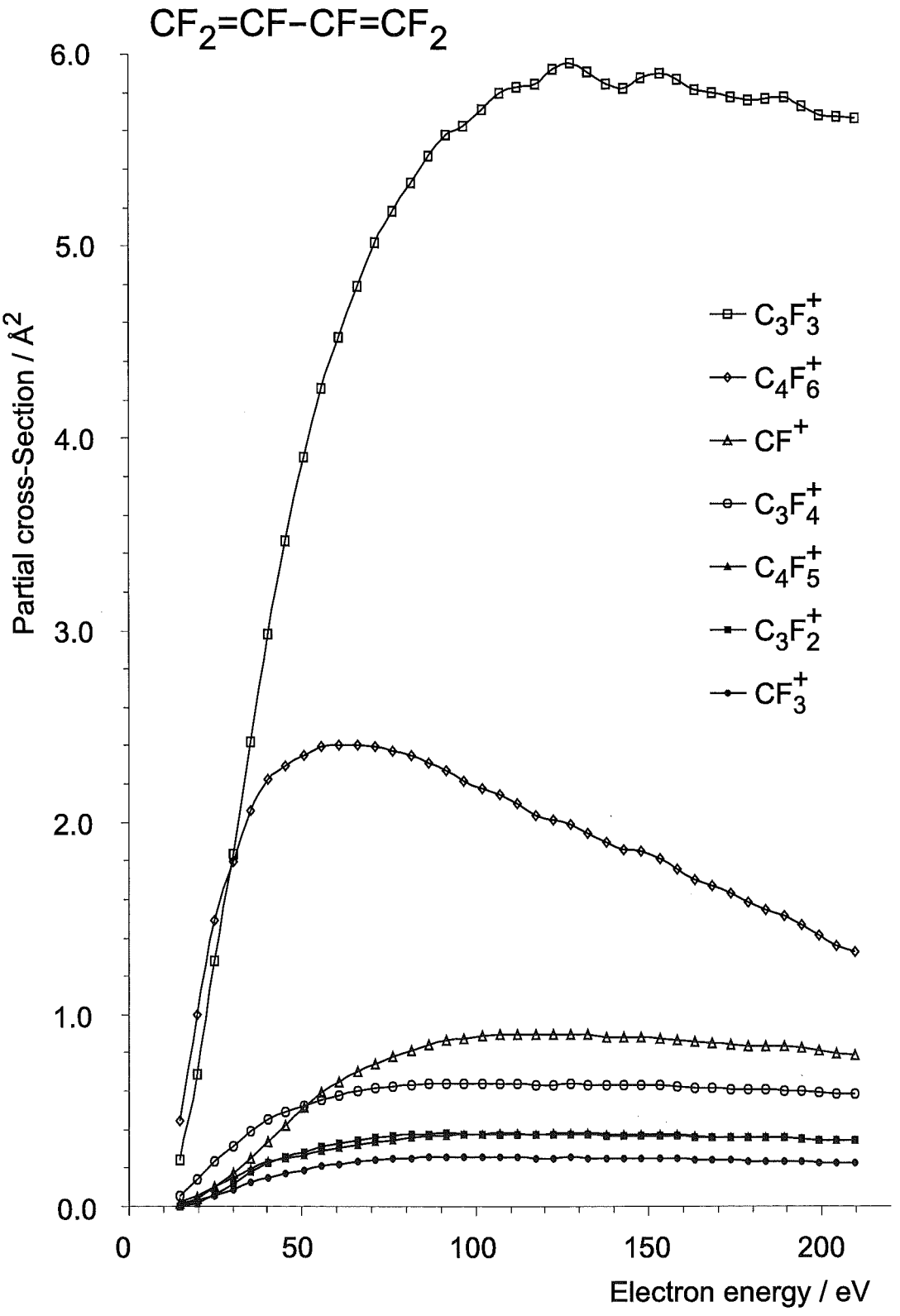

Figure 4.8: Absolute partial ionization cross-sections for CF_2=CF-CF=CF_2.

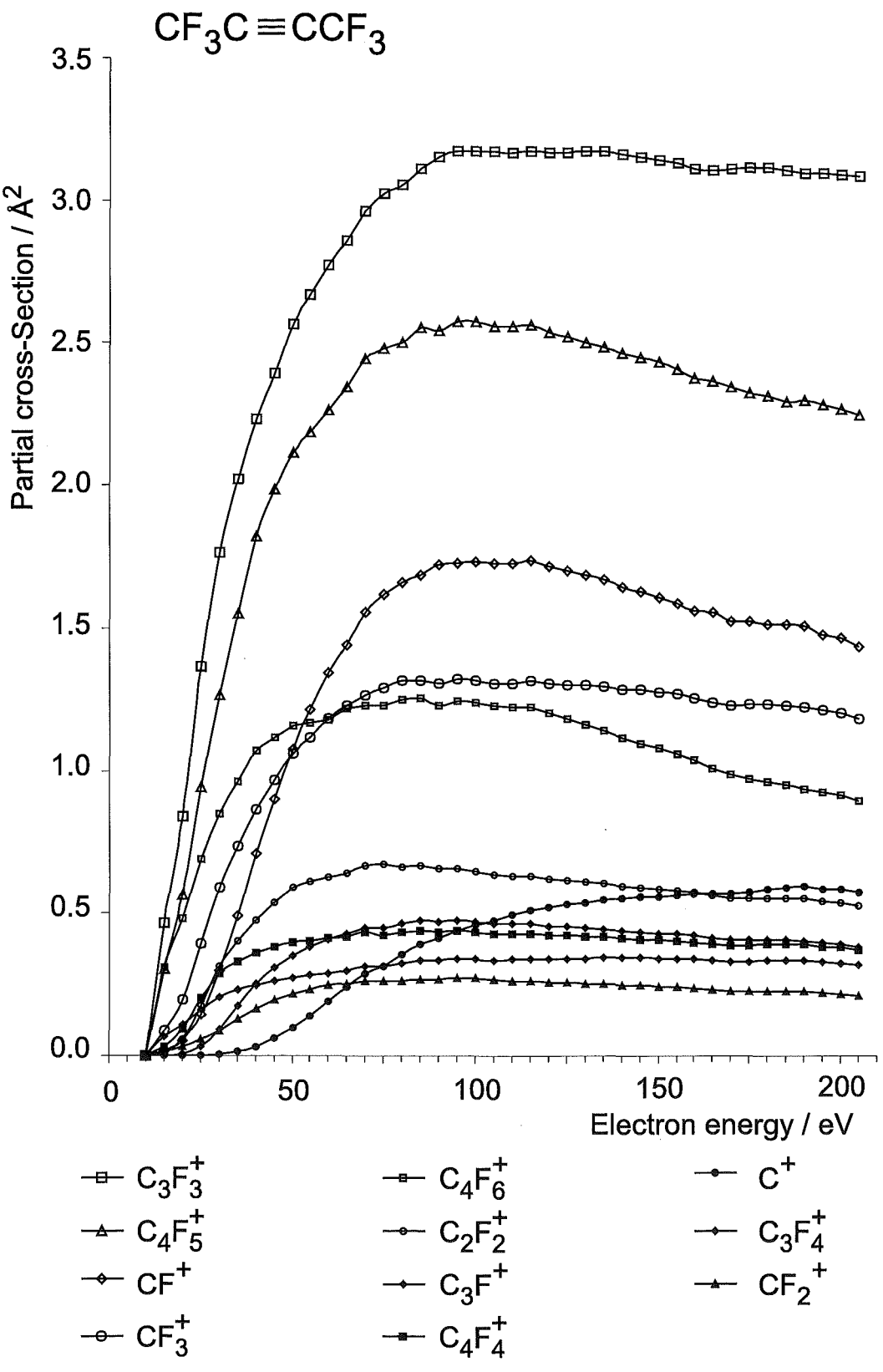

Figure 4.9: Absolute partial ionization cross-sections for CF_3-C≡C-CF_3.

4.4 Discussion

Despite 90 years of mass spectroscopic measurements, and hundreds of thousands of publications containing mass spectroscopic data, modeling of partial cross-sections and mass spectral cracking patterns has not been performed with any great deal of success. The only theory of note is the quasi-equilibrium theory based on a statistical approach using an equation derived by Rosenstock *et al.*[97] A prior knowledge of the ion decomposition scheme is required, so this theory cannot be applied without measuring the actual mass spectrum first. The rates of decomposition from parent ions into fragments are calculated followed by the rates for further fragmentation. The rate constants can then be used to calculate the fraction of each ion produced. A significant amount of calculated and experimental data are required in order to apply this theory, including a knowledge of the density of states of the internal rotations and vibrations of the molecule and the appearance potentials for the various product ions. The most useful practical application of the quasi-equilibrium theory involves comparing proposed decomposition mechanisms to measured mass-spectra until a satisfactorily similar result is achieved. In the case of the perfluorocarbons, the required spectroscopic data are not all available and there is little to be learned from an analysis of this type. Although the partial ionization cross-sections for the individual ions cannot be calculated directly the fragmentation pattern may be rationalized from the following considerations:

1. Stevenson's rules[98] and energy considerations;

2. statistical considerations - in many cases there is more than one route to the formation of an ion;

3. bond dissociation requirements for the formation of a particular ion, for example, the formation of CF_2^+ from CF_4 requires that at least two bonds are broken and possibly the formation of F_2 as a neutral product;

4. previous observations based on the electronic stability of an ion.

Stevenson's rule states that for the ionization-fragmentation process

$$e^- + AB \longrightarrow A^+ + B + 2e^-$$

A^+ will be formed preferentially if $E_0(A) < E_0(B)$, and B^+ will be a minor component.

This section will outline possible contributing factors for decomposition schemes leading to the formation of the observed fragment ions and the ratio of those ions for the six perfluorinated compounds measured. None of the saturated perfluorocarbon compounds in the range CF_4 to C_8F_{18} have stable molecular ions.[6] In the unsaturated cases, presumably either the carbon double or triple bonds contribute to charge stabilization of the molecular ion, or ionization involves the removal of an electron from a π orbital that does not lead to fragmentation.

Decomposition schemes for each of the six targets have been considered, however, analyses of this kind become more involved with increasing number of carbon atoms in the molecular backbone. In many cases, ionization potentials of the fragments are not known, or there are a range of values. Data used in this section have been taken from the National Institute of Standards and Technology website (NIST)[6] and the National Bureau of Standards publication *Ionization Potentials, Appearance Potentials, and Heats of Formation of Gaseous Positive Ions.*[99] The ionization potentials of the fragment ions of interest are given on Table 4.1.

Table 4.1: Ionization potentials for the ions of interest. (N/A not available)

Fragment	Ionization Potential (eV)	Fragment	Ionization Potential (eV)	Fragment	Ionization Potential (eV)
CF_3	10.2	C_2F_5	10.0	C_4F_5	N/A
CF_2	11.4	C_2F_4	10.1	C_4F_6	12.3
CF	9.1	C_2F_3	10.2	C_4F_4	9.3
F	17.4	C_2F_2	11.2	C_3F_4	10.9
C	11.3	C_3F_3	N/A	C_3F_7	10.1
C_3F	N/A				

4.5 Rationalization of observed partial cross-section patterns

4.5.1 Partial ionization cross-sections – CF_4

A plot of the partial ionization cross-sections of CF_4 as a function of electron energy is given in Figure 4.2. The magnitude of the measured partial cross-sections for the decomposition of CF_4, in descending order are:

$$CF_3^+ > CF_2^+ > F^+ \gtrsim CF^+ \tag{4.4}$$

As the inbound electron approaches the molecule, energy is transfered from it to the target *via* an electrostatic Coulomb interaction. From average bond energy data,[100] for each CF bond that is broken the molecule needs to absorb approximately 5.03 eV. Therefore it is expected and observed that the partial cross-section for each of the fragment ions should decrease as the number of bonds broken to form that fragment increases. Possible fragmentation processes are given below. The indicated product ions are those favoured by Stevenson's rules, the other fragments may ionize and are observed as minor contributors to the partial cross-section.

$$CF_4 + e^- \longrightarrow CF_3^+ + F + 2e^- \tag{4.5}$$

$$\longrightarrow CF_2^+ + 2F + 2e^-;\ \ CF_2^+ + F_2 + 2e^- \tag{4.6}$$

$$\longrightarrow CF^+ + 3F + 2e^-;\ \ CF^+ + F_2 + F + 2e^- \tag{4.7}$$

The next consideration is the statistical probability of ion formation. F^+ has many possible routes to ion formation and should therefore be enhanced. Stevenson's rule, the ion with the lowest ionization potential will form preferentially on bond cleavage, works against F^+ formation. But since F^+ has a significant statistical probability of formation it appears in the mass spectrum with approximately the same probability as CF^+.

Literature appearance energies[6] of the product ions from CF_4 may also be consid-

ered:

$$AE(CF_3^+) = 14.2 - 15.6 \text{ eV} \quad (4.8)$$

$$AE(CF_2^+) = 20.3 \text{ eV} \quad (4.9)$$

$$AE(F^+) = 24.0 \text{ eV} \quad (4.10)$$

$$AE(CF^+) = 22.6 \text{ eV} \quad (4.11)$$

The observation from these data is that the ion with the lowest appearance energy will form preferentially, apart from the case where the the statistical significance of one ion dominates. In terms of the functional dependence of the electron energy, the only curve crossing is F^+/CF^+. This may be rationalized in terms of a combination of the energy required to break three bonds for the formation of CF^+ and the relatively high ionization potential of F. At low energy F^+ dominates because of the statistical preference for the formation of this ion, but at high energy the inbound electron has a greater chance of delivering the additional ~10 eV to the target molecule required for the cleavage of two additional C-F bonds with the formation of the energetically favoured CF^+. The CF_3^+ cross-section exhibits a greater attenuation rate than the other ions because the likelihood of cleavage of more then one bond increases with the energy delivered to the target from the inbound electron.

4.5.2 Partial ionization cross-section C_2F_6

A plot of the partial ionization cross-sections of C_2F_6 as a function of electron energy is given in Figure 4.4. In the case of C_2F_6 the observed cracking pattern is:

$$CF_3^+ > C_2F_5^+ > CF^+ > CF_2^+ \quad (4.12)$$

The same arguments used to analyze the CF_4 spectrum can be applied in this case, however, the difficulty in assessing the factors that might be seen to favour particular fragmentation product becomes evident. From statistical considerations the smaller

fragments should form preferentially because there are many routes to their formation, however F^+ is not formed at all. This observation may be rationalized by reference to Table 4.1. The ionization potential of F is significantly higher than for the other fragments. The following reaction mechanisms can contribute to fragment ion formation. The fragment with the positive charge indicates the favorable route according to Stevenson's rule, the other fragments may ionize but will be observed as minor components.

$$
\begin{aligned}
C_2F_6 + e^- &\longrightarrow CF_3^+ + CF_3 + 2e^- && (4.13)\\
&\quad\; CF_3^+ + CF_2 + F + 2e^- && (4.14)\\
&\quad\; CF_3^+ + C + F_2 + F + 2e^- && (4.15)\\
&\quad\; CF_3^+ + C + 3F + 2e^- && (4.16)
\end{aligned}
$$

$$
C_2F_6 + e^- \longrightarrow C_2F_5^+ + F + 2e^- \qquad (4.17)
$$

$$
\begin{aligned}
C_2F_6 + e^- &\longrightarrow CF^+ + CF_4 + F + 2e^- && (4.18)\\
&\quad\; CF^+ + CF_3 + F_2 + 2e^- && (4.19)\\
&\quad\; CF^+ + CF_3 + 2F + 2e^- && (4.20)\\
&\quad\; CF^+ + CF_2 + F_2 + F + 2e^- && (4.21)\\
&\quad\; CF^+ + CF_2 + 3F + 2e^- && (4.22)\\
&\quad\; CF^+ + CF + 2F_2 + 2e^- && (4.23)\\
&\quad\; CF^+ + CF + F_2 + 2F + 2e^- && (4.24)\\
&\quad\; CF^+ + CF + 4F + 2e^- && (4.25)\\
&\quad\; CF^+ + C + 2F_2 + F + 2e^- && (4.26)\\
&\quad\; CF^+ + C + F_2 + 3F + 2e^- && (4.27)\\
&\quad\; CF^+ + C + 5F + 2e^- && (4.28)
\end{aligned}
$$

From the above equations it is clear why analysis of mass spectra become highly involved very quickly. The literature appearance energies[6] are listed below.

$$
\begin{aligned}
AE(C_2F_5^+) &= 14.9 - 15.5 \text{ eV} && (4.29)\\
AE(CF_3^+) &= 13.6 \text{ eV} && (4.30)
\end{aligned}
$$

$$AE(CF^+) = 16.1 - 16.8 \text{ eV} \quad (4.31)$$

$$AE(CF_2^+) = 23.8 \text{ eV} \quad (4.32)$$

In this case the appearance energies of the product ions match the observed ionization cross-sections at all electron energies because there are no curve crossings and the partial cross-sections are essentially independent of electron energy.

4.5.3 Summary partial ionization cross-sections

Inspection of the partial cross-sections (Figures 4.6 to 4.9) as a function of electron energy indicates that the complexity quickly reaches a point where analysis of dominant reaction pathways and observed peak intensities becomes speculative.

New data has been presented on the partial electron impact ionization cross-sections of perfluoromethane, perfluoroethane, perfluoropropane, perfluoropropene, perfluorobuta-1,3-diene and perfluorobuta-2-yne. The partial ionization cross-sections for the three unsaturated perfluorocarbons have not been previously reported. Rationalization of the reaction schemes are very difficult even for relatively simple perfluorinated compounds using traditional thermodynamic methods, because, firstly a plethora of complicated reaction schemes lead to the observed reaction products and secondly many of the required thermodynamic data are not available.

It is evident from the plots for CF_4 and C_2F_6 that the mass spectra for these molecules are almost independent of electron energy. However, as the complexity of the compound increases the mass spectrum changes significantly with electron energy and peak cross-overs are evident. In general, the formation of fragments that require the breaking of C-F bonds have much shallower gradients up to the peak partial cross-section compared with those fragments that form by cleavage of a C-C bond only. A general observation is that ion fragments that are formed with an odd number of fluorine atoms tend to be more stable than those formed with an even number of

fluorine atoms.

The electron energy corresponding to the peak in the ionization cross-section, E_{max}, is strongly dependent on the number of bonds broken. In general, the greater the fragmentation, the higher the value of E_{max} for that fragment. The unsaturated perfluorocarbons may also undergo structural changes in the ion source. For example, the formation of CF_3^+ from the diene. A mass spectrometer cannot identify the routes and exact mechanisms for fragment ion formation only the end products and the quantities. Interestingly, although the shape of the electron impact partial ionization cross-sections are vastly different for the two C_4F_6 isomers, the total ionization cross-sections are measured with a total difference of only 1.5%, less than the experimental uncertainty of the experiment.

4.6 Summary of Chapters 3 and 4

Electron impact ionization cross-sections have been measured for a range of compounds for which no values were previously available in the literature. These cross-sections now account for a significant fraction of all the values of molecular cross-sections available in the literature. The equations that have been presented for both the polarizability model and the bond contribution model allow for a rapid estimation of the maximum electron impact ionization cross-section for systems where measurements are not available with a high degree of confidence using simple models. This will enable researchers measuring electron impact ionization cross-sections in the future to rapidly establish whether their results are close to the true value with some degree of confidence. Partial cross-sections have been measured for six perfluorocarbons using a simple quadrupole mass spectrometer experiment, and compared to other values, in the literature where available. Further investigation of theoretical models used for the calculation of total electron impact ionization cross-sections, and the applicability of these models to particular compounds, will be discussed further in the following Chapter.

5. THEORETICAL DETERMINATION OF ELECTRON IMPACT IONIZATION CROSS-SECTIONS

5.1 Introduction

Theoretical modeling of electron impact ionization processes and the calculation of ionization cross-sections date back as far as the experimental measurement of electron impact ionization cross-sections. With the emergence of powerful computers it is now possible to model and perform calculations for very complicated systems with many parameters. The theoretical calculation of electron impact ionization cross-sections using a simple classical approach dates almost a century to an equation derived by J. J. Thomson.[92] Since then, several different models have been developed based on this equation (Section 5.4.2). Other approaches to the modeling of electron impact ionization cross-sections include the development of an observation by Bethe that the probability of ionization from a particular $\langle n, l \rangle$ atomic orbital is proportional to the mean square radius of that orbital and the atomic bond contribution approach based on an observation by Otvos and Stevenson.[30] A simple model was developed in this research group based on the electrostatic interaction between the target and the inbound electron.[88,101] This Chapter will assess the available models used to calculate electron impact ionization curves: quantum mechanical methods; semi-empirical methods; and the electrostatic and polarizability models. Ionization cross-sections using two of the more successful models will be compared to the experimental results discussed in Chapter 3, and the polarizability model will be explored further.

5.1.1 Calculation methods

Quantum mechanical methods refer to calculations for which only physical constants are used as input data. Energy minimization is performed by calculating the wave functions using only constants such as m_e, $\hbar$ e, c etc with various approximations and assumptions; no experimental data for the particular system under study is required. The laws of quantum mechanics are strictly followed and no classical approximations are made. Semi-classical models are those for which the laws of quantum mechanics are approximated to classical laws of physics. Most calculations in this category are actually a combination of semi-classical approximations and semi-empirical theories. Semi-empirical models refer to theory which uses empirical input data to match experimental data. The theory is then applied using the previously determined input data to determine the cross-section for the unknown system.

5.1.2 Resonances

The term resonance, when applied to electron impact ionization cross-sections, refers to a resonance energy condition. When the energy of the N-bound electron system plus the energy of the free electron is equal to the energy of the (N+1)-bound electron system, the system is said to be at resonance. There are two separate cases when resonance occurs in electron impact ionization. The first is a resonance in the entrance channel, and the second is a resonance in the exit channel. The effect of the former type of resonance is the appearance of sharp spikes in the total integrated cross-section at specific incident electron energies. The effect of the latter type of resonance is the appearance of sharp spikes in the differential cross-section and abrupt steps in the total integrated cross-section. These exit channel resonances are also called excitation–auto-ionization resonances. Resonances are most important for electron impact ionization of ions, especially highly charged ions such as Fe^{15+}. Resonances can enhance the total integrated cross-section by as much as an order of magnitude, especially for the group one and group two metals, but tend to decrease in importance as the number of valence

electrons increases.

5.2 Important symbols

Table 5.1 contains important symbols used in this section; they are included here for ease of reference.

Table 5.1: Important symbols relating to Jain-Khare, BED, BEB and DM theories.

Symbol	Meaning
σ	Cross-section
$\sigma_{\max}$	Maximum ionization cross-section
$E_{\max}$	The electron energy where $\sigma_{\max}$ occurs.
$\mathrm{d}\sigma$	Differential cross-section
$\sigma(E)$	Integrated cross-section at specific electron energy, E
E	Energy of incident electron
Z	Atomic number
ϵ	Energy of secondary (ejected) electron
E_0	Threshold ionization energy
w	$\epsilon + E_0$, the energy loss of the incident electron, to form the ion.
a_0	Bohr radius (5.292×10^{-11} m)
R	Rydberg energy (2.1798×10^{-18} J, 13.606 eV)
$\mathbf{K}$	The change in the momentum vector of the incident electron due to scattering
$f = \left[\frac{8\pi^2 m_e \nu}{3he^2}\right] \lvert\boldsymbol{\mu}_{fi}\rvert^2$	Oscillator strength.
$\left[\frac{\mathrm{d}f(w)}{\mathrm{d}w}\right]$	Differential oscillator strength.
$N_i = \int \left[\frac{\mathrm{d}f(w)}{\mathrm{d}w}\right] \mathrm{d}w$	Integral oscillator strength.
$C(w)$	Collisional parameter.[102]
s	Number of electrons that participate in "hard" collisions.
ϵ_0	"Mixing parameter."
E_j	Binding energy of ejected electron.
ξ	Number of bound electrons in that particular sub-shell.

Table 5.1: (Continued). Important symbols relating to Jain-Khare, BED, BEB and DM theories.

Symbol	Meaning
KE	Average kinetic energy of target electron.
V	Potential energy.
r	Displacement.
μ	Reduced mass.
n	Principle quantum number.
l	Angular momentum quantum number.
M	A matrix element.
α	Polarizability.
m_e	Mass of electron.
$t = \frac{E}{E_j}$	Normalization parameter.
$w = \frac{\epsilon}{E_j}$	Normalization parameter.
$u = \frac{KE}{E_j}$	Normalization parameter.

5.3 Quantum mechanical methods

After searching through the literature it has become apparent that little progress has been made in this area in recent years for atoms with $Z > 2$. The most comprehensive review of quantum mechanical calculations of electron impact ionization cross-sections is by Younger[103] in 1985 and the current discussion is based around that review, although some progress has been made since then especially with regard to the ionization cross-section of hydrogen.[104]

Although no quantum mechanical calculations were carried out for the present work it is necessary to include a brief description and literature review of the available techniques in order to appreciate the problems associated with these calculations. Most of the theoretical work relating to the calculation of electron impact ionization cross-sections falls under the semi-classical and semi-empirical banners.

The quantum mechanical modeling of electron impact ionization cross-sections is an inherently difficult task because there are two free electrons in the field of the ionized atom in the exit channel. This leads to the so-called three body problem and, in the case of electron impact ionization, this has been a particularly difficult problem to formulate. Recently, however, Jones and Stelbovics,[104] from the University of Perth, have published a paper which efficiently applies the Temkin-Poet[105–107] model to find a solution for the electron impact ionization cross-section of the hydrogen atom at several electron energies using a three body model. It will be interesting to see if this model can be extended to other systems in the future.

Quantum mechanical calculations have so far been limited to selected atomic and atomic ion targets with varying success. The theory often disagrees with experimental results by a factor of between 2 and 10. As the atomic number, Z, increases, the theory becomes less successful. However McGuirie,[108–111] has performed quantum mechanical calculations in the Born approximation for heavy atoms. Calculations were accurate to within 20% of experimental values for atoms in the range $2 < Z < 11$ and within 30% of experimental values for atoms $19 < Z < 54$ for electron energies greater than 200 eV using an extended Bethe binary encounter equation and a generalized oscillator strength model. Calculations were also performed for the ionization of individual subshells for a range of heavy atoms including Hg.

Generally, as the electron energy exceeds the maximum electron impact ionization cross-section, σ_{max}, the theory (using the approximations outlined below) and the experimental results tend to converge. This is because the interaction between the ion, the primary electron and the secondary electrons are short lived at high energy and hence cause less perturbation to the system.

5.3.1 The partial wave approximation.

Quantum mechanical calculations generally rely on some variation of the partial wave approximation. This approach has had mixed success but both the calculations and

theory are relatively straight forward. At large distances from the target, where the interaction between the detected particles can be ignored, a quantum mechanical scattering experiment can be conceptualized in terms of three waves, an incident wave, a transmitted wave and a scattered wave. Partial wave theory is concerned with scattering by a central potential $V(r)$ that depends only on distance r between the incident and target particles. The amplitude of the scattering from the time-independent scattering state (also called the stationary scattering state) depends only on the magnitude of the incident wave-vector $\mathbf{k}$ and the angle between the incident wave vector and $\mathbf{r}$. For simplicity $\mathbf{k}$ is chosen to lie along the z axis, so that the scattering amplitude is independent of ϕ. Using the Schrödinger wave equation and partial wave analysis, the following equation can be derived as described in Appendix **C**.

$$\left[\frac{\hbar^2}{2\mu r} + \frac{\hbar^2 l(l+1)}{2\mu r^2} + V(r)\right] F_l(r) = E F_l(r) \tag{5.1}$$

In equation (5.1), the first two terms in the parentheses are the kinetic energy contributions to the total energy and $F_l(r)$ is a function that depends on the angular momentum quantum number l, and the type (s, p, d, f) of orbital that is ionized. $V(r)$ is the potential that describes the free electron, of which there are three choices that will be considered here.

1. Plane wave Born approximation.

   In this case the potential $V(r) = 0$ and the effect of the target on the free electron is ignored. The radial functions $F_l(r)$ are simply spherical Bessel functions[a]

2. Coulomb attraction approximation.

   In this case the potential $V(r) = \frac{-Z_{\text{eff}}}{r}$, where Z_{eff} is the effective nuclear charge that the electron experiences. A change in the radial scale of the many electron Hamiltonian gives:

[a] Spherical Bessel functions are solutions to the spherical Bessel differential equation, derived from the Helmoltz differential equation $\nabla^2 F + k^2 F = 0$ in spherical coordinates. A full description can be found in any standard calculus text or from Wolfram Research[112]

a. a zeroth order Hamiltonian term equivalent to the hydrogen case;

b. a perturbation term equal to the interaction multiplied by $\frac{1}{Z_{\text{eff}}}$. For a large Z_{eff} this will be small compared to the zeroth order term.

A variation on this is the infinite Z_{eff} approximation. This variation gives the ionization cross-section for the n, l orbital for any ion or atom based on a computation for $Z = 1$. For targets where Z_{eff} has a significant effect on the partial wave this approximation fails, but it has been successfully applied to systems where $\frac{Z_{\text{eff}}}{N} > 2$ or 3, where N is the number of electrons in the target.

3. The distorted wave approximation.

In this case $V(r) = -\frac{Z_{\text{eff}}}{r} + V_{DW}(r)$. This is similar to the Coulomb attraction model but includes a contribution due to the partial wave being distorted by $V_{DW}(r)$, which is an approximation to the distortion of the incident electron potential due to the target electrons.

The ionization event can be described by the following steps:

1. The incident electron approaches the target with energy E.

2. The incident electron interacts with a bound electron orbital in the target via the Coulomb interaction, $V_{1,2}(r_1, r_2)$.

3. An inelastic collision occurs which scatters the free electron into a state E_f and ejects the bound target electron into state E_e.

The first order perturbation matrix element is then given by:

$$M_d = \langle \psi_b \psi_i \left| \frac{1}{r_{1,2}} \right| \psi_e \psi_f \rangle \tag{5.2}$$

Where the subscrips b, i ,e and f indicate the bound, inbound, the ejected and the scattered electron respectively. The probability of the transition is then given, from the Born interpretation, as approximately $|M_d|^2$ giving a $\frac{1}{r^2}$ dependence on the force

between the charged particles. After the substitution the appropriate kinematic factors, the integrated ionization cross-section can be found by integrating over the distribution of incident electron energies:

$$\sigma_i(T) = \int_0^{T_{\max}} \sigma(E, E_e, E_f) \mathrm{d}E_e \tag{5.3}$$

The upper integration limit is given by:

$$T_{\max} = \frac{1}{2}(E - E_0) \tag{5.4}$$

Where $T_{\max}$ is the average available energy for ionization, known as the half-range Born approximation. Since the primary and secondary electrons are indistinguishable except for their respective energies, there are two types of electron exchange:

1. Potential exchange.

   In this case there is an exchange of potential energy between the free electron and target electron, this can be taken into account in a straight forward manner. (For details see Younger[103]).

2. Scattering exchange.

   This case describes the possible interchange of the two continuum electrons. Unfortunately problems arise immediately with the scattering exchange term,

$$M_{ex} = \langle \psi_b \psi_i \left| \frac{1}{r_{1,2}} \right| \psi_f \psi_e \rangle \tag{5.5}$$

The new probability for ionization (including equation (5.2) – the first order perturbation matrix element) is then given by:

$$|M_d + M_{ex}|^2 = |M_d|^2 + |M_{ex}|^2 - \alpha |M_d||M_{ex}| \tag{5.6}$$

Where $|M_d|$ represents the matrix element for direct ionization, $|M_{ex}|$ represents the matrix element for the exchange ionization and $|M_d||M_{ex}|$ represents a mixing or interference term from the direct and exchange ionization matrix elements. α is known

as the phase factor and is related to the relative phases of the direct and exchange matrix elements; it depends on the interaction of the two continuum electrons in the final state. This immediately poses the question: what is an appropriate choice for α? There are several possibilities:

1. Apply the Born-Oppenheimer approximation, giving $\alpha = 0$.

   This has the effect of making the cross-section far too large since the exchange term is often comparable in magnitude to the direct term;

2. Apply the Born-exchange approximation (The Rudge and Swartz model[113]).

   α is chosen to cancel the imaginary part of the scattering matrix element. As a result of applying this approximation, the cross-section, including the exchange, is comparable to the direct cross-section, $|M_d| \simeq |M_d + M_{ex}|$, hence the inclusion of the exchange term results in unnecessary computing expense;

3. Apply the Born-exchange approximation (The Peterkop model[103]).

   $\alpha = 1$, $|M_{ex}|$ is maximized and $|M_d||M_{ex}|$ is minimized. This gives a cross-section slightly larger but still very similar to the Rudge and Swartz model.

Since the partial wave theory is limited to first order perturbation anyway, the choice of α is somewhat moot, since it contributes little to improve the results. The difference in the theoretical cross-section, as a result of changing α from 0 to 1, is often smaller then the difference between the theory and the experiment.

For the inclusion of resonances in the quantum mechanical calculations it is normally the case that the non-resonant components of the cross-section are calculated first, and then the contribution to the cross-section from the auto-ionization–excitation cross-section are added in. This method assumes that all of the atoms excited to the resonance state will auto-ionize but this may not be the case, especially for highly charged ions, where radiative stabilization may lead to a bound state with (N+1) electrons. In this case branching ratios for auto-ionization and radiative stabilization will

need to be calculated. This is a non-trivial task and may not actually increase the accuracy of the final results due to the limitations of the partial wave theory initially applied.

5.3.2 The *ab inito* electrostatic method

The *ab inito* electrostatic model, developed at the University of Canterbury by Vallance, Harland and Maclagan,[88,101] uses an electrostatic approach to the calculation of maximum electron impact ionization cross-sections.

The ionization cross-section for different orientations of the target molecule is calculated as a function of approach geometry of the electron and the target species. The total ionization cross-section is then taken as the average cross-section over the three Cartesian coordinates in both the positive and negative directions.

This model assumes that the critical impact parameter, r_c, corresponds to the separation for which the Coulomb potential of the electron-molecule system is equal to the ionization potential of the molecule. The ionization cross-section for a particular geometry of the electron–molecule collision is then given by:

$$\sigma = \pi r_c^2 \tag{5.7}$$

The energy of the system is calculated at a series of r values using a systematic approach that converges on r_c, with a Coulomb potential, Φ. This is calculated using:

$$T = E_n + \Phi = E_n - E_0 \tag{5.8}$$

The vertical ionization energy, E_0, is calculated using geometry optimization of the neutral molecule in order to calculate E_n. The zero point energy E_{zpe} is then calculated and the neutral geometry of the molecule is then applied to the positive ion to determine

the energy of the positive ion, E_i:

$$E_0 = E_i - (E_n + E_{\text{zpe}}) \tag{5.9}$$

Once the maximum ionization cross-section has been calculated, the incident energy at which the maximum occurs must also be calculated. This is achieved using a method that treats an electron as a de Broglie matter wave, and assumes that the maximum in the ionization energy occurs when the frequency of the electron wave matches the orbital frequency of the electron in the highest occupied atomic orbital. The energy of the orbital is assumed to be made up of the kinetic and potential contributions. The kinetic energy is simply given by the classical orbital motion, and the potential energy, V, is given by the Coulomb potential between the electron charge and the effective nuclear charge, Z_{eff}.

$$\begin{aligned} E &= V + E_k \\ &= \frac{Z_{\text{eff}} q}{4\pi\epsilon_0 r} + \frac{1}{2} m_e r^2 \omega^2 \end{aligned} \tag{5.10}$$

With m_e as the mass of the electron, ω as the angular velocity and r as the orbital radius. The orbital frequency is the angular velocity divided by 2π.

$$\begin{aligned} \nu &= \frac{\omega}{2\pi} \\ &= \frac{1}{2\pi}\sqrt{\frac{2E_k}{m_e r^2}} \end{aligned} \tag{5.11}$$

E_{max} corresponds to the point when the de Broglie frequency of the inbound electron matches the orbital frequency.

$$E_{\text{max}} = h\nu = \frac{h}{2\pi}\sqrt{\frac{2E_k}{m_e r^2}} \tag{5.12}$$

The geometric optimization configurations are calculated using a molecular orbital package such as *Gaussian*.[114] This method could be readily applied to the inert gases, since the cross-section is independent of approach geometry. The maximum cross-

section was calculated, using a HF/6-31G* level of theory, to within 25% for Ne and, at best, within 1% for He.[88] when compared to Rapp and Englander-Golden's experimental results.[14] It was found that increasing the level of theory only had a marginal effect on the calculated cross-section. For the inert gases, the average difference between the calculated[88] and measured[14] results using this method was 14%.

The method has also been applied to molecules with a similar level of success, with the cross-section taken as the average over the Cartesian axes. This model is unique in that, when applied to molecules the ionization cross-section is calculated from six different approach geometries, hence an "ionization volume" can be determined. This enables steric effects on the ionization cross-section to be explored. The model is limited in that it can only calculate the maximum ionization cross-section. The calculations assume that the electron and the target species are static with respect to each other at the moment of ionization.

5.4 Semi-empirical methods

In the absence of a rigorous quantum mechanical solution to the electron impact ionization problem, a range of semi-empirical and semi-classical theories have been devised, with mixed success. Semi-empirical methods are methods that incorporate selected experimental results into the theory to describe the electron impact ionization cross-section. The advantages of this approach are that the results produced often match the experimental results much more closely than the quantum mechanical approach, they are far less computationally intensive and they are applicable to polyatomic molecules. The disadvantage of these methods is that they require experimental inputs. Semi-empirical methods involve the inclusion of empirical scaling factors so that the theoretical results match the experimental results without a full understanding of all of the physical factors involved. Recently, there have been several review articles that have covered the more widely used methods, which seem to get more elaborate as more electron impact ionization cross-sections become available in the literature and computers

become more powerful.[115–117]

Semi-classical and semi-empirical methods used in calculations of electron impact ionization cross-sections date back nearly 100 years to an equation developed by J. J. Thomson.[92] Since then, development of these theories has slowly improved[93] through the equations of Mott, Bethe, Gryzinski, Post, Darwin, Vriens and Burgess, Seaton, Lotz, Jain and Khare, Bell and, more recently, the Kistemaker additivity rule,[118] the binary encounter Bethe (BEB) model of Kim and Rudd,[119] the DM model of Deutsch, Märk and co-workers[66,120,121] and the Polarizability Method developed at the University of Canterbury.[88,101] In this section the polarizability, Deutsch-Märk and BEB models, will be discussed since these methods are generally regarded as the more successful of the models.[88,116,117] Calculations have been performed using these models for most of the molecules for which electron impact ionization cross-section curves have been measured and discussed in Chapter 3. The BEB and DM models and the method of Jain and Khare share the concept of additivity embedded in the theoretical frame-work. Molecular ionization cross-sections are determined by summing up the contributions to the cross-section from the atomic or molecular orbitals, but do not rely directly on the addition of the various bond contributions using the bond contribution method discussed in Section 3.3.1.

5.4.1 Polarizability model

A simple equation to predict the shape of the ionization efficiency curve based on only two parameters, the ionization potential, E_0 and the polarizability volume, α', was derived by the Canterbury group.[88,122] It is important to introduce a distinction here between the polarizability model, used to calculate the functional form of the ionization efficiency curve, and the observed empirical relationship between the maximum ionization cross-section σ_{max} and the polarizability of the target species, as discussed in Section 3.3.2. The polarizability model is based around the interaction or tuning of the electron wave with the root–mean–square of the polarizability volume. The theory

on which the polarizability model is based is limited however because it cannot predict the value of the ionization cross-section at any electron energy, it only explores the relationship between the molecular parameters α', E_0 and σ and attempts a crude easily calculated representation of the electron impact curve. The derivation of the equation for the ionization efficiency curve may be rationalized as follows.

The radius of the "polarizability sphere", from the polarizability volume α', can be written as

$$r_\alpha = \left(\frac{3\alpha}{4\pi}\right)^{\frac{1}{3}} \tag{5.13}$$

Assuming that the electron charge is distributed uniformly throughout the polarizability volume the root-mean-square radius, r_{rms}, of the electron distribution may be written as

$$r_{\text{rms}} = \sqrt{\frac{3}{5}r_\alpha^2} \tag{5.14}$$

giving a root-mean-square diameter, d_{rms}, for the molecule as $2r_{\text{rms}}$. Assuming that the peak in the ionization cross-section occurs when d_{rms} matches the de Broglie wavelength, λ, of the inbound electron the maximum coupling between the electron and the highest occupied molecular orbital will correspond to a wavelength of

$$\lambda = \frac{h}{p}$$

where

$$p = mv = \sqrt{2m_eE}$$

$$\therefore \lambda = \sqrt{\frac{h^2}{2m_eE}} \tag{5.15}$$

where m_e, p and E are the mass, momentum and energy of the electron, respectively,

and h is Planck's constant. By setting λ equal to d_{rms} an expression for the electron energy corresponding to the maximum electron impact ionization cross-section, E_{max}, can be derived from equations (5.13), (5.14) and (5.15):

$$E_{\text{max}} = \frac{5h^2}{24m_e}\left(\frac{4\pi}{3\alpha'}\right)^{\frac{2}{3}} \tag{5.16}$$

Harland and Vallance[122] showed that this equation correctly predicted E_{max} for a range of molecules for which experimental data were available. The shape of the ionization curve was then rationalized in terms of the deviation of the inbound electron de Broglie wavelength from the wavelength corresponding to d_{rms}, λ_{max}

$$\sigma = \sigma_{\text{max}}\left(1 - \frac{|\lambda - \lambda_{\text{max}}|}{\lambda_{\text{max}}}\right) \tag{5.17}$$

The ionization curves calculated using equation (5.17) were found to fall off too rapidly after the peak value compared to experimental values and and the threshold energy was often over estimated by 10 - 20 eV for many of the target species. In order to improve the correspondence to the measured curves the equation was modified through the incorporation of the function $\frac{E-E_0}{E}$, from the classical binary encounter treatment of electron impact ionization, and subsequently normalized using a factor of $\frac{E_{\text{max}}}{E_{\text{max}}-E_0}$ giving an expression for the functional shape of the ionization cross-section as

$$\sigma = \frac{\sigma_{\text{max}}}{2}\left[\left(\frac{E_{\text{max}}}{E_{\text{max}} - E_0}\right)\left(\frac{E - E_0}{E}\right) + 1 - \frac{|\lambda - \lambda_{\text{max}}|}{\lambda_{\text{max}}}\right] \tag{5.18}$$

where λ_{max} is calculated from $d_{\text{rms}}(= 2r_{\text{rms}})$ using equation (5.14). The normalization factor of $\frac{1}{2}$ is necessary because the extra terms in the equation add to the cross-section, giving double the cross-section at $E = E_{\text{max}}$. Although this equation has very simple roots, and is far from a rigorous solution, it was previously found to reproduce the experimental curves quite well over the electron energy range used in the present work. The biggest advantage of the method is its simplicity and ease of use, with only two

parameters required to determine the shape of the ionization efficiency curve – the molecular polarizability volume and the ionization potential of the target species. The curve must then be fitted to the appropriate ionization cross-section value obtained by either: experimental measurement; an estimated value using the bond contribution model; an estimated value using empirical polarizability equations described in Section 3.3.1 and Section 3.3.2; a calculated value using the electrostatic *ab initio* method described above.

The calculated shape of the electron impact ionization curve does not have the correct functional form. From equation (5.16) the electron energy corresponding to the maximum ionization cross-section has an $\alpha'^{-2/3}$ dependence, as shown by the lower curve in Figure 5.1. However, experimentally the point at which the maximum ionization cross-section occurs is independent of the polarizability as shown by the upper curve in Figure 5.1. This limits the use of the theory since there is no correlation between the polarizability volume and E_{max}, the electron energy corresponding to the maximum in the electron impact ionization curve occurs. The reason that the theory works quite well for some of the smaller hydrogen containing compounds such as CH_4, C_2H_6, CH_3F and ammonia, as well as the inert gases is that for compounds with a polarizability in the range of 2.4Å^3– 3.5Å^3 the predicted E_{max} is in the range 92 eV – 72 eV, which is the range of the typical observed electron energy values where the maximum electron impact ionization occurs. A further limitation to the polarizability method is that polarizabilities are unknown for many compounds including some of those studied in this work.

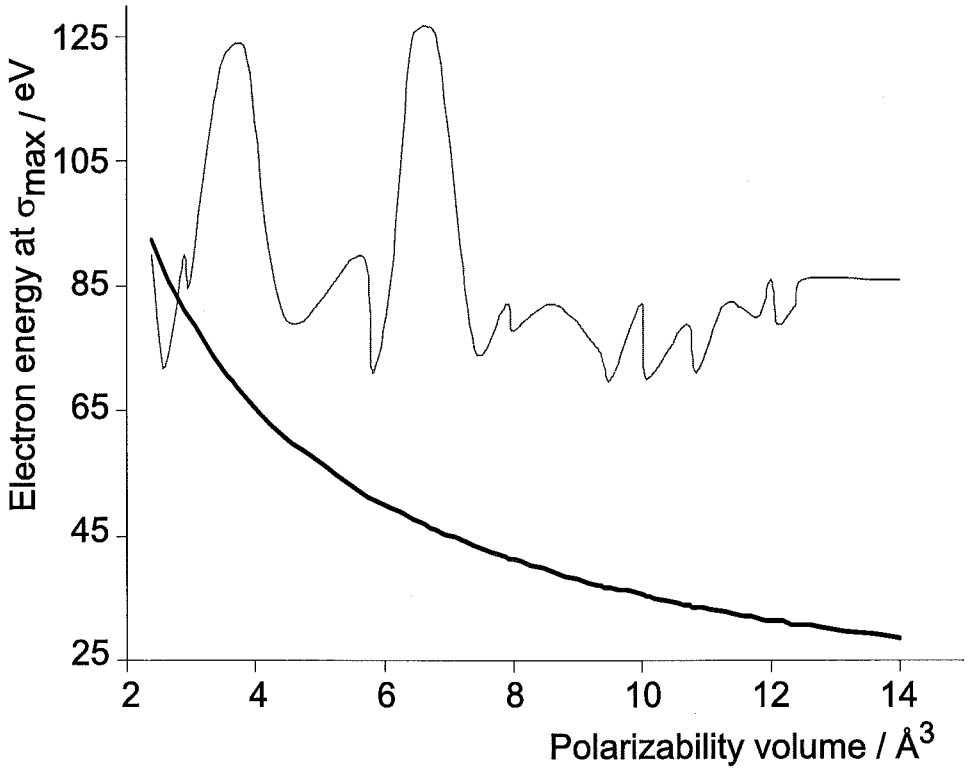

Figure 5.1: The relationship between $E_{\max}$ and α'. The thin line shows the relationship between measured values of $E_{\max}$ and α' and the heavy line shows the calculated relationship between $E_{\max}$ and α' using equation (5.16)

5.4.2 The Deutsch-Märk model

The Deutsch-Märk (DM) model was developed on the basis of a classical equation derived by J. J. Thomson[92]

$$\sigma = \sum_{n,l} \sigma_{in} = \sum_{n,l} 4\pi a_0 \xi_n \left(\frac{R}{I_n}\right)^2 \frac{u-1}{u^2} \tag{5.19}$$

with σ_{in} as the ionization cross-section of the target, leading to the formation of ion i from the nth sub-shell. ξ_n is the number of electrons in the nth sub-shell, R is the ionization potential of hydrogen, I_n is the binding energy of the electrons in the nth sub-shell and u is the available energy for ionization given as $\frac{E}{I_n}$, where E as the

energy of the incident electron. Gryzinski[123–125] improved this method significantly by introducing a continuous velocity distribution to the electrons in the atomic target species. Earlier methods had ignored the energy distribution of the target electron entirely. The energy distribution was incorporated by multiplying equation (5.19) by a function $f(u)$ with

$$f(u) = \frac{\mathrm{d}}{u}\left[\frac{u-1}{u+1}\right]^{a} \times \left(b + c\left[1 - \frac{1}{2u}\right] \times \ln[2.7 + (u-1)^{0.5}]\right) \tag{5.20}$$

with $a = \frac{3}{2}, b = 1, c = \frac{2}{3}$ and $d = 1$

The improved expression still failed to correctly predict the ionization cross-sections for some of the most simple target species such as Ne, N_2 and F_2. Subsequently Deutsch, Märk and Margreiter improved this expression further[66,126] by applying an observation by Bethe that the cross-section of an atomic electron with quantum numbers n, l is approximately proportional to the radius of that sub-shell $\langle r_{n,l}^2 \rangle$:

$$\sigma = \sum_{n,l} \sigma_{in} = \sum_{n,l} g_{n,l} \pi \langle r_{n,l}^2 \rangle \xi_{n,l} f(u) \tag{5.21}$$

with the weighting factor, $g_{n,l}$, originally calculated by Bethe as a function of the $\langle n, l \rangle$ quantum numbers from the hydrogen atom wave function. Deutsch, Märk and Margreiter used empirical data derived from experimentally measured electron impact ionization cross-sections of the rare gases and uranium to establish the $g_{n,l}$ weighting factors. In the first approximation $g_{n,l}$ was taken as 3 for the s electrons and 0.5 for all other electrons.[126] Later it was shown that $g_{n,l}$ should not be taken as a constant, but as a function of $E_{0(n,l)}$, the ionization energy of the $\langle n, l \rangle$ sub-shell.[66] The product $E_{0(n,l)} \times g_{n,l}$ is referred to as the reduced weighting factor. It was also found that the a, b, c and d constants in equation (5.20) should be different for each of the s, p, d and f orbitals.[127,128] In the case of an electron ionized from the s orbital of hydrogen or the alkali metals, a special weighting factor g_{ns} was needed to reconcile the low energy part of the ionization cross-section with experiment. The appropriate factors for $E_{0(n,l)} \times g_{n,l}$

and a, b, c and d are available in table format.[116]

The Deutsch-Märk model can be extended to molecular targets using the following equation:

$$\sigma = \sum_{n,l} \sigma_{in} = \sum_{j} g_j \pi \langle r_j^2 \rangle \xi_{n,l} f^*(u) \tag{5.22}$$

With the label j replacing n, l for molecular orbitals, and a new energy function $f^*(u)$ replacing $f(u)$. The $\langle r_j^2 \rangle$ and $f^*(u)$ are very difficult, if not impossible, to calculate and hence the preferred method of applying the Deutsch-Märk model to molecular targets is to reduce equation (5.22) to the form of equation (5.21) *via* a Mulliken population analysis using the appropriate atomic weighting factors and the effective atomic occupation numbers. The Deutsch-Märk model is very sensitive to the Mulliken population representation and care needs to be taken to optimize the Mulliken analysis.

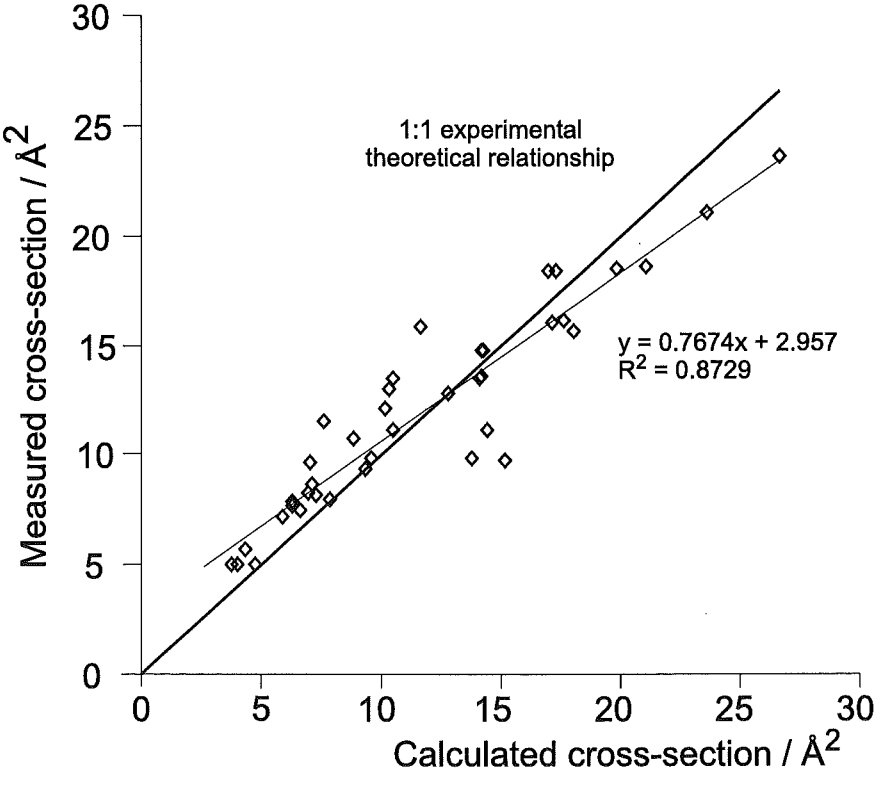

Figure 5.2: The thin line represents the maximum DM calculated electron impact ionization cross-section plotted against the maximum measured cross-section. The heavy line represents the perfect fit between theory and experiment.

A comparison between the measured and calculated total electron impact ionization cross-sections, shown in Figure 5.2, demonstrated that the DM model is most effective at predicting the maximum cross-section for molecules that contain heavy atoms. On inspection of Figure 5.3 it is clear why this is the case. Figure 5.3 shows the percentage deviation between the calculated and measured cross-section. A decrease in the calculated cross-section occurs as the number of heavy atoms increases. The DM model has an offset from zero making it most successful for target species that contain one heavy atom. The DM model over-estimates the cross-section for molecules that do not include a heavy atom by ~25% on average but may over estimate the cross-section by as much as 50%.

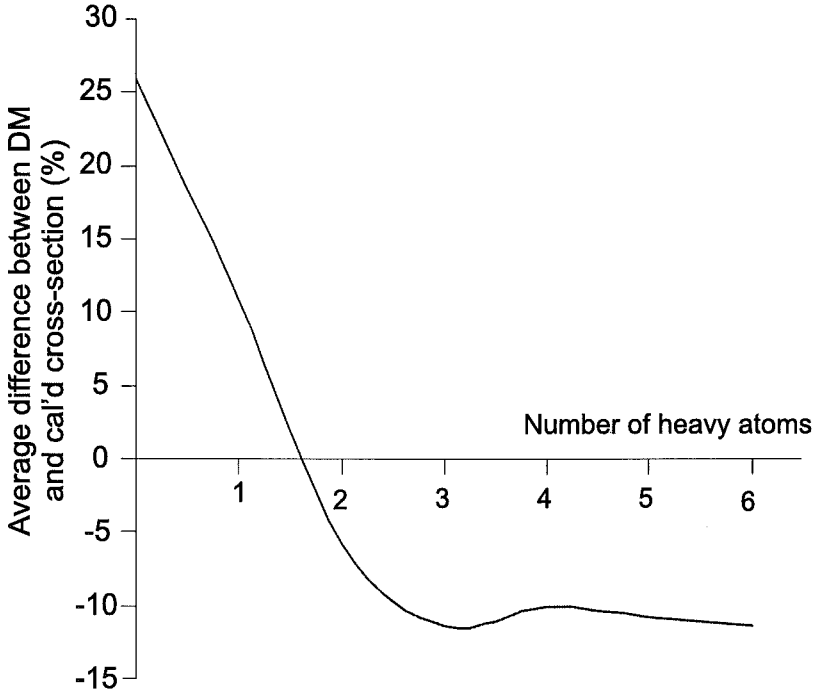

Figure 5.3: The percentage deviation of the DM theory as a function of the number of heavy atoms in the target molecule.

The DM model is not as successful at predicting the shape of the curve as the BEB model (Section 5.4.3) with an over-estimation of the attenuation of the cross-section at high electron energy. These problems were recognized by the original authors,[66,126] even for the simple target atoms such as H, He, Ne, Ar, C, N and O. It was recognized that the limiting factor on the success of the DM model was going to be the quality

of the Mulliken analysis. This is a very important consideration when applying this theory. The DM model generally underestimates the electron energy $E_{\max}$ by as much as 30 eV. Unlike the BEB model which can be scaled by a constant factor in order to improve the agreement with measured values for all electron energies, this is not possible with the DM model because of the poor agreement with the shape of the electron impact ionization cross-section versus electron energy curve compared to the measured curves.

5.4.3 Binary encounter Bethe model

The Binary encounter Bethe model has its roots in theory developed by Hans Bethe to describe glancing collisions, which involve small energy transfer between the colliding species, also known as "soft" collisions, and a theory developed by Mott, to describe direct collisions which involve large energy transfer between the colliding species, also known as "hard" collisions.

The first successful combination of the Bethe and Mott theories to model electron impact ionization cross-sections was made by Jain and Khare,[129] who used a description of the single differential ionization cross-section by Inokuti[130]

$$\frac{\mathrm{d}\sigma(E,\epsilon)}{\mathrm{d}\epsilon} = \frac{4\pi a_0^2 R^2}{Ew} \int \frac{\delta f(w, K^2 a_0^2)}{\delta w} \mathrm{d}[\ln(Ka_0)^2] \tag{5.23}$$

This equation was then reduced into two parts, the Bethe cross-section and the Mott cross-section given by equations (5.24) and (5.25)

$$\left.\frac{\mathrm{d}\sigma(E,\epsilon)}{\mathrm{d}\epsilon}\right|_{\mathrm{Bethe}} = \frac{4\pi a_0^2 R^2}{Ew} \frac{\delta f(w,0)}{\delta w} \ln[C(w)E] \tag{5.24}$$

$$\left.\frac{\mathrm{d}\sigma(E,\epsilon)}{\mathrm{d}\epsilon}\right|_{\mathrm{Mott}} = 4\pi a_0^2 R^2 s \left(\frac{1}{\epsilon^2} - \frac{1}{(E-\epsilon)\epsilon} + \frac{1}{(E-\epsilon)^2}\right) \frac{1}{E} \tag{5.25}$$

In the case of the Bethe cross-section, the asymptotic behavior in the high energy case is governed by the $\frac{\ln(E)}{E}$ part of the function. In the case of the Mott cross-section, there is a direct collision term, an interference term between the direct and exchange parts, and an exchange term, given by the three terms in the parentheses in equation (5.25). The overall energy dependence is governed by the $\frac{1}{E}$ term. Both the Bethe and Mott cross-sections are applicable in the limit of high E. Jain and Khare added the two cross-sections together, and multiplied each by a factor, f_1 and f_2 respectively, chosen to reproduce the available experimental data.

$$f_1(E,\epsilon) = \left[\frac{1}{(1-\frac{E_0}{E})}\right] \tag{5.26}$$

$$f_2(E,\epsilon) = \left[\frac{\epsilon^3}{\epsilon^3+\epsilon_0^3}\right]\left(1-\frac{E_0}{E}\right) \tag{5.27}$$

The "mixing parameter" ϵ_0 controls the mixing between the "hard" and "soft" collisions. The f_1 term controls the differential cross-section for small values of ϵ and the f_2 term controls the differential cross-section at large values of ϵ. The problem with the method of Jain and Khare is that the actual mixing parameter cannot be calculated and it varies depending on the molecule under investigation. The additional information required for the application of this model is the dipole oscillator strength and the collision parameter $C(w)$, both of which are difficult to calculate.

Kim[b] and Rudd[119,132–134] developed this idea further by assigning a momentum distribution, derived from the wave function of the target particle, to the target particle in place of the Mott cross-section (known as the binary encounter approximation). The differential ionization cross-section per orbital, labeled the binary encounter dipole (BED) method by Kim and Rudd, is given by equation (5.28)

[b] The NIST Electron Impact Ionization website is administered by Y-K Kim. For more references and information see reference[131]

$$\begin{aligned}\frac{\mathrm{d}\sigma(E,\epsilon)}{\mathrm{d}\epsilon} &= 4\pi a_0^2 \left(\frac{R}{E_j}\right)^2 \frac{\xi}{E_j(t+u+1)} \\ &\times \left[\left(\left[\frac{N_i}{\xi}-2\right]\frac{1}{t+1}\right)\left(\frac{1}{(w+1)}+\frac{1}{(t-w)}\right)\right. \\ &+ \left(2-\frac{N_i}{\xi}\right)\left(\frac{1}{(w+1)^2}+\frac{1}{(t-w)^2}\right) \\ &+ \left.\left(\frac{\ln(t)}{\xi(w+1)}\right)\left(\frac{\mathrm{d}f(w)}{\mathrm{d}w}\right)\right] \end{aligned} \tag{5.28}$$

The integrated cross-section is then given by:

$$\sigma(E) = 4\pi a_0^2 \left(\frac{R}{E_J}\right)^2 \frac{\xi}{t+u+1}\left[D(t)\ln(t)+\left(2-\frac{N_i}{\xi}\right)\left(\frac{t-1}{t}-\frac{\ln(t)}{t+1}\right)\right] \tag{5.29}$$

with

$$D(t) = \xi^{-1}\int_0^{(t-1)}\left(\frac{1}{1+w}\frac{\mathrm{d}f(w)}{\mathrm{d}w}\right)\mathrm{d}w \tag{5.30}$$

equation (5.29) is the integrated cross-section for a specific sub-shell. To obtain the total cross-section for the entire target the cross-sections for the individual sub-shells need to be summed. The binary encounter dipole model is particularly hard to apply, with information required for E_j, ξ and the differential oscillator strengths for each sub-shell of the target. The kinetic energy distribution can be calculated using a quantum mechanical package. Because of these difficulties a simpler version of the theory, known as the binary encounter Bethe (BEB) method is usually applied to calculate the ionization cross-sections. Using this method:

$$\sigma_Q(E) = 4\pi a_0^2 \left(\frac{R}{E_j}\right)^2 \frac{\xi}{t+u+1}\left[\left(\frac{Q\ln(t)}{2}\right)\left(1-\frac{1}{t^2}\right)\right.$$
$$\left. + (2-Q)\left(\frac{t-1}{t} - \frac{\ln(t)}{t+1}\right)\right] \tag{5.31}$$

where the integrated dipole Q is given by

$$Q = \frac{2E_j}{\xi R} m_{\text{ion}}^2 \tag{5.32}$$

with

$$m_{\text{ion}}^2 = \frac{R}{E_j}\int \frac{1}{1+w}\left(\frac{\mathrm{d}f(w)}{\mathrm{d}w}\right)\mathrm{d}w \tag{5.33}$$

Kim and Rudd assigned the value of 1 to Q, and found this worked well for the compounds for which experimental values were then available in the literature.[131]

Comparison between the experimental and calculated cross-section using the BEB model clearly demonstrated its effectiveness for calculating the shape of the electron impact ionization curve.[94,135,136] The success of the BEB model in predicting the magnitude of σ however, is strongly dependent on the system under study. Figure 5.4 shows that as the number of heavy atoms (in the third row of the periodic table or higher) in the target molecule increases the absolute value of the average percentage deviation of the BEB model from the measured cross-sections also increases. For molecules with no heavy atoms the average percentage deviation from the maximum cross-section is very slightly higher than 1%, but as the number of heavy atoms increases from 1 to 6 the average percentage deviation increases to nearly -50%. The shape of the ionization cross-section curve as a function of electron energy is generally in very good agreement with the measured curve, with the calculated maximum ionization cross-section typically occurring within 5-10 eV of the measured value for E_{max}. For the series of chlorocarbons measured in this work, the BEB curve can be made to fit the

the measured cross-sections very well by multiplying the BEB calculated cross-section by a constant factor in the range of 1.135 to 1.9.[136] The appropriate scaling factor can be determined by obtaining the maximum electron impact ionization cross-section by another method, either by calculating it using the *ab initio* method described in the previous section, by measurement, or by estimating it from the molecular polarizability or bond contributions. Recently Kim and Rudd introduced an empirical scaling factor[137] for molecular orbitals that are dominated by heavy atom orbitals and this has made matters more complicated. The dipole oscillator strengths in this work are assumed to be unity, in keeping with the assumption of Kim and Rudd. Figure 5.5 shows the

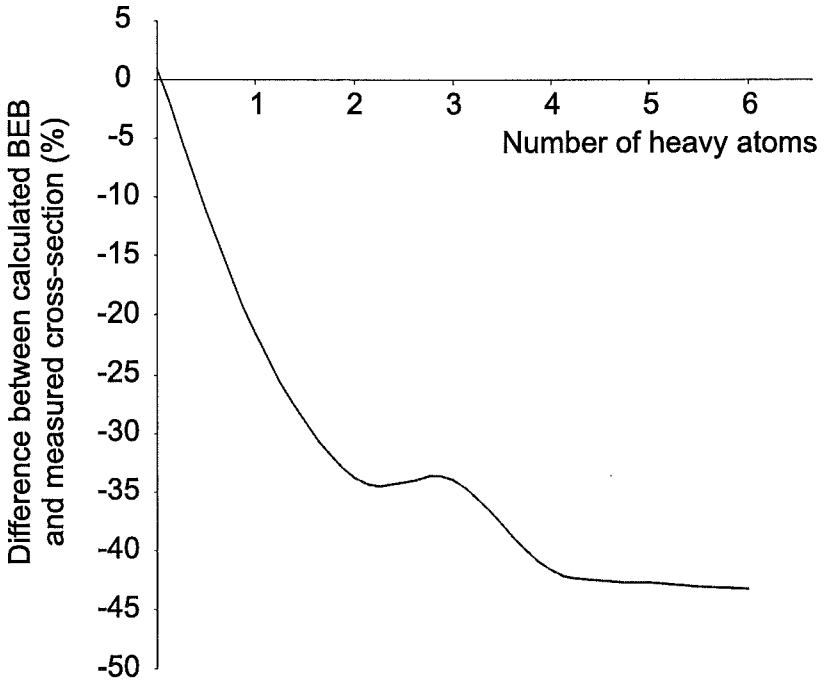

Figure 5.4: The percentage deviation of the BEB theory as a function of the number of heavy atoms in the target.

relationship between the maximum measured electron impact ionization cross-section and the maximum BEB calculated ionization cross-section. For molecules with only row one and two atoms the relationship is very good, however, the deviation from the measured values becomes significant very quickly as the number of heavy atoms increases.

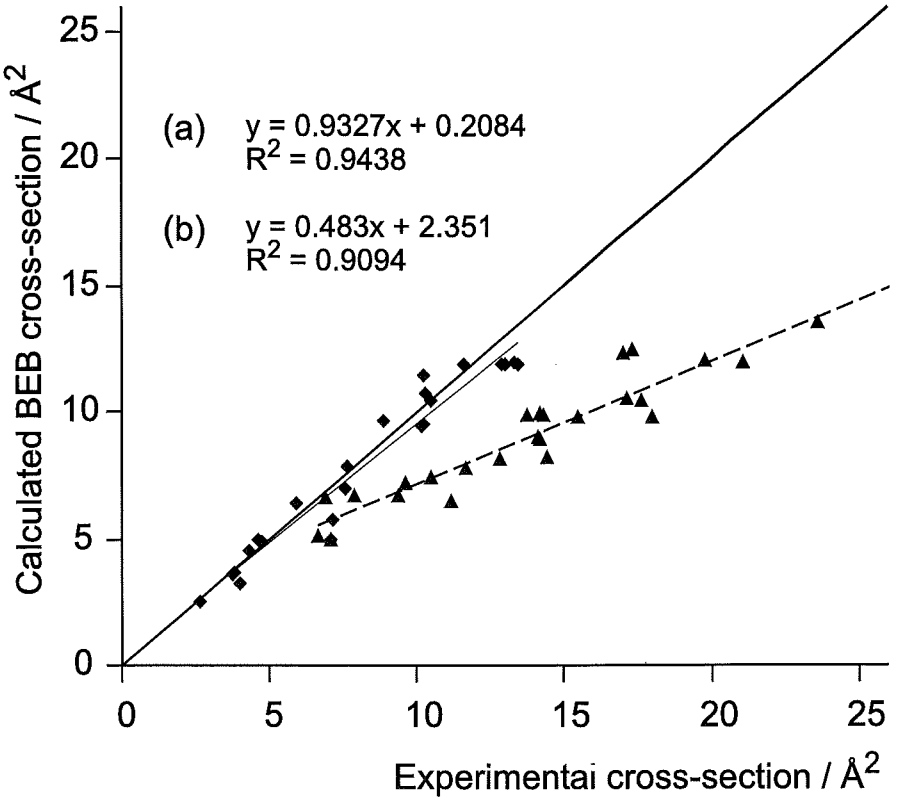

Figure 5.5: The heavy line represents the 1:1 relation between theory and experiment. The thin trend line shows the relation between experimental results and the BEB theory for molecules that do not contain any row three or four atoms (a) and the dashed trend line shows the relation between experimental results and the BEB theory for molecules that contain row three and four atoms (b).

5.5 A modification of the BEB model

5.5.1 Polarizability

In order to try and improve the performance of the BEB model some research was carried out into the meaning and origin of oscillator strength, f, since terms including f are set to unity for each atomic orbital in the BEB theory.

Prior to this, some consideration was also given to molecular polarizability, since polarizability and oscillator strength are related.

Polarizability is a first order perturbation in a molecule caused by an external electric field. The higher the polarizability the greater the response to the external field. The first order perturbation may be written as

$$H^{(1)} = -\boldsymbol{\mu} \cdot \mathbf{E} \tag{5.34}$$

with $\mathbf{E} = \varepsilon\hat{\mathbf{k}}$. To keep matters simple, it is sensible to assume that the electric field is applied in the $z-$direction, where the $z-$axis refers to the axis of greatest symmetry. The perturbation may then be written as

$$H^{(1)} = -\mu_z\varepsilon \tag{5.35}$$

$$\frac{\partial H^{(1)}}{\partial \varepsilon} = -\mu_z \tag{5.36}$$

At the expectation value of μ_z, $\langle\mu_z\rangle$, $\mathbf{E} = H^{(0)}$ therefore;

$$\frac{dE}{d\varepsilon} = -\langle\mu_z\rangle \tag{5.37}$$

The total energy of a molecule in the presence of an electric field may be written as a Taylor expansion relative to $E^{(0)}$, the energy under field free conditions.

$$E = E^{(0)} + \frac{1}{1!}\left(\frac{\mathrm{d}E}{d\varepsilon}\right)_0 \varepsilon + \frac{1}{2!}\left(\frac{\mathrm{d}^2E}{\mathrm{d}\varepsilon^2}\right)_0 \varepsilon^2 + \frac{1}{3!}\left(\frac{\mathrm{d}^3E}{\mathrm{d}\varepsilon^3}\right)_0 \varepsilon^3 + \ldots \tag{5.38}$$

Substituting equation (5.37) into the above expression and labeling the term that contains the first derivative α and the term that contains the second derivative β etc, gives

$$\langle \mu_z \rangle = \mu_{oz} + \alpha_{zz}\varepsilon + \frac{1}{2}\beta_{zzz}\varepsilon^2 + \ldots \tag{5.39}$$

Where the label z serves as a reminder that this is the equation for the electric field in the z direction. Substitution of equation (5.39) into equation (5.38) gives an equation to which perturbation theory can be applied.[c]

$$E = E(0) - \mu_z\varepsilon - \frac{1}{2}\alpha_{zz}\varepsilon^2 - \frac{1}{6}\beta_{zzz}\varepsilon^3 + \ldots \tag{5.40}$$

For the extraction of α the second order perturbation term must be applied and the derivative of the resulting equation must be taken. Only the $H^{(1)}$ terms need to be considered for $|0\rangle$. From equations (5.37) and (from Appendix **D**) (D.13)

$$E = E_0^{(0)} - \langle 0|\mu_z|0\rangle\varepsilon - \left\{\sum_{n=1} \frac{\langle 0|\mu_z|n\rangle\langle n|\mu_z|0\rangle}{E_0 - E_n}\right\}\varepsilon^2 + \ldots \tag{5.41}$$

Taking the first derivative at $\varepsilon = 0$ leaves only the $\langle 0|\mu_z|0\rangle$ term. This is simply the permanent dipole of the molecule. Taking the second derivative at $\varepsilon = 0$ leaves only the third term giving the quantum mechanical polarizability, α, in the $z-$direction, as

$$\left.\frac{dE}{d\varepsilon}\right|_{\varepsilon=0} = -2\sum_{n=1} \frac{\langle 0|\mu_z|n\rangle\langle n|\mu_z|0\rangle}{E_0 - E_n} \tag{5.42}$$

[c] See Appendix **D** for an account of perturbation theory.

For a randomly oriented molecule the average polarizability over all orientations may be written as,

$$\alpha = \frac{1}{3}(\alpha_{xx} + \alpha_{yy} + \alpha_{zz}) \tag{5.43}$$

Replacing $E_0 - E_n$ with ΔE_{n0} and noting that, because $\boldsymbol{\mu}$ is Hermitian[d], $\langle 0|\mu_z|n\rangle\langle n|\mu_z|0\rangle$ may be written as $|\mu_{n0}|^2$ giving the final polarizability as

$$\alpha = \frac{2}{3}\sum_{n=1}\frac{|\mu_{n0}|^2}{\Delta E_{n0}} \tag{5.44}$$

Now that an equation for α has been determined it is possible to examine the effect of α on properties of a molecule. To calculate α exactly all the wave-functions and energies of the excited states in the molecule need to be determined. An analytic solution cannot be derived for this an approximation needs to be made.

According to the closure approximation the energy differences ΔE_{n0} of all of the states from 0 to n may be approximated by an average value ΔE and the sum from 1 to n may be rewritten as the sum from 0 to n less the $0th$ term.

$$\alpha \simeq \frac{2}{3\Delta E}\sum_{n=1}\boldsymbol{\mu}_{0n}\cdot\boldsymbol{\mu}_{n0} \simeq \frac{2}{3\Delta E}\left\{\sum_{n=0}\boldsymbol{\mu}_{0n}\cdot\boldsymbol{\mu}_{n0} - \boldsymbol{\mu}_{00}\cdot\boldsymbol{\mu}_{00}\right\} \tag{5.45}$$

$$\simeq \frac{2}{3\Delta E}\left\{\langle\mu^2\rangle - \langle\mu\rangle^2\right\} \tag{5.46}$$

$$\simeq \frac{2(\Delta\mu)^2}{3\Delta E} \tag{5.47}$$

Where $\Delta\mu = \sqrt{\langle\mu^2\rangle - \langle\mu\rangle^2}$, the root-mean-square deviation from the mean electric

[d] Hermitian operators are real operators corresponding to observables, therefore they commute

dipole moment. $\Delta\mu$ is referred to as the fluctuation and may be considered classically as the fluctuation of the electron density about the nucleus from the root-mean-square value. This leads to the conclusion that the expected polarizability is proportional to the square of the radius of the molecule. To illustrate this, consider a one electron atom. The electric dipole operator is $\boldsymbol{\mu} = -e\mathbf{r}$ and the unperturbed system is non polar because of the symmetry of the electron distribution. By substitution into equation (5.46), is is clear that α is proportional to $\langle r^2 \rangle$ the mean square electron radius. By making two further assumptions, i) ΔE is approximately the same as the ionization energy, E_0, and ii) $\langle r^2 \rangle \simeq R_a^2$, the radius of the atom, it follows that[e]

$$\alpha \simeq \frac{2e^2 N_e R_a^2}{3\Delta E} \sim \frac{e^2 N_e R_a^2}{E_0} \tag{5.48}$$

where N_e is the number of electrons in the atom or molecule.

5.5.2 Oscillator strength

The oscillator strength, f, for a transition is a measure of the transition intensity. Oscillator strength is defined as

$$f = \frac{4\pi m_e \nu |\mu|^2}{3\hbar e^2} \tag{5.49}$$

The magnitude of f depends on the ratio of the calculated absorption intensity using a three dimensional Hooke's law harmonic oscillator to the observed intensity of the absorption of the radiation. For strongly allowed transitions $f \simeq 1$ but for symmetry forbidden transitions f is typically of the order of 10^{-1} and for spin forbidden transitions f is typically of the order of 10^{-5}.

The Kuhn-Thomas sum rule, Appendix **E**, establishes a relationship between the sum of the oscillator strengths and the number of electrons in the atom or molecule, N_e.

[e] $\Delta E \simeq E_0$ is such a gross approximation that the 2/3 factor has been ignored

$$\sum_n f = N_e \tag{5.50}$$

The oscillator strength f is related to molecular polarizability, α, by recognizing that μ occurs in both equations.

$$\alpha = \frac{\hbar^2 e^2}{m_e} \sum_{n=1} \frac{f_{n0}}{\Delta E_{n0}^2} \tag{5.51}$$

By substituting an average ΔE for ΔE_{n0}^2 and applying the Kuhn-Tomas rule, it follows that

$$\alpha \simeq \frac{\hbar e^2 N_e}{m_e \Delta E^2} \tag{5.52}$$

Thus the oscillator strength provides a link between the polarizability of a molecule, the electric dipole moment, the ionization potential, the orbital radius and the number of electrons in a molecule.

5.5.3 Back to BEB

Figure 5.6 shows the general functional form of the electron impact ionization cross-section as a function of electron energy predicted by the BEB model by applying equation (5.31). The curve with the highest maximum has been calculated with an oscillator strength of 0, the remaining plots are calculated with increasing oscillator strength values in increments of 0.1. An interesting point is that as the oscillator strength decreases the actual maximum ionization cross-section increases in direct contrast to photo-absorption cross-sections, where a higher oscillator strength equates to a stronger absorption. A decrease in the value of Q, the integral of the differental osscilator strength, also has the effect of decreasing the rate of attenuation of the ionization cross-section as the electron energy increases.

The BEB model assumes that the probability for each transition to the contin-

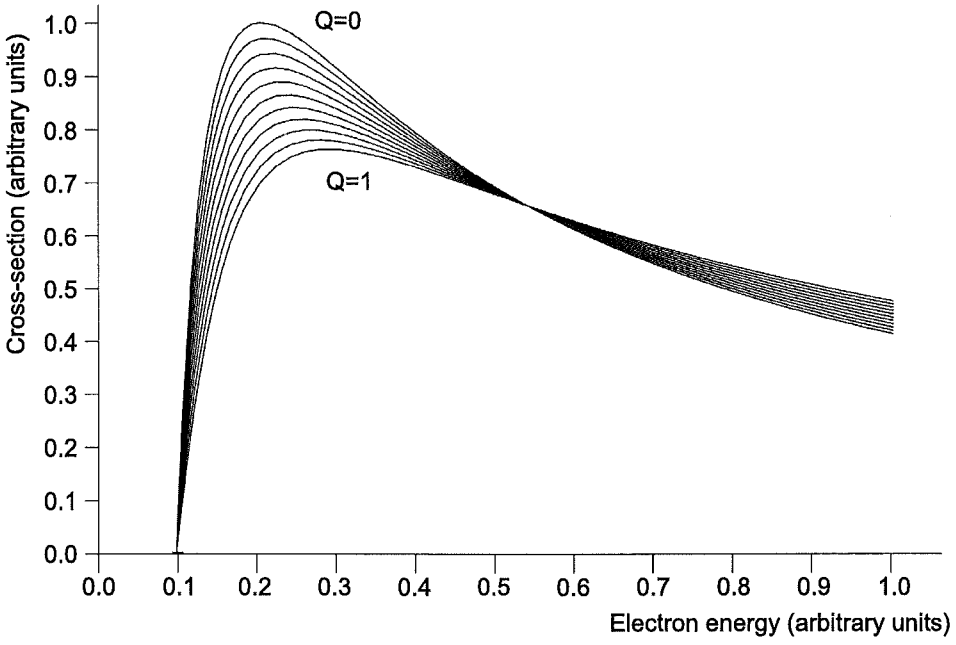

Figure 5.6: A plot of equation (5.31), σ_c against Q to examine the importance of the effect of oscillator strength on the BEB cross-section.

uum from each molecular orbital is related only to the binding energy, the number of electrons and the average kinetic energy of the electrons in that orbital. Despite differences in binding energy between orbitals due to molecular and electron shielding, the BEB theory still assumes equal transition probabilities for each electron orbital. Because the number of electrons in the target is related to the oscillator strength *via* the Kuhn-Thomas rule it was reasoned that a plot of the number of electrons in the target against the difference between the BEB and experimental cross-section might yield some insight into the systematic deviation of the BEB model from the experimental cross-section as the number of electrons in the target increases with an increasing number of heavy atoms.

Curves of $\sigma_{\text{exp}}/\sigma_{\text{BEB}}$ and $\sigma_{\text{exp}} - \sigma_{\text{BEB}}$ were plotted against the total number of electrons and the number of valence electrons for compounds for which electron impact ionization cross-sections had been measured. Initially a plot of (a) $\sigma_{\text{exp}}/\sigma_{\text{BEB}}$ and (b) of $\sigma_{\text{exp}} - \sigma_{\text{BEB}}$ against total number of electrons are shown by the upper plots in Figure 5.7. The difference plot was more successful at generating a straight line function

than the ratio plot. The number of valence electrons were then considered, plots (c) and (d) in Figure 5.7. Plot (c) relates the number of valence electrons in the target to $\sigma_{exp}/\sigma_{BEB}$ and plot (d) relates the number valence electrons to $\sigma_{exp} - \sigma_{BEB}$. This improved the relationship for the chlorinated compounds ($R^2 = 0.86$), plot (i), but the fit was destroyed when the perfluorinated compounds were considered. ($R^2 = 0.028$), plot (ii). The inclusion of the mixed halocarbons as indicated on the plot had a detrimental effect, plot (iii), because of the large weighting factor due to fluorine atoms. Recall that carbon-fluorine bonds have a very similar cross-section contribution to hydrogen when considering bond additivities. A weighting factor for each of the electrons was then included but this led to only a small improvement over the valence electron contributions. Subsequently it was found that the best method for finding the appropriate correction factor simply involved assigning a weighting factor for each constituent atom in the molecule, 0.5 for atoms in the second row of the periodic table, and using the number of valence electrons for constituent atoms in the third row of the periodic table. The lower plots in Figure 5.7 show these correlations for the correction factor against $\sigma_{exp}/\sigma_{BEB}$ (e) and $\sigma_{exp} - \sigma_{BEB}$ (f).

The recently published alcohol data of Hudson *et al.*,[94] using the apparatus described in Chapter 3, were included in the analysis and were found to fit very well. Recently OCS and CS_2 were measured and the sulfur compounds were also considered but there is not enough data to make a conclusive comparison (only 2 compounds), although indications point toward a weighting factor of six for sulfur, equal to the number of valence electrons. As an example of the application of the correction factors shown in Table 5.2, the BEB correction factor for CF_4, is given by

$$c' = n(N_e) = (1 \times 0.5) + (4 \times 0.5) \tag{5.53}$$

and the BEB correction factor for $C_2H_4Cl_2$ is given by

$$c' = n(N_e) = (2 \times 0.5) + (4 \times 0.5) + (2 \times 7) \tag{5.54}$$

Table 5.2: Correction factors N_e used to apply the BEB correction.

Value	Correction Factor	Row in periodic table
Hydrogen	0.5	1
Carbon	0.5	2
Oxygen	0.5	2
Fluorine	0.5	2
Sulfur	6.0	3
Chlorine	7.0	3
Bromine	7.0	4

From the plot of $n(N_e)$ against $\sigma_{\text{exp}} - \sigma_{\text{BEB}}$, Figure 5.7(f), a slope M and an intercept C were optimized to maximize the agreement between the measured and BEB cross-sections. The corrected BEB cross-section, $\sigma'_{(\text{BEB})}(E)$, for electron energy E, was then calculated by

$$\sigma'_{(\text{BEB})}(E) = \sigma_{(\text{BEB})}(E)\left(\frac{c' - C}{M\sigma_{\text{BEB(Max)}}} + 1\right) \tag{5.55}$$

where $\sigma_{(\text{BEB})\text{E}}$ represents the original BEB cross-section at electron energy E and $\sigma_{\text{BEB(Max)}}$ is the maximum uncorrected BEB cross-section.

$$M = 2.9589 \tag{5.56}$$

$$C = 3.739 \tag{5.57}$$

A plot of σ_{exp} against σ'_{BEB}, is shown in Figure 5.8.

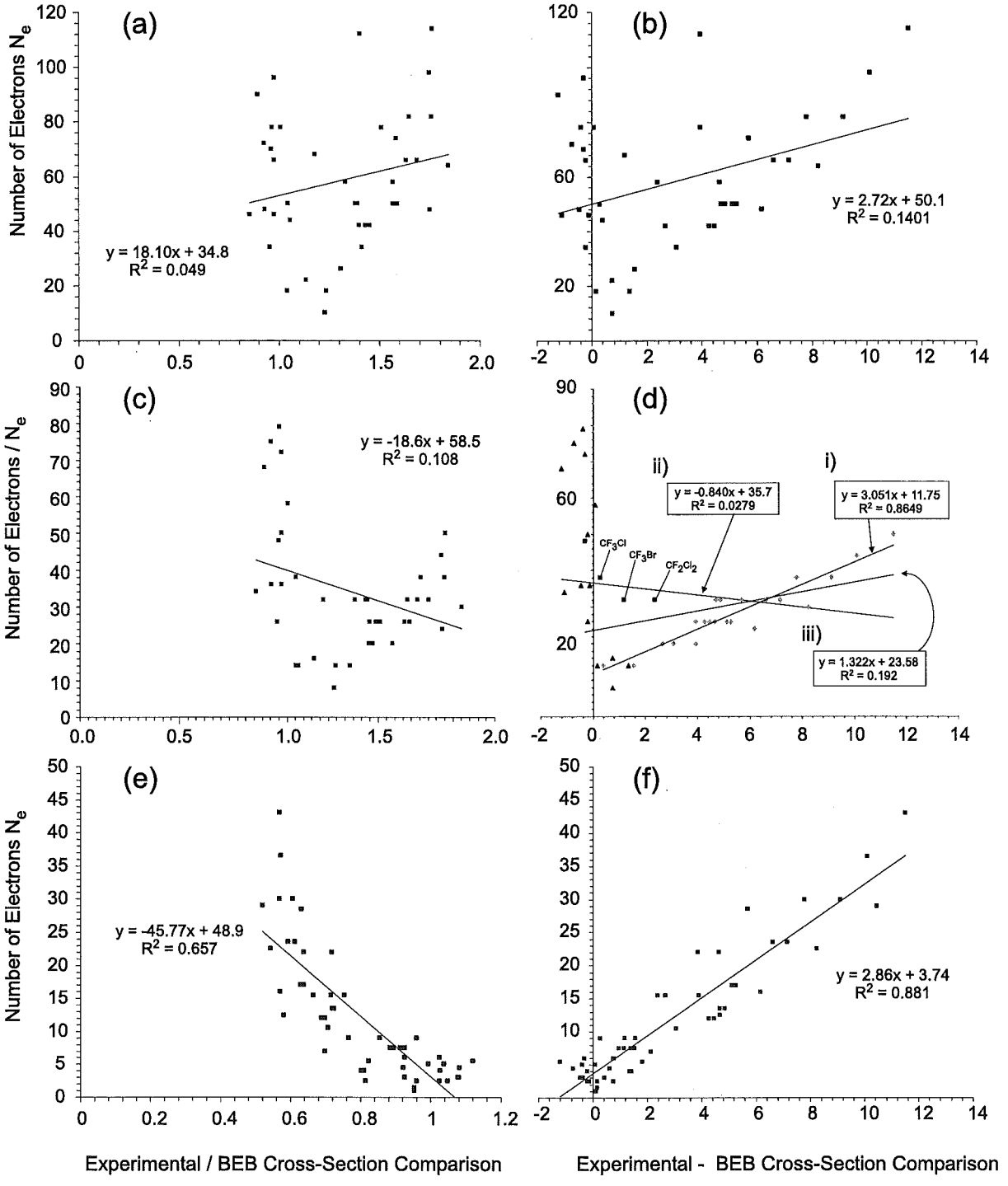

Figure 5.7: Trial plots to determine systematic deviation in the BEB theory relating to the number of electrons in the target (plots (a) & (b)), the number of valence electrons in the target (plots (c) & (d)) and the weighted nuber of electrons in the targets (plots (e) & (f)) See text for further details.

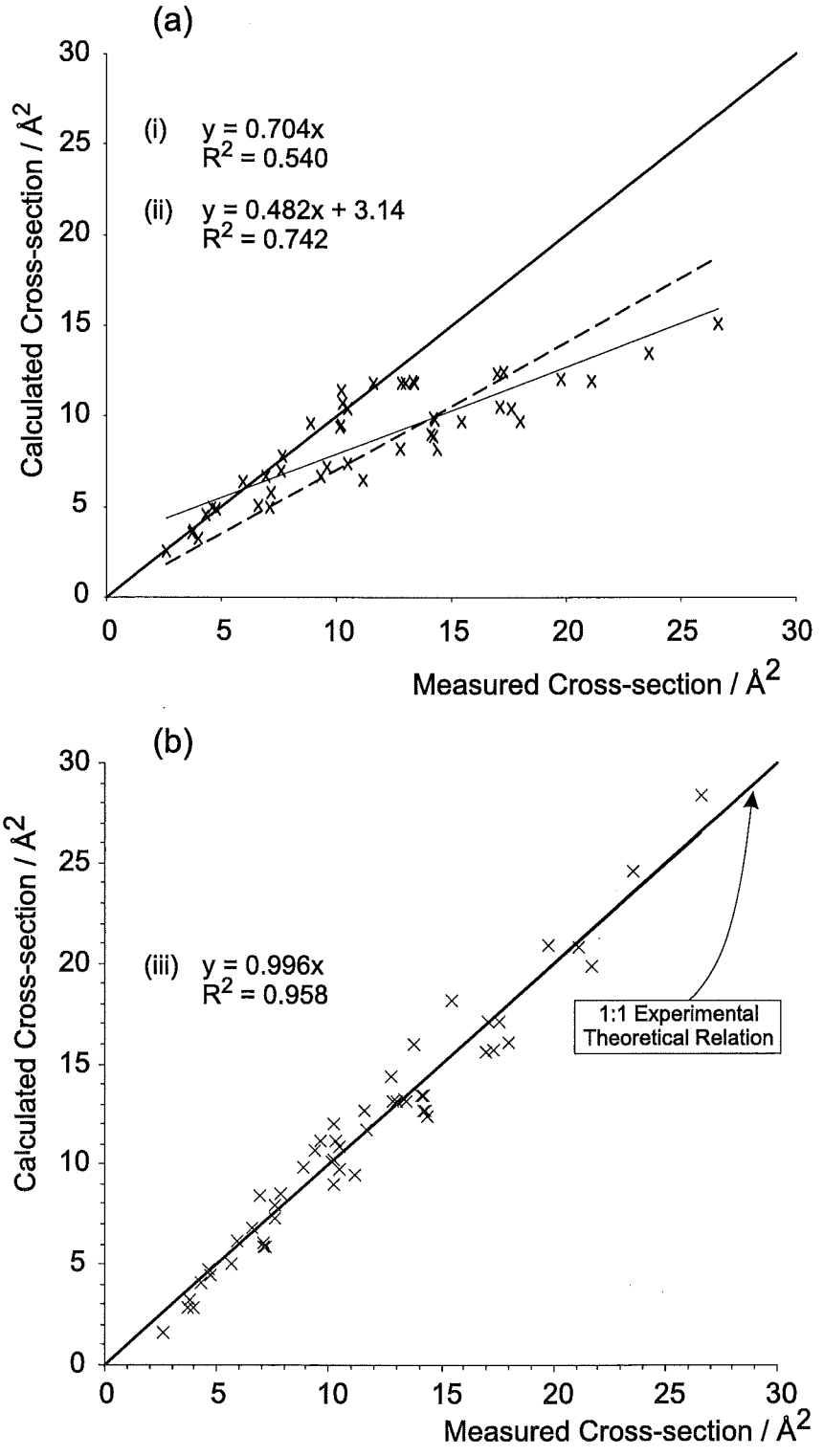

Figure 5.8: Plot (a) shows the original relationship between the measured cross-section and BEB cross-sections. The dashed line is forced though the origin (i), and the thin line is the least squares fit (ii). The heavy line is the 1:1 relation between experiment and theory. Plot (b) shows the improved relationship between the calculated and measured BEB cross-sections forced though origin (iii). The heavy line indicates the 1:1 best fit relationship.

5.5.4 Summary and comments

Agreement between the calculated and experimental cross-sections may be improved further by considering the ionization energy of the target. Intuitively, targets that contain heavy atoms have orbitals that are more loosely bound to the molecule, it is therefore anticipated that the ionization cross-section should be inversely proportional to the ionization energy. A further improvement to σ'_{BEB} can be made by including the ionization energy of the target species to the correction factor $n(N_e)$. Equation (5.55) remains the same but for the following:

$$\sigma'_{(\mathrm{BEB})}(E) = \sigma_{(\mathrm{BEB})}(E)\left(\frac{c''-C'}{M''\sigma_{\mathrm{BEB(Max)}}}+1\right) \tag{5.58}$$

$$c'' = c'/E_0 \tag{5.59}$$

$$M' = 0.2648 \tag{5.60}$$

$$C' = 0.3292 \tag{5.61}$$

Where E_0 is the ionization energy of the target in electron volts. Figure 5.9 shows the improved relationship.

Comparison between the three theoretical models discussed in the previous Sections and the experimental results obtained using the collision cell discussed in Chapter 3 give insight into the validity of some of the assumptions incorporated into the models, and the range of molecules to which the models can be applied. The measured experimental and theoretical cross-sections are presented in Figures 5.11 to 5.15. In general, both the BEB and DM models predict the shape of the electron impact ionization curves better than the polarizability model. The advantage of the polarizability model is that it is much easier to apply then the other two models. Table 5.3 compares the experimental results to the theory for the compounds studied. Figures 5.8(a) and 5.8(b) and 5.9 show the comparisons between the original BEB and improved BEB calculations and Figure 5.10 shows the effect of the improved BEB theory applied to C_2F_6, a perfluorinated ethane, CH_3Cl a chlorinated methane, $CHC{=}CCl_2$, a hydrocarbon containing a double bond, and 1,1,1,2-$C_2H_2Cl_4$ a chlorine substitution of ethane.

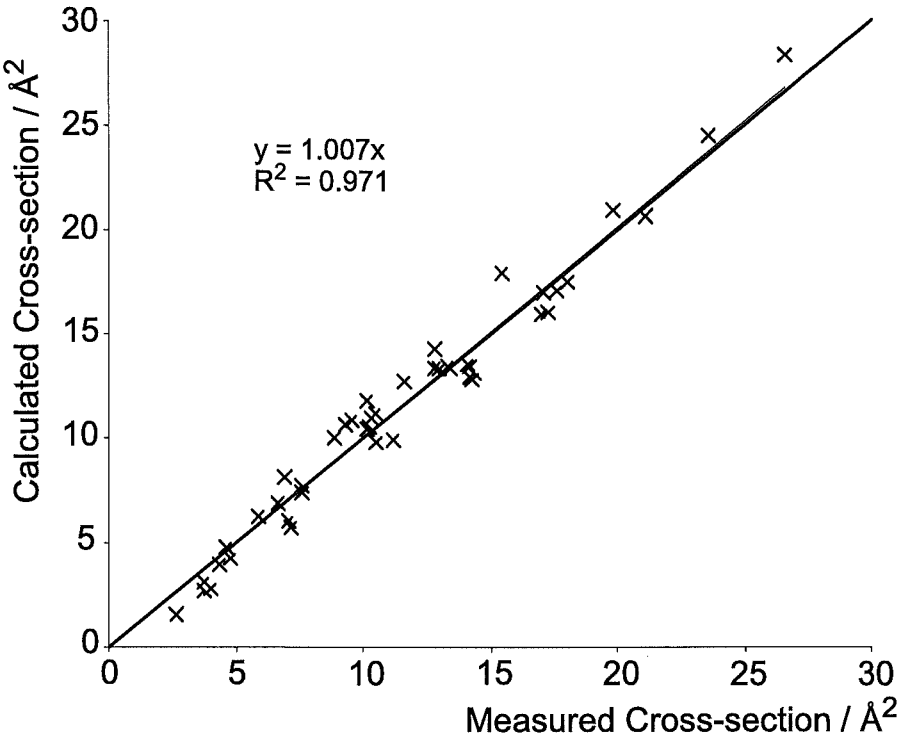

Figure 5.9: Improved relationship between the experimental and BEB cross-sections by including E_0.

Table 5.3: Comparison between experimental and calculated results, percent differences are given in parentheses. The BEB corrected values are calculated using equation (5.58)

Molecule	Expt (max)		BEB (max)			DM (max)	
	σ	EE	σ	σ(corr)	EE	σ	EE
CF_4	4.77	123	4.89(+2.2)	4.29(-10.1)	136	4.97(+4.7)	90
C_2F_4	5.92	126	6.38(+7.8)	6.25(+5.6)	125	7.19(+21.9)	88
C_2F_6	7.64	120	7.85(+2.7)	7.76(+0.40)	125	11.46(+50.0)	90
CF_3CFCF_2	9.89	126	9.62(+8.2)	9.98(+12.3)	122	10.69(+21.1)	88
C_3F_8	10.20	126	11.42(+12.0)	11.73(+15.0)	134	12.11(+17.2)	92
CF_3CCCF_3	10.30	123	10.70(+3.9)	10.99(+6.7)	120	13.51(+31.5)	92
$CF_2CFCFCF_2$	10.50	108	10.43(+0.7)	11.17(+6.4)	120	13.02(+24.5)	86
$CF_3CFCFCF_3$	11.60	108	11.90(+2.6)	12.67(+9.2)	120	15.79(+36.1)	92
CH_3F	3.79	85	3.64(-4.0)	3.15(-16.8)	100	4.99(+32.0)	70
CF_3H	4.32	120	4.53(+4.9)	3.97(-8.4)	125	5.69(+31.7)	90
CF_2Cl_2	9.60	82	7.23(-24.7)	10.86(13.2)	106	9.84(+2.8)	64
CF_3Cl	6.93	105	6.65(-4.0)	8.10(16.9)	105	8.30(+19.8)	90
CF_3Br	7.87	86	6.72(-14.6)	7.84(-0.4)	116	7.99(+1.5)	74

Molecule	Expt (max)		BEB (max)			DM (max)	
	σ	EE	σ	σ(corr)	EE	σ	EE
CF_3CN	6.33	105	7.45(+17.7)	—	110	7.69(+21.5)	80
CH_3CN	6.33	85	5.60(-11.5)	—	85	7.90(+24.8)	70
CCl_3CN	14.11	86	—	—	—	—	—
CF_2Br_2	—	—	8.42	12.48	106	11.29	64
CH_2Br_2	11.67	78	7.76(-33.5)	12.14(+4.0)	86	11.5(+1.4)	56
$CHBr_3$	13.75	80	9.86(-28.3)	16.53(+20.2)	90	14.78(+7.5)	57
CBr_4	22.10	86	—	—	—	—	—
SF_6	7.03	126	7.33(+3.2)	—	134	9.67(+36.2)	86
CH_4	4.23	71	3.26(-22.9)	2.77(-30.9)	76	5.05(+19.4)	64
CH_3Cl	6.63	70	5.08(-23.4)	6.86(+3.4)	75	7.45(+11.4)	65
CH_2Cl_2	9.35	74	6.69(-28.4)	10.61(+13.5)	90	9.93(+6.3)	66
$CHCl_3$	12.73	70	8.17(-36.2)	14.30(+11.8)	70	12.8(+0.5)	65
CCl_4	15.45	71	9.76(-36.8)	17.9(+13.5)	96	15(-2.9)	64
C_2H_4	5.70	90	5.28(-7.4)	5.11(-10.3)	72	6.97(+22.3)	64
E-$C_2H_2Cl_2$	14.49	79	8.23(-42.8)	13.15(-8.7)	88	11.14(-23.1)	70
C_2HCl_3	18.05	82	9.78(-45.7)	17.52(-2.7)	94	15.62(-13.5)	64
C_2Cl_4	21.74	79	11.3(-48.0)	21.79(+0.27)	92	17.33(-20.3)	66
C_2H_6	7.20	90	5.78(-19.7)	5.85(-18.8)	96	8.68(+20.6)	66
C_2H_5Cl	10.50	79	7.43(-29.2)	9.80(-6.7)	84	11.6(+9.4)	64
1,1-$C_2H_4Cl_2$	14.10	80	8.99(-36.2)	13.56(-3.8)	82	13.52(-2.0)	64
1,2-$C_2H_4Cl_2$	14.23	78	8.93(-37.2)	13.49(-5.0)	88	13.57(-4.6)	65
1,1,2-$C_2H_3Cl_3$	17.10	82	10.49(-38.7)	16.98(-0.7)	88	16.02(-6.5)	66
1,1,1-$C_2H_3Cl_3$	17.60	79	10.45(-40.6)	17.09(-2.8)	92	16.09(-6.7)	64
1,1,2,2-$C_2H_2Cl_4$	19.80	79	12.02(-39.3)	20.98(+6.0)	92	18.53(-5.7)	66
1,1,1,2$C_2H_2Cl_4$	21.10	79	11.99(-43.2)	20.64(-2.2)	94	18.55(-12.7)	66
C_2HCl_5	23.61	82	13.51(-42.8)	24.48(+3.7)	94	21.06(-10.8)	66
C_2Cl_6	26.61	90	15.10(-43.2)	28.33(+6.5)	96	23.59(-11.3)	66
C_3H_8	10.2		8.39(-17.7)	9.05(-11.3)	76	12.31(+20.7)	64
1-C_3H_7Cl	14.20	82	9.93(-30.1)	12.88(-9.3)	82	14.72(+4.4)	64
2-C_3H_7Cl	14.22	82	9.85(-31.1)	12.81(-10.4)	82	14.72(+2.9)	64
C_4H_{10}	—	—	10.93	—	76	14.94	64
1-C_4H_9Cl	17.4	80	12.45(-28.4)	16.00(-7.5)	82	18.35(+5.5)	64
2-C_4H_9Cl	17.12	80	12.32(-27.5)	15.90(-6.5)	82	18.35(+7.2)	64
t-C_4H_9Cl	17.14	86	—	—	—	—	—
t-$C_5H_{11}Cl$	19.53	86	—	—	—	—	—
CH_3OH	4.61	97	4.98(+7.9)	4.78(+3.6)	85	5.88(+27.5)	78
C_2H_5OH	7.60	91	7.00(-7.9)	7.36(-3.2)	85	9.82(+29.2)	75
1-C_3H_7OH	10.15	97	9.41(-7.3)	10.39(2.4)	83	13.65(+34.5)	73
2-C_3H_7OH	10.24	93	9.48(-7.4)	10.48(+2.3)	83	13.66(+33.4)	73
1-C_4H_9OH	12.85	85	11.9(-7.4)	13.37(+4.0)	82	17.47(+36.0)	72
2-C_4H_9OH	13.06	93	11.88(-9.0)	13.37(+2.8)	82	17.48(+33.8)	72
iso-C_4H_9OH	13.33	89	11.94(-10.4)	13.45(+0.9)	82	17.48(+31.1)	72
tert-C_4H_9OH	13.41	101	11.87(-11.5)	13.33(-0.6)	82	19.9(+48.4)	72

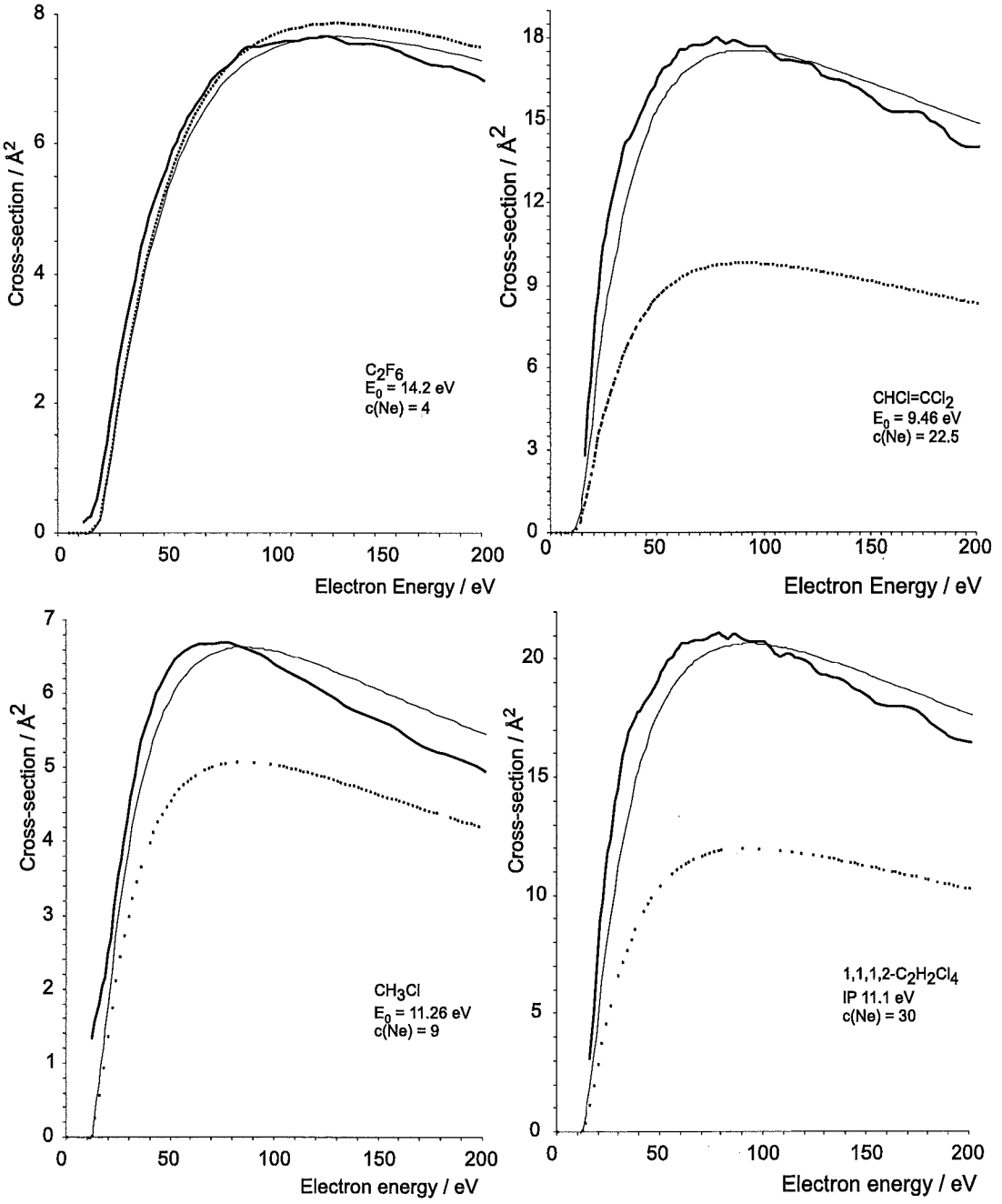

Figure 5.10: Comparison between experimental, BEB and improved BEB theories for selected molecules. The original BEB calculations are shown by the dotted line, the experimental curves are shown by the heavy black line and the improved BEB cross-section calculations are shown by the thin black line.

For large molecules, such as *t*-amyl chloride, BEB and DM calculations were not performed due to the time and processor demands for molecules of this size. The discrepancy between the calculated and measured cross-sections has been considered in terms of the level of theory applied. Because 'large' molecules have been examined in the present work, only a low level of theory can be applied to make the models computationally manageable. The calculations in the present work were carried out at the HF/6-31G level of theory using the *Gaussian94* molecular orbital package.[114] For a selection of the smaller molecules a higher level of theory was applied, and it was found that this had only a marginal effect (less than 5%) on the calculated cross-section over the entire electron energy range studied.

Two models based on polarizability have been considered, the first involved the derivation of the relationship $\sigma_{max} \propto \sqrt{\alpha/E_0}$ and the second was an attempt to model the ionization cross-section as a function of electron energy. The former provides a convenient method to predict the maximum ionization cross-section when the polarizability volume is known, the latter model, although simple to apply, cannot accurately predict the shape of the ionization curve.

The BEB model is the most successful of the theories. It is very good at predicting the maximum cross-section for target species without heavy atoms and it is very good at predicting the shape of the ionization efficiency curve for all target species. The DM model is more sensitive to input data and fails to adequately predict the shape of the ionization efficiency curve. The calculated electron energy at which the maximum occurs is generally below the measured value by 15-30 eV and the cross-section attenuates too rapidly as the electron energy increases. Application of the BEB or DM models to an unknown system depends on the system under study. In general the BEB model works best for molecules with only row one and two constituent atoms and the DM model works better for targets that include at least one heavy atom. The BEB model is a better choice for finding the shape of the electron impact ionization curve in all cases. A simple correction factor to the BEB model has been developed and this has extended the applicability of the BEB method to include molecules with

row 3 elements. In a future study an extension of this work to include additional systems with heavier atoms could be used to extend Figures 5.4 and 5.3. Unfortunately the calculations become much more demanding as the number of atoms in the target species increases making such a study a difficult task. The following figures compare the experimental results to the cross-section curves calculated using the uncorrected BEB, DM and polarizability models.

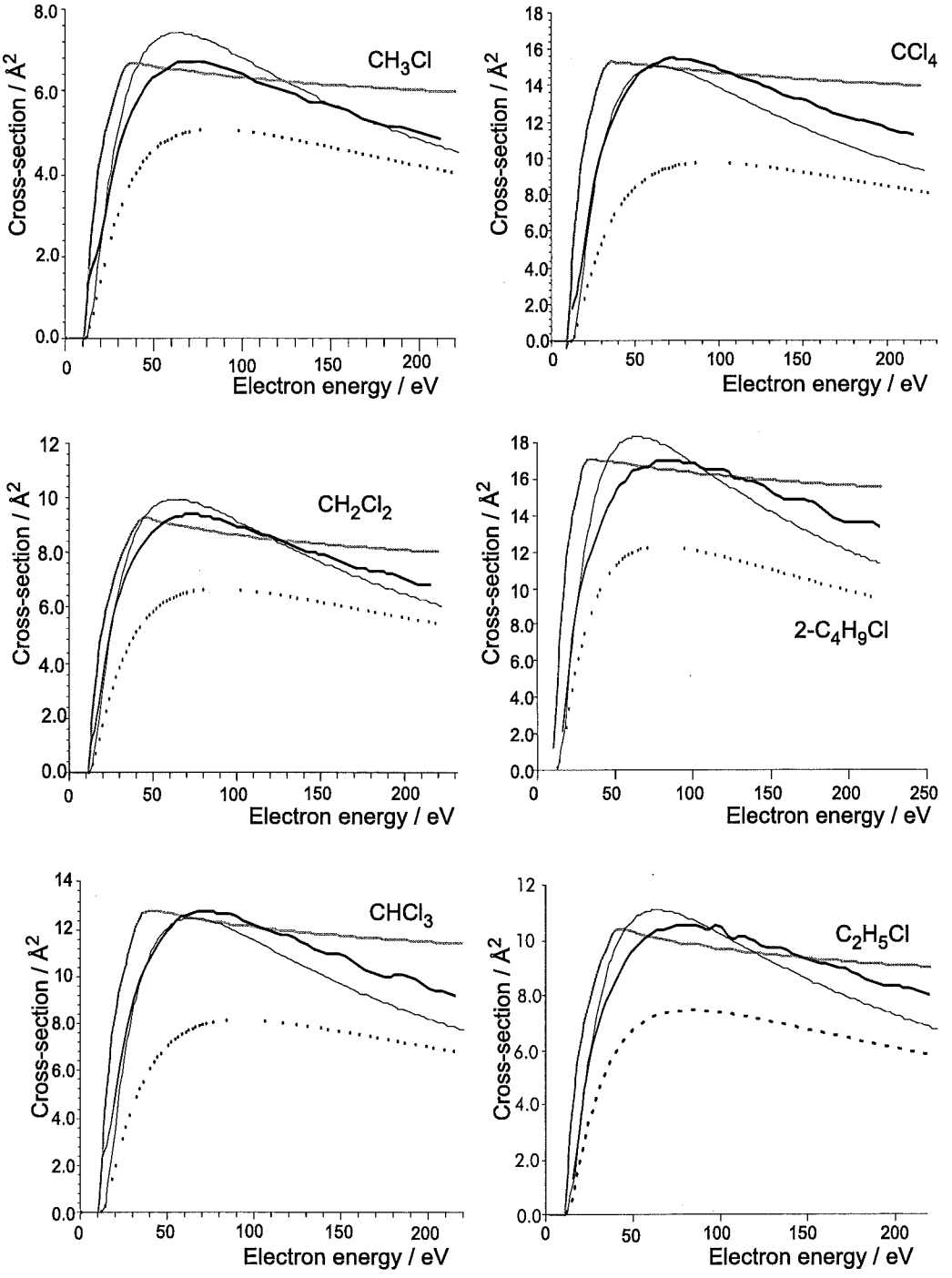

Figure 5.11: Comparison between the experimental and calculated cross-sections. The heavy black line represents the experimental data, the thin black line represents the DM calculations, the heavy gray line represents the polarizability model (normalized to experimental data) and the dashed black line represents the BEB calculations (without application of the correction factor).

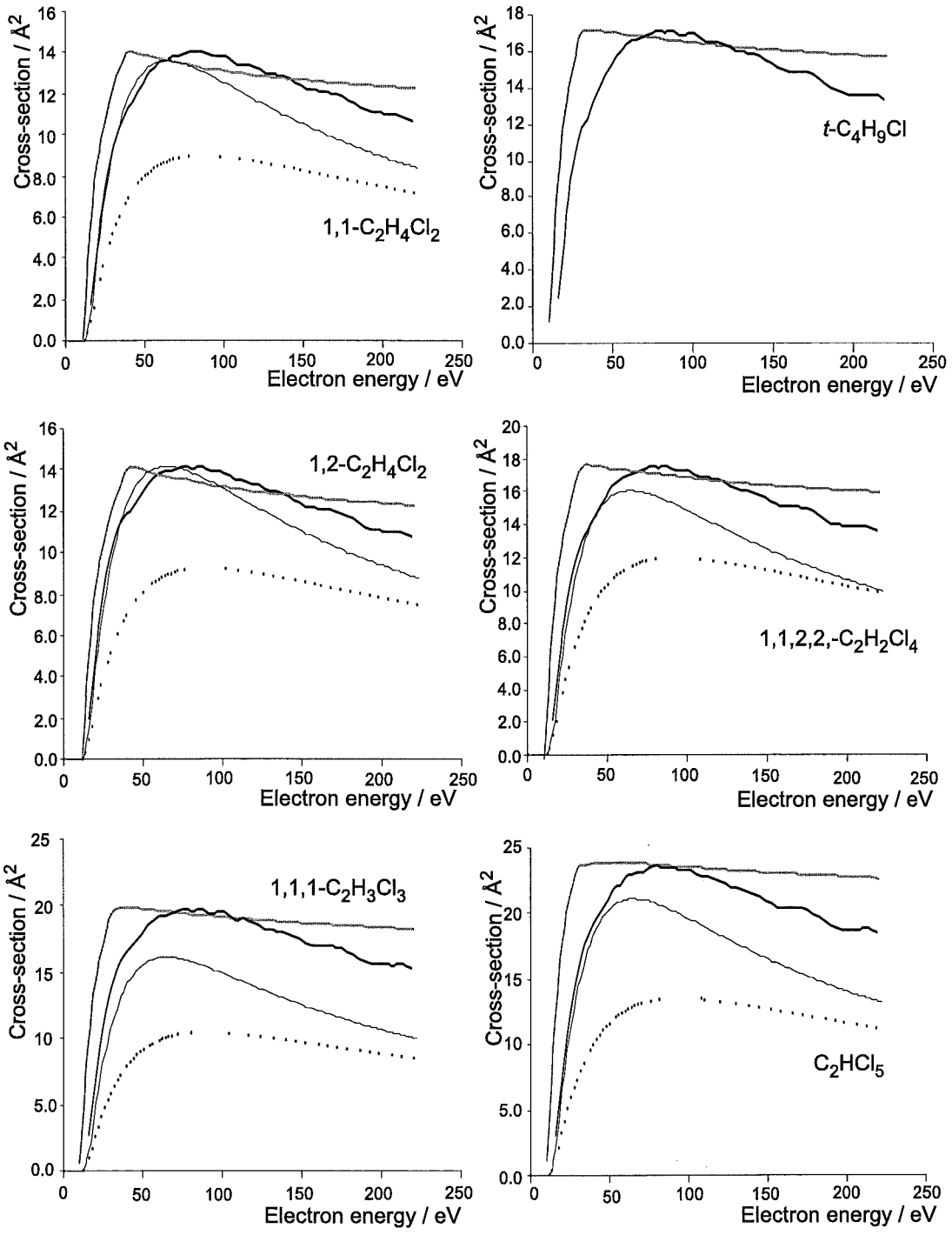

Figure 5.12: Comparison between the experimental and calculated cross-sections. The heavy black line represents the experimental data, the thin black line represents the DM calculations, the heavy gray line represents the polarizability model (normalized to experimental data) and the dashed black line represents the BEB calculations (without application of the correction factor).

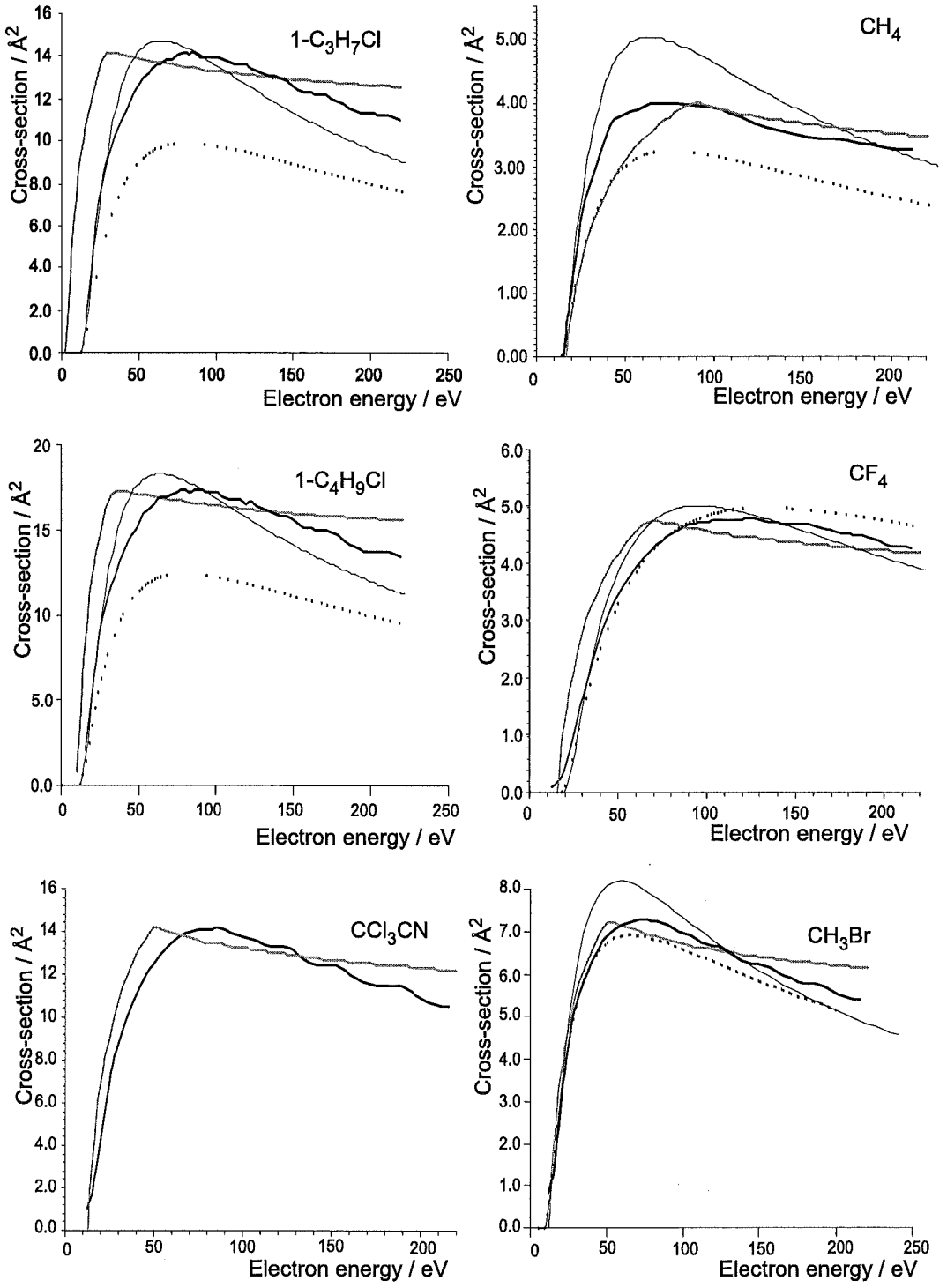

Figure 5.13: Comparison between the experimental and calculated cross-sections. The heavy black line represents the experimental data, the thin black line represents the DM calculations, the heavy gray line represents the polarizability model (normalized to experimental data) and the dashed black line represents the BEB calculations (without application of the correction factor).

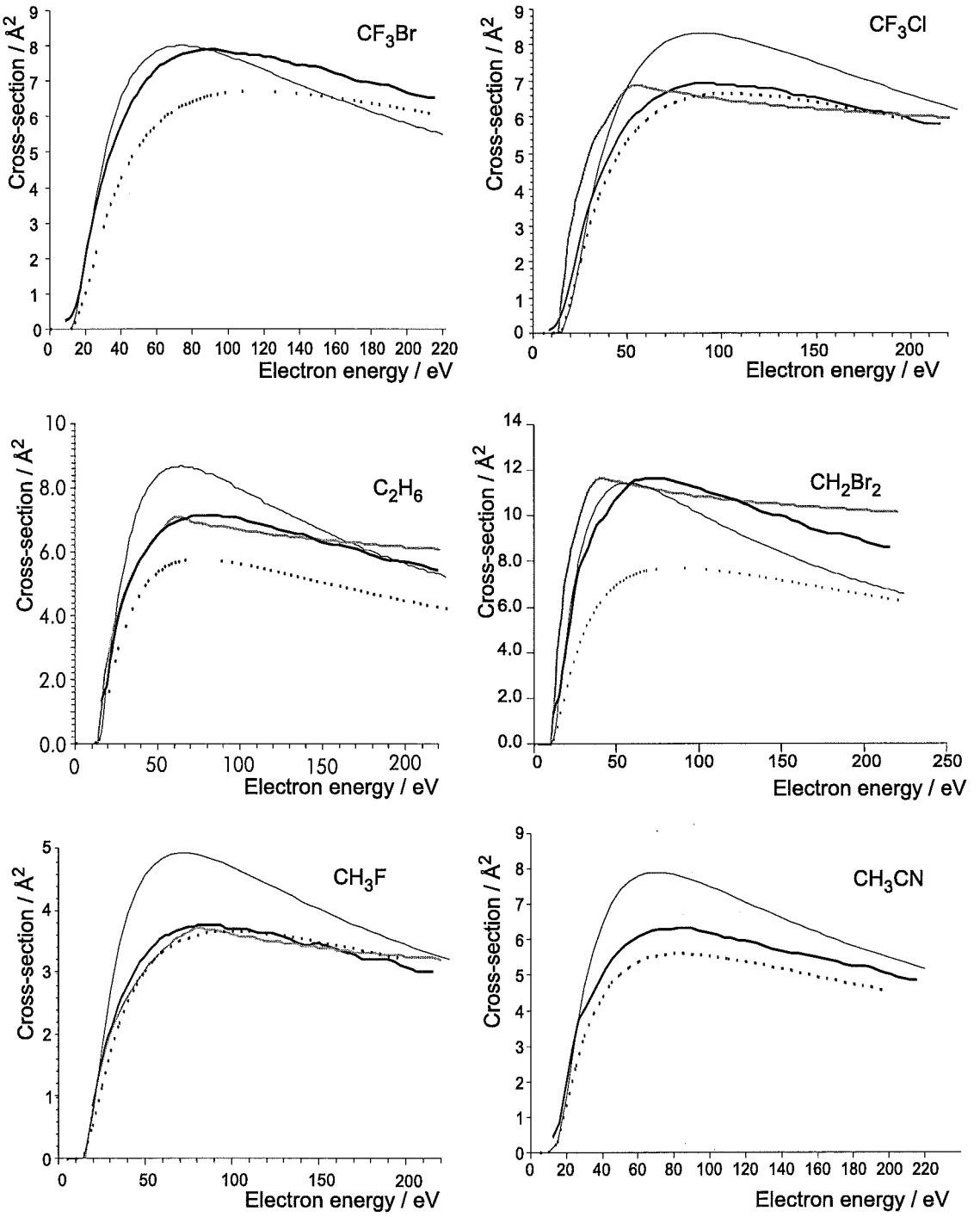

Figure 5.14: Comparison between the experimental and calculated cross-sections. The heavy black line represents the experimental data, the thin black line represents the DM calculations, the heavy gray line represents the polarizability model (normalized to experimental data) and the dashed black line represents the BEB calculations (without application of the correction factor).

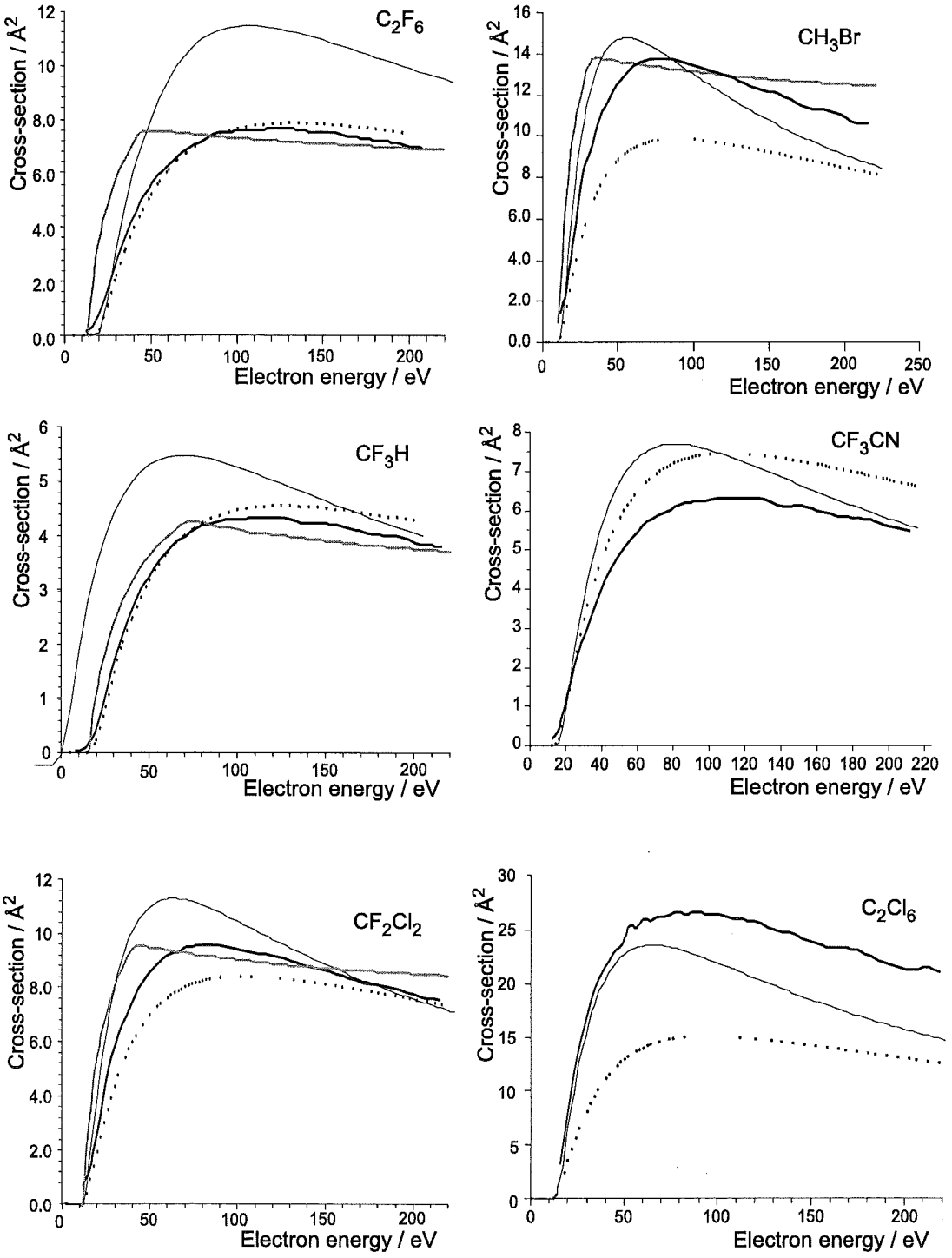

Figure 5.15: Comparison between the experimental and calculated cross-sections. The heavy black line represents the experimental data, the thin black line represents the DM calculations, the heavy gray line represents the polarizability model (normalized to experimental data) and the dashed black line represents the BEB calculations (without application of the correction factor).

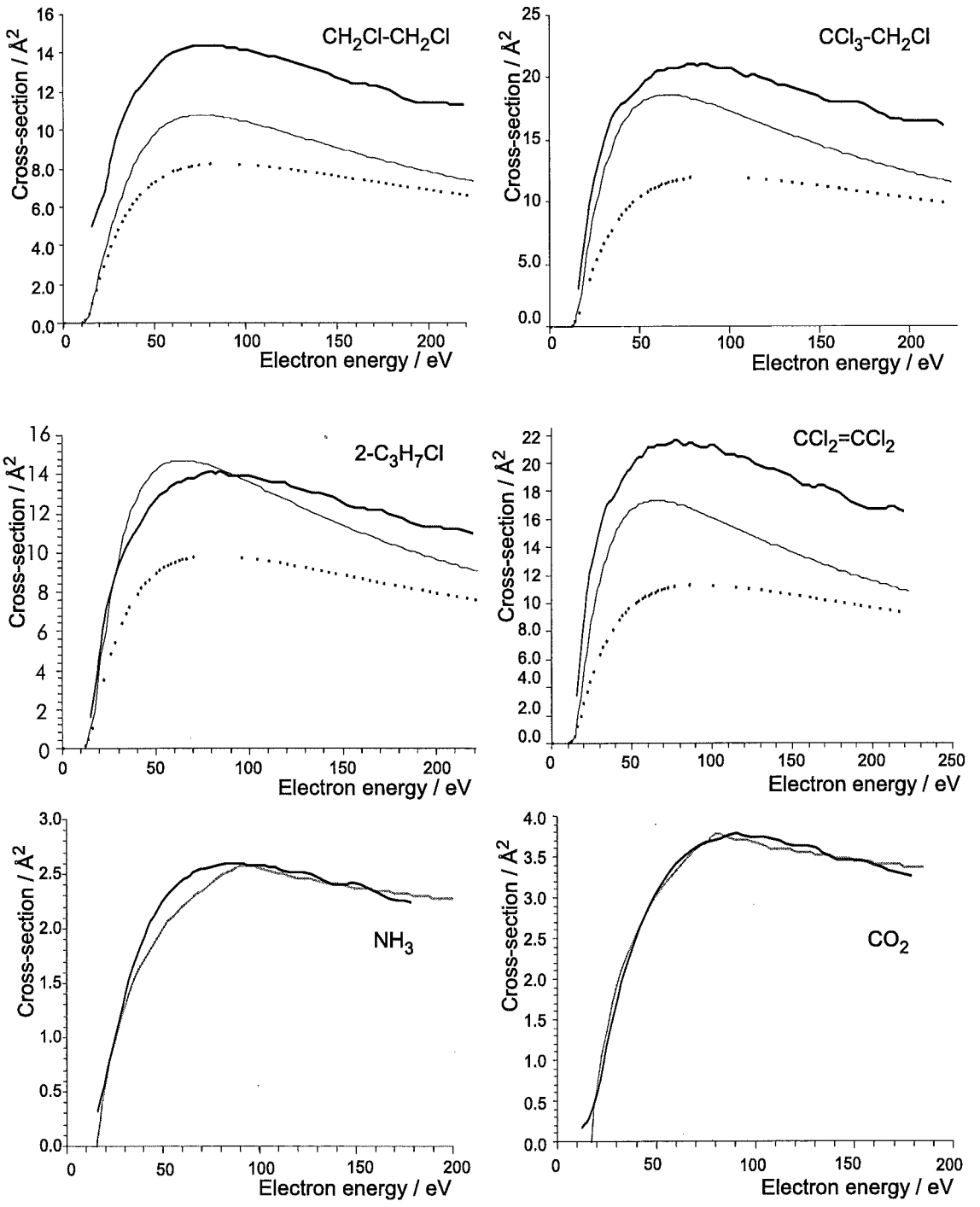

Figure 5.16: Comparison between the experimental and calculated cross-sections. The heavy black line represents the experimental data, the thin black line represents the DM calculations, the heavy gray line represents the polarizability model (normalized to experimental data) and the dashed black line represents the BEB calculations (without application of the correction factor).

Part II

ELECTRON IMPACT IONIZATION: CROSSED BEAM STUDIES

6. CROSSED MOLECULAR BEAMS

6.1 Introduction

The development of crossed molecular beam techniques has greatly advanced our basic knowledge of chemical and physical processes, for example, elastic, inelastic and reactive scattering, product energy disposal in bimolecular collisions, effect of molecular orientation, molecular beam electric resonance spectroscopy, and photolytic dissociation dynamics. Crossed molecular beam techniques facilitate a large degree of control over the particles in the beam, including temperature distribution, beam velocity, quantum state selection and molecular orientation.

There are four main beam types that have been used in crossed molecular beam experiments:

1. effusive beam sources;
2. photon beam sources;
3. supersonic (hydrodynamic) beam sources;
4. charged particle beam sources, including ion and electron beam sources.

In the present work the latter two sources have been used extensively and will be described in detail.

Crossed molecular beam experiments involve the generation and intersection of two

beams, usually at right angles, and detecting the reaction products.[a] The greatest advantage of using two crossed molecular beams, as opposed to a beam through a static target gas (Part I), is that the crossing point of the two beams can be regarded as a point source for the nascent products.

The advantage of a point source is that information on the angular distribution of the products and their energy disposal can be directly obtained. If the initial and final reactant and product quantum states are known the state-to-state differential cross-section can be obtained. If the reactant orientation is also known the orientation dependence on the state-to-state differential cross-section may be determined. R. B. Bernstein and R. D. Levine described the orientation dependent measurement of a state-to-state differential cross-section as the "ultimate experiment".[138]

The research objectives for this work were two-fold:

1. Measurement of the kinetic energy release and associated scattering patterns for the dissociative ionization of diatomic and oriented symmetric top molecules by electron impact using crossed molecular beams and ion imaging detection;

2. Measurement of the differential state-to-state ion-molecule reaction cross-sections using a beam of oriented symmetric top molecules of the type CX_3Y with H_3^+, Cl^-, and Br^- where X and Y = H, F, Cl or Br.

There have been significant technical problems associated with these experiments, especially the ion molecule reactions and although a lot of experience has been gained in areas of ion imaging, signal enhancement and experimental methods the "ultimate experiment" has remained beyond our reach.

This chapter will begin with a brief historical overview of molecular beam techniques followed by a description of the mechanics of molecular beam scattering. In Chapter 7 a brief historical overview and description of the development of the molecular beam

[a] For the remainder of this work x is the molecular beam axis, z is vertical axis and y is the remaining axis.

machine at the University of Canterbury will be presented. This will be followed by a Chapter devoted to the beam sources used and their characterization. Technical aspects of ion imaging will be discussed followed by a review of the methods for recovering three dimensional product distributions from recorded two dimensional ion images. Ion trajectory simulations will then be described, followed by preliminary results on the ionization of oxygen. Conclusions will be presented with a discussion of possible improvements to the machine, and suggestions for future work.

6.2 Literature review and mechanics of crossed beam experiments

A crossed beam experiment for the study of reaction dynamics involves the intersection of a beam of neutral molecules, electrons, ions or photons with another beam under single collision conditions. The basic components of a crossed beam experiment are shown in Figure 6.1. The beam sources used depend on the reactions of interest. In the present work, an electron beam source, an ion beam source and a supersonic molecular beam source have been used. Selectors 1 and 2 shown in Figure 6.1 may be used to select the velocity, quantum states and/or molecular orientation of the reagents. The type of detection used for the products generated at the beam crossing must be selected according to the information required, i.e., kinetic and/or internal energy, angular distribution, or chemical composition of the products. The term reaction is used in the broadest sense and may include collisions where only kinetic energy is transfered (elastic collisions), or collisions where intramolecular rearrangement or internal energy transfer occurs (inelastic collisions), or reactive collisions where intermolecular rearrangement occurs.

Particles interact in the center-of-mass reference frame. The interaction potential between the beam particles depends only on their relationship to each other in space and not on the geometric constraints applied by the beams traveling through the machine. A transformation between the laboratory reference frame and the particle reference frame needs to be applied in order to analyze the results. For electron

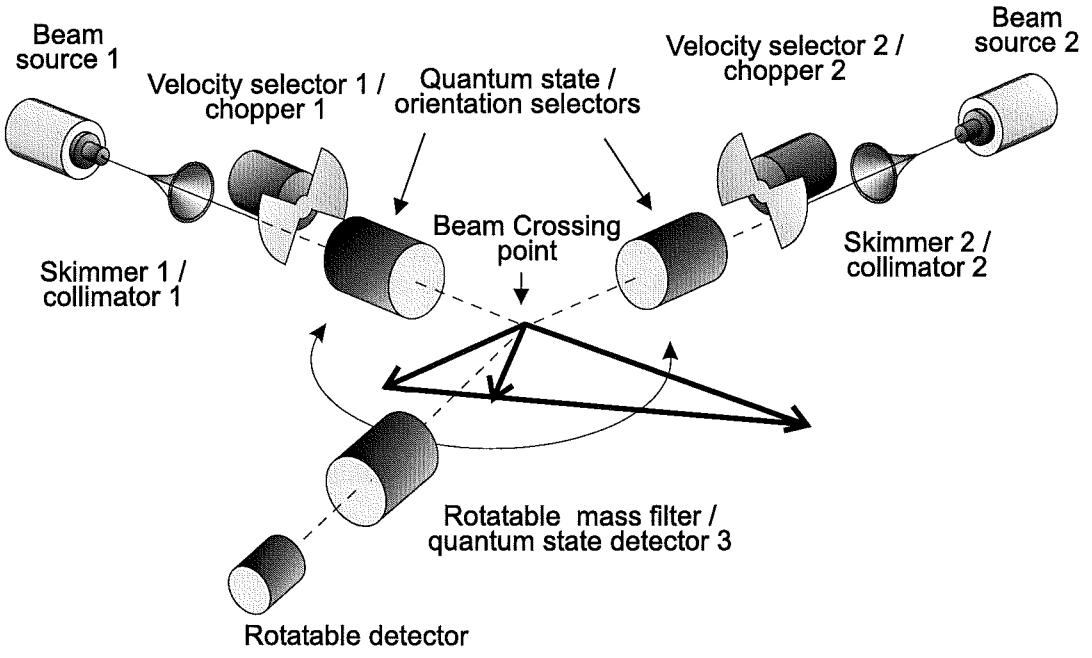

Figure 6.1: Schematic of generalized crossed molecular beam experiment.

– molecule collisions this transformation is simplified, because the molecular mass of the neutral is much greater than the electron mass. Thus the molecular beam axis is considered to be the resultant center-of-mass vector.

Further discussion of crossed molecular beam methods can be found in Levine and Bernstein,[138] Fluendy and Lawley[139] and Casavecchia.[140] The 1986 Nobel lecture transcripts[141–143] are also an excellent source.

6.3 Electron impact ionization by crossed beam methods

The following parameters of the electron impact ionization process can be explored using crossed beams:

1. partial or total electron impact ionization cross-sections;
2. kinetic energy distribution of fragments ions;
3. angular scattering patterns of fragment ions;

4. steric effects for electron impact ionization of symmetric top molecules when a hexapole quantum state selector orienting field is employed.[3]

Characterization of the dissociative ionization process requires the identification of the fragment ions, measurement of the ion kinetic energies, E_k, determination of ion appearance potentials AP, and the availability of bond energy, D, and the ionization energy of the fragment ions E_0.

For example, for the dissociative ionization process represented by

$$AB + e^- \longrightarrow A^+ + B + 2e^- \tag{6.1}$$

$$AP(A^+) = D(A - B) + E_0(A) + E^* \tag{6.2}$$

Where E^* is the excess energy of the products, which may be partitioned between internal and translational energy of both A^+ and B. Figure 6.2 illustrates the potential energy curves for some of the possible mechanisms leading to positive ion formation. Referring to Figure 6.2 the following processes are considered.

a. Ionization to the ground electronic state of the molecular ion.

$$AB + e^- \longrightarrow AB^+ + 2e^- \tag{6.3}$$

b. Dissociative ionization into the ground electronic state of the fragments.

$$AB + e^- \longrightarrow A^+ + B + 2e^- \tag{6.4}$$

c. Ionization and transition to an electronically excited molecular ion.

$$AB + e^- \longrightarrow (AB^+)^* + 2e^- \tag{6.5}$$

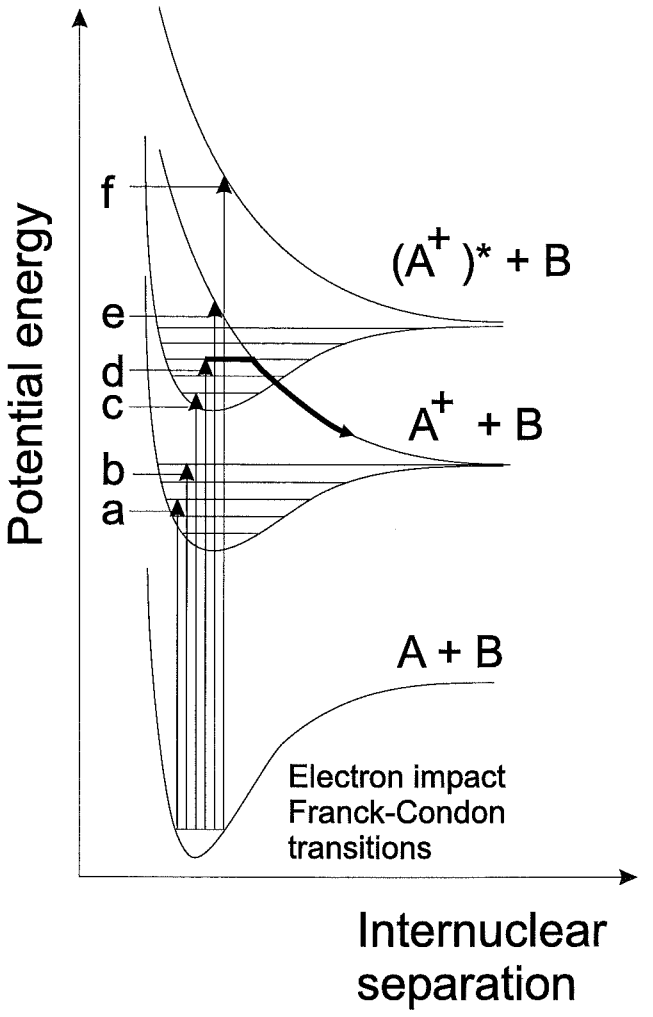

Figure 6.2: Schematic representation of Franck-Condon dissociation processes.

d. Predissociation of a stable molecular ion or autoionization of a highly electronically excited molecular state (Rydberg state).

$$AB + e^- \longrightarrow (AB^+)^* \longrightarrow A^+ + B + 2e^- \tag{6.6}$$

e. A transition to a repulsive state of the molecular ion dissociating to ground state fragments.

$$AB + e^- \longrightarrow A^+ + B + 2e^- \tag{6.7}$$

f. A transition to a repulsive state of an electronically electronic state of the molecular ion dissociating to electronically excited fragments.

$$AB + e^- \longrightarrow (A^+)^* + B + 2e^- \tag{6.8}$$

Ion pair formation has not been considered here. In all cases, a continuous distribution of kinetic energies of the dissociation products will be observed. If the predissociation lifetime is longer then the vibrational relaxation period, the measured ion energy distribution will reflect the vibrational structure of the predissociated state.

After the dissociation event the total energy is distributed between A and B. Applying the principle of conservation of momentum, for the ion A^+

$$E_k(A^+) = \frac{m_B}{m_A + m_B} E_k \tag{6.9}$$

Where E_k is the total available kinetic energy.

If the energy of ion A^+ is measured then the kinetic energy of B can be determined. The application of equation (6.2) then enables the internal energy of the fragments to be determined.

6.3.1 Cross-section measurement

Crossed beam methods to study the electron impact ionization process were initially applied to target species that were unstable at ordinary temperatures and pressures, for example, atomic targets such as H, N and O, the alkali and alkaline earth metals, ions, radicals and targets in metastable states.[23,144] Because the beam crossing volume in a crossed beam experiment is very small, the pathlength over which target ions are formed is also very small. This leads to low ion currents, making the detection of the ion signal very difficult. In addition, the background signal is often of the same order or even larger than the target signal. In the early 1960's Dolder[145] introduced modulation of both the electron beam and molecular beam in order to reduce the interference from

background collisions. This facilitated the measurement of the target - background difference signal.

In order to apply equation (2.3) to a crossed electron – molecule beam experiment it is necessary to include an energy correction for the velocity of the molecular beam, v_t, a beam overlap function, F, and a value for particle density S. A Jacobian transformation also needs to be included

$$\frac{I_i}{I_e} = \sigma(E_{\text{collision}})S\left[\frac{(v_e^2 + v_t^2)^{1/2}}{v_t v_e}\right]F \tag{6.10}$$

The electron current I_e is typically measured using a Faraday plate and electrometer. The ions may be measured using either a Faraday plate or a particle multiplier. Previously these were channeltron type multipliers but are increasingly being replaced by microchannel plate detectors, which offer a higher gain and, more importantly, a wider angle of acceptance for the product ions.

The collision energy is given by:

$$E_{\text{collision}} = \frac{1}{2}\mu v^2 \tag{6.11}$$

where

$$v^2 = v_e^2 + v_t^2 \tag{6.12}$$

$$\mu = \frac{m_e m_t}{m_e + m_t} \tag{6.13}$$

because the mass of the electron is much less than that of the target molecules the denominator in equation (6.13) may be approximated to m_t, leaving $\mu \approx m_e$. Multiplying equation (6.12) by $\frac{1}{2}m_e$ then gives

$$E_{\text{collision}} \approx \frac{1}{2}m_e v^2 = \frac{1}{2}m_e v_e^2 + \frac{1}{2}m_e v_t^2 \tag{6.14}$$

$$= E_e + \frac{m_e}{m_t}E_t \tag{6.15}$$

A further approximation may be made when the molecular beam has a low kinetic energy, for example, a supersonic molecular beam. The total kinetic energy of molecules in the beam is $\sim$ 100 meV compared to the energy of the electrons which typically must have energy in excess of 10 eV for ionization. In this case the collision energy may be approximated to the electron energy.

The beam overlap function, given by the following expression, is the integral of the spatial distribution of the target and electron beam, and may be very difficult to determine.

$$F = \frac{\int j_e(z) j_t(z) dz}{\int j_e(z) dz \int j_t(z) dz} \tag{6.16}$$

where j_t and j_e represent the spatial distribution of particles in the target and electron beams, respectively.

Determination of the neutral target beam density is particularly difficult and for this reason an electron impact ionization cross-section determined using a crossed beam method is typically normalized to a cross-section using the condenser plate method. The normalization factor for a particular crossed beam machine may be determined and then applied to other target species measured using the same apparatus under similar experimental conditions to determine unknown cross-sections. An early review article that was prepared by Kieffer and Dunn[23] considered early crossed beam methods using alkali target species.

Stevie and Vasile[146] measured electron impact ionization cross-sections for F_2 and Cl_2 using a supersonic crossed beam apparatus. The machine was calibrated to Rapp and Englander-Golden's Ar, Kr and O_2 results. The normalization factor was found to be in excellent agreement for each of those targets, suggesting that the machine did not suffer from major discrimination effects. The supersonic beam intersected the electron beam (up to 102 eV energy) at 90 degrees and was modulated at 70 Hz. The products were detected using a Varian MAT magnetic sector mass spectrometer normal to both the molecular beam and the ion beam.

Syage[147] used a supersonic molecular beam of NH_3 produced with an electromag-

netic nozzle. The pulsing sequence involved a 400 ns electron pulse, followed by a 200 ns delay, followed by a 6 μs extraction pulse. The ions were detected by time-of-flight mass spectrometry using a multichannel plate detector. The flight tube contained two parallel deflection plates to correct for the molecular beam velocity component. The chief advantage of this technique over other methods was that the multichannel plate detector had a very large sampling area compared to channeltron type multipliers. The results were normalized to the results of Märk *et al.*[57] and Stephan *et al.*[60]

Syage[147] identified some problems associated with the crossed beam technique for electron impact studies that have also been experienced in the present work:

1. the importance of maintaining a uniform ion extraction field;
2. differences in focusing ions with excess kinetic energy into the mass spectrometer so that all of them are detected with the same efficiency;
3. the necessity to maintain constant beam fluxes over the period that measurements are made and between subsequent measurements in order to ensure a consistent overlap and particle density;
4. product mass and energy detector sensitivity considerations.

Wetzel, Baiocchi, Freund, Hayes and Schul measured ionization cross-sections for a wide range of targets over the electron energy range of 0–200 eV. Systems studied included methyl and methylene radicals,[148] SiF,[149] SiF_2[150] and SiF_3[151] radicals, a range of atomic targets,[152,153] GaCl, GeCl and SnCl,[154] and N, CO, CO_2, CS and CS_2.[155] The target species were ionized, collimated, mass selected and accelerated to $\sim$ 3 keV to form an ion beam. This ion beam was then passed through a charge transfer cell where the neutrals were reformed after which any remaining ions in the beam were removed by a charged plate parallel to the beam and Rydberg species were removed by field ionization. An electron beam then passed through the high energy neutral beam and ions were formed. The product ions were detected using a magnetic sector mass spectrometer. The neutral beam was collected with a reported 100% efficency on

a hot nichrome wire with a secondary electron collector. The neutral beam flux was also calibrated using a piezoelectric crystal which absorbed energy from the ~3 keV neutrals, giving a small voltage change. The reported sensitivity of the piezoelectric crystal was 1 VW^{-1}. The neutral beam was modulated at 1.5 Hz. The molecular and electron beam profiles were measured using a beam stop on a linear motion feed-through which was passed into the beam while monitoring the beam signal. This enabled the beam overlap function to be calculated. The electron beam was collected using a Faraday cup. Since the particle density of both electron and neutral beams were known and the beam overlap was known, absolute total ionization cross-sections were claimed.

Torres *et al.* measured total and partial electron impact ionization cross-sections for CH_2F_2,[156] CF_4[156] and CH_3F[157] as well as nascent kinetic energy distributions for the fragment ions using a commercial time-of-flight mass spectrometer coupled to a supersonic molecular beam source and a pulsed electron gun. A microchannel plate detector was used to detect the ion products normal to both the electron beam and the molecular beam. Both the extractor and repeller were maintained at 2000 V during the collision process. After the electron beam had passed through the molecular beam the extractor plate was pulsed to 1815 V leaving a potential difference across the extractor repeller region of 185 V. A set of $x-$ $y-$ deflector plates was used to correct for the initial supersonic beam velocity which was super-imposed on the recorded kinetic energy distribution. The kinetic energy distribution of the nascent products, $E_k(u(t))$, was calculated using

$$E_k(u(t)) = \frac{2m}{(qE^2)} \frac{df(t)}{dt} \tag{6.17}$$

Where $f(t)$ describes the shape of the time-of-flight peak for the ion of interest, and m, q and E are the mass, charge and electric field strength in the ionization region, respectively. The product ions were produced with kinetic energies of up to 10 eV. The recorded kinetic energy was strongly dependent on the energy of the ionizing electron beam.

6.3.2 Measurement of differential electron impact ionization cross-sections

The differential electron impact ionization cross-section offers a more complete description of an ionization event than the total cross-section measurements described in Part I. There are two approaches to the measurement of the differential cross-section. The first involves the measurement of the energy and momentum of the scattered and ejected electrons. This method is applicable to both non-dissociative and dissociative ionization. The second method involves measuring the momentum vector of the scattered product ion. This method of measuring the cross-section is applicable to the measurement of dissociative differential cross-sections only, because the momentum transfer from the electron to the parent ion is negligible.

Using the former approach there are two types of differential cross-section that can be measured; the five-fold differential cross-section, also referred to as the triple differential or (e,2e), cross-section and the three-fold differential cross-section, also referred to as the double differential cross-section. The five-fold differential cross-section offers the most complete description of an ionization event, it involves the measurement of the momentum vectors of the incident electron $\mathbf{k}$, the scattered incident or primary electron, $\mathbf{k}_A$, and the ejected or secondary electron $\mathbf{k}_B$ (and hence the energy, E, of those electrons) defined by the three scattering angles θ_A, θ_B and ϕ_B as illustrated in Figure 6.3. $\mathbf{K}$ is the difference vector, $\mathbf{k}$ - $\mathbf{k}_A$, of the incident and primary electrons. In the case of dissociative ionization, analysis of the five-fold differential cross-section data are greatly complicated because of the many possible intermediate states which may participate in the reaction. The three fold differential cross-section involves the measurement of $\mathbf{k}$ and $\mathbf{k}_A$ only, the ejected electron is ignored thus simplifying measurement and analysis considerably.

Measurement of the kinetic energy distribution of the dissociation products provides information on the electronic transitions of the reactants to form the products and enables the functional form of the potential energy curves to be determined as well as the relative spacing between the initial and final states.

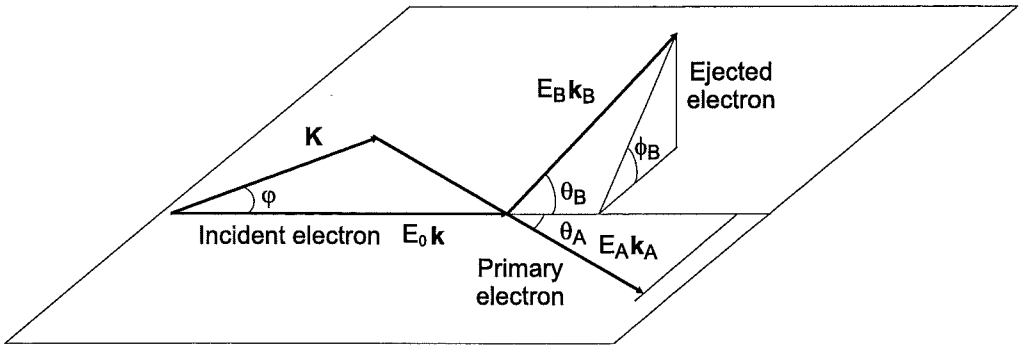

Figure 6.3: Scattering angles, energies and vectors in electron scattering experiments.

6.3.3 Symmetry selection rules for ionization of homonuclear diatomics

The majority of the early electron impact studies were focused on the anisotropic scattering of protons from electron impact ionization of hydrogen.[144] Dunn[158] established symmetry-based selection rules to describe the anisotropic scattering of atomic fragment ions from hetero- and homo-nuclear diatomic targets. Since the electronic transitions are much faster then the rotational period of the diatomic the reaction products will dissociate in a direction dictated by the vibrational motion of the reactant immediately before the electronic excitation event. This means that if the transition probability is proportional to orientation then an angular product distribution may be expected. A $\cos^2\theta$ dependence of the product distribution on the dissociation of H_2 by electron impact had been observed previously.[158] Dunn used symmetry selection rules in order to explain the observed results. The selection rules were based around the premise that the symmetry prior to the collision must be preserved after the ionization event. He considered two possibilities:

1. that the target molecule has the axis of symmetry aligned perpendicular to the electron plane wave vector $\mathbf{k}$;

2. that the target molecule has its axis of symmetry aligned parallel to the electron plane wave vector $\mathbf{k}$;

In the first case, for a transition to be symmetry allowed the product ion must possess the same symmetry as the reactant for the rotation and reflection operators. In the second case the only transitions for non-vanishing overlap integrals[159] are those for which A $\nleftrightarrow$ E, + $\rightarrow$ + and − $\rightarrow$ −. First Dunn considered transitions that do not cause ionization of the target, these are less complex because there are only two particles involved throughout the collision event. In the limit of the Born-Oppenheimer approximation it was reasoned that the scattered electron can be represented by the plane wave vector $\mathbf{k}_A$. The total wave vector, which is the combination of $\mathbf{k}$ and $\mathbf{k}_A$, as shown in Figure 6.3, was then given by $\mathbf{K} = \mathbf{k}$ - $\mathbf{k}_A$. Dunn then defined ψ as the angle between $\mathbf{K}$ and $\mathbf{k}$, and established the following relation:

$$\sin\theta_A \sim \frac{\theta_A}{(\delta^2 + \delta\theta_A + \theta_A^2)^{1/2}} \tag{6.18}$$

where $\delta = (|\mathbf{k}| - |\mathbf{k}_A|)/|\mathbf{k}_A|$ and θ_A is the angle through which the electron is scattered. The average angular distribution was then given as

$$\langle \sin\psi \rangle_{Av} = \frac{\int \sin\psi F(\theta_A, k) \sin\theta_A d\theta_A}{\int F(\theta_A, k) \sin\theta_A d\theta_A} \tag{6.19}$$

In the low energy case it was then proposed that $\delta \gg \theta$, hence $\sin\phi \sim 0$ and the symmetry axis $\mathbf{K}$ is nearly along $\mathbf{k}$, and consequently the observed transitions should follow the same transition selection rules as photo-absorption cross-sections.

In the high energy case δ becomes smaller and hence $F(\theta, k)$ should become more strongly peaked near $\theta = 0$. The function $F(\theta, k)$ must then be known in order to determine if $\sin\phi$ tends toward unity, which is the case if $\delta \ll \theta$. In this case, the axis of symmetry would be perpendicular to $\mathbf{k}$. Dunn then drew an analogy between this analysis and that of molecular excitation by photons. The allowed perpendicular transitions for a homonuclear diatomic are given on Table 6.1 and the allowed parallel transitions for a homonuclear diatomic are given on Table 6.2.

If dissociative ionization occurs then the symmetries are even less well defined than for the excitation case because there are two scattered electrons. From momentum

Table 6.1: Allowed perpendicular transitions for a homonuclear diatomic molecule.

Transition	Transition	Transition
$A_{1g} \leftrightarrow E_{1u}$	$A_{1g} \leftrightarrow E_{2g}$	$A_{2g} \leftrightarrow E_{1u}$
$A_{2g} \leftrightarrow E_{2g}$	$A_{1u} \leftrightarrow E_{1g}$	$A_{1u} \leftrightarrow E_{2u}$
$A_{2u} \leftrightarrow E_{1g}$	$A_{2u} \leftrightarrow E_{2u}$	$E_{1g} \leftrightarrow E_{2u}$
$E_{1u} \leftrightarrow E_{2g}$		

Table 6.2: Allowed parallel transitions for a homonuclear diatomic molecule.

Transition	Transition
$A_{1g} \leftrightarrow A_{1u}$	$A_{2g} \leftrightarrow A_{2u}$
$E_{1g} \leftrightarrow E_{1u}$	$E_{2u} \leftrightarrow E_{2g}$

considerations, however, it was assumed that the ejected electron lies along the **K** vector. Furthermore the transitions from a stable state to the continuum are governed by Krönigs selection rules[159]

> *For molecules with identical nuclei, states that can combine with one another with emission or absorption of radiation cannot predissociate into one another and vice–versa.*

6.3.4 Measurement of kinetic energy and angular distribution of fragment ions

The measurement of the kinetic energy and angular scattering of the fragment ions from an electron impact ionization event was first performed in the 1930's, but that work was largely ignored until the early 1960's when G. H. Dunn proposed the selection rules discussed above. For a decade the measurement of the kinetic energy of the dissociation products and the angular scattering pattern of electron impact on diatomic molecules was examined by several workers. This resulted in some debate over the anisotropy of the scattering pattern, the effect of Rydberg atoms and the electronic states that participated in the reactions. As lasers began to find wide-spread use,

the study of photo-dissociation reactions became more wide spread and the electron impact ionization of molecules for dissociative ionization studies lost popularity. New technological advances, such as ion imaging using charge-coupled device video cameras, coupled with particle beam techniques will provide a lot of information about both the electronic states participating in the ionization/dissociation event as well as information on the angular scattering patterns and insight into the validity of Dunn's selection rules.

A paper was published by Dunn[160] on the ionization of H_2 in order to investigate the validity of the selection rules. The target gas was admitted into a vacuum chamber and ionized with an electron beam from a rotatable electron gun. The products were detected using a magnetic sector mass spectrometer with a small angle of acceptance. The predicted distribution of product ions was given by

$$\cos^2\theta + \frac{\eta_r}{\eta_s} sin^2\theta \tag{6.20}$$

Where η_r and η_s relate to the energy of rotation of the target before dissociation and the energy of the particles at infinite separation of the dissociating particles respectively. For the case of H_2 the ratio of η_r/η_s is expected to be small and hence a $\cos^2\theta$ distribution of H^+ should be observed. The observed results were in good agreement with the predicted distribution at low energy but the scattering became more isotropic as the ionizing energy increased.

Subsequently Zare[161] published a theoretical paper that used Kerners analysis of the Born approximation in an attempt to predict the scattering pattern more rigorously. The outcome was that the distributions should be peaked around the direction of the electron beam regardless of the initial rotational state of the molecule. The analysis showed that the distribution of product ions should follow a $\cos^2\psi\cos^2\theta_A + \frac{1}{2}\sin^2\psi\sin^2\theta_A$ dependence, where ψ is the angle between $\mathbf{K}$ and $\mathbf{k}$ and θ is the angle between the scattered product and the electron beam. At low electron energies the anisotropy was found to be the greatest and followed a $\cos^2\theta_A$ dependence, but as the electron energy increased the scattering became more isotropic. At very high electron

energies it was predicted that the scattering pattern actually reverses and scattering perpendicular to the electron beam becomes favoured.

A crossed molecular beam machine was built by Stockdale and Delenau[162] to measure both the kinetic energy of the O^+ and N^+ fragment ions, and their angular scattering pattern for the electron impact ionization of oxygen and nitrogen. The apparatus used a continuous effusive molecular beam source with a pulsed electron beam source that could be rotated from 30° to 110°. No mass spectrometer was used to separate the ions on the basis of their m/z ratio, but background subtraction was performed with the molecular beam turned off. The channeltron detector was mounted in a cylinder that also contained several collimators attached to the front of the channeltron which defined the angular resolution of the instrument. The collimator closest to the crossing region had a retarding potential applied to it, the magnitude of which was used to determine the kinetic energy of the fragment ions. The N^+/N_2 fragment ion showed a broad peak at 2.5 eV with a FWHM of 3 eV at 80 eV electron energy, broadening to 4 eV at 150 eV electron energy. This was the only distinguishing feature observed in the N^+/N_2 energy spectrum. The angular distribution was quite different to that of Keiffer and Dunn[163] with a slight peak at about 90° and a trough at about 45°. No significance was assigned to the observed anisotropic scattering. The O^+/O_2 energy spectrum showed four peaks at approximately 1 eV, 2 eV, 3 eV and 5 eV for an electron energy of 50 eV. Previous measurements by Keiffer[163] using electron impact, Doolitle using photoionization[164] and Freund using photoionization and production of Rydberg atoms,[165] had shown similar kinetic energy distributions. The observed angular scattering pattern for O^+ was essentially isotropic independent of excess energy. The explanation for the observed anisotropy in terms of Dunn's selection rules were given by one of the three following possibilities:[162]

1. involvement of both perpendicular and parallel transitions that contribute such that the observed scattering pattern is isotropic;

2. predissociation involving long cross-over times to the repulsive states;

3. the inclusion of non-dipolar terms in the selection rules.

By making measurements closer to the dissociation threshold, it was proposed that it should be possible to test each of these possibilities more thoroughly.

Schopman and Locht[166,167] measured the kinetic energy distribution of O^+/O_2 by electron impact. Ions were formed in a Neir ion source, passed through a retarding potential lens system and detected using a quadrupole mass spectrometer. The oxygen was admitted into the vacuum chamber at low pressure in order to prevent the filament burning out, but this resulted in a low signal level. The O^+ ion was detected with thermal kinetic energy, as well as distinct kinetic energies of 0.79 eV, 2.20 eV, 2.85 eV, 4.32 eV and 5.5 eV. The energy of the ionizing electron had an affect on the shape of the recorded energy distribution and it was is suggested that this must be due to the formation of Rydberg states. The peaks were assigned to possible transitions but no conclusive assignments were made.

More recently Matsuo *et al.*[168] used a crossed supersonic molecular beam experiment to measure kinetic energy distributions from O_2 and identified a band at about 0.2 eV which had not been previously observed. The initial velocity of the supersonic expansion was used to carry the particles produced without excess kinetic energy away from the detector. The kinetic energy distribution measured up to 4 eV was similar to that obtained by Stockdale and Delenau[162] and van Brunt *et al.*[169] using electron impact ionization and Doolittle *et al.*[164] and Ukai *et al.* using photoionization. A rotatable detector was used to measure the angular scattering distribution. The peak at 0.8 eV was used to normalize the results for each of the angles examined. The 0.2 eV peak was found to be weakest at 90° and was assigned to the following transition.

$$O_2 + e \longrightarrow O_2^{**}(2\pi_u - \text{Rydberg series}) + e_s \tag{6.21}$$

$$\longrightarrow O^* + O(^3P) \longrightarrow O^+(^4S) + O(^3P) + e_j \tag{6.22}$$

Using the apparatus to be described in Chapter 7, Aitken, Blunt and Harland[3–5] measured relative ionization cross-sections for the production of CH_3Cl^+ and CH_3^+, CH_3Br^+ and CH_3^+, CF_3^+ and $CHCl_2^+$ from the electron impact ionization of CH_3Cl, CH_3Br, CF_3Br and $CHCl_3$, respectively, using 200 eV electrons. This experiment was unique in that the target molecules were oriented in space before crossing a collimated electron beam.

The cross-section for the formation of CH_3Cl^+ was found to be higher by a factor of 2.1 for electron collisions on the positive (CH_3) end of the molecule, whereas the formation for CH_3^+ was found to be independent of orientation. For the case of CH_3Br the results were inconclusive, a possible reason for this is that the more prolate CH_3Br could orientate to a lesser degree than CH_3Cl, making the CH_3 end of the molecule less accessible to the ionizing electron. Another factor could be the fact that the Br atom is very large, meaning that it will be influenced by the ionizing electron at much greater impact parameters than the Cl atom, thus dominating the ionization cross-section and scattering pattern. CF_3^+ was found to form preferentially from collisions on the Br-end of CF_3Br although no molecular ion is produced in this case. It was proposed that a short-lived excited $(CF_3Br^+)^*$ formed preferentially for electron impact on the positive end of the molecule. In the case of $CHCl_3$ a small preference for the formation of $CHCl_2^+$ was found for electron impact at the positive end of the molecule and a similar explanation to the CF_3Br case was given.

Because of the inconsistencies in the angular dependence measurements and the limited data on orientation effects, further investigations of the processes are required in order to understand electron impact ionization measurements. The molecular beam machine that is to be discussed in the following Chapters has been designed to resolve these problems.

7. THE MOLECULAR BEAM MACHINE

7.1 History

The development of the molecular beam machine has been an on-going project for several years. Initially it consisted of three vacuum chambers, and was used to investigate the flow dynamics of supersonic molecular beams. The parameters that could be measured included time-of-flight and temperature distributions for chopped and unchopped supersonic molecular beams, the effects of velocity slip (the difference in the flow velocity for a supersonic expansion in the $x-$direction where both of the species are in a binary gas mixture) and the temperature slip (the difference in the temperature, or parallel velocity, in the $y-$ and $z-$axis of each component in the expanding gas mixture). The molecular beam machine was then modified for the measurement of appearance potentials by electron impact of van der Waals clusters, generated by expanding seeded mixtures of SO_2, NH_3, N_2O and H_2O, NO and NO_2 in helium. Appearance potentials of pure argon clusters were also measured.[170] Subsequently the machine was modified to include a hexapole filter[4,171] so that relaxation cross-sections for upper stark state molecules could be measured. Orienting field plates were added to enable the measurement of ionization asymmetry of oriented symmetric top molecules. A second hexapole was then added so that orientation lifetimes of symmetric top molecules could be determined and individual stark states could be selected and examined.[88,172] The ion imaging assembly was added in 1999.

7.2 Components of the molecular beam machine.

A detailed description of the molecular beam machine and pumping systems is given in Appendix **F** for completeness. In this Section schematic overviews of the molecular beam machine components are given in Figures 7.1 to 7.5. Con-Flat flanges are used throughout except for the lid of the scattering chamber and radio frequency spectrometer chamber (C-Cell) which are sealed with a Viton 'O'-ring. Each pump is separated from the main chamber by a gate valve and liquid nitrogen trap. Standard rated high vacuum fittings and techniques apply throughout and each chamber is separated from its neighboring chambers with 0.5 mm stainless steel shims. The diffusion pumps are valved off at night but the turbo-molecular pumps run 24 hours per day to maintain a high quality vacuum. The pressures are typically 10^{-6} Torr for the nozzle chamber (the C-cell for the present experiments), 10^{-7} Torr for the remaining vacuum chambers that are pumped by diffusion pumps and 10^{-7} to 10^{-8} Torr for the scattering and quadrupole mass spectrometer chambers, depending on the experimental condition and neutral beam gases used.

The electron beam stop is removed when the ion gun is installed so that the ion beam can be detected by the quadrupole mass-spectrometer. Details of the electron and ion guns are given in Chapter 9.

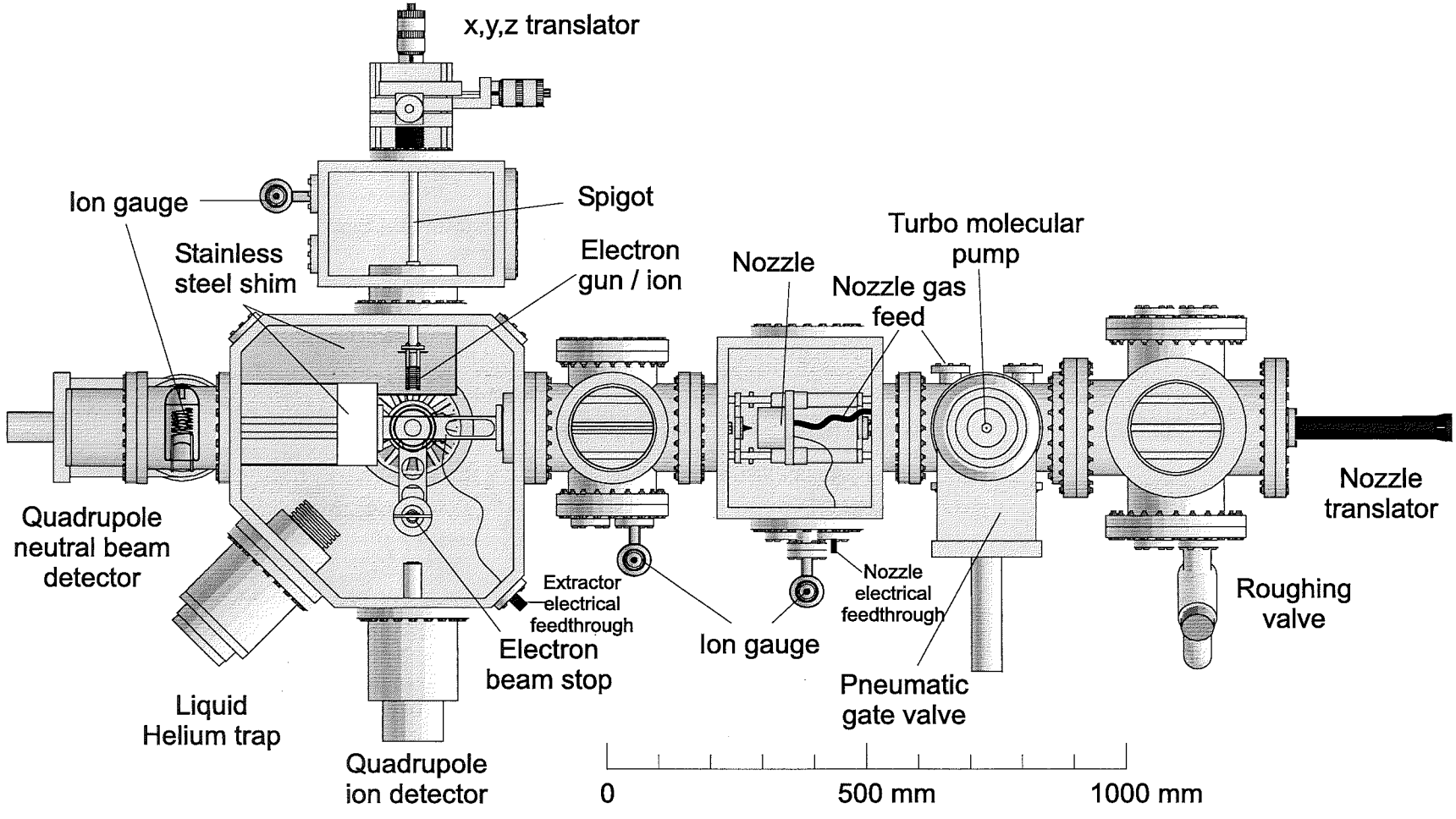

Figure 7.1: Plan view of molecular beam machine.

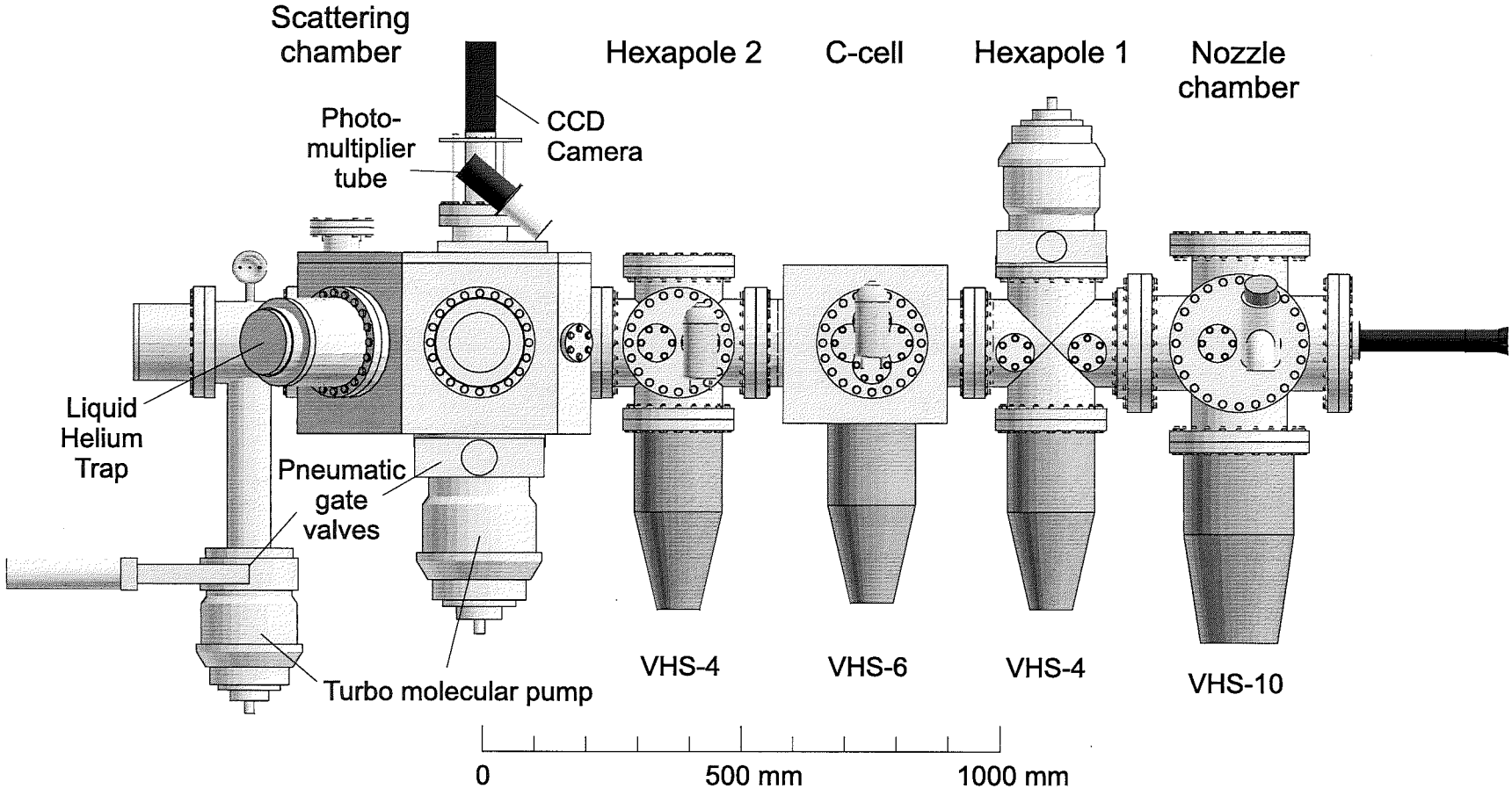

Figure 7.2: Elevation of molecular beam machine - western side.

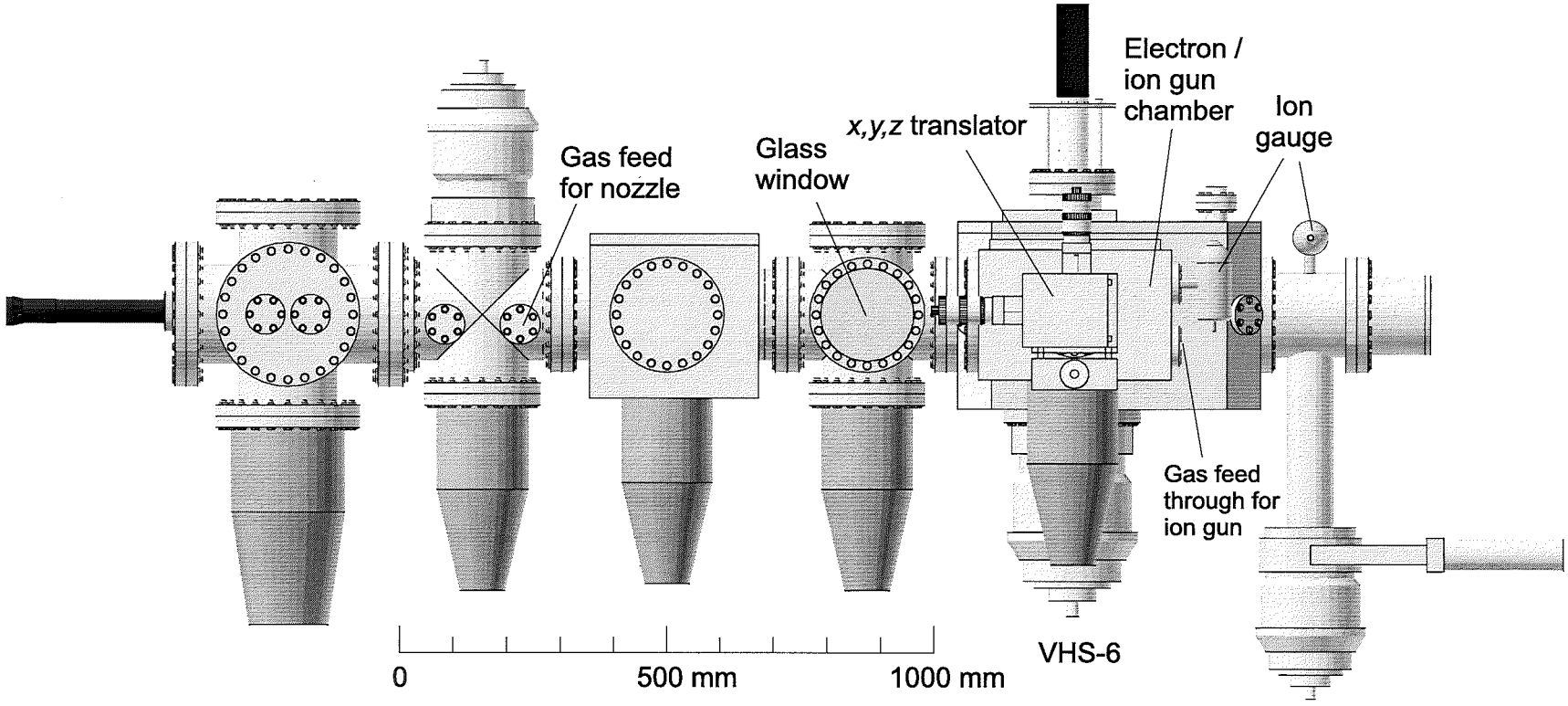

Figure 7.3: Elevation of molecular beam machine - eastern side.

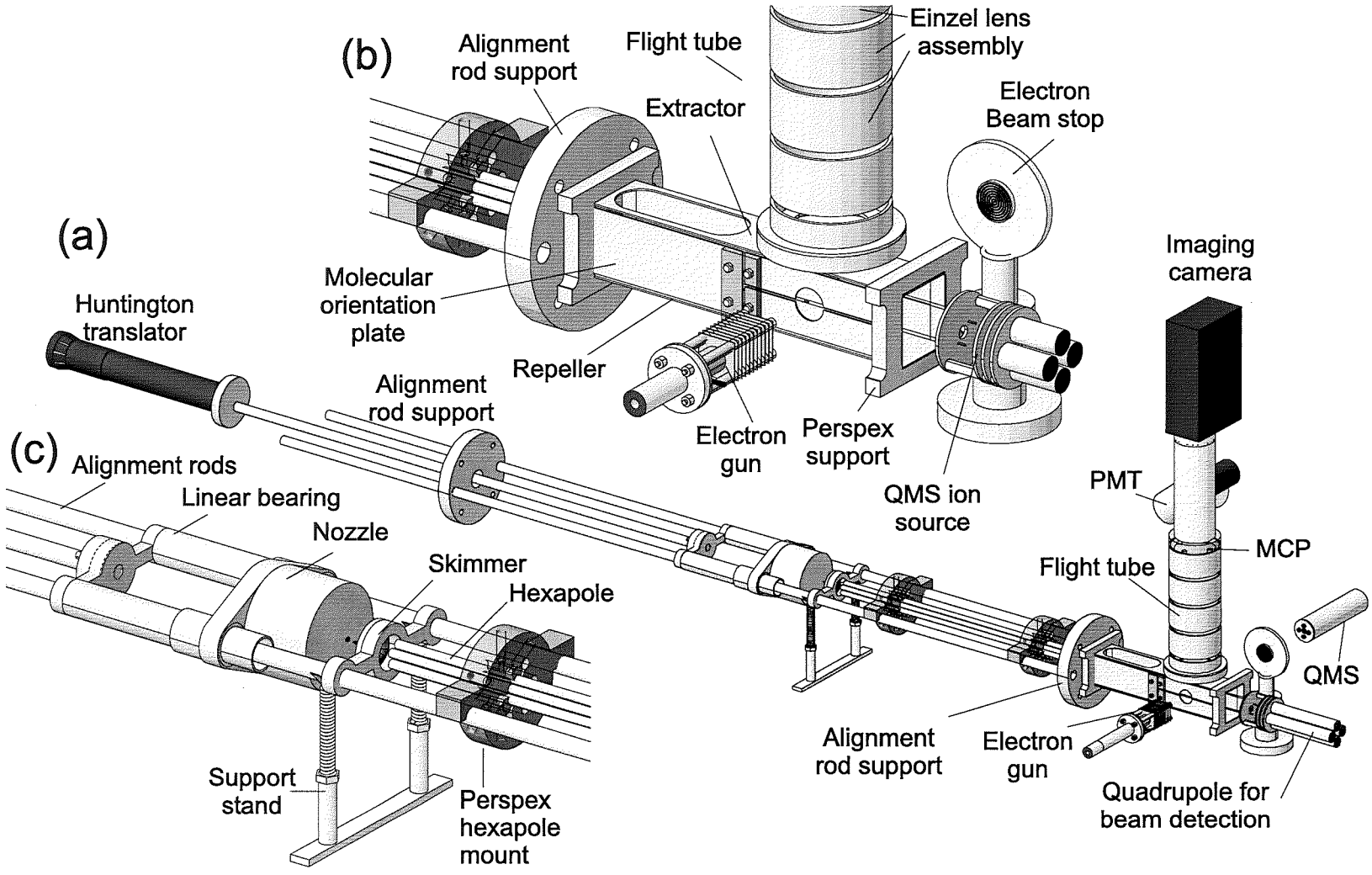

Figure 7.4: Internal components of molecular beam machine.

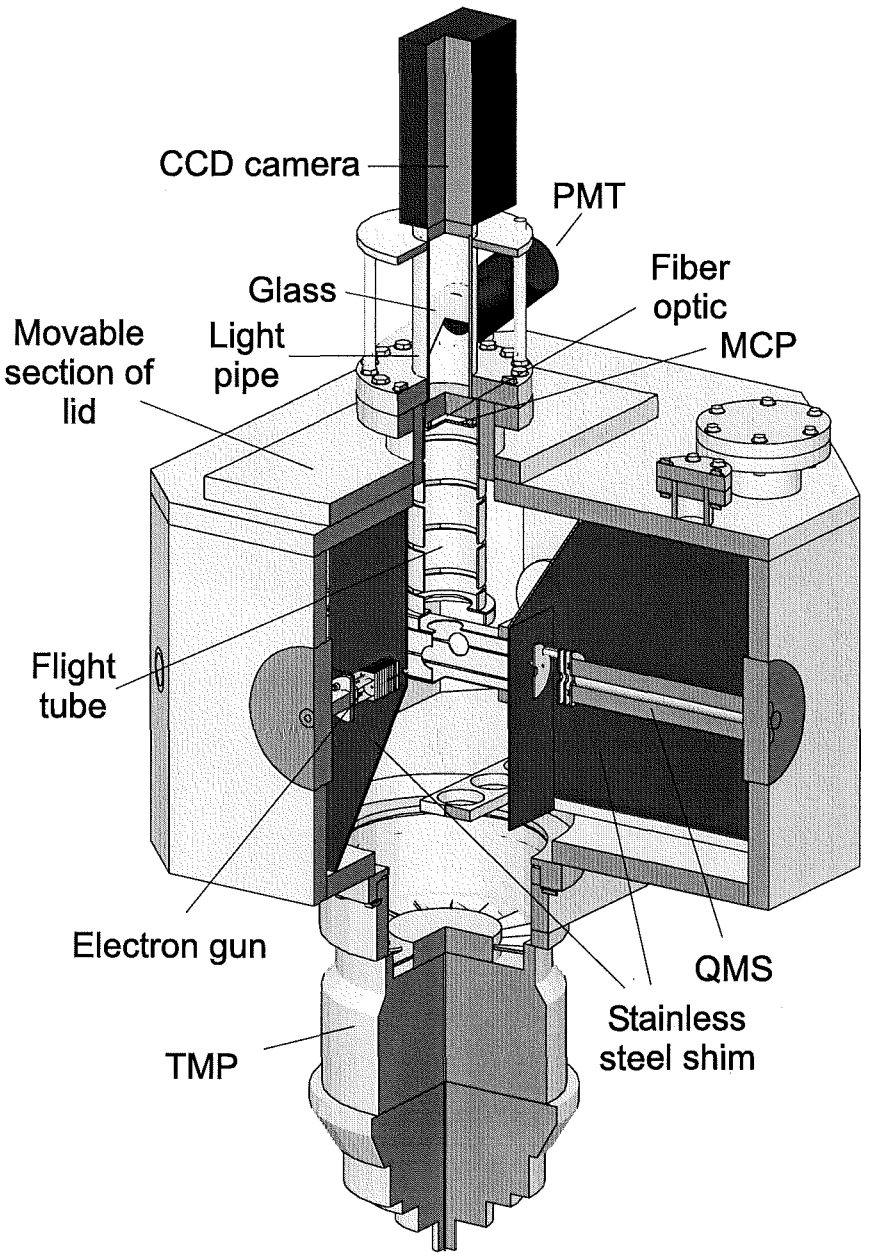

Figure 7.5: Cutaway view of scattering chamber.

7.3 Electronics

There are several important electronic systems that form part of the molecular beam machine. The electronics can be broadly divided into three categories: pulsing electron-

ics that control experimental parameters, static electronics that control experimental parameters, and the auxiliary passive electronics such as the ion gauge controllers, capacitance manometers, diffusion pump controllers and thermocouple gauges. The pulsing electronics will be discussed below. A description of the static control electronics will be discussed in the sections pertinent to the individual components that are controlled by those electronics.

7.3.1 The molecular beam machine pulsing sequences and control electronics

There is a very important predefined order of events for the molecular beam ion/electron beam crossing reactions in the beam machine, as listed below.

1. The molecular beam nozzle opens for a short time, typically 0.1 ms allowing a burst of gas to traverse the length of the machine in the form of a supersonic molecular beam.

2. If the molecules in the molecular beam are to be oriented the orienting field plates need to be switched to ground immediately before the electron/ion beam fires.

3. The electron/ion beam fires for approximately 1 μs such that the beam of electrons/ion collides with the molecular beam at the center of the crossing region.

4. The ion product sphere expands in field free space for a period of nanoseconds to microseconds.

5. The extractor/repeller plates are then rapidly switched to extract the ions into the flight tube assembly.

6. The charge couple device (CCD) camera is synchronized with the nozzle. Images of individual product ions may be resolved using CCD delay and gate functions.

7.3.2 The multichannel pulse controller

All of the events in the above list are controlled by a custom-built keypad or computer programmable multichannel pulse generator (MCPG) which was designed for the machine because of the high cost of purchasing commercial high speed pulse generators. The electron impact experiment requires a minimum of five trigger pulses: nozzle, electron beam, repeller, extractor, and camera gate. The camera gate is also used to trigger the frame grabber card. Pulses delivered to fast transistor switches need to be programmed with the appropriate delays and widths, with the pulse widths defining the on-time for the high-voltage pulses applied to the system control elements. For ion–molecule studies, three additional triggers are required for switching positive and negative homogeneous field plates and a second pulse to the ion gun for time-of-flight ion filtering. The multichannel pulse generator operating at 32 Hz triggers the field plates and all other downstream pulsed elements with appropriate delays and widths. The delay is set to be greater than the maximum flight time for the heaviest sample gas to be used. The nozzle is separately triggered by the system clock through a variable delay so that the nozzle firing can be triggered to match the arrival of the gas pulse with the electron/ion pulse at the crossing center. The nozzle delay is adjusted until the electron/ion gating pulse sits over the maximum in the gas pulse arrival time distribution after making allowances for the flight-time correction from the crossing center to the mass filter detector.

The unit currently in use has six output channels, expandable with hardware modifications to 12 or more channels. A clock speed of 50 MHz fulfilled the requirements for these experiments, although the unit will run without modification for clock frequencies up to 100 MHz and with hardware modifications to higher clock speeds. The start pulse repetition frequency is programmable. Channels have individually programmable start time and pulse length input through a front panel keypad with a 20 character two row LCD display or through computer control operated *via* a custom software interface. Output pulses are carried by fiber optics to facilitate interference-free operation and electrical isolation.

The 50 MHz clock drives a 24-bit binary counter. The binary value of the counter is compared with a binary value stored in a 24-bit latch. If the counter and stored binary values are the same then the output from the comparator is set. For each channel there are two 24-bit comparators and two 24-bit latches. One of the comparators is the turn-on value and the other is the turn-off value. When the turn-on comparator is set the optical output logic turns the optical output device on. When the turn-off comparator is set the optical output logic turns the optical output device off. The controller board allows the on and off values for each output card to be read and programmed. The controller uses a PIC16C64/74 microcontroller to interface with a LCD and a keypad to set the timing values. The microcontroller displays the digital data in readable form and translates the input to binary form for uploading to each output channels electronically erasable programmable read-only memory (E2PROM) and latches. The controller reads and stores the output channel values using the I2C bus and I2C based E2PROMS. The values are also sent to the 24-bit latches by addressing each of the individual 8-bit latches that make up the 24-bit latch and writing the data 8 bits at a time; this is done for each of the output channels. The back plane used in the unit is 32-bit allowing for future expansion.

The six channel 50 MHz MCPG currently in use has a set timing resolution of 20 ns and a timing range from 40 ns to 335,544,320 ns. The minimum programmable pulse width is 20 ns and the maximum is 335,544,300 ns. The optic output transducers use standard ST connectors into 62.5/125 mm fiber transmitting pulses at 820 nm wavelength. 10 m cables were used in these experiments, although cable lengths can readily exceed 100 m. Standardizing on cable length precludes timing differences between cables. The cables terminate into fiber-optic receivers with Schmitt trigger buffers with typical rise times of 3 ns. The receivers are powered by isolated 5 V power supplies. Trigger pulses are directed into standalone optically isolated high voltage pulse generator units using standard BUZ92 1000 V transistors biased for either positive or negative pulse output (ground or HV referenced) as shown by the circuits in Figure 7.6, or by commercial high voltage supplies. Transistors can be cascaded for higher voltages or a higher voltage transistor substituted.

The nozzle driver The important feature of the nozzle, (Physik Instrumente P-286.20) is that it contains a piezoelectric crystal that distorts when a voltage is applied to it. As it distorts it pulls back a plunger, breaking the seal between front face of the gas reservoir and the vacuum, allowing molecules to stream through a 70 μm orifice into the vacuum chamber, thus forming the supersonic molecular beam. (Chapter 8) The nozzle driver can be internally or externally triggered. The delay from the start trigger can be set from 0 to 1 ms, and the pulse width can be set anywhere between 0.1 and 3 ms. Both the delay and width are set with ten turn potentiometer. The voltage level on the piezoelectric crystal is also manually set controlled with a ten turn potentiometer.

The high speed switches Up to five high speed high voltage switches are required for the experiment. These are the electron or ion beam pulse, the extractor pulse, the repeller pulse, and the positive and negative field plates for molecular orientation

The the electron beam is prevented from passing into the scattering chamber by a retarding potential on one of the lens elements in the electron gun. The electron beam passes into the scattering chamber when the field on the retarding plate collapses to ground. In this case the required configuration of the high-speed switch is normally negative pulsing to ground.

The extractor and repeller plates must be at ground as the electron beam passes through the interaction region, then after a short delay they need to switch positive for a short time. In this case the required configuration of the high speed switch is normally ground pulsing to positive.

One of the orienting field plates is normally negative, switching to ground immediately before the electron gun fires. The other orienting field plate is normally positive, switching to ground immediately before the electron gun fires.

The high voltage switches that control these pulsing requirements were built in the departmental electronics workshop. The circuit diagram for the high voltage switch

and the four modes of operation are given in Figure 7.6.

The high voltage switch is composed of a 470 μF capacitor, a 47 Ω resistor, an optically isolated field effect transistor (FET) and an LM311 high speed voltage comparator. When the transistor switch closes there is either a direct short to ground, causing the retarding field to collapse, or a direct short to the high voltage power supply causing the voltage to rise rapidly. The capacitor/resistor combination forms an RC circuit. This regulates the current being drawn from the voltage supply for the duration of the pulse, provided it is transient.

Two commercial HTS 81-09 0-8000 V transistor switches have also been used when pulsing requirements exceeded 1 kV. These were typically used for the extractor/repeller assembly. These can be configured in exactly the same configurations as the in-house high voltage switches. The main switching circuit is replaced by the HTS unit, but the four configurations shown in the lower part of Figure 7.6 are retained.

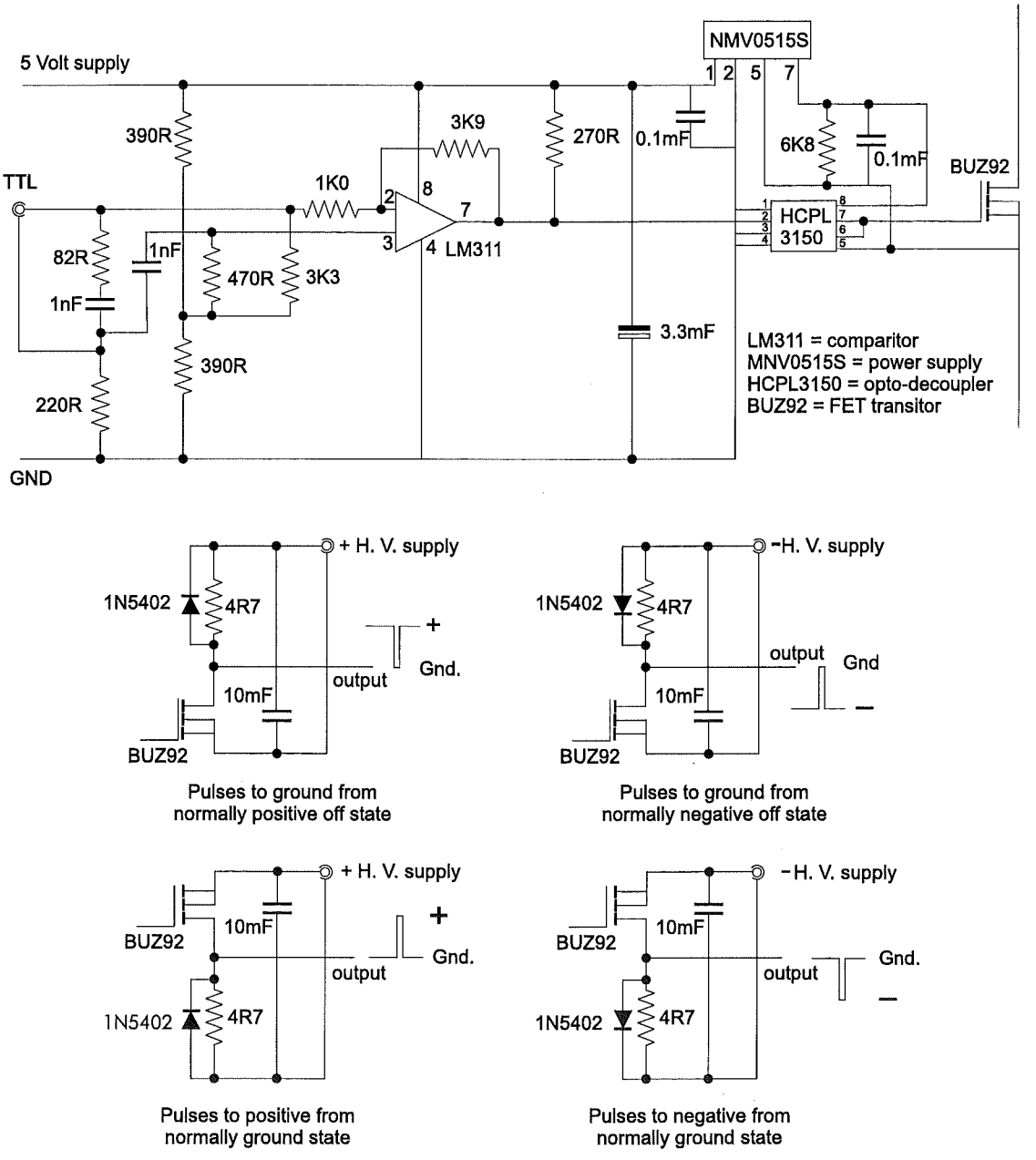

Figure 7.6: Circuit diagram of the high voltage pulsing switch with the four different configurations.

8. MOLECULAR BEAM PRODUCTION AND CHARACTERIZATION

8.1 Beam sources

A molecular beam is formed when a gas flows through a small orifice from a high pressure reservoir into a vacuum. Because the gas will spread out in all directions a collimator is required to select only the molecules that are traveling in the direction of beam propagation. As the distance from the beam source increases the intensity of the beam diminishes, but the opportunity for a lower background gas pressure becomes possible through the introduction of additional vacuum chambers between the nozzle and crossing region, providing a means for differential pumping.

There are two types of neutral molecular beam source, effusive and supersonic (also called hydrodynamic). Whether a beam is effusive or supersonic depends on the ratio of the mean free path of the molecules inside the source λ to the diameter of the orifice d. This ratio is called the Knudsen number K and is defined as follows.

$$K = \frac{\lambda}{d} \tag{8.1}$$

8.1.1 Effusive sources

An effusive molecular beam source is one where there are no collisions as the atoms or molecules pass through the throat of the nozzle source. This means that the mean free path must be greater than the diameter of the nozzle, hence the Knudsen number $K > 1$. While effusive sources have some advantages over supersonic sources, they

have a serious disadvantage in that they have very low beam fluxes.

Because collisions do not occur as the molecules leave the nozzle, the velocity profile of the molecules in the beam is not disturbed. The speed distribution inside the gas reservoir can be described by the Maxwell-Boltzmann relation:

$$N_s(v)\mathrm{d}v = \frac{4n_0}{\sqrt{\pi}}\frac{v^2}{v_{\mathrm{mp}}^3}e^{-v^2/v_{\mathrm{mp}}^2}\mathrm{d}v \tag{8.2}$$

where v_{mp} is the most probable speed. A correction based on statistics must be applied however because the fast moving molecules have a greater probability of flowing through the orifice than the slow moving molecules, because they encounter the orifice more often. The speed distribution in the beam is therefore skewed toward a distribution favoring higher speeds than in the reservoir.

$$N_b(v)\mathrm{d}v = \frac{v}{v_{\mathrm{mp}}}N_s(v)\mathrm{d}v = \frac{n_0}{\sqrt{\pi}}\left(\frac{v}{v_{\mathrm{mp}}}\right)^3 e^{-v^2/v_{\mathrm{mp}}^2}\frac{\mathrm{d}v}{v_{\mathrm{mp}}} \tag{8.3}$$

Molecules can leave the source at any angle, which is maintained until the molecule undergoes a collision, usually with the wall of the vacuum chamber. The angular distribution of the intensity of the molecules is given by a $\cos\theta$ dependence in the y plane and a $\cos\phi$ dependence in the z plane with respect to the molecular beam axis.

This gives a beam flux of

$$I(\omega)\mathrm{d}\omega = \frac{1}{4\pi}n_0\bar{v}A\cos\theta\mathrm{d}\omega \tag{8.4}$$

per steradian. A is the area of the orifice and $\bar{v}$ is the average velocity in the source given the expression

$$\bar{v} = \left(\frac{8k_bT}{\pi m}\right)^{1/2} \tag{8.5}$$

The total beam flux, I, is then the beam flux integrated over all angles θ and ϕ:

$$I = \frac{1}{4}n_o\bar{v}A \tag{8.6}$$

The major advantage of an effusive source over a supersonic source (see following Section) is that the molecular beam can be described by the kinetic theory of gases. Because the gas retains its initial thermal equilibrium in the beam, the distribution of vibrational and rotational states in the source are retained. This provides a mechanism to control the vibrational and rotational states by heating or cooling the source. Because of the angular distribution of the molecules leaving the source, collimation is required in order to form a well defined molecular beam. This has the side-effect of reducing the flux considerably compared to equation (8.4). The beam flux from an effusive source is very low compared to supersonic beams, although this has been ameliorated somewhat through the use of multichannel capillary array nozzles. The properties of the effusive beam are retained by using the multichannel arrays but the beam flux is greatly enhanced because each channel in the array behaves as an individual nozzle source. The beam energy may be controlled by heating the source but only to a maximum beam temperature of about 0.1 eV. Since most cross beam experiments require a fairly narrow distribution of velocities, a rotating velocity selector is normally used to obtain a beam with the required energy. Effusive sources have been relegated to the preparation of metal atom beams (in particular alkali beams) and other species where the reservoir pressure cannot be increased to a sufficient level to produce supersonic beams. They have also been used in experiments where beam intensity must be accurately known to measure an absolute cross-section.

8.1.2 Supersonic sources

Supersonic beam sources have the advantage of having beam fluxes two to three orders of magnitude higher than effusive sources. Supersonic beams are highly directional and the beams have a very narrow velocity distribution. As the molecules accelerate out of the source, multiple collisions occur causing a transfer of random momentum into motion in the direction of beam propagation. This results in a large translational velocity of the beam along the direction of propagation but a very small random speed distribution about the three Cartesian coordinates. The magnitude of the random

speed component defines the beam temperature, T. The distance between the nozzle source and the detector divided by the flight time to the detector is known as the flow velocity, u, of the beam.

There are several characteristic features of the supersonic expansion. Experimentally these features may be observed in terms of beam flow velocity u, source pressure P_s, background pressure P_b, nozzle-skimmer distance X_s and gas characteristics such as molar mass m, heat capacity at constant volume C_v, heat capacity at constant pressure C_p, and rotational and vibrational energy level spacings as as well as system specific functions such as the design of the molecular beam source, skimmer and pumping system.

The supersonic expansion has been extensively used and studied since its development in the 1950s. The region immediately downstream from the nozzle between the nozzle and skimmer is of greatest interest, as this region defines the beam characteristics. The term supersonic refers to a unique characteristic of the expansion. Since the gas is expanding at a rate greater than the local speed of sound, information about the structure of the boundary conditions downstream is not transfered back to the expanding gas. This causes the escaping gas to over-expand. As a result, non-isentropic regions characterized by large density, pressure, velocity and temperature gradients are formed. The structure of the shock-waves is illustrated in Figure 8.1.

Shock wave formation depends on the critical ratio of the pressure inside the supersonic source to the background pressure in the expansion chamber; for G_c greater than unity a supersonic expansion will form:

$$\frac{P_s}{P_b} = G_c = \left(\frac{\gamma+1}{2}\right)^{\frac{\gamma}{\gamma-1}} \tag{8.7}$$

where γ is the ratio of the heat capacities C_p/C_v. The Mach number M, is the ratio of u to the local speed of sound u_s, which is greater than unity.

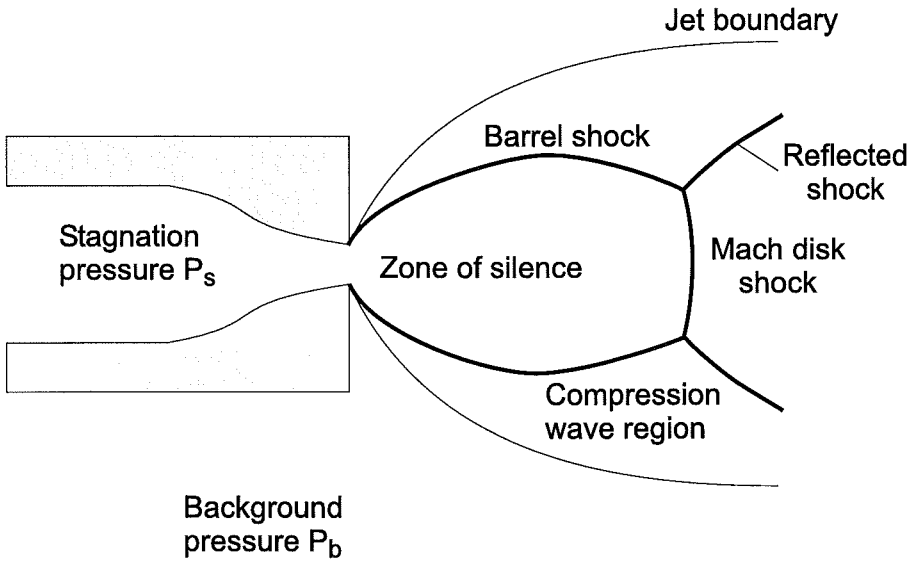

Figure 8.1: Structure of supersonic expansion.

$$M = \frac{u}{u_s} \tag{8.8}$$

where

$$u_s = \left(\frac{\gamma k_b T_0}{m}\right)^{1/2} \tag{8.9}$$

As it stands the barrel shock will combine with the Mach disk resulting in turbulence that will destroy the structure of the supersonic beam. In order to extract a useful molecular beam from the expanding gas a skimmer is required such that the tip of the skimmer samples the zone of silence. Both the design geometry of the skimmer and the nozzle-skimmer distance are very important.

Empirically, the optimum nozzle skimmer distance has been found to fit the following relationship[173]

$$\left(\frac{X_s}{d}\right)_{\text{optimum}} = 0.124 \left(\frac{1}{K}\frac{P_s}{P_b}\right)^{1/3} \tag{8.10}$$

In the present experiments, however, the nozzle skimmer distance was simply adjusted while the signal from the quadrupole mass spectrometer molecular beam detector was monitored for maximum signal.

To ensure maximum cooling of the supersonic expansion, collisions between the expanding particles in the zone of silence should be allowed to continue unperturbed for the maximum length of time. This means that the nozzle-skimmer distance should be maximized in order to minimize the random velocity distribution in the beam. If the pumping requirements cannot be met to maintain a good vacuum in the nozzle chamber or the nozzle skimmer distance is too small, the skimmer may act as a virtual source, producing an effusive molecular beam.

There are several requirements for a skimmer to produce a satisfactory molecular beam:[174]

1. the orifice should have edges that are as sharp as possible;
2. the exterior angle should be small to ensure that the Mach disk is attached to the skimmer;
3. the interior angle of the skimmer should be as large as possible to ensure that the scattering of gas molecules from the skimmer surface is kept to a minimum;
4. the orifice that the molecular beam passes through must be symmetric and perfectly perpendicular to the direction of propagation of the molecular beam.

Although the flow characteristics of the beam cannot be calculated directly, because of the complex structure of the supersonic expansion, a few of the properties can be described by thermodynamic theory. The properties of the molecular beam may be described by v_{mp}, the most probable random speed of the molecules in the beam, S the speed ratio of the molecules in the beam, which is a measure of the width of the distribution of the random component of beam speed, and M the Mach number.

$$v_{mp} = \left(\frac{2k_BT}{m}\right)^{1/2} \tag{8.11}$$

$$S = \frac{u}{v_{mp}} > 1 \tag{8.12}$$

$$M = \frac{u}{(\gamma k_BT/m)^{1/2}} = \left(\frac{2}{\gamma}\right)^{1/2} S \tag{8.13}$$

Using the Mach number several important quantities may now be calculated, including the ratio of the beam temperature to the source temperature, the beam velocity, and the ratio of beam pressure to source pressure.

$$\frac{T}{T_0} = \left(1+\frac{\gamma-1}{2}M^2\right)^{-1} \tag{8.14}$$

$$v = M\left(\frac{\gamma k_B T_0}{m}\right)^{1/2}\left(1+\frac{\gamma-1}{2}M^2\right)^{-1/2} \tag{8.15}$$

$$\frac{P}{P_0} = \left(\frac{T}{T_0}\right)^{\gamma/(\gamma-1)} = \left(1+\frac{\gamma-1}{2}M^2\right)^{-\gamma/(\gamma-1)} \tag{8.16}$$

An expression for the maximum flow velocity may be derived by considering the transfer of energy from the enthalpy of the gas inside the source, H_0, to the translational energy of the beam. The maximum translational energy is then given by:

$$\frac{1}{2}mv_{\max}^2 = H_0 = \int_{T_f}^{T_0} C_p \mathrm{d}T \tag{8.17}$$

where T_0 and T_f are the temperature of the source and the final beam temperature, respectively. If it is assumed that C_p is constant during the expansion process and the final beam temperature is much less than the initial beam temperature then the maximum flow velocity $u_{\max}$ is given by:

$$u_{\max} = \left(\frac{k_b T_0}{m}\frac{\gamma}{\gamma-1}\right)^{1/2} \tag{8.18}$$

This expression agrees with the experimental flow velocity in cases where C_p is constant over the temperature range T_0– T_f. In the case of polyatomic beam species C_p over the temperature range T_0 to T_f is not constant and full integration of equation (8.17) will need to be carried out.

8.1.3 Arrival time distributions

The velocity of a particle in the beam, v, is simply given by

$$v = \frac{X_d}{t} \tag{8.19}$$

The detector is fixed at some distance, X_d, from the nozzle. The time, t, it takes from beam formation[a] to beam detection is recorded, and the beam velocity determined. The speed distribution $f(v)$ of the molecules in the beam has been found empirically to be given by a Maxwell-Boltzmann type distribution given by equation (8.20):

$$f(v)\mathrm{d}v = Av^2 e^{-m(v-u)^2/2k_\mathrm{B}T_\parallel}\mathrm{d}v \tag{8.20}$$

where A is a normalization coefficient. $T_\parallel$ is the parallel beam temperature, v is the instantaneous speed and u is the flow velocity of the beam. k_B is the Boltzmann constant and m of the species of interest. In the case of a seeded beam m is the weighted average mass of the carrier gas and the seed gas.

It is important to note that measured distribution does not accurately represent the molecular speed distribution. This is primarily because the nozzle is not open for an infinitely short period of time. The faster molecules leaving the beam source as it closes catch up with the slower molecules that left the source as the nozzle opened. This skews the molecular beam arrival time distribution. Another factor to consider is the actual shape of the nozzle gate function. The opening of the nozzle is not an exact square wave function. In the case of the present experiments the piezoelectric crystal opens against the high stagnation pressure, P_s, of the molecules, and closes toward the high vacuum. The electronic response of the detection equipment is another important consideration. The amplifier and associated electronics are not infinitely fast, this is also convoluted into the measured arrival time distribution of the molecules.

[a] In the case of a pulsed nozzle source the start time is the point at which the nozzle opens. In the case of a chopper the start time is the point at which the beam passes through the chopper window

The characteristic shape of the arrival time distribution is a steep rise time with a steep initial fall-off in signal. After the beam intensity has decreased to about 2/3 of its peak value, the attenuation rate decreases, producing a relatively long tail. This characteristic of the arrival time distribution is due to a 'machine function' and is a convolution of detector response, nozzle gate function and pumping characteristics. The 'machine function' is loosely defined as the function that includes all of the factors that contribute to the broadening of the measured arrival time distribution. Although this function would be impossible to calculate exactly, there have been several different approaches to the determination of actual beam temperatures from arrival time distributions, including Fourier transform deconvolution methods, moment analysis, Monte Carlo simulation methods and the method of fitting a parameterized function to the experimental data in order to establish the machine function.

Fitting a parameterized function is not the recommended approach[170] because it is impossible to derive a perfect function that includes all of the parameters in the 'machine function', and - equally importantly - it is impossible to guarantee a unique solution. This method can also be very computationally intensive. The fitting method of Vallance[88] involves using a set of Monte Carlo trajectories to fit a series of trial solutions to the trailing edge of a measured arrival time distribution. The basic method is as follows:

1. a molecular trajectory with velocity v is selected using a random number generator. This trajectory is then given a weighting according to equation (8.20), and converted into a flight time;

2. a time t_i is then randomly selected over the time interval of interest. A contribution from the molecule to the signal is then determined;

3. the data are binned and summed to give the final time-of-flight distribution, which is subsequently normalized to the experimental data;

4. the parameters u and $T_{\|}$ are then optimized such that simulated data matches the experimental data;

Like the parameterized method, this method is computationally very intensive and does not guarantee a unique solution.

The method adopted in the present work uses a Fourier transform deconvolution method similar to the approach used by Cameron.[170,175] If the beam temperature of one species is known, either from a previously determined experimental technique such as using a chopper for velocity selection, or from a fitting technique using Monte Carlo methods, it is possible to determine the beam temperature for another species by establishing the machine function, and deconvolving it from the measured velocity distribution. An arrival time distribution is measured in the time domain, but equation (8.20) describes the speed distribution in the velocity domain. A Jacobian transformation from the time domain is applied.

$$\mathrm{d}v = -\frac{X_d}{t^2}\mathrm{d}t \tag{8.21}$$

In the time domain equation (8.20) is then given by:

$$g(t)\mathrm{d}t = -\frac{X_d}{t^2}Av^2 e^{-m(X_d/t-u)^2/2k_bT_\parallel}\mathrm{d}t \tag{8.22}$$

After $T_\parallel$ and u have been determined, the distribution of beam speeds has been established. The procedure for calculating the machine function is as follows An arrival time distribution is calculated for a monatomic species such as argon. The argon arrival time distribution is then measured and the machine function is deconvolved using a fast Fourier transform and equation (8.23):

$$G(\omega) = F(\omega)H(\omega) \tag{8.23}$$

where $G(\omega)$ is the Fourier transform of the measured arrival time distribution; $F(\omega)$ is the Fourier transform of the calculated arrival time distribution; $H(\omega)$ is the Fourier transform of the machine function. This allows multiplication or division of the Fourier transforms to establish the machine function directly. Problems with this approach

include the observation that Fourier transforms are very sensitive to noise, and division of the two Fourier transforms increases noise further. Another potential problem is the singularity caused by division by zero at $H(\omega) = 0$, this may be treated by adding a small offset to all of the data.

The best method for taking care of the significant noise contribution is to ensure that the experimental input data is of very good quality. Averaging the arrival time distribution over 2048 samples is usually sufficient to improve the signal-to-noise ratio level. Filtering and smoothing may also be carried out in order to improve the signal-to-noise ratio. The level of smoothing and the width of the filtering window must be assessed on a case-by-case basis. Filtering usually involves applying a rectangular window as a simple low pass filter that cuts out high frequency noise, although more complicated cutoff filters may also be applied, such as a cosine function between 0 and $\pi/2$, or Gaussian attenuation. A more complete discussion of the filtering of the Fourier transforms may be found in Cameron,[170] and Cameron and Harland.[175]

The software used to deconvolve the arrival time distributions was implemented in Visual Basic for Applications in Microsoft Excel. The major advantage of this method is the speed of implementation by exploiting Excel's inbuilt mathematical functionality. The basic structure and functionality of the program was developed in a matter of hours. A further advantage is the straight forward display of data using Excel's inbuilt graphing functionality. One disadvantage is the actual speed of data processing, about 2 minutes to process one data set on a 350 MHz personal computer.

The following steps are used to calculate the arrival time distribution:

1. the arrival time distribution (ATD) is measured for argon - the most well characterized beam gas;

2. the expected arrival time distribution is calculated for argon, using $u = 555\ m/s$, $T_{\|} = 1.3\ K$, the values determined by Cameron using a chopper;[170]

3. the measured and expected arrival times are normalized so that the peak signal

is equal to unity in both cases;

4. the fast Fourier transform of the measured and calculated arrival time distribution is calculated;

5. a smoothing window may be applied to the measured distribution;

6. the machine function is determined from the ratio of the fast Fourier transforms of the measured ATD and calculated ATD;

7. the measured arrival time for the species of interest is then loaded, and the machine function deconvolved using (6) above and equation (8.23);.

8. the arrival time distribution is reconstructed using initial estimates for the beam temperature and flow velocity;

9. T and u in equation (8.20) are adjusted until the calculated and deconvolved experimental curves match using a linear least squares fitting procedure and adjusting the temperature until the slope and co-variance values are both optimized to a value close to unity.

The shape of the arrival time distribution is very sensitive to small changes in temperature, giving a high level of confidence that the solution will be very close to the actual value. One point to note is that if too much smoothing is applied then the calculated beam temperature will be too high due to the smearing effect of the smoothing technique. If insufficient smoothing is applied a solution may not be found, because the co-variance value will not converge. The most important point is the quality of the input data. If the measured arrival time distribution has a strong signal level and has been averaged over many data sets then confidence in the final deconvoluted beam temperature and flow velocity will be much higher.

Measured arrival time distributions are shown in Figures 8.2 to 8.5. Figure 8.2 shows the arrival time distributions for helium, argon, oxygen and nitrogen all measured under the same experimental conditions. The helium signal appears to be much

lower than the other signals, this is because the electron impact ionization cross-section of helium is small (Chapter 3) compared to the other three gases which have similar ionization cross-sections. The arrival time distribution peaks are broader for the molecular species than for the atomic species because the rotational energy states of the molecules are not efficiently quenched by the collisions in the expanding gas. Equipartition of the rotational and translational energy components contribute to the the random translational energy increase of the beam formed from diatomic species. Initially the O_2^+ and O^+ and N_2^+ and N^+ peaks appear to have similar arrival times, even though the molecular ions are heaver by a factor of two. This is because ionization and fragmentation occurs in the quadrupole ion source and the flight time through the quadrupole mass filter is very short compared to the total flight time of the molecular beam. The small O^+ and N^+ peaks reflect the small partial electron impact ionization cross-sections for the formation of these fragments.[6]

The upper graph in Figure 8.3 shows the effect of hexapole enhancement[b] on a beam of 25% CH_3Br in an argon carrier gas. A hexapole voltage of 10 kV enhances the signal by a factor of approximately three by focusing the upper Stark states to the beam axis. The lower figure compares the signal from the quadrupole mass spectrometer for Ar^+, CH_3Br^+, CH_3^+ and Br^+. It is clear from this Figure that the argon peak has slowed and broadened significantly when compared to the argon peak from the previous plot. This is because the molecular beam takes on the average flow characteristics of the species in the beam weighted to the proportional mole fraction of those species. This is demonstrated even more clearly by examining the lower plot in Figure 8.4, which shows the arrival time distributions of CF_3^+ ions from neat CF_3Br and seeded CF_3Br in 25% argon. The latter beam is much narrower and faster than the former. The upper plot in this Figure and the graph in Figure 8.5 shows the upper stark state focusing of CF_3Br and CH_3F respectively due to the increasing hexapole voltage.

[b] For a complete description of hexapole focusing see Vallance[88] or Hu[172] and references therein

Table 8.1: Beam temperature and velocity profiles

Target species	Mass $gmol^{-1}$	Flow velocity ms^{-1}	$T_{\|\|}$ K	C_p $Jmol^{-1}$	u_{calc} ms^{-1}
Ar	40	555	1.4	20.79	558
He	4	1258	5.7	20.79	1765
Kr	83	387	6.9	20.79	387
O_2	32	655	9.2	28.96	736
N_2	28	726	9.7	28.88	786
CH_3Br	95	480	32	43	521
CF_3Br	149	365	36	69.53	529
CF_3H	70	568	16.8	37.6	567
25% CF_3Br in Ar	67.3	455	13		
25% CH_3Br in Ar	53.8	509	5.0		

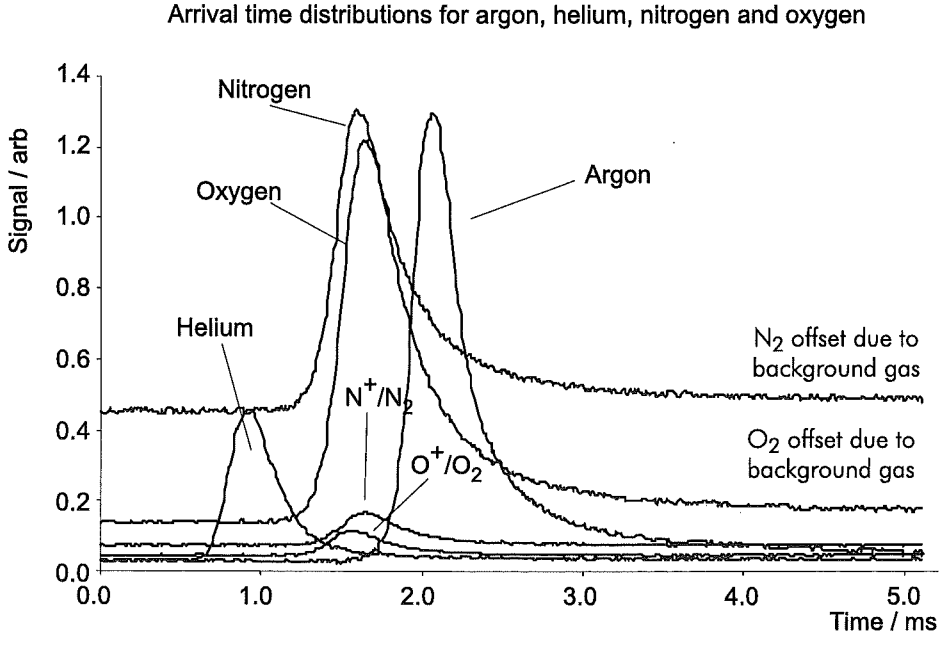

Figure 8.2: Arrival time distributions for ionized helium, argon, oxygen and nitrogen. Ions are formed by electron impact ionization in quadrupole ion source.

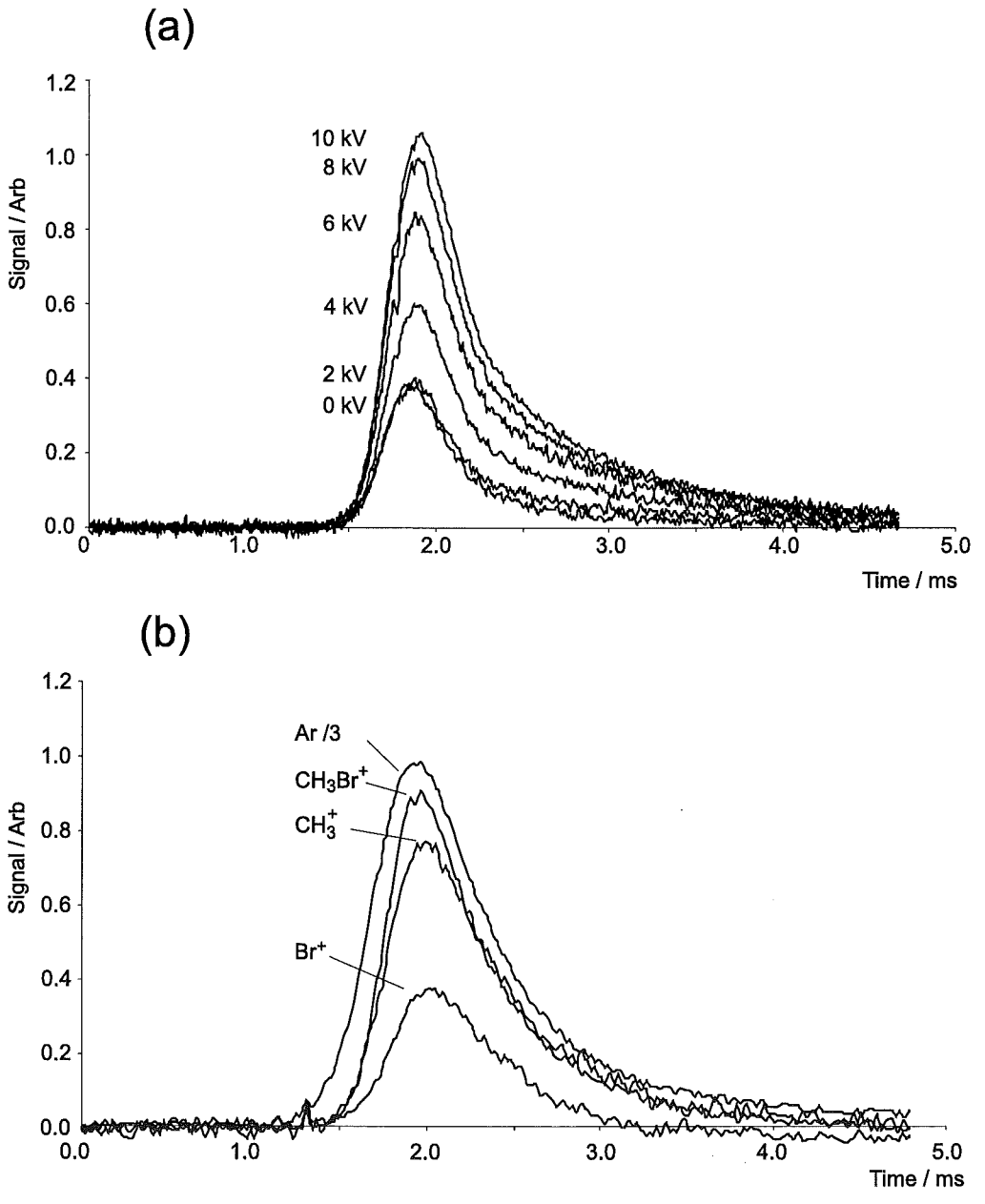

Figure 8.3: Arrival time distribution for 25% CH_3Br in argon: (a) effect of hexapole enhancement from 0 to 10 kV; (b) fragment ions from ionization process in quadrupole ion source. Note change in scale for Ar^+ ATD.

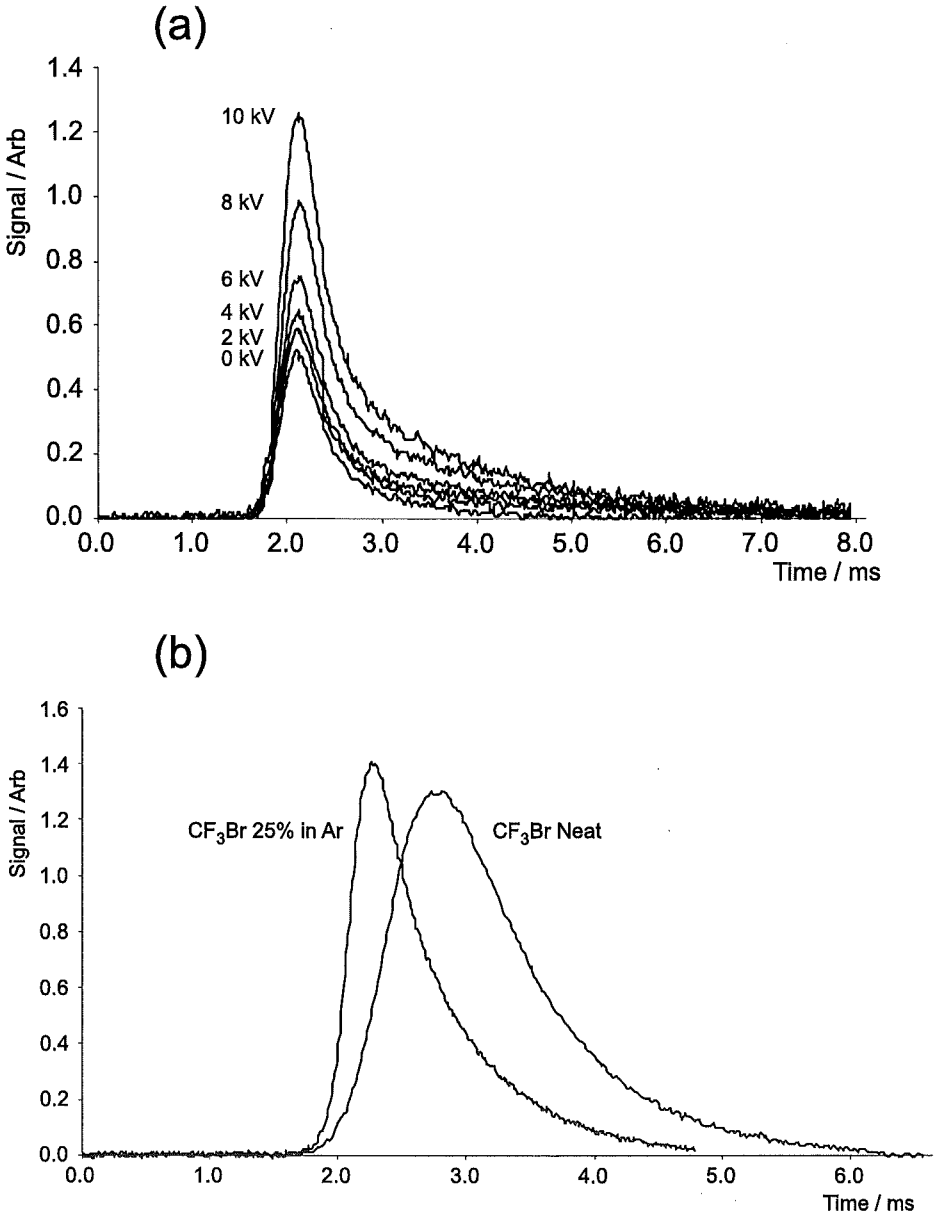

Figure 8.4: Arrival time distribution for CF_3Br in argon: (a) in 25% argon effect of hexapole enhancement from 0 to 10 kV; (b) velocity enhancement and temperature decrease due to mixing with argon carrier gas at 25%.

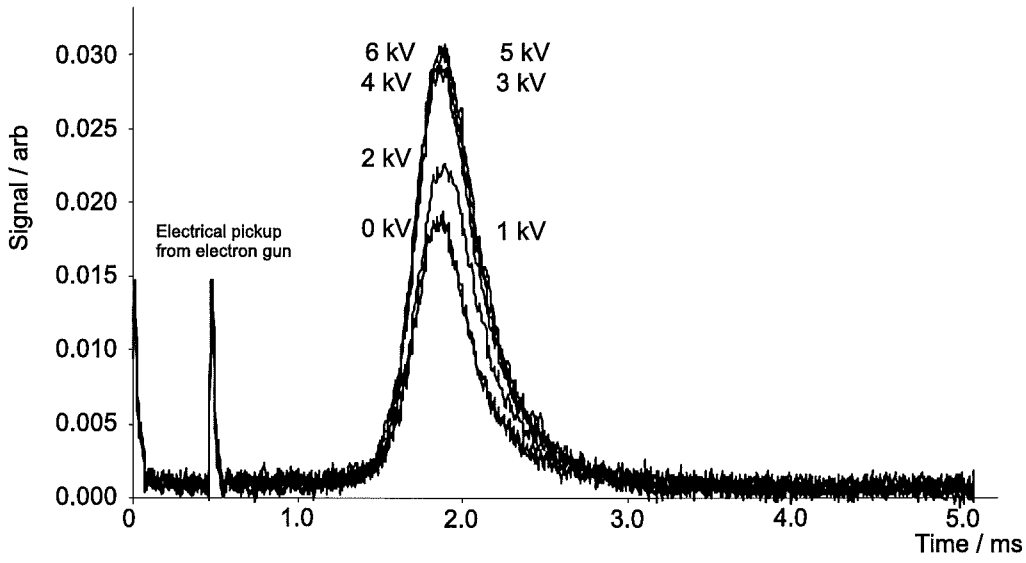

Figure 8.5: Arrival time distribution for CH_3F in argon, including hexapole enhancement from 0 to 6 kV.

9. CHARGED PARTICLE BEAMS

In this Chapter an electron gun and an ion gun designed and tested for this project are described. The ion gun has not yet been used in crossed beam experiments but will be used in future studies.

9.1 The electron gun

The difficulties that have been experienced with producing a well defined electron beam for electron impact ionization studies using crossed beam methods have been significant. Originally a Pierce type electron gun was used for electron beam production. This gun had previously been used for investigating the orientation dependence on electron impact ionization.[3,4] In the past, Pierce electron guns have been primarily used in high energy electron beam sources such as cathode ray tubes and klystron sources. The advantage of a Pierce electron gun is it that has only four elements; the Pierce element, an anode and two lens elements, simplifying the focusing compared to electron guns that incorporate Einzel lens systems. Although this electron gun had been previously well characterized, and was found to produce a large electron flux, it was unsatisfactory for the present experiments because of unstable focusing and beam flux.

A decision was made to simplify the electron gun by increasing the number of lens elements. The new electron gun would act as a collimating device rather then a focusing device. A diagram of the redesigned electron gun is given in Figure 9.1.

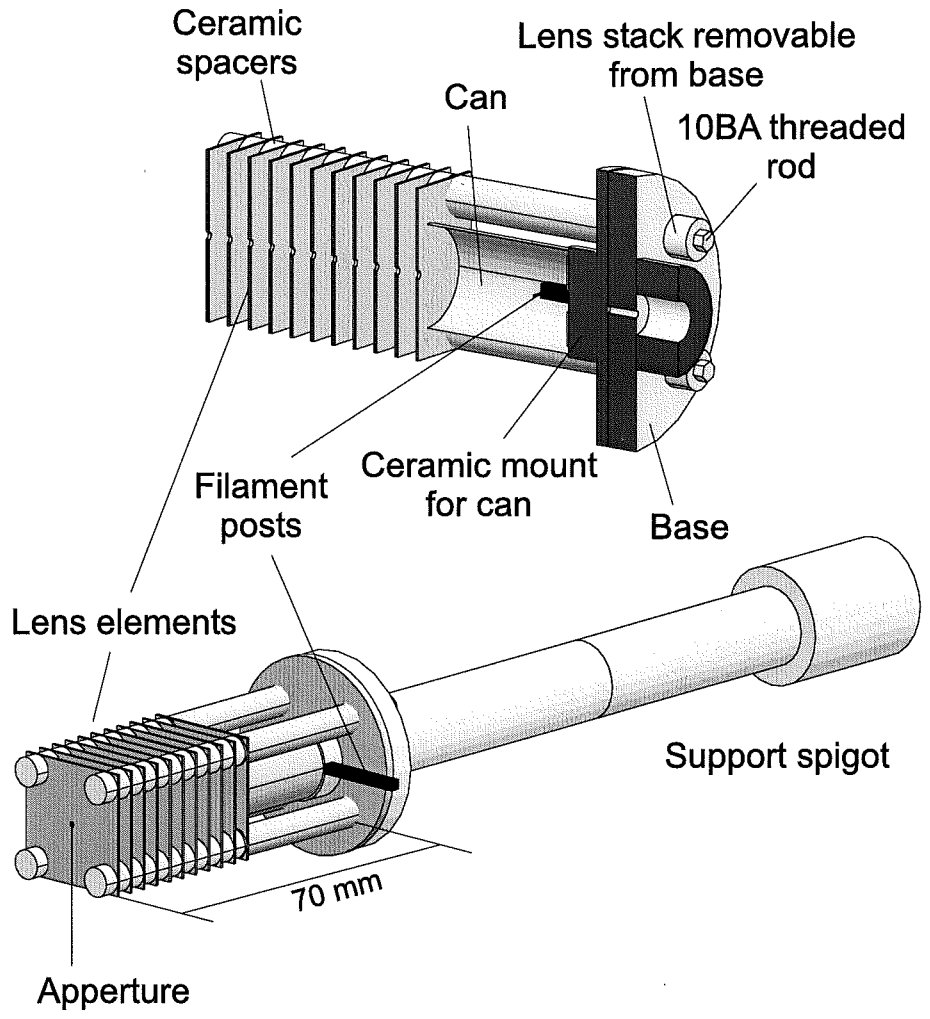

Figure 9.1: Schematic of electron gun. (a) sectional view (b) axonometric view.

The pulsing of the electron gun was controlled by one of the fast, high-voltage switches discussed in Section 7.3. The electron gun lens elements were controlled by a fully floating six channel ±0-300 V supply built by the departmental electronics workshop. The current to the filament was provided by a Topward 33010D 0-10 A, 0-30 V DC power supply. For a 0.007″ diameter rhenium wire filament the heating current was typically 3.0-3.8 A and for a 0.03″ tungsten ribbon filament the heating current was typically 6-7 A. The electron energy was provided by a 0-1 kV DC supply, built in the departmental Electronics Workshop.

The lens elements were mounted on 10BA threaded rods insulated by ceramic

sleeves and separated by 3.2 mm ceramic spacers. The whole lens assembly could be readily unscrewed from the base so that the filament could be easily replaced. The filament was spot welded to molybdenum filament posts and coated, in a inert gas atmosphere, with $BaZrO_3$ to decrease the work function. All the lens elements were 25 mm $\times$ 25 mm made from 0.5 mm thick stainless steel. The first nine lens elements had a 3 mm aperture in the center and the last two elements had a 1 mm aperture through the center. All of the lens elements were coated in colloidal graphite to minimize contact potentials. Lens elements 4 and 5, 6 and 7, and 8 and 9 were internally connected together. This configuration has two advantages; the lenses act as the traditional Einzel three lens system and focusing was simplified because there were fewer adjustable parameters.

A Burle microchannel plate electron imaging stack was used to try and establish the best focusing conditions for the electron gun. The imaging stack was mounted on an adjustable 'lollipop' shaped stainless steel stand with a heavy stainless steel base. The electron beam image was viewed on a television monitor using a Sony Handycam TR315E. It was possible to change the size of the spot on the image by changing the voltage on the lens elements but only by a small amount and the spot was always in the center of the image. This was not consistent with the focusing effects observed from the collected images by the product imaging system. The voltage on the microchannel plates had the effect of drawing the electron beam to the center of the microchannel plate stack, making the beam appear more focused then it really was. Field penetration from the microchannel plate stack also had a large effect on the ion trajectories in the crossing region. Because of these problems the electron imaging stack was replaced by an electron beam stop consisting of eight 0.8 mm wide concentric copper rings mounted on a ceramic disk as shown in Figure 9.2. The concentric ring design of detector allowed for more realistic beam profiles to be recorded than the microchannel plate imaging stack. For optimum electron beam focusing the bulk of the electron beam current should be collected on the center two rings. There was still one drawback with this system of electron beam focusing. The detector was at the focal point but the molecular beam crossing point was not, thus the electron beam focusing

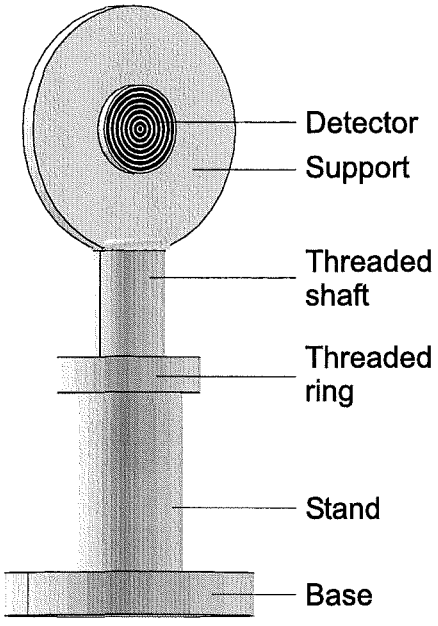

Figure 9.2: Schematic of electron beam detector.

at the detector may have been better than at the beam crossing region. To ensure that the electron beam focusing was not affected by the pulsing of the electron gun, the beam was pulsed while the electron current was monitored. The current collected on each of the rings decreased as the mark:space ratio was decreased, but the ratio of the current collected from the different rings remained the same, suggesting that the electron gun retains its focus. Another method that has been applied to examine the focusing of the electron gun was to bleed argon into the scattering chamber to a relatively high pressure, 1×10^{-4} Torr. It was then possible see the electron beam track directly, due to the characteristic blue emission of an argon plasma. As the focusing conditions of the electron beam were changed it was possible to see the electron beam moving and defocusing. The typical operating conditions of the new electron gun are given in Table 9.2, and the current collected off the different concentric rings, along with the area of the ring is given in Table 9.1.

Both of the electron guns used in this work have caused serious and as yet unresolved problems. The focusing of the electron beam has been unreliable, the electron beam

current has been unstable and obtaining consistent short pulsing of the gun has also presented a problem.

The upper plot in Figure 9.3 shows the electron beam retarding potential difference curve, and the derivative. The FWHM of the electron beam was about 2 eV. The lower plot illustrates the arrival time distribution of electrons at the beam stop after applying a gate function as shown. 5 μs was about the narrowest gate that can applied for these measurements because of the bandwidth/gain limitations of the Stanford Research Systems SR570 amplifier used to measure this signal, which was typically of the order of 50 nA when the electron gun was operated continuously. Capacitance in the coaxial cable also contributed to the broadening of the signal, as well as ringing in the trailing edge of the pulse.

Table 9.1: Electron beam stop area and current values.

Ring	Area (mm^2)	Percentage area of total	Typical Current (nA)	Current / Area ($nAmm^{-2}$)
Center + 2	0.7854	0.91	21.0	26.7
3 + 4	14.58	16.8	14.0	0.96
5 + 6	28.65	33.0	10.2	0.36
7 + 8	42.75	49.3	2.8	0.07

Table 9.2: The electron gun settings. Lenses 4 and 5 were pulsed. All values are recorded in volts. (gnd is the machine ground)

Electron energy	70	80	90	100	110	120	130	140	150
Pulse (L4 & L5)	-80	-90	-100	-110	-120	-130	-140	-150	-160
Can	-92	-105	-118	-131	-144	-157	-170	-183	-197
Lens 1	-55	-64	-72	-80	-88	-96	-104	-112	-120
Lens 2	gnd	gnd	gnd	gnd	gnd	gnd	gnd	gnd	gnd
Lens 3	-66	-75	-85	-94	-103	-113	-122	-132	-141
Lens 6 and 7	gnd	gnd	gnd	gnd	gnd	gnd	gnd	gnd	gnd
Lens 8 and 9	gnd	gnd	gnd	gnd	gnd	gnd	gnd	gnd	gnd
Lens 10	-67	-77	-86	-96	-106	-115	-125	-134	-144
Lens 11	gnd	gnd	gnd	gnd	gnd	gnd	gnd	gnd	gnd

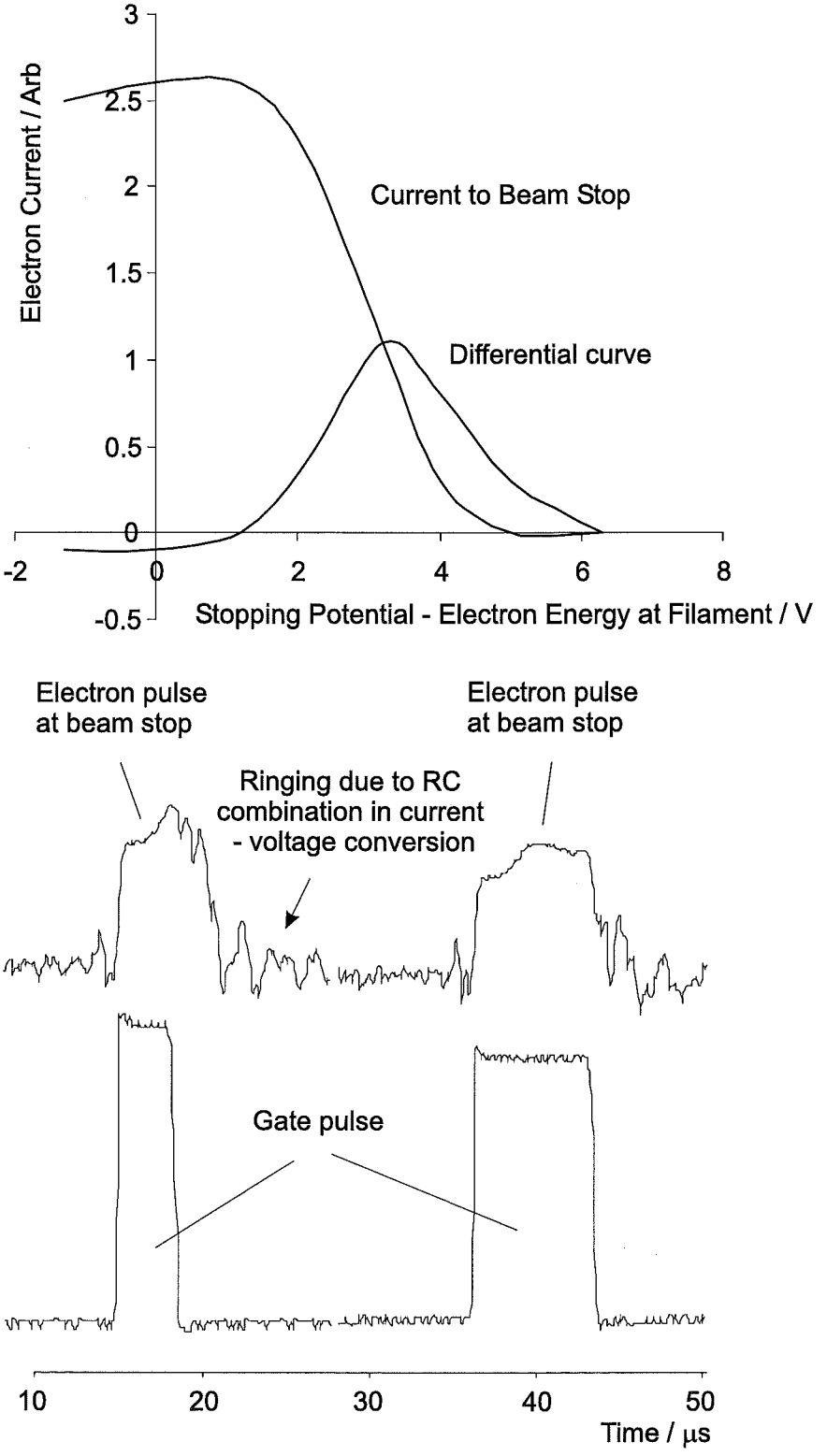

Figure 9.3: Electron beam retarding potential difference and arrival time distribution.

9.2 Ion–molecule reactions.

Gas phase ion–molecule reactions are important in many areas and applications of chemistry, including analytical applications, in semiconductor processing and in atmospheric and interstellar processes.

9.2.1 H_3^+ production and reactions

The H_3^+ ion is extremely reactive which makes it an interesting candidate for the study of ion–molecule reactions. It will charge transfer to most other neutral molecules to form a protonated neutral and H_2. Table 9.3 lists the proton affinies of symmetric top target species of interest, as well as some other neutral targets that may be studied in the crossed molecular beam machine.

Table 9.3: Proton affinities for neutral target species of interest.

Target species	Proton affinity (eV)	Target species	Proton affinity (eV)
H_2	4.88	CH_3F	7.16
CH_3F	6.82	$CHCl_3$	–
CH_3Cl	7.74	$CHBr_3$	–
CH_3Br	7.68	CH_4	6.28
CH_3OH	8.72	CF_4	6.12
CH_3SH	8.94	N_2	5.71
CF_3Br	6.71	O_2	4.87
CF_3Cl	6.61	H_2O	7.9
CH_3F	7.16		

The highly reactive H_3^+ was first identified by J.J. Thomson in 1913.[176] Thomson postulated that only two known substances could give the mass spectral line $m/z = 3$; either a quadruply charged carbon atom , C^{4+}, or a molecule containing three atoms of hydrogen. Thomson also observed that only salts containing hydrogen were able to produce the $m/z = 3$ line, which he generated by bombarding potassium hydroxide with electrons.

Dempster[177] probed the production of H_3^+ further by using ~800 eV electrons to ionize H_2. He found that as he decreased the pressure of H_2 the relative intensities of H^+ and H_3^+ peaks decreased compared to the H_2^+ peak. He correctly proposed that H_2^+ ions formed by electron impact do not dissociate, but on collision with H_2 give rise to H_3^+ and H. Dempster also concluded that the H_3 molecule was unstable, whereas Thompson thought that it might be possible to produce stable H_3. Further investigation into the mechanism for the production of H_3^+ was carried out in 1925 by Hogness and Lunn.[178] They used a magnetic sector mass spectrometer to study the ions produced by the electron impact of hydrogen. The relative intensities of H^+, H_2^+ and H_3^+ were measured as a function of pressure and electron energy. It was found that at low pressure H_2^+ was the dominant ion but as the H_2 pressure was increased H_3^+ began to dominate. Their work supported Dempster's findings, and the following reaction scheme was proposed:

$$H_2 + e^- \longrightarrow H_2^+ + H_2 + 2e^- \tag{9.1}$$

$$H_2^+ + H_2 \longrightarrow H_3^+ + H \tag{9.2}$$

It was also found that in a mixture of He and H_2 the ratio of H_3^+ to H^+ decreased due to the dissociation of H_3^+ on collision with He. This was supported by the observation that both HeH_2^+ and HeH^+ were formed.

After this pioneering work however, little was done to investigate these reactions further, and by 1970 only a few ion–molecule reactions of H_3^+ had been studied, mostly of simple saturated hydrocarbons such as methane, ethane, butane and cyclohexane by Aquilanti and Volpi.[179,180] In their work H_3^+ was formed by bombarding H_2 with β particles from the walls of an ion source, which had a layer of tritium adsorbed to the surface. The product distribution was found to be strongly dependent on the H_2 pressure. The conclusion was that the observed product distribution was due to stabilization of the *product* by collision with a third body. For example, in the simplest case studied:

$$(H_3^+)^* + CH_4 \longrightarrow (CH_5^+)^* + H_2 \tag{9.3}$$

$$(CH_5^+)^* \longrightarrow CH_3^+ + H_2 \tag{9.4}$$

$$(CH_5^+)^* + M \longrightarrow CH_5^+ + (M)^* \tag{9.5}$$

Now it is generally accepted that the variation in product distribution is due to the collisional stabilization of the *reactant*, namely H_3^+:

1. In the low pressure case:

$$(H_3^+)^* + CH_4 \longrightarrow CH_3^+ + 2H_2 \tag{9.6}$$

2. In the high pressure case:

$$(H_3^+)^* + H_2 \longrightarrow H_3^+ + (H_2)^* \tag{9.7}$$

$$H_3^+ + CH_4 \longrightarrow CH_5^+ + H_2 \tag{9.8}$$

Since the transition state energy was lower in the high pressure case, fragmentation of the products were less likely.

Ab-initio calculations[181] indicate that the ground state geometry of the H_3^+ ion is an equilateral triangle with a bond length of approximately 0.88Å. The linear form is approximately 0.43 eV higher in energy:

$$H^+_{3(\text{triangular})} \rightleftharpoons H^+_{3(\text{linear})} \quad \Delta H = +0.43 \pm 0.09 \text{ eV} \tag{9.9}$$

Burt and coworkers[182] used the flowing afterglow technique to study the reactions of H_3^+ with several small molecules including N_2, CO, CO_2, H_2O, NO, N_2O, NO_2, CH_4, C_2H_2, NH_3 C_2H_4 and C_2H_6. Their experiments showed that proton transfer was the only observed primary reaction for all the above reactions except for C_2H_4 and C_2H_6

where dissociative charge transfer also occurred, and the case of NO_2 where dissociative charge transfer occurred exclusively. They present data on ΔH_f and the observed and theoretical rate constants. The proton affinity for O_2 is very slightly lower than H_2 and this explains the observation that proton transfer to O_2 does not occur rapidly.

In 1973 Huntress and Bowers[183] studied reactions of excited and ground state H_3^+ with C_2H_6, CH_3NH_2, CH_3OH, CH_3F, CH_3SH, and CH_3Cl using an ion cyclotron resonance (ICR) pulse injection apparatus. The product distribution that they obtained was largely dependent on the H_2 pressure in the source. As the pressure in the source increased excited state H_3^{+*} was increasingly collisionally de-excited to the ground state. At low hydrogen pressures the reaction occurred *via* direct charge transfer or hydride abstraction processes. As the hydrogen pressure was increased, the product distribution changed due to the rapid deactivation of the H_3^+ by collision with H_2. With the exception of ethane the products decomposed *via* vicinal hydrogen elimination and except for C_2H_6, CH_3SH and CH_3Cl, C-X bond cleavage to give the methyl cation. Some evidence was obtained showing that the excited H_3^+ was not be directly deactivated to the ground state, but to some intermediate state(s) which still contained a significant amount of internal energy and were subsequently slowly deactivated to the ground state. The interested reader is referred to that paper for a more complete discussion.[183]

By 1974 some discrepancy existed as to the measured rate coefficients for some of these reactions after a paper by Kim *et al.*[184] in which ion–molecule reactions of H_3^+ were studied using an ion cyclotron resonance spectrometer. Further discrepancy arose when Ryan[185] measured different results again when studying these reactions using the space–charge trapping method.

Rakshit[186] using a selected ion flow tube (SIFT) apparatus, measured and calculated rate constants for the reactions of N_2, CO, CO_2, N_2O, SO_2, CH_3Cl, COS, C_2H_4, CS_2, NOCl, and NO. The results were in disagreement with those of Burt and coworkers,[182] Kim *et. al.*[184] and Ryan.[185] Considering earlier statements about collisional stabilization of H_3^+ it is not surprising that discrepancy exists between the experimental rate constants and observed product distributions. Milligan[187] has pointed out that

impurities in the gas samples also have an effect on the product distribution, and that contributions from H_3O^+ and N_2H^+ were very important in determining the product branching ratios.

H_3^+ generation

The most popular method to generate the H_3^+ ion is to generate an H_2^+ ion first. H_2^+ reacts with H_2 to form H_3^+ and H. Two of the more common ways to generate H_2^+ are using either electron impact ionization or a microwave discharge tube.

Thompson's experiment[176] used a discharge tube at about 20 kV to generate H_2^+ ions in a bath gas of H_2 at about 3×10^{-3} Torr. H_2 subsequently reacted with the H_2^+ ions to produce H_3^+. Dempster[177] on the other hand used a Wehnelt cathode, H_2 was ionized by electron impact forming H_3^+ as before. Milligan[187] used a 2.5 MHz microwave generator to produce a discharge in his flowing afterglow tube. H_2 was passed through the discharge tube and became ionized, forming H_3^+ in the usual way. The choice of electron impact or flowing afterglow method does not seem to affect the vibrational excitation of H_3^+. The final vibrational state of the H_3^+ depends primarily on the pressure in the source. A further method of producing H_3^+ in the ground vibrational state involves the use of Kr^+ to chemically ionize H_2, as outlined in the following reaction scheme[187]

$$Kr^+ + H_2 \longrightarrow KrH^+ + H \tag{9.10}$$

$$KrH^+ + H_2 \longrightarrow Kr + H_3^+(v = 0) \tag{9.11}$$

The most important point in reactions of H_3^+ is that observed product distribution and reaction mechanism for the reactions of H_3^+ is strongly dependent on the internal energy of the reactant ion. It has been shown[183] that the reactions of highly excited H_3^+ occur mainly *via* the direct process of charge transfer and hydrogen ion abstraction. For collisional stabilized H_3^+, the reaction proceeds chiefly *via* proton transfer to form a long-lived complex which may decompose *via* hydrogen elimination and C-X bond

cleavage.

H_3^+ generation scheme:

$$H_2 + e^- \longrightarrow H_2^+ + 2e^-; \quad IE = 15.42 \text{ eV} \tag{9.12}$$

$$H_2 + e^- \longrightarrow H^+ + H + 2e^-; \quad AE = 18.08 \text{ eV} \tag{9.13}$$

$$H_2^+ \longrightarrow H^+ + H; \quad \Delta H = +2.65 \text{ eV} \tag{9.14}$$

$$H^+ + H_2 \longrightarrow H_3^+ + H; \quad PA = 4.88 \text{ eV} \tag{9.15}$$

$$\text{Overall: } H_2 + H_2 + e^- \longrightarrow H_3^+ + H + 2e^-; \quad \Delta H = -2.23 \text{ eV} \tag{9.16}$$

$H_3^+ + CH_3X$ reaction scheme:

$$H_3^+ + CH_3X \longrightarrow CH_3X^+ + H_2 + H; \quad \text{Charge transfer} \tag{9.17}$$

$$\longrightarrow CH_2X^+ + 2H_2; \quad \text{Hydrogen elimination} \tag{9.18}$$

$$\longrightarrow CH_3XH^+ + H_2; \quad \text{Protonation} \tag{9.19}$$

$$\longrightarrow CH_3^+ + HX + H_2; \quad \text{Elimination of H-X} \tag{9.20}$$

9.3 Ion gun design and characterization

The ion gun has been used for H_3^+ and $C_2H_2^+$ beam production, but could be applied to any gaseous sample. A filament and two small lens elements produced a beam of electrons that passed through a cell filled with gas of interest. The gas undergoes electron impact ionization, and the positive ions that were produced were repelled by a charged plate at the back of the ionization cell toward a series of electrostatic lens elements for focusing. A diagram of the ion gun is given in Figure 9.4.

Using H_2 as the sample gas, electron impact ionization forms protons, which reacts with H_2 to produce H_3^+ and focused into a beam. The same power supplies and pulsing electronics that control the electron gun were used to control the ion gun. The H_3^+ source was installed into the molecular beam machine to allow it to be characterized and calibrated. The same Vacuum Generators SXP-300 quadrupole mass spectrometer that was used for the measurements of partial ionization cross-sections was used for ion

gun calibration. An MKS 690A.1TRC 0.1 Torr full scale Baratron was used to monitor the hydrogen pressure in the source. Typical settings of the ion gun are given in Table 9.4. Figure 9.5 shows mass spectra recorded by the quadrupole mass spectrometer for five different ion source pressures; 100 mTorr, 70 mTorr, 50 mTorr, 30 mTorr and 20 mTorr, measured on the same scale. For crossed beam experiments a lower pressure is desirable because the gas escaping from the ion source contributes to a significant increase in scattering chamber pressure; unfortunately lowering the source pressure is also detrimental to the ion signal. Quadrupole instability at low m/z made it difficult to clearly resolve the ion peaks. An irregular shifting of the H_3^+ peak from left to right, as illustrated by the small peak in the spectrum at 70 mTorr to the right of the H_3^+ peak, further contributed to these difficulties.

In order to carry out ion–molecule reactions using the molecular beam machine, the ion gun must be pulsed. An experiment to test the pulsing of the ion gun was carried out using a Nagard 5002C pulse generator. The pulse was applied to ion lens 1 with a repetition rate set at 2kHz, a pulse width of 3 μs and a pulse height of +37.5 V Using the SXP-300 quadrupole mass spectrometer, some variation in the H_2^+ and H_3^+ ions signals, were observed but it was not possible to quantify an ion arrival time distribution. The same set of Burle MCP's and Sony camera that were used to image the electron beam were used to monitor the ion beam. With a pulse width of 2.5 μs at a rate of 5 Hz, pulsing of the ion beam was clearly visible on the television monitor.

Table 9.4: H_3^+ ion source operating parameters.

Operating Parameter	Value	Operating Parameter	Value
Filament current	3.48 A	Case	+20 V
Cathode	-76.7 V	Ion Extractor	-11.9 V
Shield	-113.3 V	Ion Lens 1	-53.4 V
Electron Lenses	-28.2 V	Ion Lens 2	+4.1 V
Electron Trap	82.4 V	Ion Lens 3	+6.8V
Electron Current	3.10 μA	Ion Lens 4	-117.7V

One limiting factor in detecting the reaction products from the point source was

formation of the ion–molecule reaction products from the background gas, primarily H_2O, N_2 and O_2 when the ion beam traverses the scattering chamber. In order to minimize this, the selection of an ion that will charge-transfer to the target species in the beam but not the background gas was desirable. For this an ion which has an ionization energy above the target species but below these background species must be selected. A search indicated that a lot of the potential precursor candidates were difficult to obtain, and/or highly toxic or corrosive. However the $C_2H_2^+/CH_3Br$ charge transfer reaction was a good candidate to trial, as acetylene was readily available and simple to handle. Acetylene has an ionization energy of 11.4 eV, and CH_3Br has an ionization energy of 10.54 eV. H_2O, N_2 and O_2 have ionization energies of 12.32 eV, 15.58 eV and 12.67 eV respectively. A further advantage was the high molecular mass of the CH_3Br^+ ion, thus increasing the time-of-flight resolution. An experimental trial of this system revealed that no CH_3Br^+ signal could be detected, although this was probably due to unrelated technical difficulties with the detection system. When these problems are resolved this approach warrants further investigation. Nascent product and energy distributions from reactions (9.17) to (9.20) using beams of oriented molecules under single collision conditions would certainly provide much more data on the mechanisms of charge transfer than the reactions carried out using the methods described above which can only determine bulk rate constants. This part of the project is still in the development phase but the successful development and characterization of an ion gun was an important step in developing this line of research further.

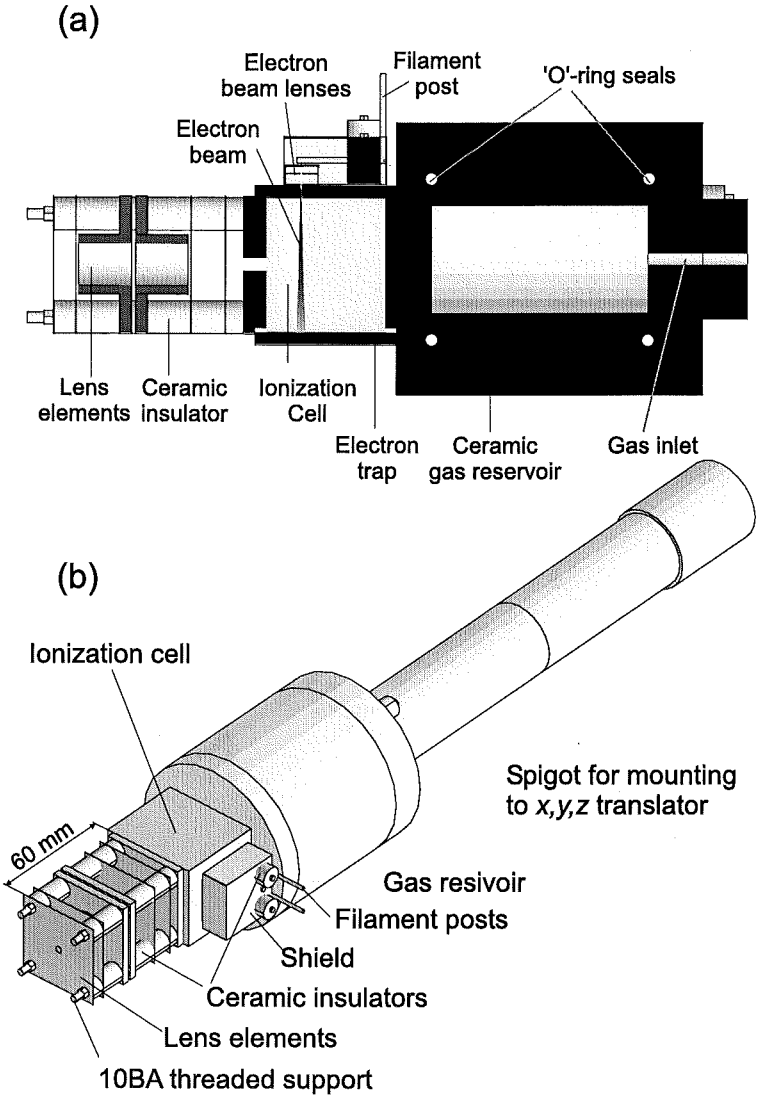

Figure 9.4: Schematic of ion gun. (a) Sectional view. (b) Axonometric view.

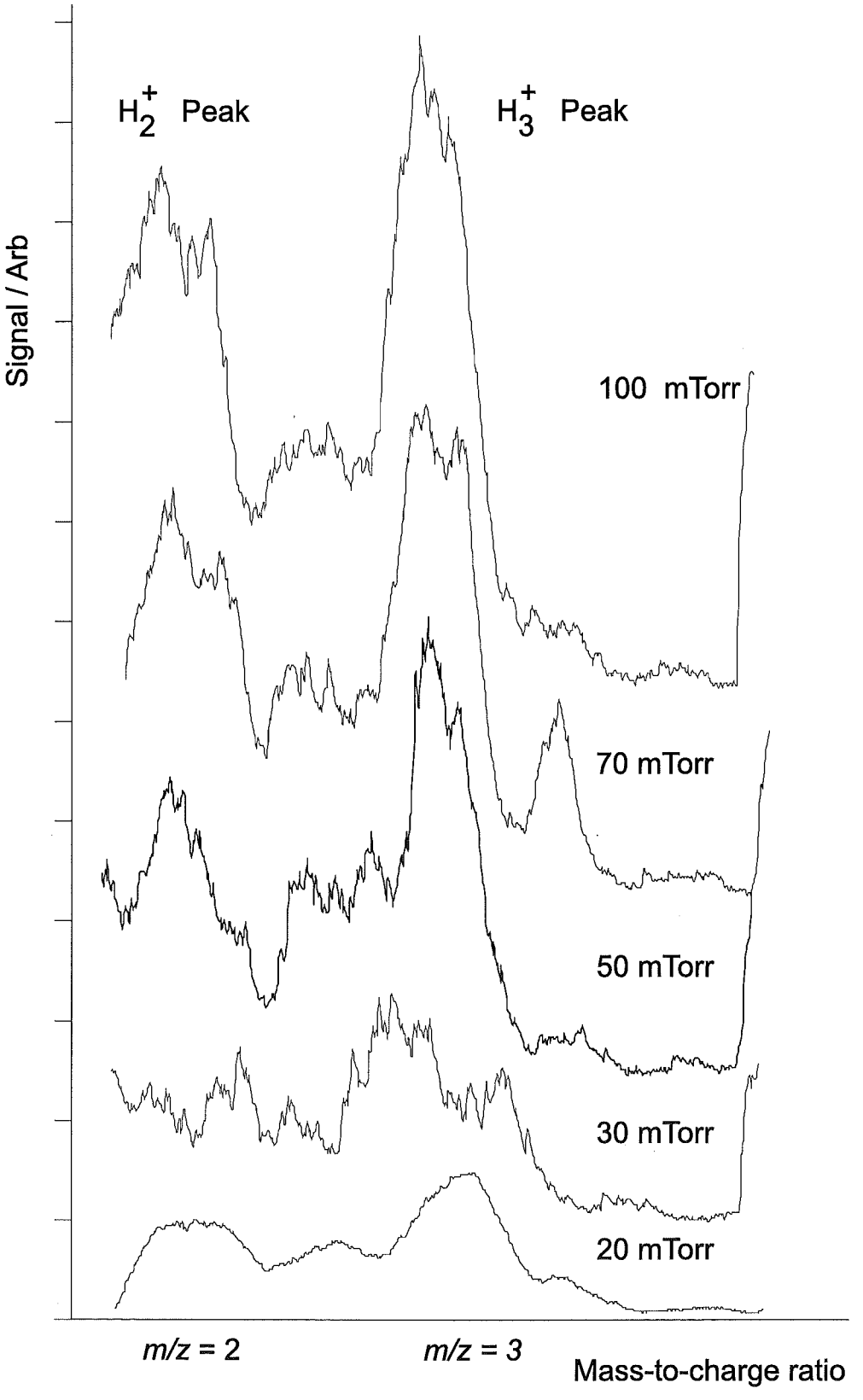

Figure 9.5: H_3^+ mass spectra recorded using the quadrupole mass spectrometer.

10. ION IMAGING

10.1 Introduction and general principles of ion imaging

Ion imaging is a very powerful technique in that it enables complete collection of a quantum state resolved velocity map of a chemical reaction or photolytically induced unimolecular dissociation. The steps involved to obtain an ion image are relatively straightforward compared to the data collection methods for other chemical dynamics experiments, which typically use a rotatable mass-spectrometer for product detection. The steps typically occur in the following order:

1. a reaction, dissociation or electron impact event occurs;
2. the reaction or dissociation products are ionized by a REMPI laser dissociation scheme;
3. the ion products expand on the surface of a sphere;
4. the ion products are extracted and projected onto the imaging detector plane;
5. the image is processed to extract the differential cross-section *via* the inverse Abel transform or other method;

Step 2 is not necessary if the products of event 1 are ions.

Modern ion imaging was first developed by Chandler and Houston in 1987,[188] although the idea of using a 2-dimensional detector to collect data on the products of a

photolysis reaction is credited to Solomon and Bersohn[189] who in the late 1960's experimented with a method that involved coating a glass bulb with a layer of tellurium. Bromine and chlorine were photolysed using a beam of polarized light from a mercury vapour lamp. After several hours of exposure, etching patterns due to the halogen reacting with the tellurium surface were observed. Unfortunately the method was not very successful because it was difficult to quantify the level of etching.

Chandler and Houston had 20 years of technological development on their side. In their experiments 266 nm laser photolysis of CH_3I was carried out from a supersonic expansion of CH_3I in helium. A second laser at 330 nm subsequently ionized the CH_3 product using a (2 + 1) multiphoton ionization scheme. The products were accelerated toward the detector by a repeller plate at 200 V, which pushed the ions through a grounded grid and an ion shutter that could be pulsed to select ions of the desired (m/z) ratio. The ions then collided with the front surface of a microchannel plate – phosphor 'sandwich'. The light from the phosphor was recorded using either a Polaroid film or a two-dimensional intensified Reticon array. Since then many other research groups around the world have used ion imaging to measure the product and energy distribution from photolysis reactions. There have been significant improvements in recent years important in advancing the technique. The present work is unique in that all previous ion imaging experiments have used laser beams to produce the ion products for detection, whereas in the present work ion products are created using either ion or electron beams crossed with the molecular beam, increasing the scope of the technique significantly, particularly from a chemistry point of view. This Chapter will begin by discussing the methodology of the technique, followed by a review of some of the technical aspects associated with imaging and ion imaging.

10.1.1 Equations of motion

As mentioned in the introduction, information on the differential cross-section may be obtained if ions are formed in a well defined region of space, known as a point

source. Ion imaging involves the production of ions from a point source and projecting them onto a plane for detection. Figure 10.1 represents a schematic of the ion imaging experiment.

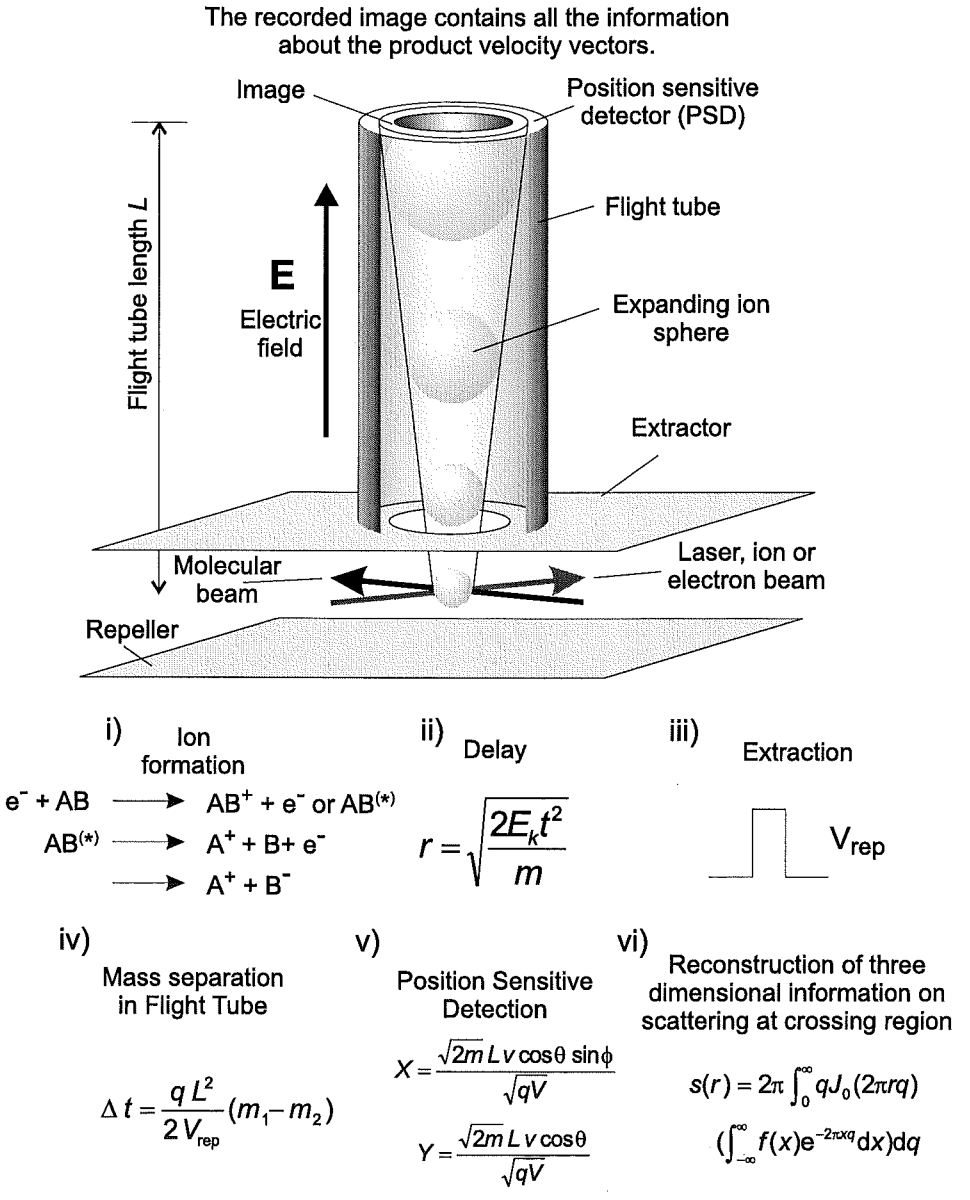

Figure 10.1: The essential components of an ion imaging experiment.

The following equations of motion may be established[190] for ions originating from a point source under space focusing conditions. At the time of ion formation, $t = 0$, all of

the ions are at $r = 0$, where r is the distance from the point source. After period t the ions have expanded on the surface of a sphere with radius r, which may be calculated from $v = r/t$ and $E_k = 1/2mv^2$.

$$r = \sqrt{\frac{2E_k}{m}}t \tag{10.1}$$

At time t an extraction pulse is applied, which projects the expanding ion sphere onto the surface of a position sensitive detector (PSD), which is a two dimensional surface. Thus an 'image' of the ion sphere is generated. Equation (10.1) is only valid in the center-of-mass velocity frame of the colliding particles, which may be approximated to the laboratory frame when one of the colliding particles is a photon or electron, but in the case of ion molecule reactions, r needs to be offset by the center-of-mass momentum vector of the colliding particles. For a true projection of the expanding ion sphere an infinitely large extraction field $\mathbf{E}$ would need to be instantaneously applied at t. In the real laboratory this is unrealistic but provided the kinetic energy release of the products is small compared to $\mathbf{E}$, equation (10.1) is a good first approximation to the radius of the expanding ion sphere.

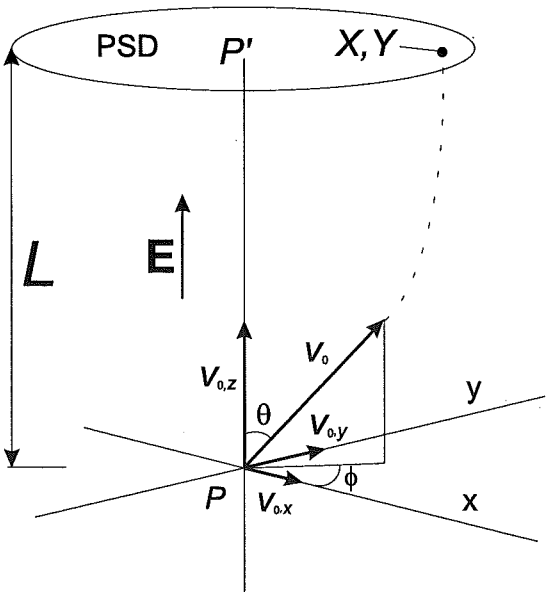

Figure 10.2: Definition of vectors and angles for the calculation of the equations of motion for an ion imaging experiment.

With reference to Figure 10.2, x_0, y_0 and z_0 are the coordinates at the point source P; P' represents the projection of the point source onto the detector plane, with coordinates x_0, y_0 and $z_0 = L$. An ion formed at P with initial kinetic energy E_k along velocity vector $\mathbf{v}$ at angles θ, ϕ may be described by the following equations of motion.

$$\begin{aligned} \mathbf{v}_{0,x} &= \mathbf{v}_0 \sin\theta \cos\phi \\ \mathbf{v}_{0,y} &= \mathbf{v}_0 \cos\phi \\ \mathbf{v}_{0,z} &= \mathbf{v}_0 \sin\theta \sin\phi \end{aligned} \tag{10.2}$$

A homogeneous field $\mathbf{E}$ is applied in order to extract the ions. The x, y location of the charged particle X, Y at the detector may be described by the following equations of motion.[190a]

$$X = \frac{2L \sin\theta \sin\phi}{\rho}\left(\sqrt{\sin^2\theta \sin^2\phi + \rho} - \sin\theta \sin\phi\right) \tag{10.3}$$

$$Y = \frac{2L \cos\theta}{\rho}\left(\sqrt{\sin^2\theta \sin^2\phi + \rho} - \sin\theta \sin\phi\right) \tag{10.4}$$

where the dimensionless quantity ρ is the ratio of the energy gained by the charged particle due to the extraction field to the kinetic energy E_k with which the charged particle was formed.

$$\rho = \frac{qV}{E_k} \tag{10.5}$$

In the limit where the extraction voltage is much larger than the ion energy these equations of motion may be simplified to:

$$X = \frac{2L \cos\phi \sin\theta}{\sqrt{\rho}} \tag{10.6}$$

$$Y = \frac{2L \cos\theta}{\sqrt{\rho}} \tag{10.7}$$

In this case, for a fixed value of ρ the charged particles are seen as a line across the

[a] A complete derivation of equations (10.3) and (10.4) is given in Appendix **G**.

detector. As ρ decreases the situation becomes more complicated as $\mathbf{E}$ and E_k interact. From equation (10.3) and (10.4) the angles ϕ and θ may be determined.[190]

$$\phi = \tan^{-1}\left(\frac{-2 \pm \sqrt{4(\rho+1) - [\rho^2(X^2+Y^2)/L^2]}}{\rho X/L}\right) \tag{10.8}$$

$$\theta = \tan^{-1}\left(\frac{X}{Y\cos\phi}\right) \tag{10.9}$$

Physical parameters may then be established from equation (10.8). The first relates to the maximum size of the image; the radius of the image R must be less then $R_{\max}$ for a positive determinant in equation (10.8).

$$R_{\max} = 2L\frac{\sqrt{\rho+1}}{\rho} \tag{10.10}$$

Assuming that the detector has a radius R_0, at distance L from the point source the minimum value of ρ is then given by

$$\rho_{\min} = \frac{1+\sqrt{1+R_0^2/L^2}}{R_0^2/2L^2} \tag{10.11}$$

This corresponds to the lowest ρ value for which an image is observable in the system. Ion imaging using this type of extraction regime is limited because a real image does not emanate from a point source, meaning that the image will blur significantly. Intense laser beams may be focused to points as small as 0.1 mm, but tight focusing the case of charged particle beams is somewhat more difficult because of stray fields and space-charge repulsion. The effect of crossing volumes will be explored further in Chapter 11.

A partial solution to the problem of crossed beam interaction volume was introduced by Eppink and Parker[191,192] using the velocity mapping approach. Ions were projected onto the detector using an electrostatic lens so that ions with the same initial velocity vector arrived at the same X, Y location on the detector plane. In this case an extractor and repeller were used, both with a positive voltage applied to them. The voltage ratio between the extractor and repeller was adjusted to optimize the focusing, and

found to be approximately 0.7. Ions traveling away from the detector experienced a larger force from the field and therefore a larger force than the particles traveling toward the detector. The conditions can be adjusted such that the imaging plane is the location where the slower ions are just being overtaken by the faster ions. The sphere of ions has been focused into a 'pancake' of ions, as represented in Figure 10.3. Each particular m/z ratio arrives at the detector at a different time according to the equations of motion for particles in that field. The exact equations of motion are much more complicated for velocity map imaging than space focusing, because the extraction field is inhomogeneous and the equation of motion of the particle also depends the location in space where it was formed, meaning that X, Y depends on x_0, y_0 and z_0, as well as the angles θ and ϕ, the ratio $V_{\text{xtr}}/V_{\text{rep}}$, and the absolute values of V_{rep} and V_{xtr}. Assuming that the ion is formed half way between the extractor and repeller plate, the flight time t_{TOF}, under velocity mapping conditions with a extractor:repeller ratio of 0.7. The approximate flight times may be calculated using the following equations expressions:

$$E_k = qV\frac{1}{2}mv_z^2 \tag{10.12}$$

$$t = \frac{L}{v_z} \tag{10.13}$$

$$= \sqrt{\frac{mL^2}{2qV}} \tag{10.14}$$

$$t_{\text{CR}} = \frac{1}{2}L_{\text{CR}}\left(\frac{m}{2q \times 0.3V_{\text{rep}}}\right)^{\frac{1}{2}} \tag{10.15}$$

$$t_{\text{FT}} = L_{\text{FT}}\left(\frac{m}{2q \times 0.7V_{\text{rep}}}\right)^{\frac{1}{2}} \tag{10.16}$$

$$t_{\text{TOF}} = t_{\text{CR}} + t_{\text{FT}} \tag{10.17}$$

Where t_{TOF} is the total flight time, t_{CR} is the time the ion spends in the flight tube, amd t_{FT} is the time that the ions spends in the flight tube.

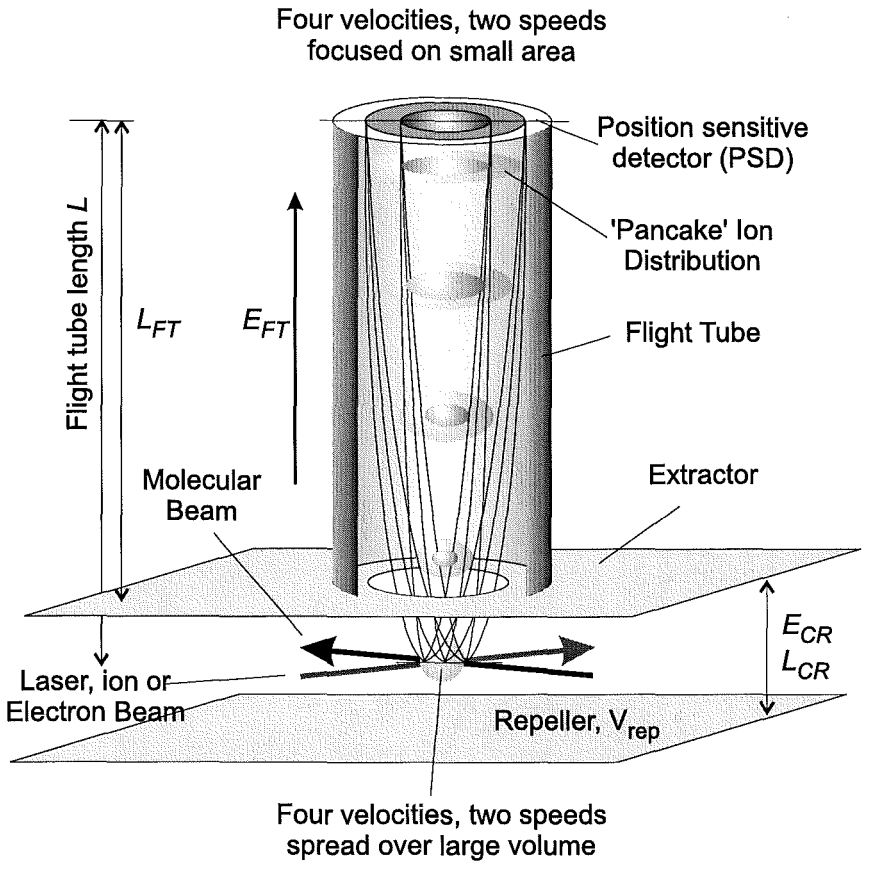

Figure 10.3: Illustration of velocity mapping process.

10.1.2 Ion counting

The ion counting method of ion imaging was originally developed by Houston's[193] group and has since been used by several other groups around the world, including our own.

The important features of the ion counting method are shown schematically in Figure 10.4. In traditional ion imaging experiments, ions are collected by a frame grabber or digital signal processor, averaged, and subsequently processed. Detector inhomogeneity, and the blurring of the pixels can occur at the MCP, phosphor, photocathode, intensifier or CCD. Coupled with lens aberrations this can lead to a significant distortion of the ion image because ions ($r \sim 10^{-9}$ m) show up as a blob on the collected image (up to $r = 1$ mm) (Figure 10.4(a)). Ion counting applies a delta function to each

ion event and assigns an intensity of unity to the ion. This is achieved by first applying a discrimination level to the image. Only data above the threshold level are retained. All of the pixels that are retained are assigned an address, reducing the size of the data set from $\sim$ 307 kB to 4 B (Figure 10.4(b)). An algorithm is applied that examines the pixel intensity for each blob. It is assumed that there is only one maximum for each blob. (Figure 10.4(c)). The maximum pixel is assigned a value of unity and all other pixels associated with that blob are assigned a value of zero. When this method was first developed the biggest difficulty was processing each frame on a frame by frame basis. State-of-the-art digital signal processors were required to perform ion counting at a maximum rate of about 10 Hz. Now this method may be routinely applied with a 2.4 GHz desktop computer at the full 32 Hz frame rate of the CCD camera using a 100 MB/s Peripheral Component Interconnect (PCI) frame grabber card.

The chief advantages of the ion counting method are the increased spatial resolution of the collected images, the removal of detector inhomogeneity, and reduction the tendency of blobs to overlap, forming one big unresolvable blob, referred to as 'spatial congestion'. As with any data manipulation method however there are also some disadvantages. The most important of these is the introduction of a large centerline noise component in the Abel inverted image because of the Fourier transform method used in the Abel inversion.[b] Other disadvantages include the heavy processor demands and the possible shifting of the delta function from the pixel centroid by as much as n/2 from for an n $\times$ n pixel blob (Figure 10.4(d)). Another factor to consider is the possibility of the loss of data. If a closely spaced cluster of ions strikes the MCP in any one particular frame, the entire cluster runs the risk of being binned into a single delta function causing a loss of data for those ions. (Figure 10.4(e)).

[b] Fourier transforms introduce ringing at sharp boundaries.

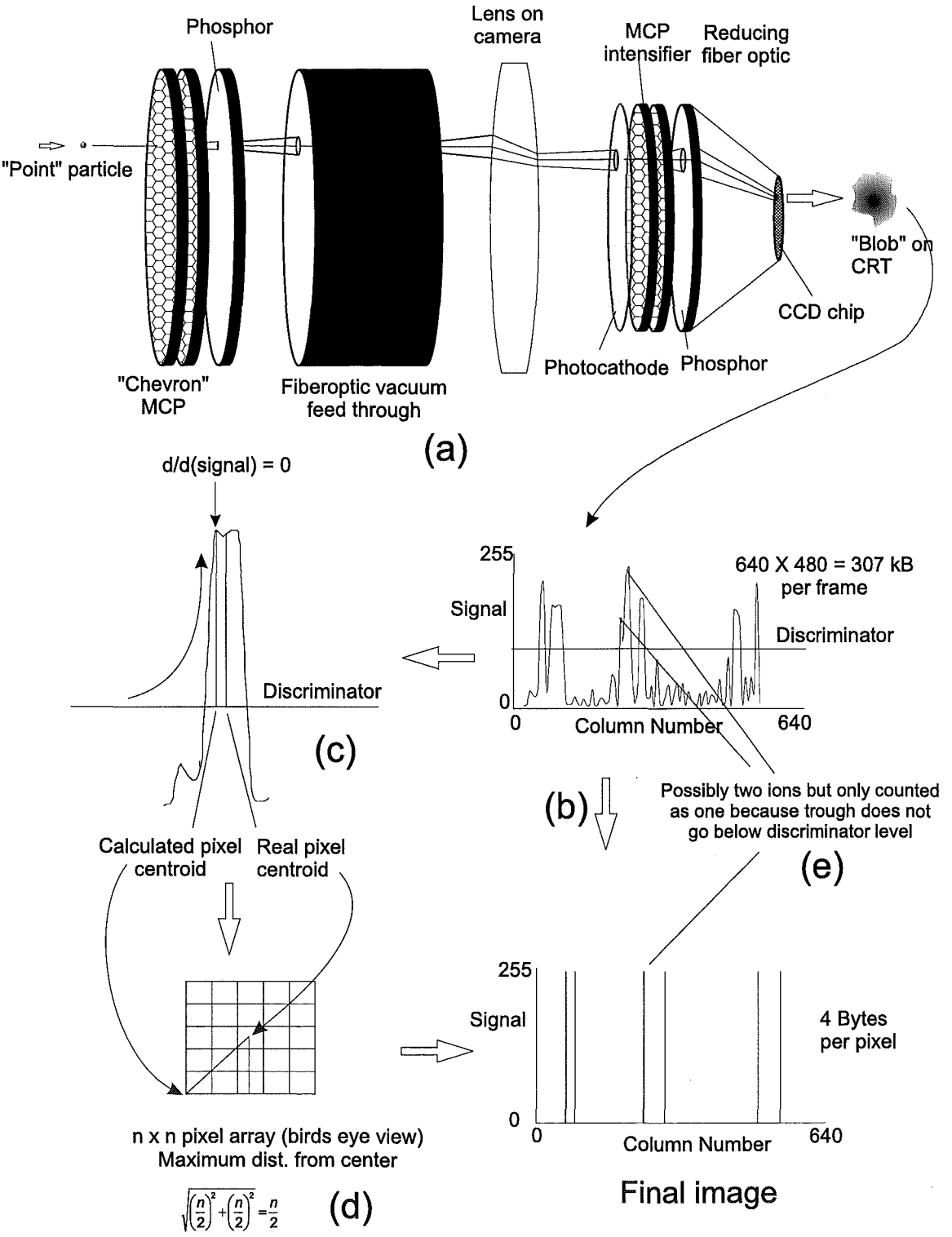

Figure 10.4: Illustration of the ion detector components and ion counting process.

10.2 Literature review - applications of ion imaging and experimental techniques

A computer literature search on the ion imaging technique reveals hundreds of publications, including several reviews[189,194–196] indicating that the technique has become firmly established as a method for investigating chemical dynamics. The vast majority of the papers published thus far refer to photodissociation or 'half collision' processes of simple 2 - 6 atom molecules. The ion imaging technique has not yet become firmly established as a method for chemical reaction investigation, although the potential for investigation of chemical reaction is enormous, particularly for ion–molecule reactions and reactions of otherwise unstable species.

10.2.1 Ion detection

Unlike the crossed molecular beam experiments that measure ionization cross-sections by simply collecting the ion signal on a channeltron multiplier or microchannel plate and converting this to a cross-section by a normalization procedure, there are some very important technical considerations associated with a position sensitive ion imaging experiment.

MCP operation

Developed in the 1960's as an image intensifier, the microchannel plate has found widespread use as an ion detector. There are several features of MCP's that make them attractive as ion detectors. They have a large active area, have a high detection efficiency, are extremely fast and have enormous gain that is very uniform over the entire active area. They are position sensitive detectors and it is this feature that makes them so attractive in the field of reaction dynamics. Up to three microchannel plates can be stacked on top of each other in a serial configuration giving a gain of up to 10^9 with a response time of about 0.2 ns. These specifications are far superior

to any solid state amplifier developed to date. The main problems with microchannel plate detectors are non-linear gain, and non-linear response to ions of different masses particularly protons.[54,55]

There are several possible methods that can be used to gain position sensitive information from a microchannel plate. These include optical methods, interpolative anode arrays, resistive anodes and wedge and strip anodes. Optical methods (ion imaging) systems feature excellent position resolution and the ability to detect multiple ion events simultaneously. Typically the output of the microchannel plate is coupled to a phosphor and a charge coupled device (CCD) or charge induction device (CID) camera for image collection and analysis. Quantitative analysis using optical microchannel plate systems may be difficult because behavior of the microchannel plate, phosphor and camera need to be well understood, Normalization procedures are usually required to determine appropriate 'machine functions' which incorporate these factors. The biggest limitation to optical systems is speed; the clock cycle of the experiment is limited by the clock cycle of the camera, typically 32 frames per second. Further details on the other methods have been detailed in Smith.[197] Consideration also needs to be given to the selection of the phosphor screen. The important features of the phosphors are decay speed, wavelength emission and quantum efficiency.

10.2.2 Imaging

Imaging is a large branch of science and electrical engineering in its own right. An image contains a massive amount of data per frame, which may be extracted without the need for complex data decoding algorithms, making this ideal for digital camera applications as well as specialist scientific applications such as ion imaging. An understanding of some of the basic concepts of imaging is an important requirement for this research. The camera used in the present work was a Photonic Science custom built 640 × 480 row pixel CCD unit. A video camera acquires an image by taking a sample of light, focusing it through an optical lens assembly and passing it onto a CCD chip, where a small potential difference is generated.

CCD gating and image intensifier operation

CCD devices were developed in the 1960's as a possible computer memory device.[198] Although they were never successful for this application the CCD device has found universal application in video and digital imaging systems, with the number of pixels per CCD growing rapidly every year. The CCD is a silicon-based device that converts ultra-violet, visible or infra-red photons into a small electrical potential. Each pixel is a photodiode, which is a reverse biased P-N junction. When a photon of light strikes the surface an electron/hole pair is formed. Provided the electron/hole pair is formed in the diffusion region of the P-N junction, the electron will move down the potential barrier and the current will increase. The P-N junction must be very close to the active surface of the photodiode, typically 0.1 μm.[199] Ideally the P-N junction band gap value of the semiconductor crystal must be very similar to the energy of the incoming photon to maximize the quantum efficiency of the detector. If the photon energy is too high then it will pass through the diffusion region, and if the energy of the photon is much lower than the band gap value then no electron/hole pair will form.

A CCD chip may contain millions of photodiodes on a disk a few centimeters in diameter. Because each channel is discrete, a two dimensional potential map which represents the photon density that is sampled by the camera lens is generated.

The feature which enables the data to be removed from the CCD device is a large array of shift registers, as illustrated in Figure 10.5. Electrons from the photodiode are stored in a potential well. When an appropriate potential is applied to the well using a parallel shift register the electrons flow from that well to the well in the (n-1)th row. A control gate sets the maximum exposure level, which may be adjusted according to the light levels that are being sampled. A row of potential wells below the first photo-active row of the CCD, called the serial shift register, moves the data sequentially from left to right through a digital to analogue converter, which then forms the basis for each row of the image. These rows can then be reconstructed by a computer or television monitor. A secondary amplifier may be used to amplify the analogue signal further.

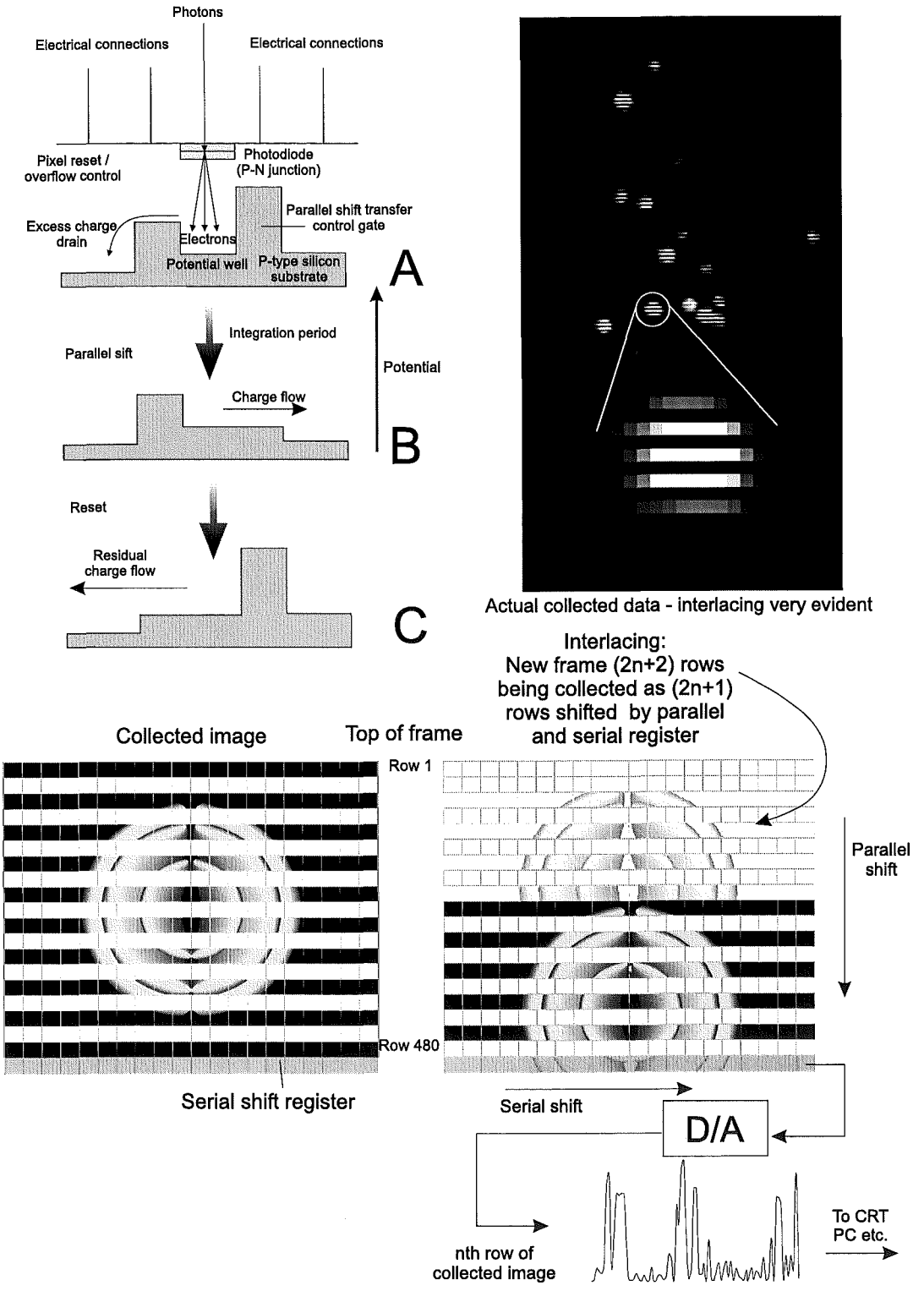

Figure 10.5: Schematic of CCD and imaging operation.

The analogue signal coming from the camera has two components. A regular -0.3 V square wave pulse at a rate of 15360 Hz which is about 2 μs wide controls the shift registers. The start of each pulse indicates a new line in the image, and the first cycle of 240 pulses generates the $(2n + 1)$ line series, where n = 0,1,2... After the shift register points to the 479th line a series of five wider (22 μs) negative going pulses are transmitted. These pulses reset the CCD and a new image is collected containing the $(2n + 2)$ series of rows. This method of 'painting' the image is known as interlacing. Superimposed in the region between the narrow negative going pulses is the analogue signal which corresponds to the intensity of the pixel across the line on the screen.

Approximately 30 ms are required to paint the whole picture to the output device, or 15 ms to paint the odd or even lines. A consideration with ion imaging is that the image changes very rapidly compared to most other imaging applications. A side effect of this is that the interlacing is very evident in the final image. Figure 10.5 shows schematically how the interlacing procedure works. During the time it takes for the shift register to move the data that forms the odd lines off the CCD, an image composed of even lines is being developed. The image collected using the camera in this work is an 8 bit gray scale image. The first image is stored in an array of numbers which range from 0 to 255 (depending on intensity), subsequent images are then added to the first image. Each element in the array is divided by the number of images that have been collected. The resulting image is displayed on a computer monitor.

Time of flight mass resolution is achieved using CCD exposure control gating. This architecture involves a reversal of the steps involved in regular image collection. Each photo-diode has a control gate and a transfer gate. Referring to Figure 10.5, charge generated by incoming photons flows into the charge drain as (Figure 10.5(C)) until exposure begins, when potential is applied to the control gate such that the CCD forms the usual potential well for that pixel (Figure 10.5(A)). After exposure the transfer gate opens and the charge flows into another well where it is stored until the image is ready to be lifted from the CCD. (Figure 10.5(B)) The charge drain is then reopened until the next exposure is required.

The camera used in the present work contains an image intensifier, which is a photocathode coupled to another microchannel plate - phosphor sandwich. The light from the phosphor is transmitted down a tapered fiber optic bundle onto the CCD device. The gain of the intensifier is controlled by the voltage across the microchannel plate and phosphor sandwich. In the camera used for the present work the phosphor is a proprietary fast phosphor, whereas in most intensified cameras, such as military night vision cameras, the phosphor used is typically a much slower P-20 type.

Other considerations

The primary considerations with ion imaging processes are the same as those with more traditional signal collection, namely:

1. the intensifier, phosphor and amplifiers need to be very fast;
2. the gain needs to be sufficient and the response of the detector assembly needs to be linear;
3. the noise has to be kept to a minimum;
4. the spatial and temporal resolution need to be sufficient to meet the requirements of the system under study;

Another important consideration is the effect of stray magnetic and electric fields on the ion trajectories. Sufficient screening of extraneous fields must be applied so that fields from the charged particle source and collector do not affect the ion trajectories.

10.3 Ion imaging at Canterbury

The ion imaging assembly was added to the molecular beam machine in 1999. As chemists it was recognized that the scope for this technique was enormous for investigation of chemical reaction dynamics. Of particular interest were the Walden inversion

(S_N2) reactions because of the capability of the molecular beam machine to orient symmetric top molecules. Before embarking on the study of ion molecule reactions it was thought prudent to investigate electron–molecule interactions first, primarily because of previous experience with these collision processes, and also to further investigate electron impact ionization asymmetry.

Initially space focusing was used to project the expanding ion sphere onto the imaging detector, and the camera frame rate was set to 100 Hz. Mass resolution was sufficient to resolve Ne, Ar, and N_2 mass peaks with the photomultiplier tube indicating that gating of the camera assembly should enable the resolution of individual mass peaks. During this early phase the microchannel plate in the ion section suffered from a breakdown. After a replacement detector had arrived, the first of a series of problems was recognized; only about 20% of the collected frames from the camera contained data. There were two reasons for this; the frame rate of the camera was 32 Hz not 100 Hz, and the Matrox Meteor frame grabber card (not triggerable) and computer that were used for data collection were of insufficient speed. These problems were rectified when the molecular beam/electron beam repetition rate was matched to the camera frame rate using the microchannel pulse generator, a new computer and a Picolo Industrial (triggerable) frame grabber card were installed. During this time it was also decided that velocity imaging would be used because of the increased spatial resolution offered by this technique.

The time-of-flight resolution however was still insufficient to collect any one particular fragment ion exclusively. This was due to the replacement P-47 phosphor (Y_2SiO_5:Ce) not being quite as fast as the original P-47 phosphor.

The flight tube was subsequently lengthened and three Einzel lenses were added to it. After this some promising time-of-flight data and images were collected for the electron impact ionization of argon (Ar^+), oxygen ($O^+ + O_2^+$) and sulfur hexafluoride (SF_5^+), to be analyzed in more detail in Chapter 12. Unfortunately technical problems began to plague us continuously after this time. Problems started when the microchannel plate began to discharge again. At first it was only a small spot on the edge of the

detector, but quickly grew to a point where most of the channels had collapsed. New detectors were ordered but on arrival these were also cracked across the surface. New detectors were replaced under warranty but when these arrived they were also damaged and had to be replaced. All these problems took the best part of six months to rectify during which time the electron gun and ion guns described in Chapter 9 were designed, built and characterized, the work on the deconvolution of the arrival time distributions was done and a modification to the beam machine so that the nozzle skimmer distance could be adjusted from the outside of the machine was carried out.

Shortly after the arrival of a working detector two of the turbo molecular pumps seized and had to be sent away for repairs, meaning that a sufficiently good vacuum could not be maintained in the scattering chamber to make use of the new detectors. A change in configuration was then applied to the beam machine, which involved mounting the microchannel plate detector along the molecular beam axis in an attempt to boost signal levels and time of flight resolution, which had become so bad after the arrival of the new detector that it was impossible to resolve even heavy ions such as Br^+ from the strong proton and water signals due to the background gas. The on-axis measurements showed strong signal enhancement compared to the off axis configuration, but the time of flight resolution was still very poor. The axial configuration also had the further disadvantage of precluding oriented molecule work.

The machine was returned to the original configuration and a new extractor-repeller plate assembly made from a heavier grade of stainless steel was installed in an effort to eliminate inhomogeneities in the electric field. This also showed little improvement of the time of flight mass spectrum, the apparent cause of which was the phosphor that formed part of the new microchannel plate assembly. This phosphor was a much slower P-20 (Y_2O_2S:Eu) type, with a decay time of 60 ms to 1% of the original intensity.

A time of flight analysis using equations (10.15) and (10.16) has shown that, assuming that peaks are partially resolvable after 0.01 ms, the m/z ratio of the target species would need to be 166 amu.

An unsuccessful attempt to measure time of flight peaks directly using the current flowing from the phosphor as the electrons from the microchannel plate stack collided with it was made using a Dallas Semiconductor MAX4106 fast operational amplifier. Although this method has been shown to be successful previously,[200] in the present case the failure of this approach has been attributed to high noise and possibly the lack of conductive coating on the P-20 phosphor.

10.4 Methods for reconstructing three dimensional distributions from two dimensional images

In order to recover three dimensional scattering data from the two dimensional projection that is the ion image, an experimental or mathematical recovery technique needs to be applied to the image. The most popular method is the inverse Abel transform method, although other methods are gaining recognition due to problems associated with the inverse Abel transform method. An important requirement for applying the inverse Abel transform is that the image has cylindrical symmetry about the vertical axis. Ion images have rings because of a 'pile up' of particles on the detector at the maximum radius that can be reached for a particular velocity as illustrated in Figure 10.6.

10.5 Inverse Abel transform

The Abel inversion method treats the two dimensional image as a series of independent one dimensional inversion problems.[c] Every line is treated as a projection of a two dimensional slice through the three dimensional image perpendicular to the symmetry axis. The image recorded by the camera is a series of one dimensional lines of varying intensity. The intensity of the three dimensional velocity distribution of the product

[c] each raster line of the collected image is inverted independently of the other raster lines.

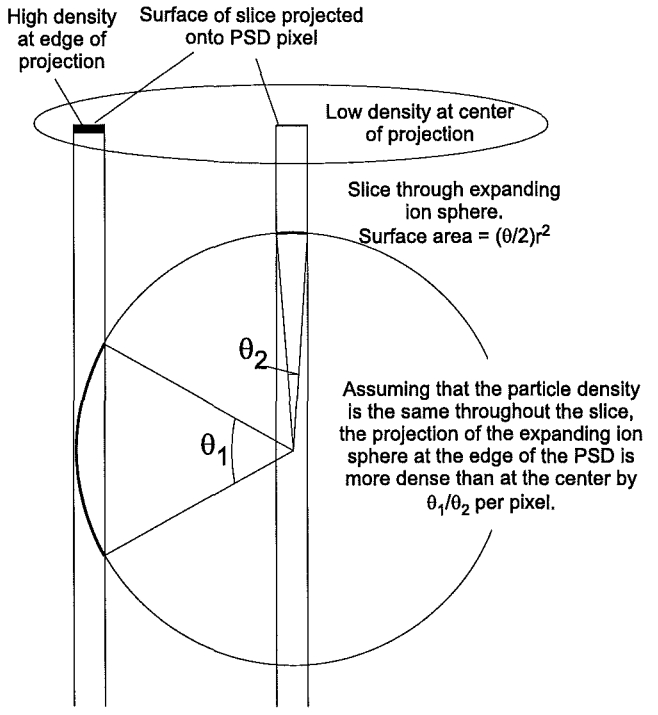

Figure 10.6: Projection of a slice through the center of an expanding ion sphere on to a position sensitive detector (PSD). This slice represents a single row on the image. For isotropic scattering the projection would be smaller at each row of the image but would otherwise have the same shape.

ions can be written as $i(x, y, z)$, where the y axis is taken as the axis of symmetry, and z axis is the projection axis or time-of-flight axis of the product ions. The image recorded by the camera can be written as:

$$p(x, z) = \int_{-\infty}^{\infty} i(x, y, z) \mathrm{d}z \tag{10.18}$$

The inverse Abel transform considers one single row of a recorded image at a time. A single row of the image is given by $f(x, y_0)$, taken along the $x-$ axis at $y = y_0$. Since the ion product distribution is cylindrically symmetric about y;

$$\begin{aligned} f(x) &= \int_{-\infty}^{\infty} s(\sqrt{x^2 + z^2}) \mathrm{d}z \\ &= 2 \int_{0}^{\infty} s(\sqrt{x^2 + z^2}) \mathrm{d}z \end{aligned} \tag{10.19}$$

where $s(x,z)$ is a slice through the three dimensional distribution perpendicular to the symmetry axis taken at y_0. Transforming to polar coordinates, $f(x)$ can be written as

$$s(r) = -\frac{1}{\pi}\int_r^\infty \frac{\mathrm{d}f(x)/\mathrm{d}x}{\sqrt{x^2-r^2}}\mathrm{d}x \tag{10.20}$$

equation (10.20) introduces a problem in practice because of the singularity at $x = r$, the lower limit of integration. This integrand also has the effect of magnifying noise in the recorded image. The singularity can be treated by taking the Fourier transform of equation (10.19):

$$\mathcal{F}\{f(x)\} = \int_{-\infty}^{\infty}\int_{-\infty}^{\infty} s(\sqrt{x^2+y^2})\mathrm{e}^{-2\pi i x q}\mathrm{d}x\mathrm{d}y, \tag{10.21}$$

and noting that the definition of the zero–order Bessel function of the first kind, J_0, is given by

$$J_0(z) = \frac{1}{2\pi}\int_0^{2\pi} \mathrm{e}^{-iz\cos\theta}\mathrm{d}\theta. \tag{10.22}$$

transforming to polar coordinates and substituting this into equation (10.21) yields

$$\mathcal{F}\{f(x)\} = 2\pi\int_0^\infty rs(r)J_0(2\pi rq)\mathrm{d}r. \tag{10.23}$$

The right hand side of this equation is the zero-order Hankel transform of $s(r)$. Since the Hankel transform is identical to its inverse, the original distribution $s(r)$ can be recovered by taking the inverse Hankel transform of the Fourier transform of the recorded image:

$$\begin{aligned} s(r) &= \mathrm{H}[\mathcal{F}\{f(x)\}] \\ &= 2\pi\int_0^\infty qJ_0(2\pi rq)\left[\int_{-\infty}^{\infty} f(x)\mathrm{e}^{-2\pi xq}\mathrm{d}x\right]\mathrm{d}q \end{aligned} \tag{10.24}$$

Because of the centerline noise due to the inverse Abel transform and the requirement that the images are symmetrical about the time-of-flight axis, there has been a

shift away from the inverse Abel transform method, although these reasons may be unjustified in many cases. As with any Fourier transform method the quality of the output data depends on the quality of the input data. An extensive range of smoothing techniques may be applied to the images in order to improve signal-to-noise ratios. Appendix **H** contains a summary of some of the mathematical smoothing procedures that may be applied to collected images. In the present work only the Abel inversion method has been used, however other methods have been considered and the following sections describe some of the latest developments in this area. As a future exercise it would be prudent to implement some of the more reliable methods discussed below as a cross-checking mechanism.

10.6 The iterative procedure.

This is a relatively new procedure introduced by Vrakking.[201] This method uses an iterative algorithm to reconstruct the three dimensional angular and velocity distribution for a cylindrically symmetrical image. The method is based on the similarities between the two dimensional radial distribution and the recovered two dimensional velocity distribution, and the two dimensional angular distribution and the recovered three dimensional angular distribution. The advantage of going straight from the measured two dimensional to the recovered three dimensional distribution is that the noise, usually projected onto the centerline with the Abel inversion method, is projected toward the center of the image, where it is usually less of a problem. The method involves writing the three dimensional velocity and angular distribution as the product of a velocity distribution and a velocity dependent angular distribution. The normalization of the three dimensional distribution is carried out by integrating over the velocity distribution dv and the angles of the radial distribution θ. Similarly the two dimensional image is written as a product of the radial distribution and the angular distribution, and also normalized. The three dimensional distribution is approximated by the measured two dimensional distribution and transformed into two dimensions.

This is compared to the measured two dimensional distribution and a correction is applied, which is proportional to the difference between the measured and calculated two dimensional distribution. The process is then repeated with the calculated two dimensional distribution, yielding a three dimensional distribution with a projection closer to the two dimensional distribution. A new correction is applied and the process is repeated until the convergence objective is achieved.

10.6.1 Three dimensional distribution.

The three dimensional velocity distribution $p(v_x, v_y, v_z)$ can be written as the product of the velocity distribution $p_1(v)$ and angular dependent velocity distribution, $p_2(v, \theta)$.

$$p(v_x, v_y, v_z) = p_1(v) \times p_2(v, \theta) \tag{10.25}$$

Normalizing the integral over all angles θ and all velocities v gives

$$2\pi \int \int p_1(v) v^2 \times p_2(v, \theta) \sin\theta \mathrm{d}\theta \mathrm{d}v = 1 \tag{10.26}$$

Vrakking leaves the velocity distribution as is and changes the $p_2(v, \theta) \sin\theta$ term to satisfy equation (10.26). The conditions for θ are as follows:

$$0 \leq \theta < \pi \quad \text{for } x > 0 \tag{10.27}$$

$$\pi \leq \theta < 2\pi \quad \text{for } x < 0 \tag{10.28}$$

10.6.2 The two dimensional distributions.

The experimental two dimensional image $s_{\mathrm{exp}}(x, y)$ can be written as the product of the two dimensional radial distribution, $s_{1,\mathrm{exp}}(r)$ and a radially dependent angular distribution, $s_{2,\mathrm{exp}}(r, \alpha)$

$$s_{\mathrm{exp}}(x, y) = s_{\mathrm{exp}}(r, \alpha) = s_{1,\mathrm{exp}}(r) \times s_{2,\mathrm{exp}}(r, \alpha) \tag{10.29}$$

Normalizing the integral over all angles α and all radii r gives

$$2\pi \int \int s_{1,\mathrm{exp}}(r) r \times Q_{2,\mathrm{exp}}(r,\alpha) \mathrm{d}\alpha \mathrm{d}r = 1 \tag{10.30}$$

Similar to the three dimensional case, Vrakking leaves the radial distribution unchanged and changes the $s_{2,\mathrm{exp}}(r,\alpha)$ term to satisfy equation (10.30). Similarly the conditions for α are as follows:

$$0 \leq \alpha < \pi \quad \text{for } x > 0 \tag{10.31}$$

$$\pi \leq \alpha < 2\pi \quad \text{for } x < 0 \tag{10.32}$$

10.6.3 The iterations

From the equations (10.30) and (10.26) and the choice of the normalization terms it is possible to determine estimates and corrections for $p_1(v)$ and $p_2(2,\theta)$. For the zeroth iteration, $i = 0$, the following relations are used as initial conditions:

$$\begin{aligned} p_{1,i=0}(v) &= \frac{s_{1,\mathrm{exp}}(r)}{2\pi r} \\ p_{2,i=0}(v,\theta) &= s_{2\mathrm{exp}}(r, \alpha = \theta) \end{aligned} \tag{10.33}$$

It is only possible to apply this assumption because of the similarity between the two dimensional projection of the three dimensional product distribution and the actual three dimensional product distribution. The velocity, v and the radius, r, are related to each other through time:

$$r = c_0 v t \tag{10.34}$$

where c_0 is a constant, typically close to 1, which depends on the electric field geometry of the experiment.[192,201] The three dimensional and two dimensional distributions are measured or calculated in terms of the dimensionless camera pixel unit so that the product $c_0 t$ is set to unity.

Based on the assumption in equation (10.33), a three dimensional image may be calculated from the experimental two dimensional image. From the calculated three dimensional image, a new two dimensional projection can be calculated by maintaining the x and y coordinates for all the points and setting the z coordinates to 0, and comparing the new two dimensional projection to the experimental image. This procedure is then repeated by including the difference between the experimental image and the calculated image, and making this difference proportional to the correction factor applied for the next iteration. Convergence may then be achieved.

$$P_{1,i}(v) = P_{1,i-1}(v) - c_1 \left[\frac{Q_{1,i-1}(R) - Q_{1\exp}(R)}{2\pi R} \right] \tag{10.35}$$

$$P_{2,i}(v,\theta) = P_{2,i-1}(v,\theta) - c_2 \left[Q_{2,i-1}(R, \alpha = 0) - Q_{2,\exp}(R, \alpha = 0) \right] \tag{10.36}$$

The constants c_1 and c_2 can be chosen to have any value. The smaller the value the smaller the change between the $(i-1)$th and ith image for each iteration, thus extending the time taken to reach a solution. If large values of c_1 and c_2 are chosen then the iteration step will be large and the solution will not be a true representation of the final image. If very large values of c_1 and c_2 are chosen then there is a risk of finding a numerically divergent solution. The definition of small and large in this case will vary on the particular application of this technique and the quality of the input image. Vrakking found that choosing c_1 and c_2 as approximately 2.0 and 1.0 respectively typically leads to a satisfactory solution in approximately 3 minutes using a 950 MHz personal computer.

One method that allows for the calculation of a solution in a shorter space of time is to use a solution that is more representative of the final solution as the input image. This can be achieved by solving the inverse Abel transform first and using the result as the input. Whether this is a favorable method depends on the quality of the Abel inverted image compared to the original two dimensional image. This method of improving the quality of the Abel transform by reconstructing the image and iterating to find a cleaner solution is probably the best application of the iterative procedure,

because although susceptible to noise the Abel transform technique does guarantee a unique mathematical solution.

10.7 Slice imaging

Slice imaging is a further method of determining three dimensional scattering data from the two dimensional projection. This differs from the methods described above in that it uses an experimental technique rather than a mathematical technique to determine the three dimensional velocity distribution directly. The ion products formed by a laser or electron beam colliding with a molecular beam expand on the surface of a sphere, with the degree of expansion depending on the available energy and orientation of molecule. Until the ions hit either the detector or some other surface in the scattering chamber or flight tube they will continue to expand. A slice through the center of the expanding ion sphere reveals the three dimensional velocity distribution of the products. By turning the detector on at exactly the appropriate moment for a very short period of time it is possible to image only the center slice of the expanding ion sphere, thus measuring the differential cross-section directly. Unlike the Abel inversion and iterative method an axis of symmetry in the collected image is not a requirement.

This technique was introduced by Gebhardt *et al.*[202] who used an experimental apparatus where ions were created in a homogeneous extraction field that accelerates them onto a microchannel plate detector. A 45 cm field free time-of-flight tube separated the products on the basis of their m/z ratio and allowed the ion sphere to expand. Using simulations it was shown that Δt, the temporal spread of the 'ion cloud', is directly proportional to the photofragment velocity with the slope proportional to the distance between the extraction plate and the location of ion formation.

If a constant DC extraction field is applied at the ion formation region then a crushing of the ion sphere occurs, This may be avoided if an extraction delay is introduced providing a means of controlling the size of the ion packet. A total temporal spread of

the ion packet of about 400 ns is sufficient to get a well resolved center slice of the ion sphere, which is equivalent to the inverse Abel transform in the infinite limit.

The advantages of the slice imaging technique include: centerline noise (due to the inverse Abel transform) or center point noise (due to the iterative procedure) is not present; the axis of symmetry about the y axis is no longer a prerequisite; by tuning the electric fields it is possible to image the fast or slow ion products providing a means for time-of-flight mass separation; an increase in extraction delay may allow the fast products to expand beyond the edge of the detector, but the slow products can be still be imaged without any loss of information. However there are also some disadvantages of the slice imaging technique: the signal level is significantly reduced because only a small part of the total signal is collected; the collected slice might only be 1% of the total ion signal; very fast and very clean, square voltage pulses must be applied to the microchannel plate stack, so that they only amplify the ion signal at exactly the correct time. This technique can still make use of the ion counting and velocity mapping methods. A schematic of the technique is shown in Figure 10.7.

10.8 Other methods

There are several other methods that have been used for image reconstruction, but these do not necessarily guarantee a unique solution. Conceptually the simplest methods are forward simulation methods. In these methods machine parameters are entered into a computer simulation of ion trajectories, as well as a possible solution to the scattering problem. An image is then calculated and projected onto a plane, which represents the detector. The collected image is compared to the calculated image until a satisfactory agreement between the calculated and measured image is obtained. These methods are very computationally intensive and require complete modeling of the machine parameters which may be very difficult to perform.

A further method, developed recently by Bass *et al.* involves calculating the Fourier

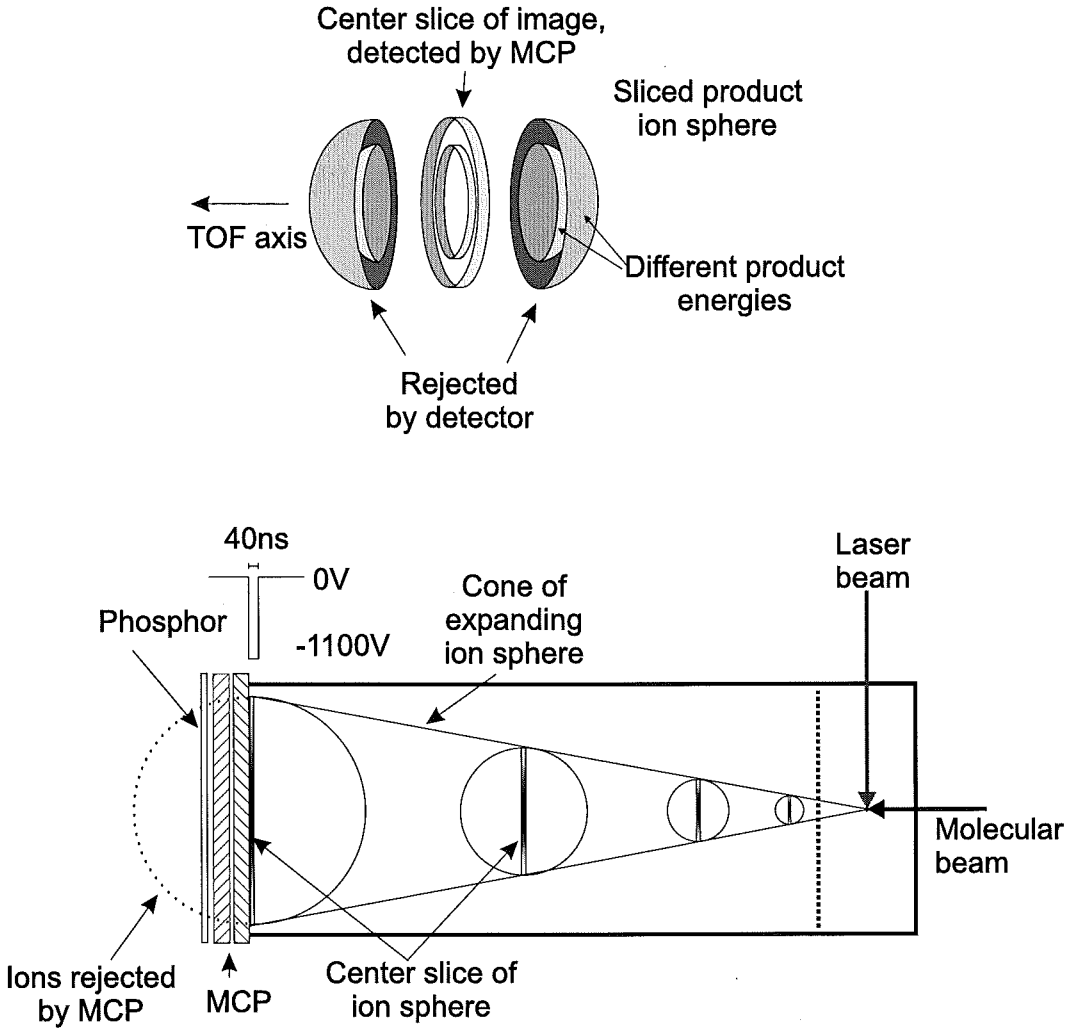

Figure 10.7: Schematic of slice imaging technique.

moments of the ion trajectories.[203] This method has the advantage of being able to reconstruct three dimensional product distributions for non-Abel invertible images. It is however a fitting procedure, and as such a unique analytic solution is not guaranteed. The method is particularly applicable to pump-probe photolysis reactions, because different pump-probe propagation and polarization configurations can be taken into account. The method applied a genetic fitting algorithm to carry out the analysis.

Yet another method uses a 'peeling' method to recover the scattering pattern.[190] In this method the equations of motion of the ion in the extraction field are solved and ion counts from high energy ions that contribute to the ion signal in the center of the

image are 'peeled' away from the image by considering the ion signal at the outermost ring of ions at the detector. Iterations progress from the outside of the image to the center of the image until all of the kinetic energies of the fragments have been 'peeled' away.

In summary there is no shortage of methods available to recover the three dimensional scattering data from the two dimensional projection of an image. The desirable qualities of any method applied are:

1. a unique and valid solution to the problem;
2. low noise introduction;
3. simple to apply and implement;
4. fast processing time.

Each of the methods described above is suited to different experimental conditions and systems under study, and care needs to be applied in choosing the most appropriate method. These methods, as well as new methods, are in continual development and it remains to be seen which method will ultimately become the most widely accepted technique for scattering pattern analysis.

11. SIMULATIONS

Simion[10] simulations were carried out in order to model the behavior of the ion products in the crossed molecular beam machine. The previously determined kinetic energy release values for the dissociative ionization of oxygen by electron impact reported by Stockdale and Delanau[162] were used as initial input values for the simulations described below. *Simion* is an ion trajectory simulation package[a] that involves the modeling of the focusing elements using a simple drawing package. Voltages are applied to the elements and an input file containing information on the kinetic energy distributions and location of the ions' formation are loaded. The equations of motion for each ion trajectory are solved in an iterative manner until the ion strikes one of the elements, preferably the detector. The x, y, z location of the ion at the end of its trajectory is appended to an output file and the initial conditions for the next ion are loaded. The output file can then be loaded into a spread sheet for further analysis. Experience has shown that while *Simion* provides a simplified solution to a complex physical problem, simulations do provide a useful guide to understanding machine parameters: extractor/repeller assembly, flight tube and position sensitive detector. The modeled machine components for both long and short flight tubes used in this work set up in *Simion* are shown in Figure 11.1.

[a] *Simion* version 6.0 for Windows was used in the present work

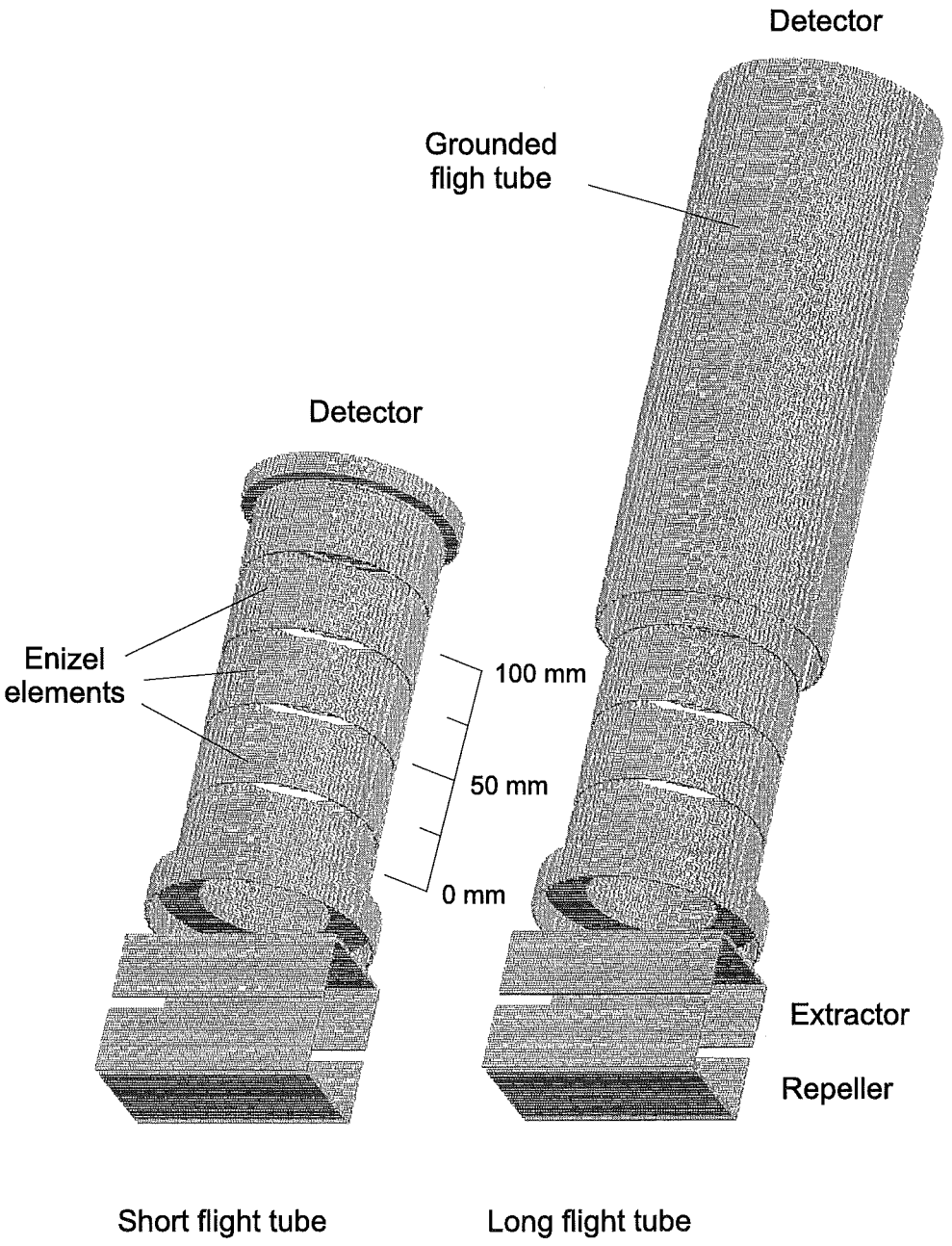

Figure 11.1: Three dimensional *Simion* model of the short and long flight tubes.

Three parameters were explored:

1. the effect of beam crossing volume on the collected images for velocity focused and space focused images;

2. the effect of changing the extractor repeller ratio, for velocity mapped images;

3. the effect of changing the absolute value of the repeller and/or extractor voltage for velocity mapped images and space focused images.

All of the simulations are centered around the reaction

$$O_2 + e^- \longrightarrow O_2^* \longrightarrow O^+(^4S) + O \tag{11.1}$$

The input ion energies were centered around thermal, 0.8 eV, 1.8 eV and 2.9 eV with a random distribution of ± 0.05 eV superimposed on the ion energies. 1000 ion trajectories have been simulated for each of the main energy steps. For a point source the velocity components are clearly resolvable and the three dimensional velocity distribution may be readily recovered from the projected image.

Figure 11.2 shows the effect on the simulated image by increasing the beam crossing volume from a point source to a 4 mm $\times$ 4 mm beam beam profiles for the electron beam and the molecular beam, modeled using the short flight tube. As the crossing volume increases from a point source to 4 mm $\times$ 4 mm beam profile the image quality degrades substantially. In the case of velocity mapped images, the three dimensional scattering pattern is still clearly resolvable in the 1 mm $\times$ 1 mm case. Blurring of the images for 2 mm $\times$ 2 mm beams may be significant in terms of recovering good quality data and in the 4 mm $\times$ 4 mm case a significant loss of resolution is observed. The simulated images obtained under space focusing conditions degrade substantially more than in the velocity mapped case when the beam overlap is increased. Simulated images using the long flight tube look very similar.

The effect of changing the extractor to repeller voltage ratio is explored in Figure 11.3, using the short flight tube. In all cases the repeller is maintained at 1 kV, the extractor is varied between 500 V and 1050 V while the the crossing volume is maintained using 1 mm diameter beams and the energy distribution that is the same as in the crossing volume simulations described above. Initially the image is inflated to fill

the microchannel plate detector and is slightly elongated but as the extractor:repeller ratio is increased to 0.7, the value reported in the literature by the authors of the velocity mapping technique,[192] the image becomes circular. As the ratio tends toward unity the image shrinks and is destroyed. Figure 11.4 show the simulation of velocity mapping from a 20 mm $\times$ 1 mm line source for thermal ions only. This simulation illustrates the power of the velocity mapping technique and is useful because it enables the direct comparison of simulated and measured images directly, as discussed in the following Chapter. In the case where the extractor voltage is larger than the repeller voltage a few of the most energetic ions escape the beam crossing region but this only represents a very small portion of the total signal. Similar results are obtained when these effects are modeled using the long flight tube.

Figures 11.5 and 11.6 relate to simulated images for the long and short flight tubes respectively under velocity mapping conditions. In all cases the short flight tube produces a larger image, under the same extractor/repeller voltage conditions. This effect may be explained by the voltage on the front end of the microchannel plate drawing the ions into the $z-$ axis, in the case of the long flight tube the ions experience this field for a longer period of time, thus shrinking the image. The very small images at low extractor voltages are caused by the loss of ions to the walls of the flight tube and extractor plate for ions that have significant velocity components in the $x-y$ plane. Only the ions initially traveling along the flight tube axis are detected. Figures 11.7 and 11.8 relate to simulated images for the long and short flight tubes under space focusing conditions respectively. Similar arguments to those above, under velocity focusing conditions, can be applied.

The advantages of the velocity mapping technique are further demonstrated by the use of a line source, with the images shown in Figure 11.9. In this case ions are produced all the way along the electron beam track. Under velocity mapping conditions many more ions are collected and the energy bands are still partially resolvable.

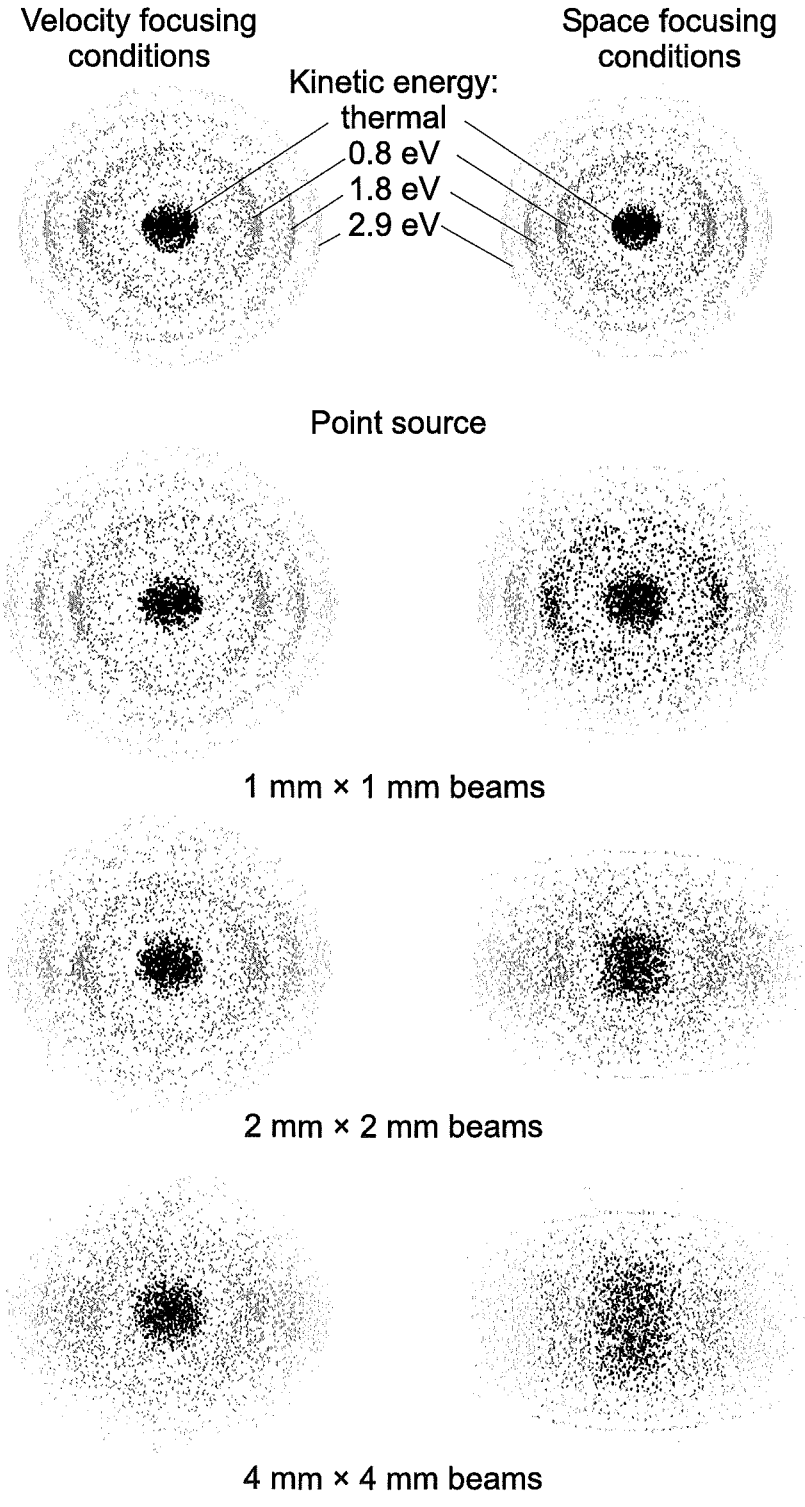

Figure 11.2: Ion image simulations for the dissociative ionization $O^+(^4S)/O_2$. The effect of increasing the beam crossing volume is explored as the ion source moves away from a point source for the short flight tube.

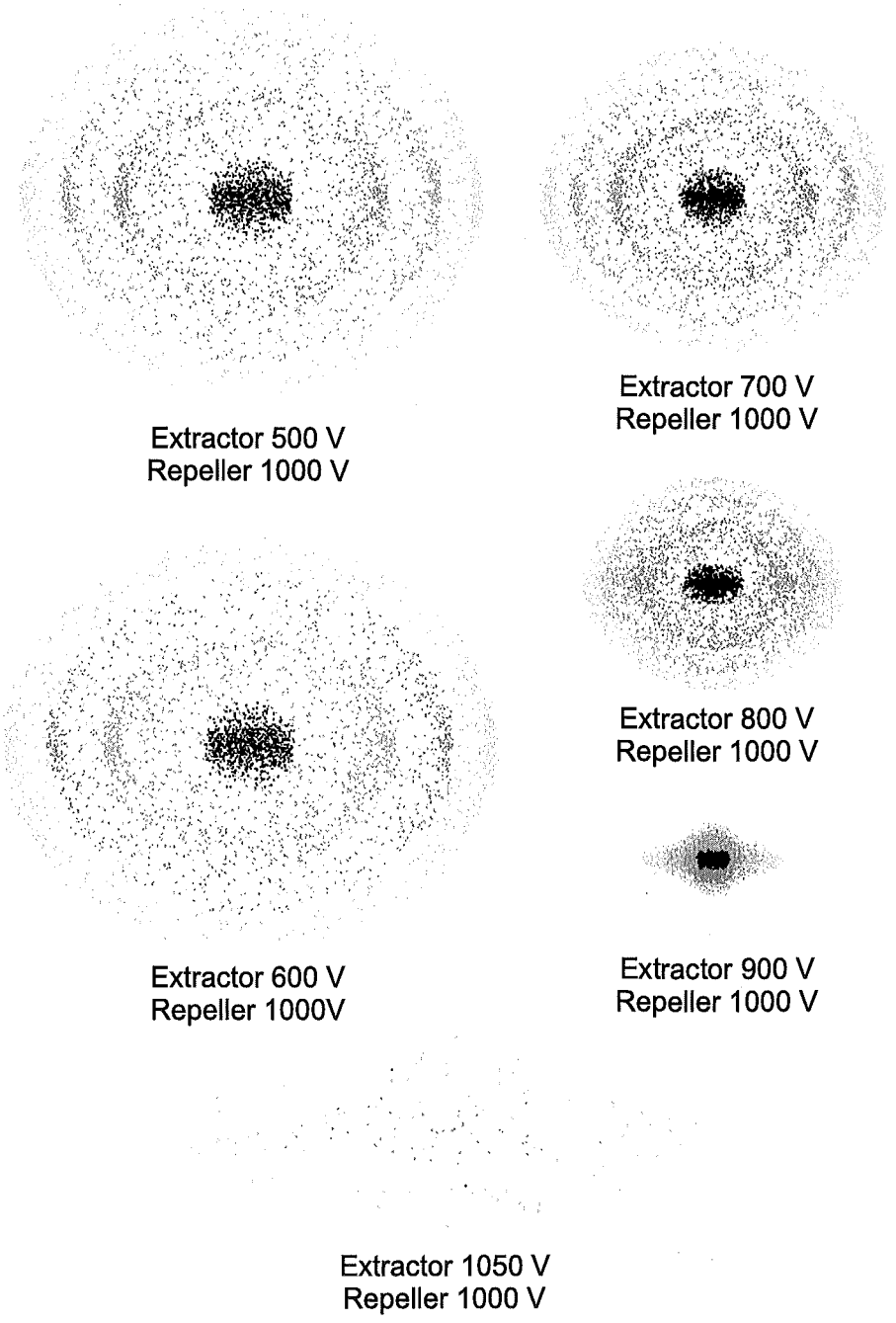

Figure 11.3: Ion image simulations for the dissociative ionization $O^+(^4S)/O_2$. The effect of changing the extractor to repeller ratio from 0.5 to 1.05 for a fixed repeller voltage of 1 kV for the short flight tube. Ions originate from a 1 mm × 1 mm point source.

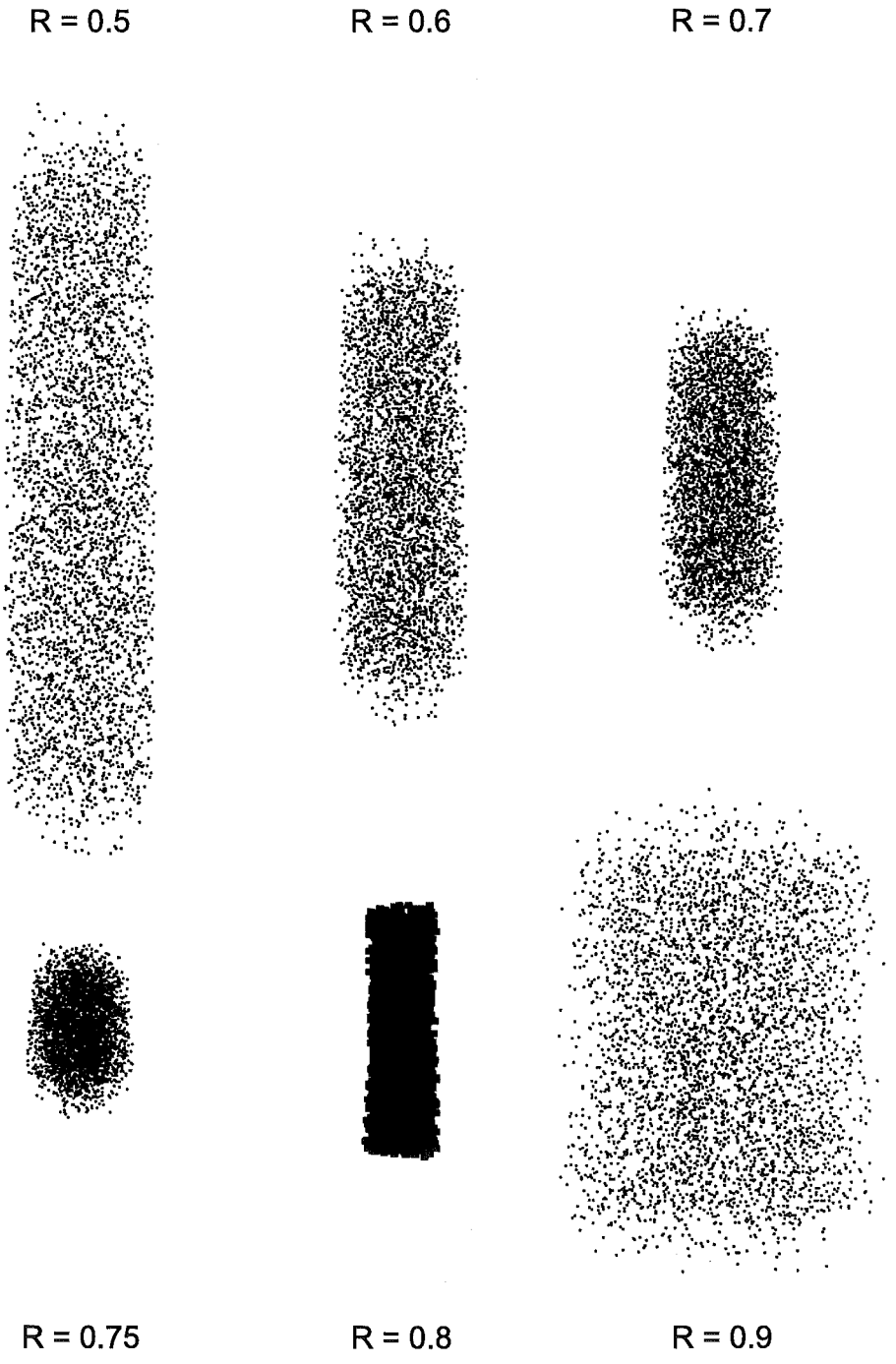

Figure 11.4: Ion image simulations for formation of thermal ions. The effect of changing the extractor to repeller ratio from 0.5 to 0.9 for a fixed repeller voltage of 1 kV for the short flight tube. Ions originate from a 20 mm × 1 mm line source.

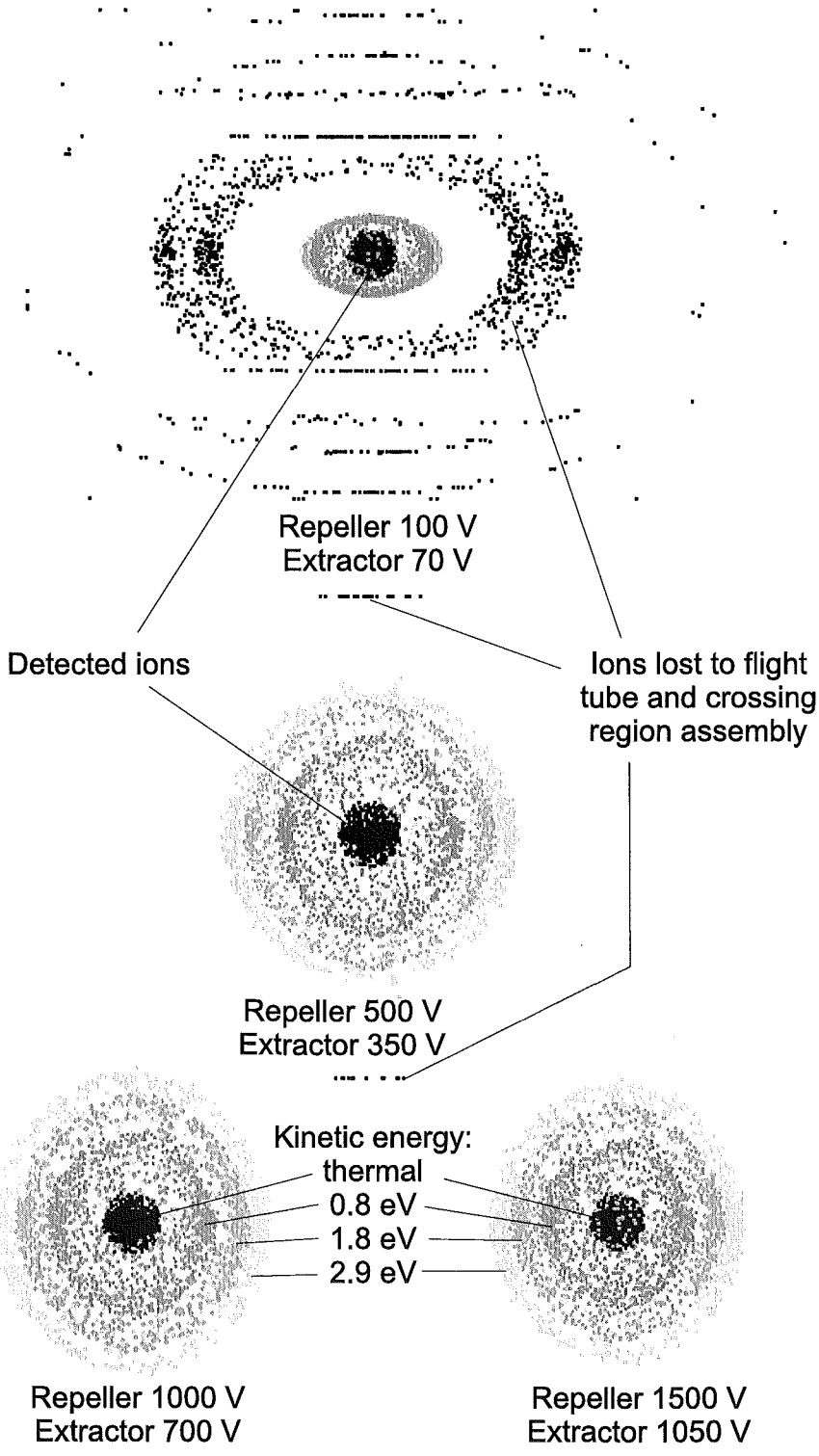

Figure 11.5: Ion image simulations for the dissociative ionization $O^+(^4S)/O_2$. Velocity focusing of the product ions for the long flight tube. The effect of changing the extractor voltage is explored while maintaining a constant extractor to repeller ratio of 0.7.

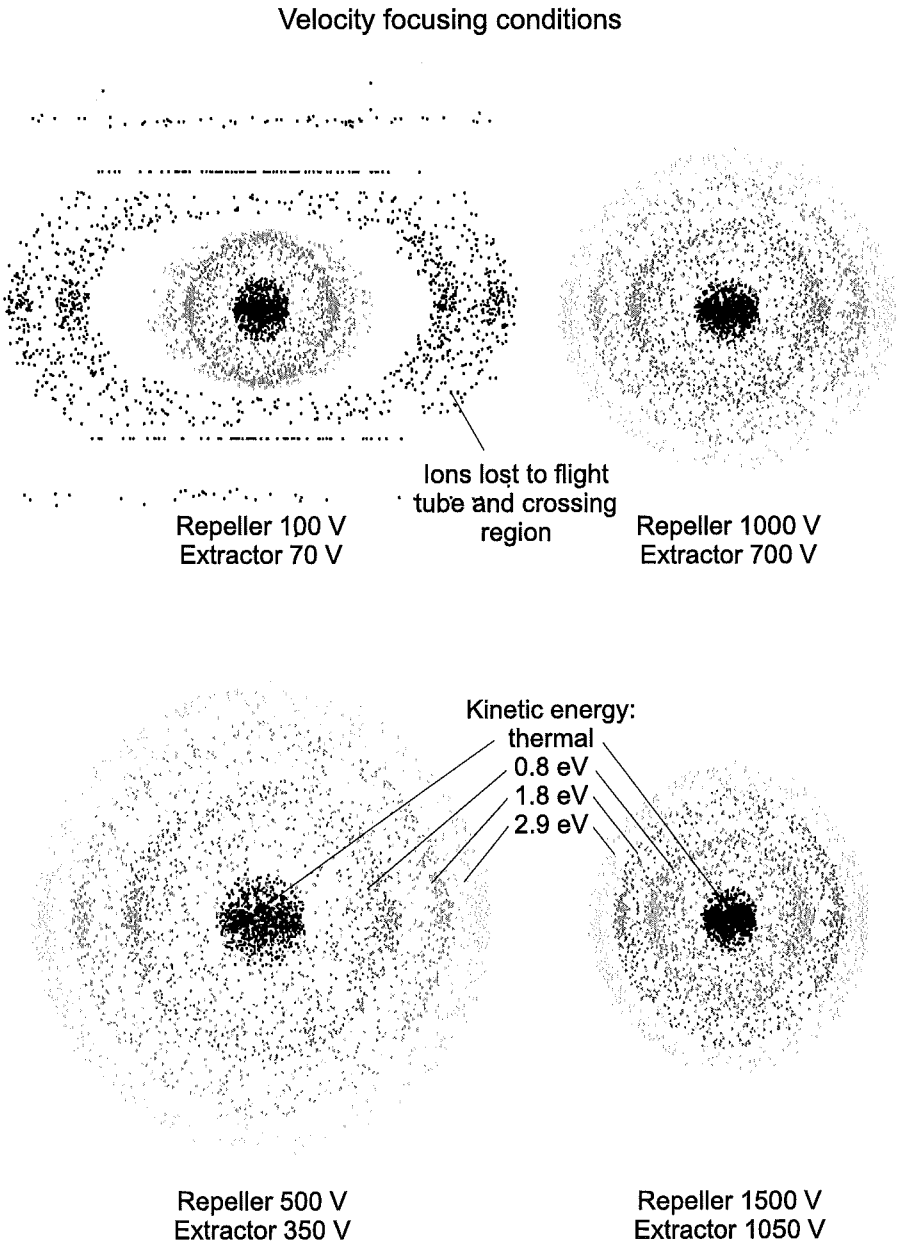

Figure 11.6: Ion image simulations for the dissociative ionization $O^+(^4S)/O_2$. Velocity focusing of the product ions for the short flight tube. The effect of changing the repeller voltage is explored while maintaining a constant extractor to repeller ratio of 0.7.

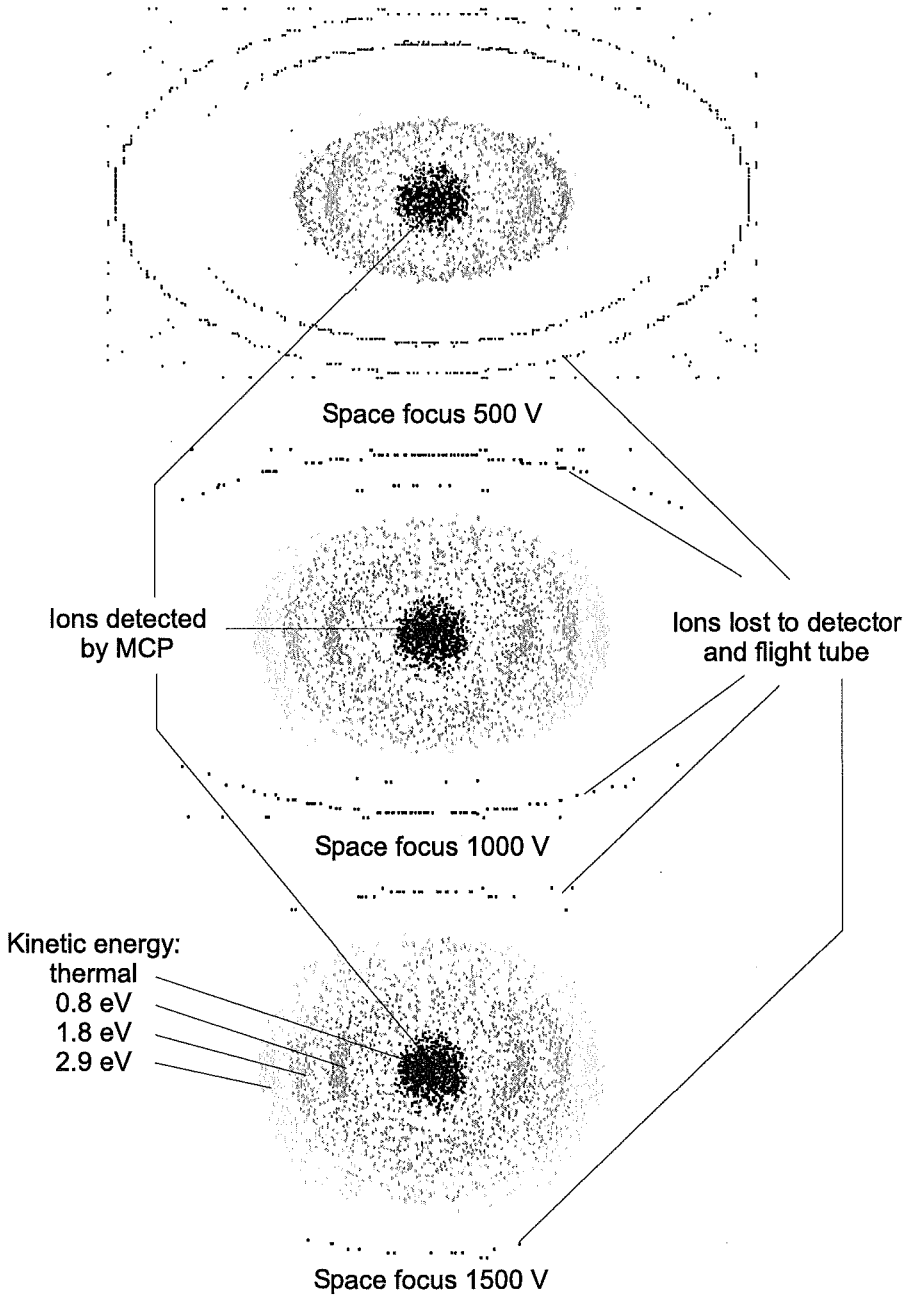

Figure 11.7: Ion image simulations for the dissociative ionization $O^+(^4S)/O_2$. Space focusing of the product ions for the long flight tube. The effect of changing the repeller is explored while the extractor is maintained at 0 V.

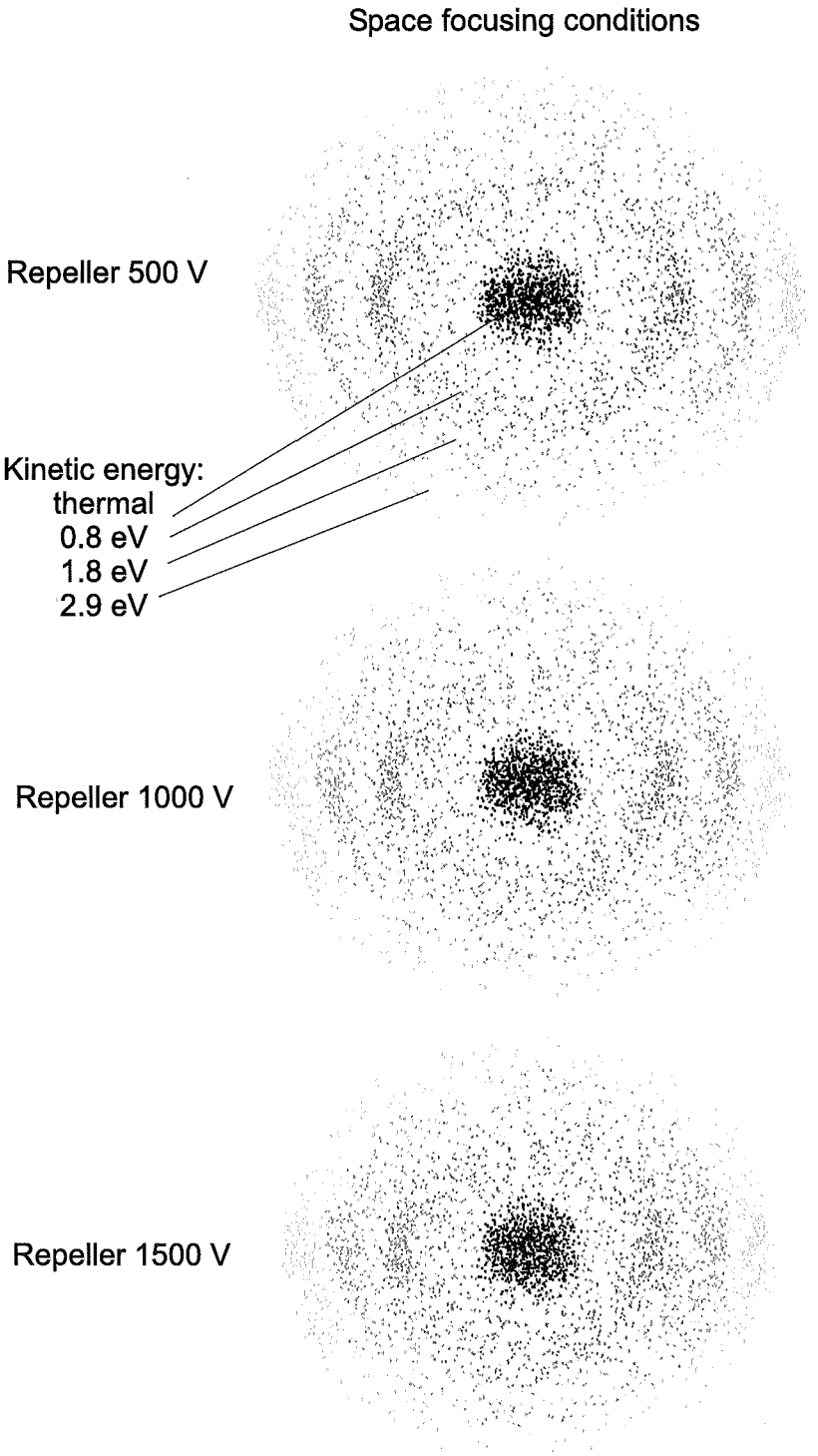

Figure 11.8: Ion image simulations for the dissociative ionization $O^+(^4S)/O_2$. Space focusing of the product ions for the short flight tube. The effect of changing the repeller is explored while the extractor is maintained at 0 V.

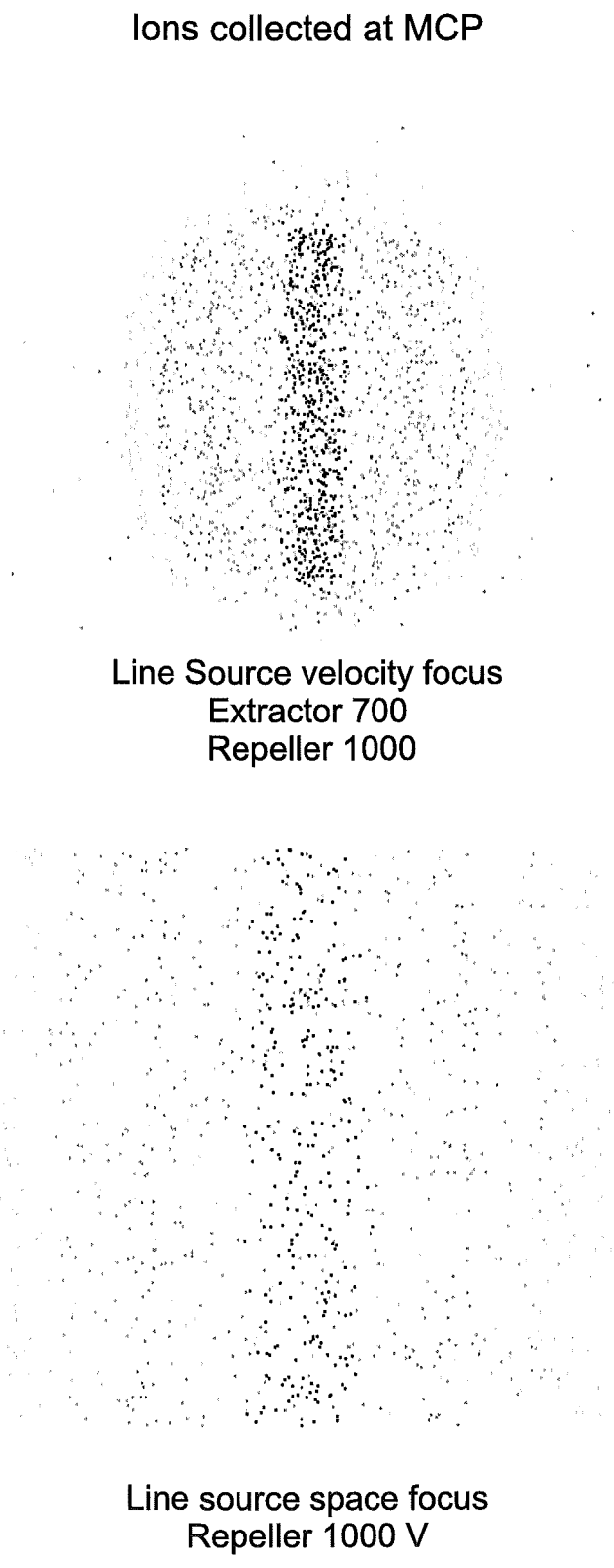

Figure 11.9: Velocity focusing and space focusing for a 50 mm line source for a beam width of 1 mm.

In summary, the simulations clearly show that the minimization of the beam crossing volume is of critical importance for crossed beam ion imaging experiments in order to prevent blurring of the image so that the three dimensional product distribution may be reconstructed. Velocity mapping provides a means to enhance the resolution of the images significantly compared to space focusing. In the case of a real molecular beam machine, the molecular and electron beams exhibit Gaussian profiles, thus enhancing the beam density in the center of the beams. This is an advantage compared to the simulated case, where the beams were of uniform density and a square cross-section. The difficulties experienced with obtaining real images were significant however and several things have contributed to this. These include field inhomogeneities in the extractor/repeller assembly and flight tube, and the ionization of background gas contributing to the collected images. The simulations confirm the basic design principles of the molecular beam machine and provide valuable insights into the limitations imposed by geometrical and electrical considerations.

12. PRELIMINARY RESULTS AND FUTURE WORK

12.1 Ion images

The images and time-of-flight data discussed below all refer to data collected with the Photonic Science MCP assembly, including the P-47 phosphor. Experiments were initially carried out with gas samples admitted to the scattering chamber in order to determine the appropriate repeller-extractor ratio for velocity mapped images. In this case the ions are produced along the electron beam track through the scattering chamber, effectively from a line source, as shown by the images presented in Figure 12.1. The experimental velocity focusing behavior is similar to the simulated images, although the simulated images indicate that the optimum ratio of extractor to repeller voltage should be slightly higher than 0.7.

The scattering chamber was charged with argon at a pressure of 5×10^{-6} Torr and the repeller set at 1.00 kV, the extractor:repeller ratio was then varied from 0.55 to 0.80. At the lower ratios, ions formed along the electron beam track between the field plates are imaged. The width of the electron beam is estimated from these images to be 2.5 mm wide. In concurrence with results from other groups[192,203] the velocity map images were optimized for a ratio close to 0.70. Crossed beam experiments were subsequently performed using a repeller:extractor ratio set to 0.70

The mass spectra in Figure 12.2 were collected from a small fraction of the light emitted by the phosphor, reflected by a 1 mm thick plate of glass set at 45° to the horizontal in the light pipe supporting the camera, into a Hamamatsu Type 5948 photomultiplier tube (Figure 7.5). Spectra were collected for helium, oxygen, argon

and sulfur hexafluoride at a repeller voltage of 500 V while maintaining a constant repeller:extractor ratio of 0.7. A plot of arrival time against the square root of the mass, Figure 12.3 shows a good linear relationship, the offset is due to the position of the trigger pulse, the extractor actually fires where the series of spikes appears in Figure 12.2 at about 1.2 μs. These experiments were carried out with a background pressure in the order of 9×10^{-7} Torr, measured with an ion gauge. The temperature was of the order of 293 K. The large proton signal is a characteristic of all of the spectra measured using this method, the microchannel plates have a much higher sensitivity to protons than to other ions. Assuming that the proton peak is twice the intensity of the H_2^+ peak, Figure 12.4, the sensitivity is ~200 times greater for H^+ because the partial cross-section of proton formation from water is approximately 0.01 times that of H_2O. This may be rationalized in terms of the enormous proton charge density compared to other ionic products.

Figure 12.5 shows the effect of changing the extractor voltage while maintaining a constant ratio of 0.7. There is a clear shift to longer arrival times for the lower extractor repeller voltages. The distance between the extractor and repeller was 50 mm, and the flight tube was 206 mm long. Assuming that the ions were formed midway between the extractor and repeller, the arrival times times under velocity focusing conditions for an ion of mass m, may be calculated from:

$$t_{\mathrm{CR}} = 25 \times 10^{-3} \left(\frac{m}{2q \times 0.3V_{\mathrm{rep}}} \right)^{\frac{1}{2}} \tag{12.1}$$

$$t_{\mathrm{FT}} = 206 \times 10^{-3} \left(\frac{m}{2q \times 0.7V_{\mathrm{rep}}} \right)^{\frac{1}{2}} \tag{12.2}$$

$$t_{\mathrm{TOF}} = t_{\mathrm{CR}} + t_{\mathrm{FT}} \tag{12.3}$$

Where t_{CR} is the flight time in the crossing region, and t_{FT} is the time that the ion spends in the flight tube. Applying equations (12.1), (12.2) and (12.3) the calculated flight time for argon for the two voltages in Figure 12.5, are 4.20 μs for a repeller voltage of 1000 V and 5.00 μs for a repeller voltage of 700 V. Measured flight times for argon are 4.6 μs and 5.3 μs in good agreement with calculated flight times, the difference

between the measured and calculated flight times is presumably due to a slight delay in the triggering electronics and a small component (~20 ns) from the time it takes for the electron beam to traverse the scattering chamber.

Using the electronic gate function on the camera to step through the delay, with a 20 ns gate it is possible to construct a time of flight spectrum, by integrating the total signal from the camera and plotting this against delay, as shown in Figure 12.4 measured under similar conditions to the argon spectrum shown above.

Figure 12.6 shows a time of flight spectrum for Ar^+ collected using the photomultiplier tube with only 50 V on the repeller, and the corresponding ion image. This image is in good agreement with the *Simion* simulations at low extractor repeller voltages. It should be emphasized that the outer rings correspond to the edge of the detector. These rings are not ions.

Figure 12.7 shows the images collected with an argon beam on and argon beam off. During image acquisition scattering chamber background pressure was maintained at a pressure of 3×10^{-8} Torr which was almost independent regardless of the beam on/off condition.

The molecular beam had been previously shown, by Hu[172] and Vallance,[88] to have a diameter close to 2.0 mm at the crossing point. A similar number of ions from the background and molecular beam are formed per electron beam shot. Because the pathlength over which ions are formed from the beam is about ten times less than those formed from the background, it follows that the molecular beam density is about ten times greater than the background gas. The beam pressure is therefore approximately 3×10^{-7} Torr.

Figure 12.8 shows ion images collected for supersonic beams of argon, oxygen, and sulfur hexafluoride under the same conditions. A wide gate camera gate was applied so that all of the ions ions were collected from each beam except for the H^+ ion from background H_2O: Ar^+ from Ar; O^+ and O_2^+ from O_2; and predominantly SF_5^+ from SF_6. The image obtained for the O_2 beam shows a high density spot in the center

corresponding to the low velocity O_2^+ ion and a series of less dense rings corresponding to O^+ ions with excess translational energy as shown in equations (12.4) and (12.5)

$$O_2(^3\Sigma) + e^- \longrightarrow O_2^+(^2\Pi) + 2e^- \tag{12.4}$$

$$O_2(^3\Sigma) + e^- \longrightarrow O_2^* \longrightarrow O^{+(*)} + O^{(*)} + 2e^- \tag{12.5}$$

O_2^* includes Rydberg states of O_2. Figure 12.9 shows the gated experimental ion image and the corresponding inverse Abel transformed ion image for O_2^+. The image profile and the kinetic energy distribution obtained from the transform are also shown. The kinetic energy distribution is consistent with an O_2 beam temperature of < 20K.

Figure 12.10(a) shows the inverse Abel transformed ion image for gated fragment O^+ ions. The image is made up of a series of overlapping rings representing fragments with different recoil energies.

Previous electron impact studies[162,204,205] and a recent photo-excitation study using ion imaging[191,192] have assigned these energies to predissociating states of O_2. The 0-6 eV kinetic energy distribution obtained from the inverse Abel transform of our image shown in Figure 12.10 exhibits shoulders and peaks close to the ion energies previously obtained from 35 to 200 eV electron impact studies. The higher resolution photo-excitation REMPI study with a photon energy of 16.53 eV shows vibrational structure in the O^+ kinetic energy release curve over the range 0-3.5 eV with additional peaks not observed in the electron impact studies.

Figure 12.10(b) is a simulated image for O^+ based on the peaks identified from electron impact studies and the physical machine parameters pertinent to image capture. The simulation uses the following equations to determine the x and y locations on the detector.

$$x = \sqrt{\frac{2E_{\text{ion}}}{m}} t \cos\theta \sin\theta \tag{12.6}$$

$$y = \sqrt{\frac{2E_{\text{ion}}}{m}} t \cos\theta \sin\phi \tag{12.7}$$

$$t = t_{\text{delay}} + t_{\text{TOF}} \tag{12.8}$$

Where E_{ion} is the ion energy, which may have a random distribution ΔE_{ion} superimposed on it, and t_{delay} is the delay between the time that the ions are formed and the extraction and repeller are switched on. A random component can also be added to x and y to take the finite beam crossing volume into account.

These simulations are different from the *Simion* simulations because the electric field lines, and hence accurate ion trajectories, are not calculated. The length of the flight tube, the crossing volume, and the extractor repeller voltages are the only input variables. The advantage of this modeling method is that it is much faster than the *Simion* method. 10^6 ion trajectories can be flown in a few minutes compared to the *Simion* method which takes about one minute to fly 10^3 trajectories.

In the simulation shown in Figure 12.10(b) the molecular and electron beams were taken to have a trapezoidal shape with a 2.0 mm top and a 2.5 mm bottom. The experimental time-of-flight velocities were used as input values, although these may also be calculated from equations (12.1), (12.2) and (12.3). The image shown in Figure 12.10(b) represents the theoretical best resolution attainable from the machine and it suggests that the influence of stray fields, contact potentials, residual effects of collapsing fields, large beam overlap volumes and high background pressure are currently limiting resolution.

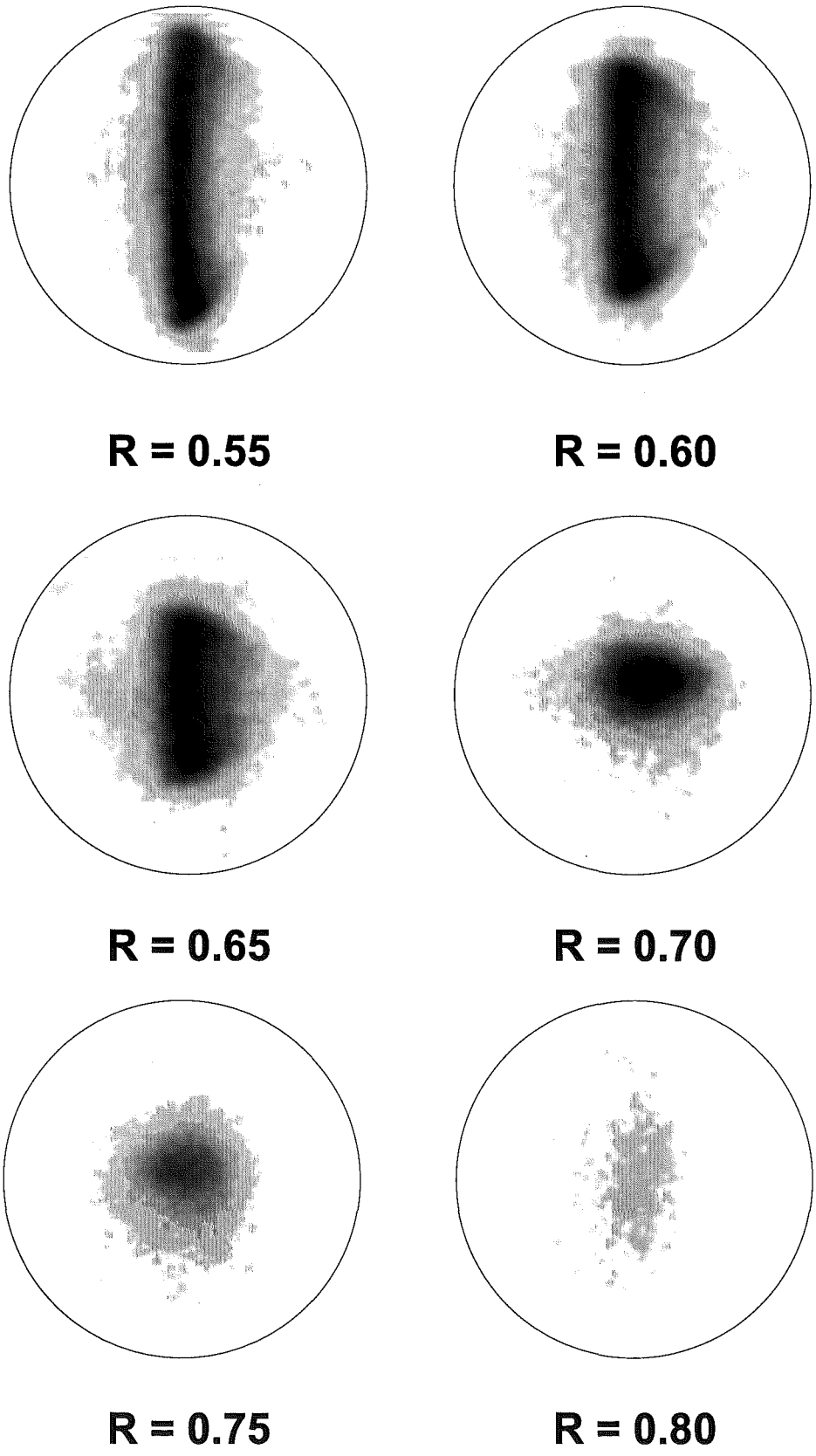

Figure 12.1: Optimization of extractor repeller voltages for velocity mapping technique. In all case the repeller has been set to 1 kV.

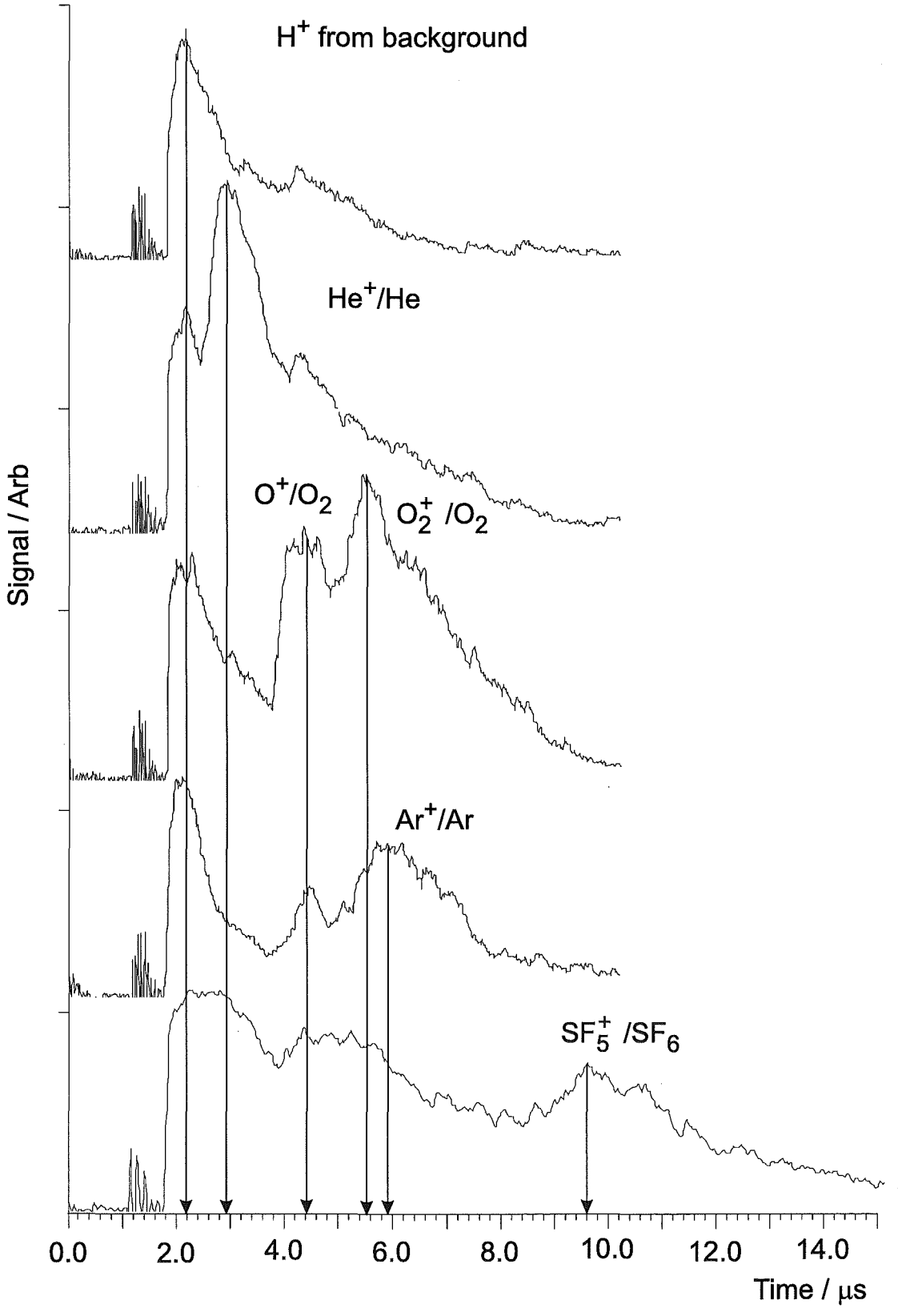

Figure 12.2: Time-of-flight spectra for protons from the background and ionization of He, O_2, Ar and SF_6 collected using photomultiplier tube.

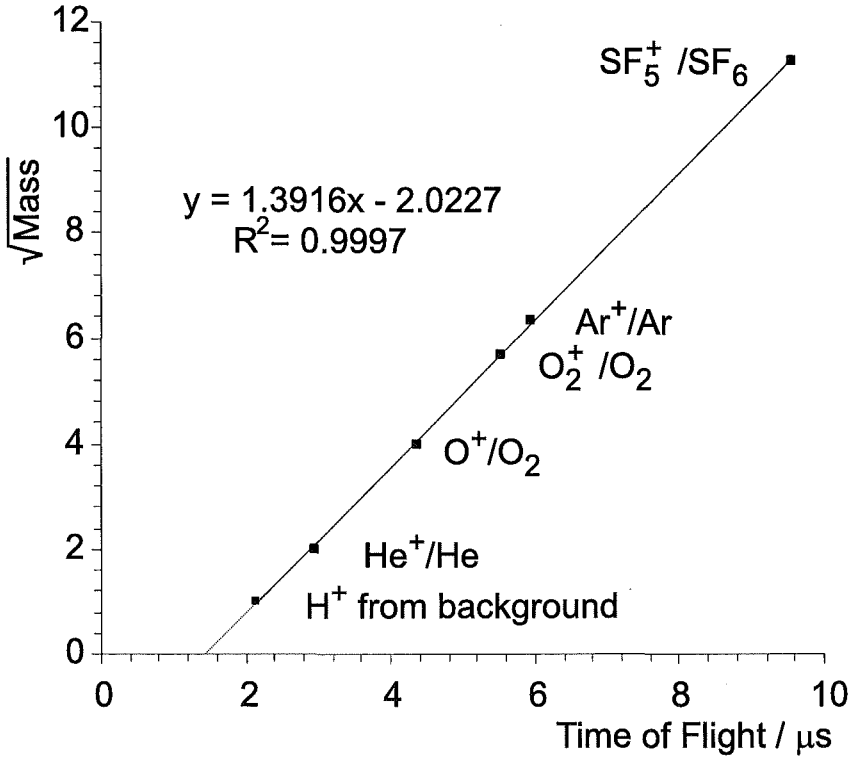

Figure 12.3: Linear relationship between $\sqrt{\text{mass}}$ and flight time for H+ from background, He^+/He, O^+/O_2, O_2^+/O_2, Ar^+/Ar and SF_5^+/SF_6.

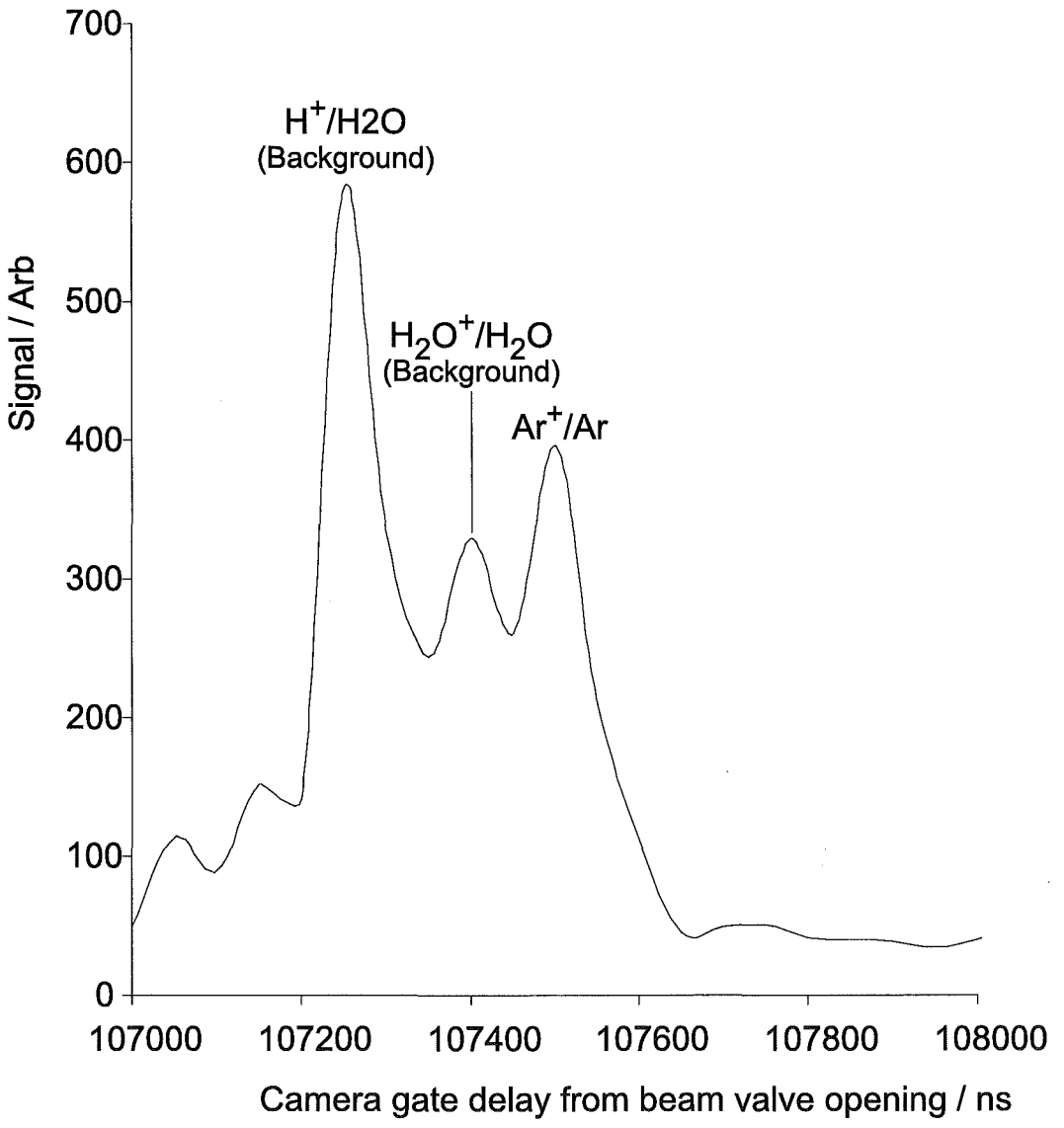

Figure 12.4: Time of flight spectra collected by integrating the signal from the CCD camera as a function of CCD gate position.

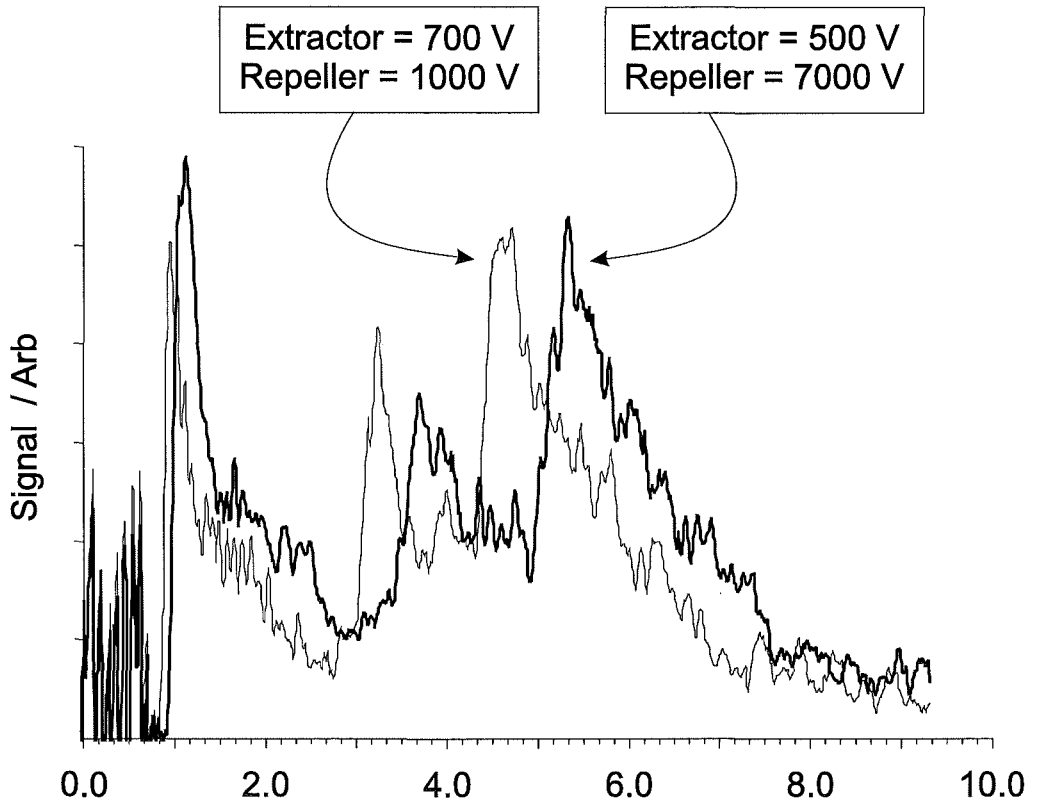

Figure 12.5: Effect of lowering the extractor repeller voltage on argon time-of-flight spectra.

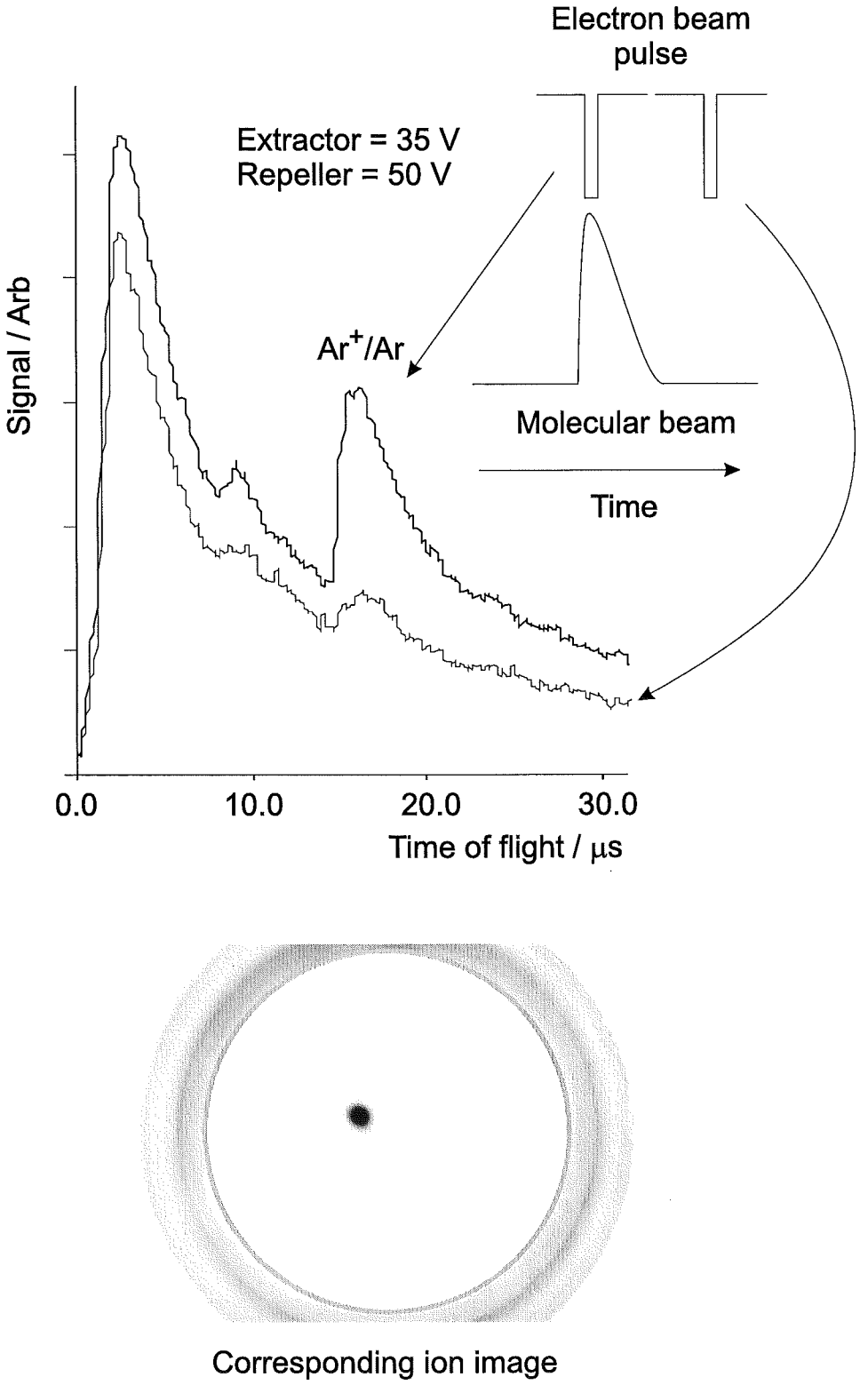

Figure 12.6: Time-of-flight spectrum of Ar^+/Ar and corresponding ion image for a 50 V repeller with an extractor:repeller ratio of 0.7.

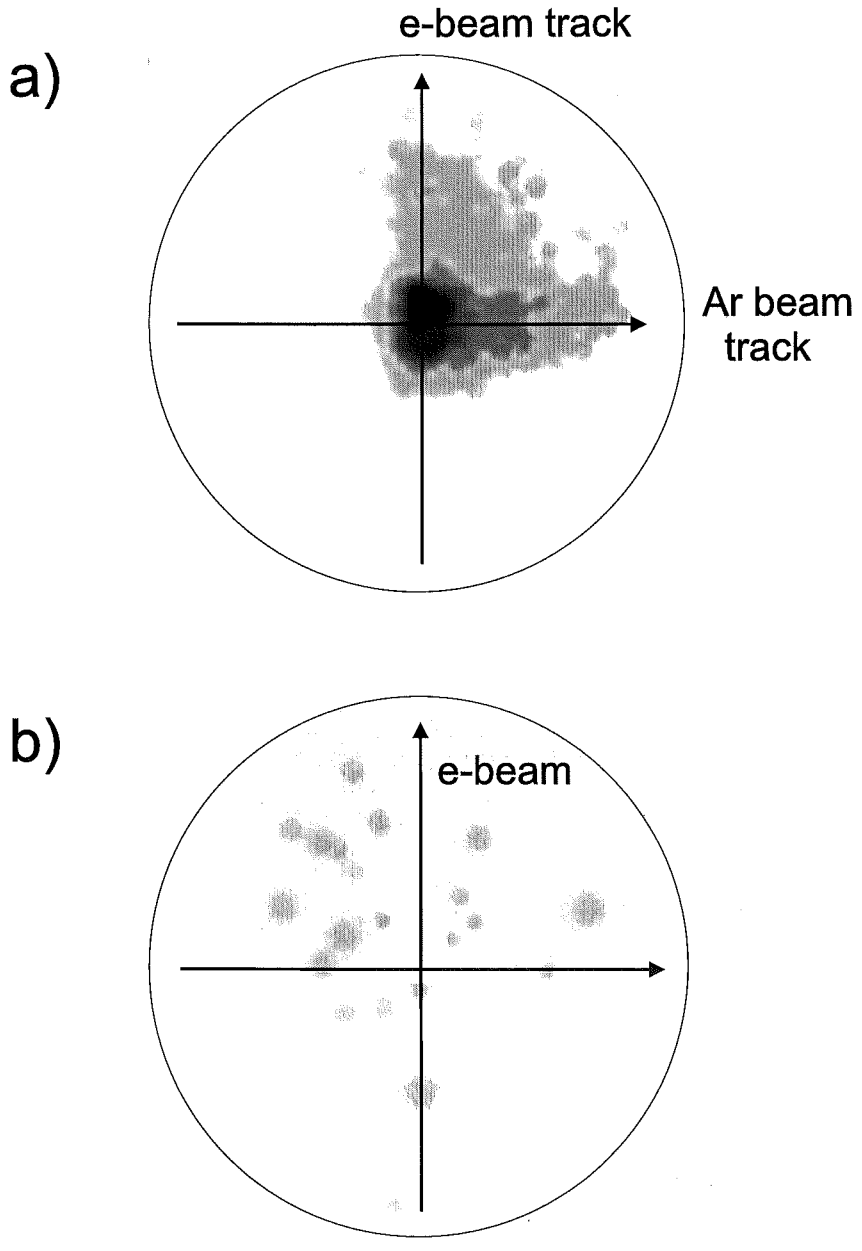

Figure 12.7: Gated ion image collected with argon beam on (a) and off (b).

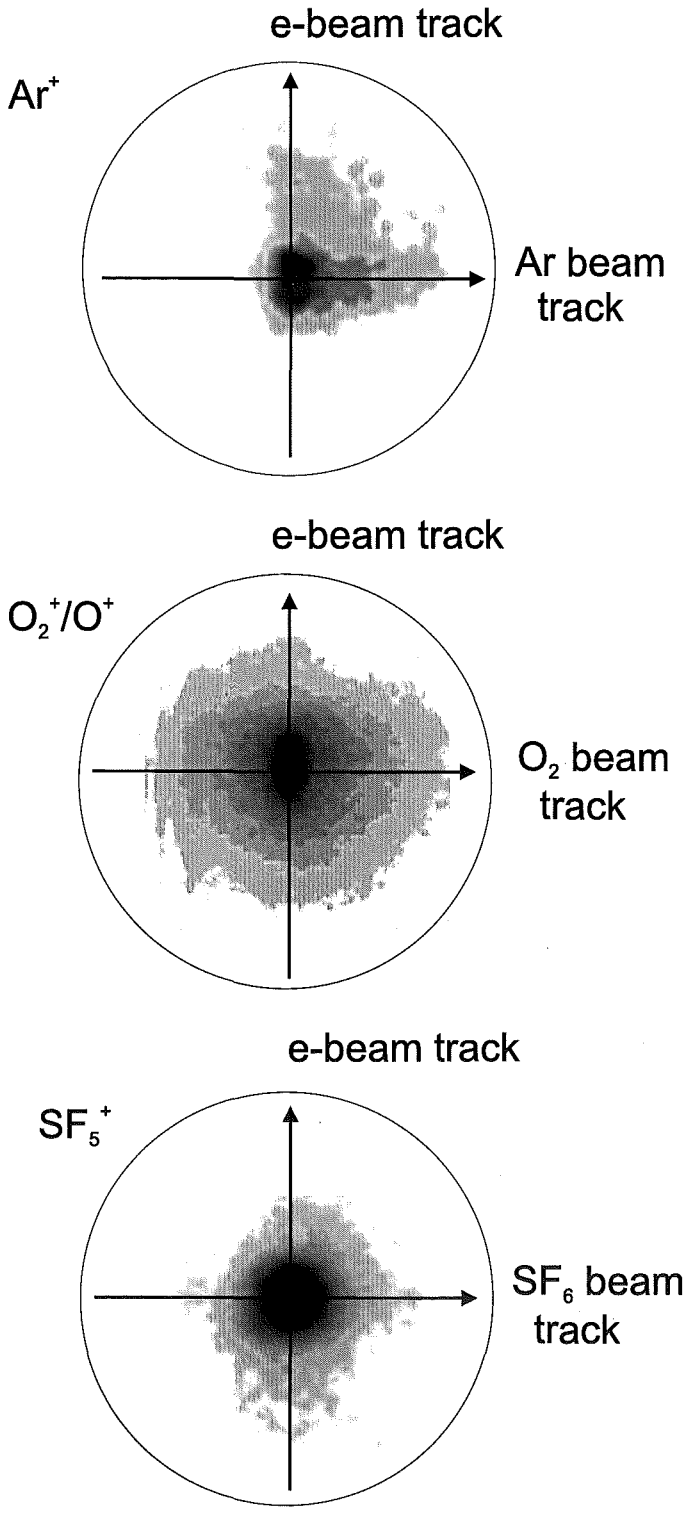

Figure 12.8: Ion images collected for Ar^+/Ar, $O_2^+/O_2 + O^+/O_2$ and SF_5^+/SF_6.

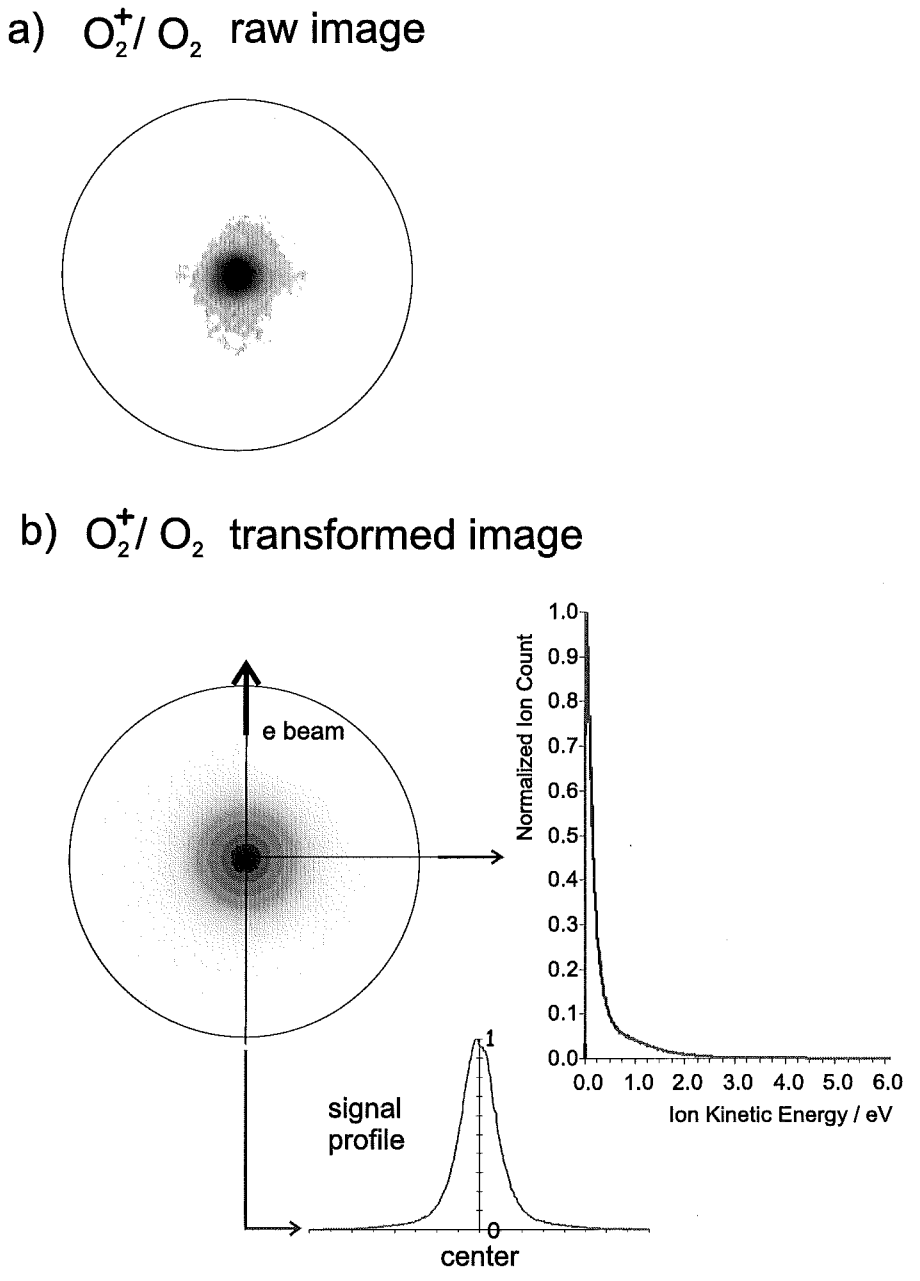

Figure 12.9: Raw O_2^+/O_2 image (a) and smoothed, balanced and inverse Able transformed image and corresponding signal profile and kinetic energy release.

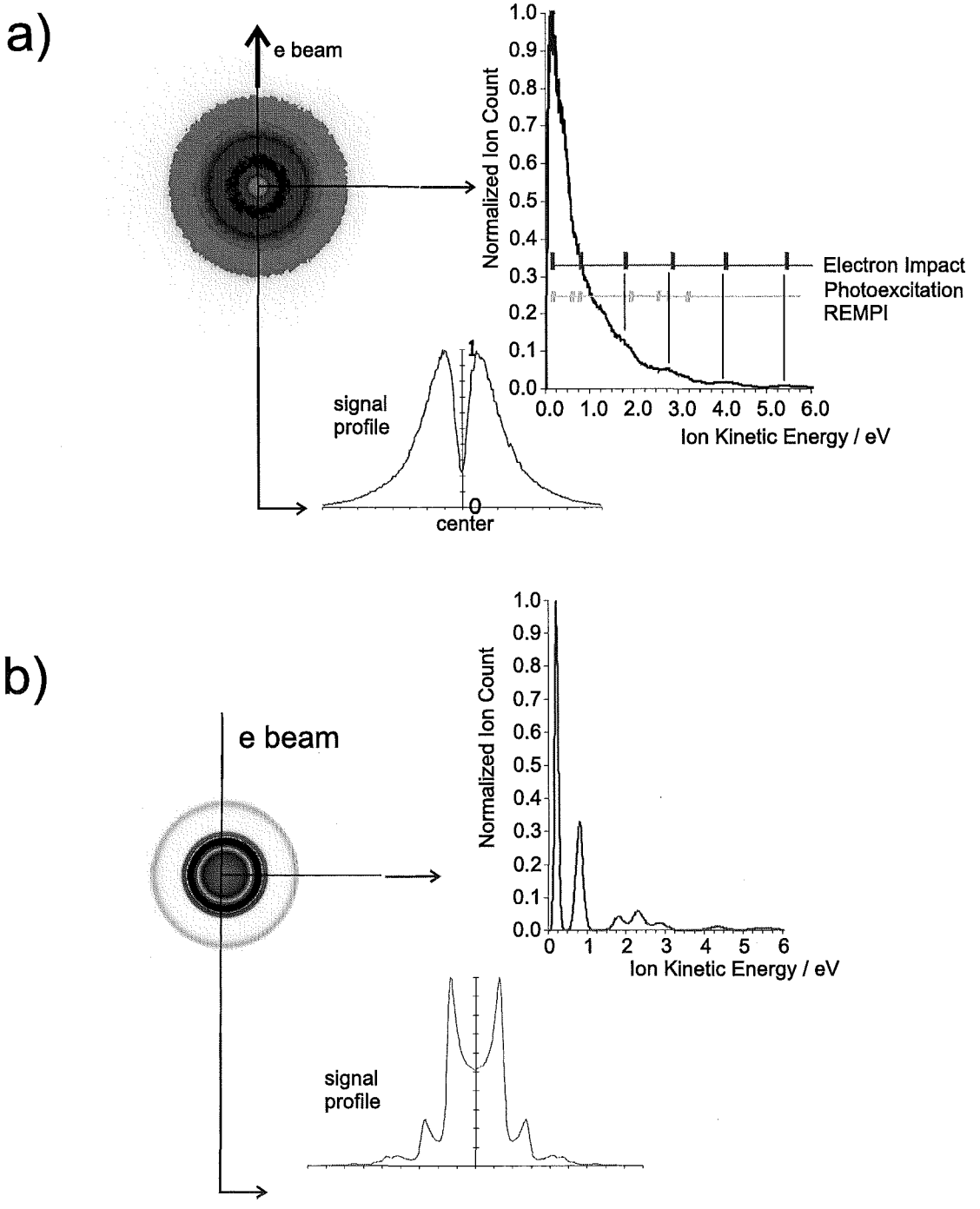

Figure 12.10: O^+/O_2 soothed, balanced and inverse Able transformed image (a), and simulated inverse Able transformed image assuming monochromatic beam energy distribution using method described in text.

12.2 Future work

In addition to electron impact ionization, which has been the focus of the present study, and ion molecule reactions of H_3^+ discussed in Section 9.3, the molecular beam machine has also been designed to investigate the reaction dynamics of oriented symmetric top molecules with alkali metal atoms and the study of S_N2 reaction mechanisms.[a] No previous attempts have been made to measure both product angular and velocity distributions of these reactions, and oriented molecule crossed beam studies of these reactions using ion imaging techniques should provide new insights into the mechanism of these reactions.

Vallance[88] has carried out calculations on the following alkali metal reaction pathways

$$K^+ + CH_3X \longrightarrow CH_3^+ + KX \tag{12.9}$$

$$K^+ + CH_3X \longrightarrow K^+CH_3X \tag{12.10}$$

Reaction channel (12.9) (halide transfer) appears to be exoergic by about 4.5 eV, because of the greater stability of the halide salt over the methyl cation. Reaction channel (12.10) (association reaction) appears to be endoergic by approximately 0.5 eV, 0.4 eV and 0.2 eV for X = Cl, Br and I, respectively, with an indicated K^+–CH_3X separation of approximately 3-4 Å. Vallance[88] suggested that in the case of the halide transfer reaction the observed scattering pattern would be similar to the neutral K + CH_3X spectator stripping reaction. In the case of the halide transfer no reaction will occur until the energy of the reactants exceeds the endoergicity of that reaction channel. The product of the association reaction simply follows the center-of-mass velocity vector of the CH_3X and K^+ reactants prior to the collision.

[a] A low energy alkali metal cation or halide anion source was designed and extensively characterized by Vallance.[88] The essential design elements of this ion gun incorporate a high power graphite tube furnace packed with ionic salt from which the ion beam was to be generated, and an acceleration / deceleration ion beam lens assembly.

The S_N2 reaction is thought to occur *via* a five coordinate transition state with the two halogen atoms in the axial positions with an overall C_{3v} symmetry.

$$Cl^- + CH_3Br \longrightarrow [Cl \cdot\cdot CH_3 \cdot\cdot Br]^- \longrightarrow ClCH_3 + Br^- \qquad (12.11)$$

Vallance[88] calculated potential energy curves which confirmed the intuitive expectations that for the reactions $CH_3Cl + Br^-$ and $CH_3Br + Cl^-$ halide attack on the CH_3 end of the molecule is favoured by about 0.5 eV in both cases when compared to attack on the halide end of the molecule. Broadside attack was found to lie between these two cases with an energy of about 0.2 - 0.3 eV higher than the direct CH_3 end attack. Crossed molecular beam experiments with oriented methyl halide molecules and a beam of negative halide ions should allow a direct measurement of the potential energy surfaces for these reactions.

Vallance[88] also considered the energetics of several other reaction pathways of K + CH_3Br leading to the formation of the following products (in order of increasing energy) ($CH_3 + ClBr^-$), ($Cl^- + CH_3 + Br$), ($CH_2Br^- + HCl$), ($Cl^- + CHBr + H_2$), ($H^- + CH_2Cl + Br$), and ($H^- + CH_2ClBr$), which had previously received very little attention from theoretical analysis. All of these reaction pathways could be studied using the molecular beam machine and appearance potentials of the products could be determined in order to make a comparison with theoretical prediction.

Before to the investigation of these ion–molecule reactions is attempted following factors will need to be addressed.

1. The temporal resolution of the phosphor will need to be increased from milliseconds to sub-microseconds.

2. The background gas pressure in the scattering chamber will need to be reduced significantly.

3. The beam overlap volume will need to be reduced significantly.

4. Stray fields in the ionization region and time-of-flight tube will need to be eliminated.

Recently a new fast P-47, phosphor was installed into the beam machine. Preliminary time-of-flight data indicates that this phosphor is fast enough to facilitate the resolution of the mass peaks of interest. Unfortunately, the piezoelectric crystal in the nozzle source failed the day after the installation of the new phosphor. Replacement parts have been ordered and are awaiting installation.

13. A FEASIBILITY STUDY ON THE APPLICATION OF AN ABSOLUTE CAPACITANCE MANOMETER FOR THE DETERMINATION OF MOLECULAR BEAM DENSITIES

13.1 Introduction

In order to measure absolute reaction cross-sections using a crossed beam method, the density and overlap function of the beams must be known. In the case of charged particle beams the flux of the electrons or ions may be measured directly with an electrometer. In the case of neutral beams however the measurement of the absolute beam flux is rather more difficult. There have been several previous studies to determine absolute beam densities using micro-mechanical devices. These include the method of Wiki *et al.*[206] where the deflection of a small amorphous paddle by the molecular beam was measured using a laser beam. The reported maximum sensitivity of the paddle detector was 6.5×10^7 helium atoms in a pulsed beam. The paddle was calibrated to a helium leak detector, and therefore the method was not truly absolute, a calibrated paddle could be used to measure the densities of other molecular beam species. Another method that used a micro-mechanical device was that of Kern *et al.*[207] In these experiments the deceleration of a magnetically levitated spinning rotor was measured as the molecular beam impinged on the surface. From the deceleration and a knowledge of the moment of inertia of the rotor, the torque applied by the molecular beam could be measured, and thus the molecular beam density calculated.

A further method was that of Wetzel *et al.*[155] A molecular beam was directed at the surface of a piezoelectric crystal, the energy transfer from the beam caused the crystal

to heat, thus generating a small voltage which was measured. The molecular beam was very fast neutrals, $\sim$ 3 keV, formed by charge transfer of an ion beam. The energy transfer to the piezoelectric crystal was much higher than for the case of a supersonic molecular beam, with typical kinetic energies of $\sim$ 0.1 eV. The piezoelectric crystal had a reported sensitivity of approximately 1 V/W. Voltages were typically of the order of 1 μV.

In this chapter some preliminary work on the absolute measurement of neutral beam density using a capacitance manometer will be detailed.

13.2 Calibration

From kinematic considerations the force that a beam of molecules applies to the surface may be calculated. In the case of a capacitance manometer this work is measured as a change in capacitance resulting from a change in distance between two charged plates caused by deflection of one of the plates by the pressure exerted on it by a gas.

The first consideration of any capacitance manometer measurement is the sensitivity of the manometer.[a] The Baratron used for these measurement was a special open architecture design based around the MKS Model 617, 1.0 Torr full scale supplied by MKS in aid of this project. Obviously if we had commissioned MKS to manufacture a Baratron for this project we would have specified the most sensitive model, 0.02 Torr full scale. Straub *et al.*[9] had previously reported that the 0.1 Torr 690A MKS Baratron was linear to 10^{-6} Torr. A sensitivity range of five orders of magnitude was thus used as a starting point for the following calculation.

Assuming that the molecular beam area that impinges on the surface of the Baratron is approximately 3 mm^2 the minimum detectable force, applied by the beam, is

[a] Because all of the measurements referred to here used an MKS Baratron type capacitance manometer, the term 'Baratron' will be used from here in place of 'capacitance manometer'

then given by;

$$F = PA \tag{13.1}$$

$$= 1.33 \times 10^{-3} \times 3 \times 10^{-6} \text{ N} \tag{13.2}$$

$$= 4.00 \times 10^{-9} \text{ N} \tag{13.3}$$

This calculation assumes that the force on the Baratron surface from a single point on the center of the diaphragm produces the same response as the same force acting over the entire surface, an assumption that will be considered in more detail below. Assuming that a beam of hydrogen is directed at the surface, the momentum transfer to the surface per particle is given as the mass of the hydrogen multiplied by the change in the velocity of the hydrogen per molecule. If one assumes that the molecules are reflected only in the normal direction of the surface the momentum transfer would be given as $2mv$, however from statistical mechanics a factor of $1/3$ has to be subtracted from this because the particles may be reflected at all angles, giving a total change in momentum per particle of $\frac{5}{3}mv$. Assuming a hydrogen beam velocity of 2000 ms^{-1}, the momentum transfer per molecule is then 6.69×10^{-24} Ns. Thus the minimum detection limit is a beam flux of $\frac{3PA}{5mv} = 3.59\times10^{14}$ molecules per second. In the case of a pulsed beam, the total number of molecules in the pulse could be obtained by integrating the arrival time distribution of the molecules.

The question of force applied over the whole surface compared to an equivalent force applied over a small portion of the surface of the Baratron needed to be addressed. Initially the idea of placing small weights on the surface was considered: if the force over the surface was equivalent to an equivalent force at a single point a straight line plot of mass against response would give a slope of 9.8 Nkg^{-1}. It was quickly realized that this would be unrealistic, a 1.5 mm diameter aluminium rod would have to be accurately cut to a length of 500 μm in order to provide a force equivalent to 0.01 Torr. The additional problem of centering the aluminum rod and keeping it centered while pumping the Baratron down renders this approach untenable. The solution to this involved using a loosely wound spring, fashioned out of a length of nichrome

wire, and attached to a small aluminium rod 1.5 mm diameter and 3 mm long to provide a Hooke's law force to counteract the gravitational force on the aluminium rod. The spring was attached to an axial translator and an accurate balance (Metler AE100) was used to calibrate the spring - weight system which was subsequently used to characterize the Baratron. Figure 13.1 schematically shows the components of the experiment and plots 13.2 and 13.4 show the calibration of the spring-weight system and the response of the Baratron when the same spring weight system is used. Because the spring-weight system turned when the axial translator was turned the observation of a slight sinusoidal dependence on the calibration curves indicated that the spring–weight system was not perfectly axial. The turning motion has since been eliminated with the use of a new axial translator fabricated in the departmental mechanical workshop from a threaded micrometer, which has a non-rotating shaft.

The two straight line functions in the upper plot of Figure 13.2 show the calibration of the spring before and after Baratron calibration, which involves inserting the spring into a vacuum chamber, directly above the Baratron, pumping down and measuring the response as the axial translator is adjusted. The slight change in slope indicates that some distortion of the spring occurs after it experiences oscillations when it is moved between the vacuum chamber and the balance. The stability of the Baratron over a seven hour period was monitored, to ensure that the drift was not significant during calibration measurements, as shown in Figure 13.3.

A coupling between the axial translator and a motor taken out of an old IR spectrometer was designed and built, and a computer interface to the Baratron was established, initially through RS-232 to a Fluke voltmeter (which was much too slow), and subsequently through a analogue to digital - digital to analogue (ADDA) converter. An optically isolated 5 V relay was used to control the direction of the motor and the number of rotations, and therefore the force applied to the surface of the Baratron. The maximum angular resolution of the motor was approximately 7°, which corresponded to a change in length of the spring of 0.01 mm.

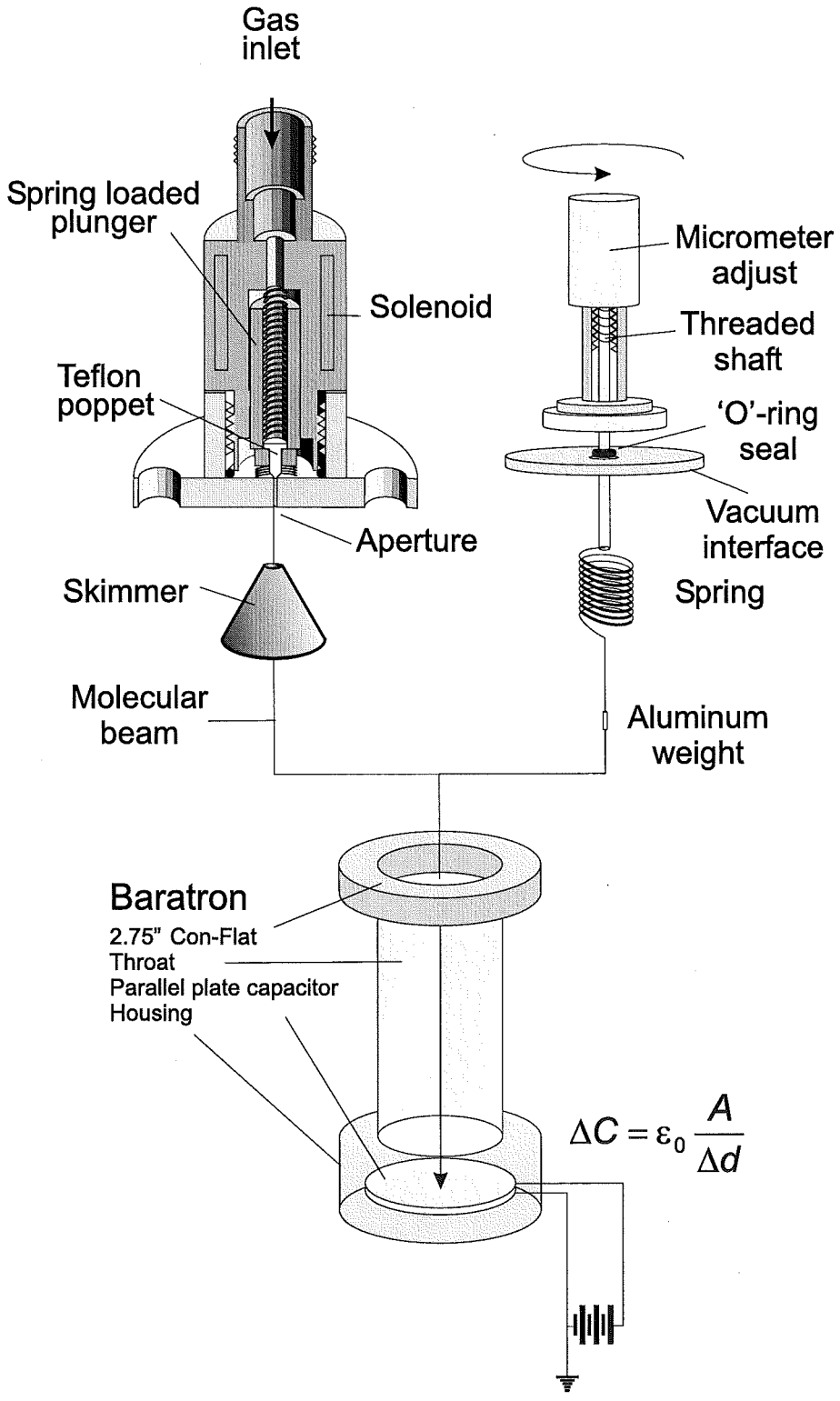

Figure 13.1: Schematic of Baratron, nozzle and axial translator, the components used for the calibration and measurement of arrival time distributions.

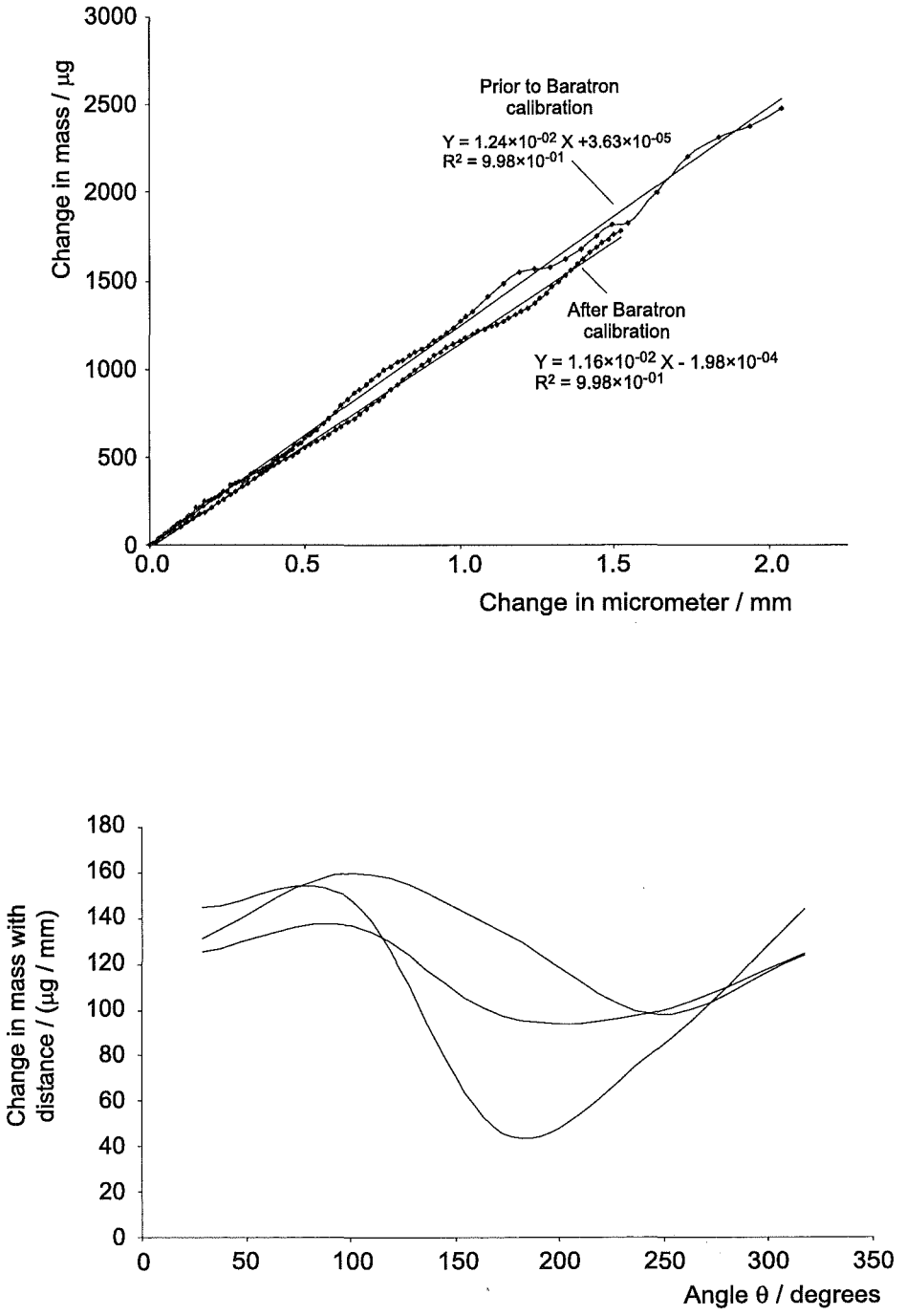

Figure 13.2: Calibration of spring using balance. The upper plot represents the calibration prior to insertion into the vacuum chamber and after insertion into the vacuum chamber and the lower plot illustrates the angular dependence on the spring calibration with turning of the micrometer.

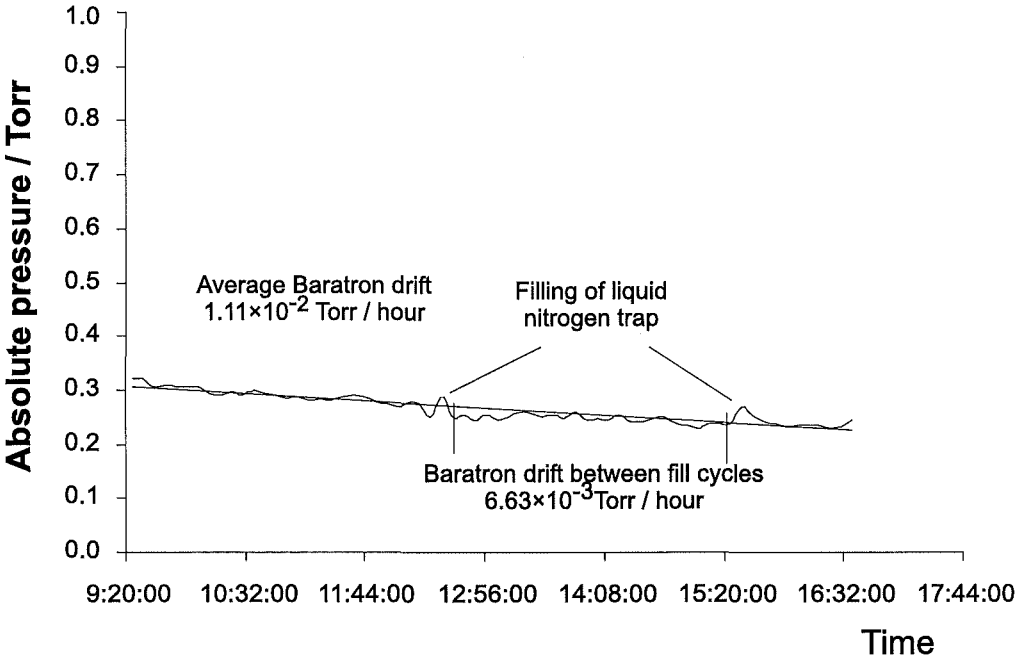

Figure 13.3: Baratron stability measurement over seven hour period.

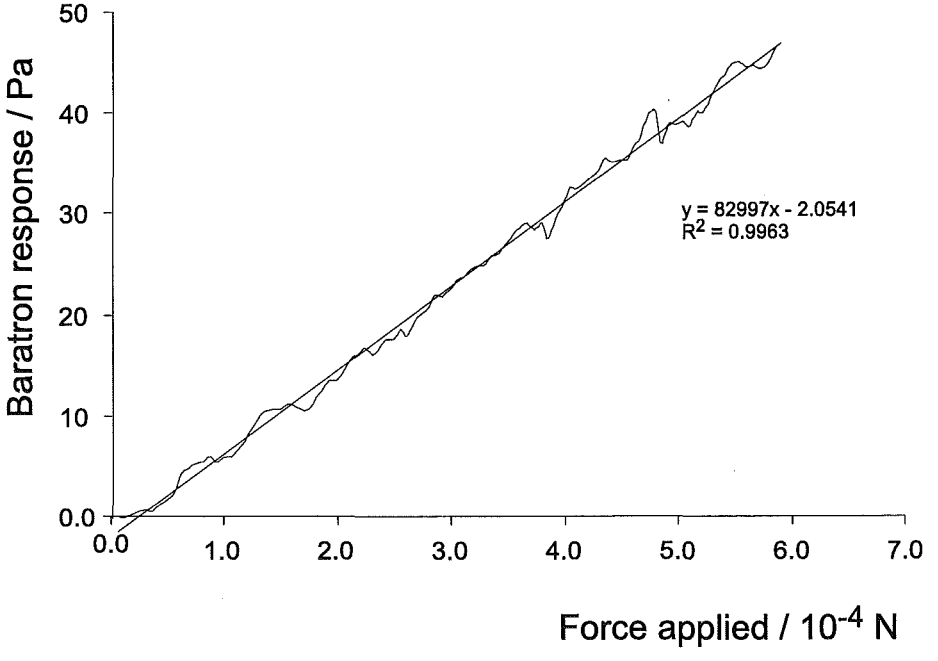

Figure 13.4: Linear calibration of Baratron using the spring assembly.

13.3 Measurement of arrival time distributions

After these preliminary measurements indicating that a calibration of the Baratron with a spring would be possible a supersonic nozzle source was installed into the vacuum chamber in place of the axial translator and spring-weight assembly. The nozzle was tested using a nude ion gauge on axis with the molecular beam line, because this would provide a very fast response. The upper plot in Figure 13.5 shows the arrival time for hydrogen using 50 Torr, 1000 Torr and 3500 Torr stagnation pressure. The lower figure shows the arrival time distributions for hydrogen at the ion gauge and the Baratron, these ATDs were measured using a repetition rate of 1 Hz with an applied gate of 1 ms. The inset shows an arrival time for argon, on the same time base, measured using the molecular beam machine.

13.4 Discussion

From the inverse of the slope of the plot in Figure 13.4, the effective surface area of the weight may be determined. The calculated diameter of the weight is thus 3.9 mm compared to actual diameter of the rod, 1.5 mm. The design of the Baratron precludes a precise measurement of the diameter of the diaphragm, but it is of the order of 20 mm. This indicates that the response of the diaphragm is strongly dependent on the location of the force applied to it, although flexing of the diaphragm around the location of the applied force contributes to a 'blurring' of actual rod diameter.

Assuming a molecular beam diameter of 1.5 mm, the flux, f, can then be calculated

$$f = \frac{3F}{5mv} \tag{13.4}$$

$$= \frac{3P_{\mathrm{B}}\zeta}{5mv} \tag{13.5}$$

where P_{B} is the Baratron response in Pascals, v is the flow velocity of the supersonic

beam, which may be determined using the method described in Chapter 8, and $\zeta = 1.20 \times 10^{-4}$ the inverse of the slope of the plot in Figure 13.4. Summing over all time intervals from the measured arrival time distribution would yield the total number of molecules in the pulse.

From Figure 13.5 it is clear that there are four considerations which need to be addressed to further the development of this absolute beam density detector:

1. the pumping speed of the vacuum system needs to be increased;
2. the electromechanical nozzle should be replaced by the piezoelectric nozzle used in the beam machine for a shorter beam pulse duration;
3. the speed of the Baratron amplifier may need to be increased;
4. the Baratron design should be modified to that the diaphragm is near the surface of the Con-Flat flange.

The long tail on the nude ion gauge measurement is presumably due to a combination of insufficient pumping speed, nozzle gate function, and may also contain a contribution from the ion gauge emission control feed-back circuit. The sensitivity of the Baratron is sufficient to detect the beam, although the temporal response is insufficient for use in the beam machine, although this is presumably due to the amplifier time constant not the mechanical response of the diaphragm. The nozzle used was a General Valve Corporation type 9-181 electromechanical nozzle which had been previously found to produce a FWHM of approximately 2 ms,[4] which is similar that which has been measured using the Baratron. Of the four factors listed above the pumping out of the spigot attaching the Baratron to the Con-Flat flange may be the most difficult to overcome. The first three requirements may be addressed using existing equipment and expertise but the fourth requirement will require input from MKS instruments.

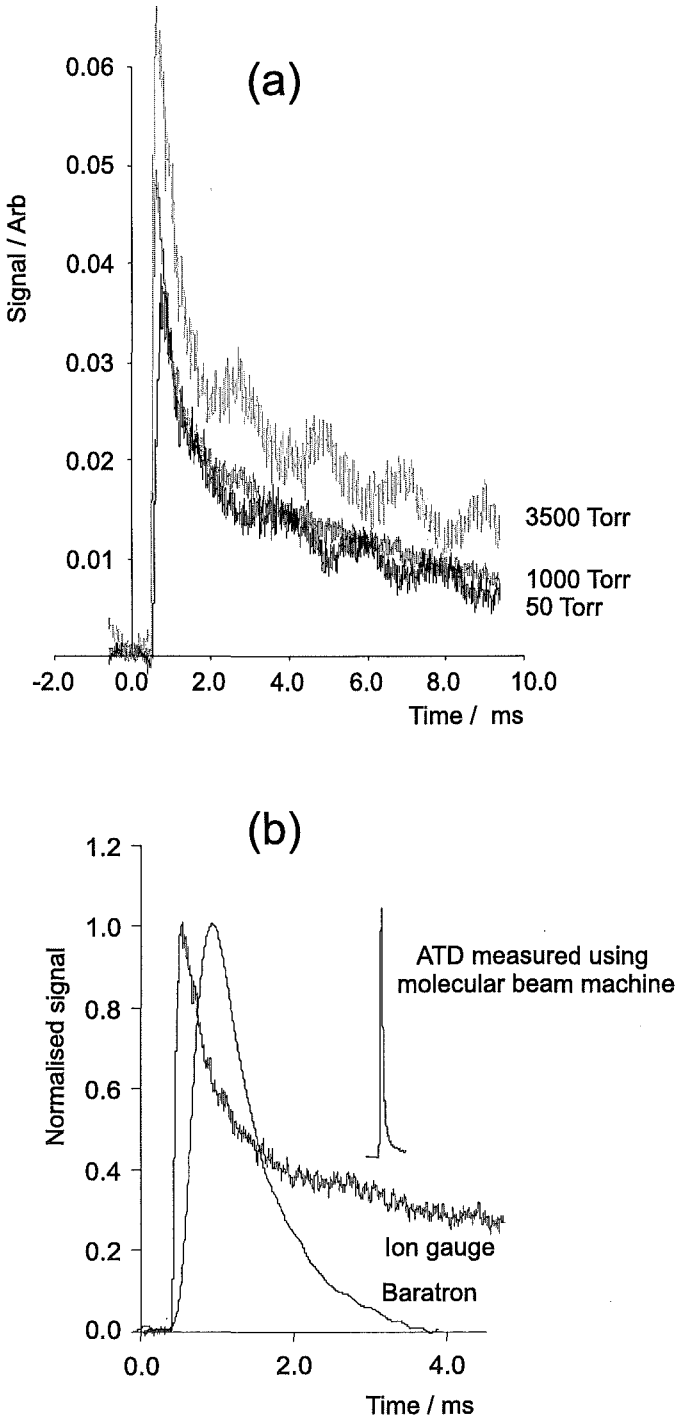

Figure 13.5: (a) Arrival time distributions for hydrogen using nude ion gauge. (b) A comparison of arrival time distributions measured using Baratron, nude ion gauge and molecular beam machine.

BIBLIOGRAPHY

[1] G. P. Collins, *Scientific American,* **September**, 14 (2003).

[2] P. R. Brooks and P. W. Harland, in *Advances in Gas Phase Ion Chemistry*, edited by N. G. Adams and L. M. Babcock (JAI Press, 1998), Vol. 2, pp. 1–39.

[3] C. G. Aitken, D. A. Blunt, and P. W. Harland, *J. Chem. Phys* **101**, 11074 (1994).

[4] C. G. Aitken, Ph.D. thesis, University of Canterbury, Christchurch, New Zealand, 1995.

[5] C. G. Aitken, D. A. Blunt, and P. W. Harland, *Int. J. Mass Spectrom. Ion Proc.* **149/150**, 279 (1995).

[6] U.S. Department of Commerce, *http://webbook.nist.gov.*

[7] See A. Crowe and J. W. McConkey, *J. Phys. B: At. Mol. Opt. Phys.* **6**, 2088 (1973), and references therein.

[8] D. Rapp and P. Englander-Golden, *J. Chem. Phys.* **42**, 1464 (1965).

[9] H. C. Straub, P. Renault, B. G. Lindsay, K. A. Smith, and R. F. Stebbings, *Rev. Sci. Instrum.* **65**, 3279 (1994).

[10] Simion 3D for Windows, *Lockheed Idaho Technologies Company and Princeton Electronic Systems,* 1999.

[11] A. L. Huges and E. Klein, *Phys. Rev.* **23**, 450 (1924).

[12] K. T. Compton and C. C. van Voorhis, *Phys. Rev.* **26**, 436 (1925).

[13] B. G. Linday and M. A. Mangan, *Landolt-Börnstien* **I/17/C**, 5.1.1 , Photon and Electron Interations with Molecules: Ionization and Dissociation, edited by Y. Itikawa, Springer–Verlag (Berlin–Heidelberg) (2003).

[14] D. Rapp, P. Englander-Golden, and D. D. Briglia, *J. Chem. Phys.* **42**, 4081 (1965).

[15] H. C. Straub, P. Renault, B. G. Lindsay, K. A. Smith, and R. F. Stebbings, *Phys. Rev. A* **52**, 1115 (1995).

[16] B. G. Lindsay, H. C. Straub, K. A. Smith, and R. F. Stebbings, *J. Geophys. Res.* **101**, 21151 (1996).

[17] F. J. de Heer and M. Inokuti, in *Electron impact ionization*, edited by T. D. Märk and G. H. Dunn (Springer-Verlag, Wien, 1985), pp. 250–270.

[18] J. T. Tate and P. T. Smith, *Phys. Rev.* **39**, 270 (1932).

[19] W. Bleakney, *Phys. Rev.* **34**, 157 (1929).

[20] P. T. Smith, *Phys. Rev.* **36**, 1293 (1930).

[21] P. T. Smith, *Phys. Rev.* **37**, 808 (1931).

[22] J. T. Tate and P. T. Smith, *Phys. Rev.* **46**, 773 (1934).

[23] L. J. Kieffer and G. H. Dunn, *Rev. Mod. Phys* **38**, 1 (1966).

[24] R. F. Stebbings and B. G. Lindsay, *J. Chem. Phys* **114**, 4741 (2001).

[25] F. J. de Heer and M. Inokuti, in *Electron impact ionization*, edited by T. D. Märk and G. H. Dunn (Springer-Verlag, Wien, 1985), pp. 239–241.

[26] B. L. Schram, F. J. de Heer, M. J. van der Wiel, and J. Kistemaker, *Physica* **31**, 94 (1965).

[27] B. L. Schram, M. J. van der Wiel, F. J. de Heer, and H. Moustafa, *J. Chem. Phys.* **44**, 49 (1966).

[28] B. L. Schram, H. R. Moustafa, J. Schutten, and F. J. de Heer, *Physica* **32**, 734 (1966).

[29] B. Adamczyk, A. J. Boerboom, B. L. Schram, and J. Kistemaker, *J. Chem. Phys.* **44**, 4640 (1966).

[30] J. W. Otvos and D. P. Stevenson, *J. Am. Chem. Soc.* **78**, 546 (1956).

[31] F. W. Lampe, J. L. Franklin, and F. H. Field, *J. Am. Chem. Soc.* **79**, 6129 (1957).

[32] A. G. Harrison, S. K. Gupta, and N. P. Nagy, *Can. J. Chem.* **44**, 1967 (1966).

[33] R. K. Asundi, J. D. Craggs, and M. V. Kurepa, *Proc. Phys. Soc.* **82**, 967 (1963).

[34] H. C. Straub, P. Renault, B. G. Lindsay, K. A. Smith, and R. F. Stebbings, *Phys. Rev. A* **54**, 2146 (1996).

[35] H. C. Straub, B. G. Lindsay, K. A. Smith, and R. F. Stebbings, *J. Phys. Chem.* **105**, 4015 (1996).

[36] H. C. Straub, D. Lin, B. G. Lindsay, K. A. Smith, and R. F. Stebbings, *J. Chem. Phys.* **106**, 4430 (1997).

[37] H. C. Straub, B. G. Lindsay, K. A. Smith, and R. F. Stebbings, *J. Chem. Phys.* **108**, 109 (1998).

[38] B. G. Lindsay, M. A. Mangan, H. C. Straub, and R. F. Stebbings, *J. Chem. Phys* **112**, 9409 (2000).

[39] M. A. Mangan, B. G. Lindsay, and R. F. Stebbings, *J. Phys. B: At. Mol. Opt. Phys* **34**, 3225 (2000).

[40] B. G. Lindsay, R. Rejoub, and R. F. Stebbings, *Chem. Phys.* **114**, 10225 (2001).

[41] R. Rejoub, D. R. Sieglaff, B. G. Lindsay, and R. F. Stebbings, *J. Phys. B: At. Mol. Opt. Phys.* **34**, 1289 (2001).

[42] R. Rejoub, B. G. Lindsay, and R. F. Stebbings, *J. Chem. Phys* **115**, 5053 (2001).

[43] D. R. Sieglaff, R. Rejoub, B. G. Lindsay, and R. F. Stebbings, *J. Phys. B: At. Mol. Opt. Phys.* **34**, 799 (2001).

[44] R. Rejoub, B. G. Lindsay, and R. F. Stebbings, *Phys. Rev. A* **65**, 42713 (2002).

[45] R. Rejoub, C. D. Morton, B. G. Lindsay, and R. F. Stebbings, *J. Chem. Phys* **118**, 1756 (2003).

[46] V. Srinivasan and J. A. Rees, *British J. Appl. Phys.* **18**, 59 (1967).

[47] I. Cowling and J. Fletcher, *J. Phys. B: At. Mol. Opt. Phys.* **6**, 665 (1973).

[48] H. Chatham, D. Hils, R. Robertson, and A. Gallgher, *J. Chem. Phys* **81**, 1770 (1984).

[49] H. Nishimura and H. Tawara, *J. Phys. B: At. Mol. Opt. Phys* **27**, 2063 (1994).

[50] N. Nishimura, W. M. Huo, M. A. Ali, and Y. K. Kim, *J. Chem. Phys.* **52**, 3811 (1999).

[51] H. F. Winters, *J. Chem. Phys.* **63**, 3462 (1975).

[52] See F. J. de Heer and M. Inokuti, in *Electron impact ionization*, edited by T. D. Märk and G. H. Dunn (Springer-Verlag, Wien, 1985), pp. 239–241, and references therein.

[53] F. F. Rieke and W. Prepejchal, *Phys. Rev. A* **6**, 1507 (1972).

[54] T. M. Stephen and B. L. Peko, *Rev Sci Instrm.* **71**, 1355 (2000).

[55] B. L. Peko and T. M. Stephen, *Nucl. Instrum. Meth. B* **171**, 597 (2000).

[56] T. D.Märk, *J. Chem. Phys.* **63**, 3731 (1975).

[57] T. D. Märk and F. Egger, *Int. J. Mass. Spectrom. Ion. Phys.* **20**, 89 (1976).

[58] T. D.Märk and E. Hille, *J. Chem. Phys* **69**, 2492 (1978).

[59] E. Hille and T. D. Märk, *J. Chem. Phys* **69**, 4600 (1978).

[60] K. Stephan, H. Helm, Y. B. Kim, G. Seykora, J. Ramler, M. Göossl, E. Märk, and T. D. Märk, *J. Chem. Phys* **73**, 303 (1980).

[61] Y. B. Kim, K. Stephan, E. Märk, and T. D. Märk, *J. Chem. Phys* **74**, 6771 (1981).

[62] E. Märk, T. D. Märk, Y. B. Kim, and K. Stephan, *J. Chem. Phys* **75**, 4446 (1981).

[63] K. Stephan, H. Deutsch, and T. D. Märk, *J. Chem. Phys* **83**, 5712 (1985).

[64] S. Matt, B. Lünser, M. Lezius, H. Deutsch, K. Becker, A. Stamatovic, and T. D. Märk, *J. Chem. Phys* **105**, 1880 (1996).

[65] K. Leiter, P. Scheier, G. Walder, and T. D. Märk, *Int. J. Mass Spec. Ion Proc.* **87**, 209 (1989).

[66] D. Margreiter, G. Walder, H. Deutsch, H. U. Poll, C. Winkler, K. Stephan, and T. D. Märk, *Int. J. Mass Spec. Ion Proc.* **100**, 143 (1990).

[67] V. Grill, G. Walder, P. Scheier, M. Kurdel, and T. D. Märk, *Int. J. Mass Spec. Ion Proc.* **129**, 31 (1993).

[68] R. Basner, M. Schmidt, C. Tarnovsky, K. Becker, and H. Deutsch, *Int. J. Mass Spec. Ion Proc.* **171**, 83 (1997).

[69] H. U. Poll, C. Winkler, D. Margreiter, V. Grill, and T. D. Märk, *Int. J. Mass Spec. Ion Proc.* **112**, 1 (1992).

[70] B. L. Schram, B. Adamczyk, and F. J. de Heer, *J. Sci. Inst* **43**, 638 (1966).

[71] B. Adamczyk, A. J. H. Boerboom, and M. Lukasiewicz, *Int. J. Mass Spectrom. Ion Phys.* **9**, 407 (1972).

[72] A. Crowe and J. W. McConkey, *J. Phys. B: At. Mol. Opt. Phys.* **7**, 349 (1974).

[73] K. Bederski, L. Mojcik, and B. Adamczyk, *Int. J. Mass. Spec. Ion. Phys* **35**, 171 (1980).

[74] T. Stanski and D. Adamczyk, *Int. J. Mass. Spec. Ion. Phys* **46**, 31 (1983).

[75] R. E. Center and A. Mandl, *J. Chem. Phys.* **57**, 4104 (1972).

[76] O. I. Smith and J. S. Stevenson, *J. Chem. Phys.* **74**, 6777 (1981).

[77] J. Perrin, J. P. M. Schmidt, G. de Rosny, B. Drevillion, J. Huc, and A. Loret, *Chem. Phys* **73**, 383 (1982).

[78] M. W. Siegel, *Int. J. Mass. Spec. Ion. Phys* **44**, 19 (1982).

[79] K. A. Newson, S. M. Luc, S. D. Price, and N. Mason, *Int. J. Mass Spec. Ion Proc.* **148**, 203 (1995).

[80] H. U. Poll and J. Meichsner, *Contrib. Plasma Phys.* **27**, 359 (1987).

[81] P. Haaland, *Chem. Phys. Lett.* **170**, 146 (1990).

[82] C. Q. Jiao, A. Garscadden, and P. D. Haaland, *Chem. Phys. Lett.* **310**, 52 (1999).

[83] R. C. Wetzel, F. A. Baiocci, T. R. Hayes, and R. S. Freund, *Phys. Rev. A* **35**, 559 (1987).

[84] A. Crowe and J. W. McConkey, *J. Phys. B: At. Mol. Opt. Phys.* **6**, 2088 (1973).

[85] A. Crowe and J. W. McConkey, *J. Phys. B: At. Mol. Opt. Phys.* **6**, 2108 (1973).

[86] A. Crowe and J. W. McConkey, *Int. J. Mass. Spec. Ion. Phys.* **24**, 181 (1977).

[87] S. A. Harris, Ph.D. thesis, University of Canterbury, Christchurch, New Zealand, 1997.

[88] C. Vallance, Ph.D. thesis, University of Canterbury, Christchurch, New Zealand, 1999.

[89] C. Vallance, S. A. Harris, J. E. Hudson, and P. W. Harland, *J. Phys. B: At. Mol. Opt. Phys.* **30**, 2465 (1997).

[90] J. A. Beran and l. Kevan, *J. Phys. Chem.* **73**, 3866 (1969).

[91] *Climate Change 1995 – The Science of Climate Change*, edited by J. T. Houghton, L. G. M. Filho, B. A. Callanader, N. H. adn A. Kattenburg, and K. Maskell (Cambridge University Press, 1996).

[92] J. J. Thomson, *Phil. Mag.* **23**, 449 (1912).

[93] See S. M. Younger, in *Electron impact ionization*, edited by T. D. Märk and G. H. Dunn (Springer-Verlag, Wien, 1985), pp. 1–23, and references therein.

[94] J. E. Hudson, M. L. Hamilton, C. Vallance, and P. W. Harland, *Phys. Chem. Chem. Phys.* **5**, 3162 (2003).

[95] W. H. Press, *Numerical recipes in C : the art of scientific computing* (Cambridge University Press, 1992).

[96] R. Basner, M. Schmidt, E. Denisov, P. lopata, K. Becker, and H. Deutsch, *Int. J. Mass Spectrom.* **214**, 365 (2002).

[97] H. M. Rosentock, M. B. Wallenstein, A. L. Wahrhaftig, and E. Eyring, *Proc. Natl. Acad. Sci.(US)* **38**, 667 (1952).

[98] See R. W. Kiser, *Introduction to Mass Spectrometry and its Applications* (Prentice-Hall, 1965), and references therein.

[99] J. L. Franklin, J. G. Dillard, H. M. Rosentock, J. T. Herron, K. Draxl, and F. H. Field, *Ionization Potentials, Apperance Potentials and Heats of Formation of Gaseous Positive Ions* (National Bureau of Standards, 1969).

[100] J. C. Kotz and P. Treichel, *Chemistry and Chemical Reactivity* (Saunders College Publishing, 1999).

[101] C. Vallance, P. W. Harland, and R. G. A. R. Maclagan, *J. Phys. Chem.* **100**, 15021 (1996).

[102] W. F. Miller and R. L. Platzmann, *Proc. Phys. Soc. A* **70**, 299 (1957).

[103] S. M. Younger, in *Electron impact ionization*, edited by T. D. Märk and G. H. Dunn (Springer-Verlag, Wien, 1985), pp. 1–23.

[104] S. Jones and A. T. Stelbovics, *Phys. Rev. A* **66**, 32717 (2002).

[105] R. Poet, *J. Phys. B: At. Mol. Opt. Phys* **13**, 2995 (1980).

[106] A. Temkin, *Phys. Rev.* **134**, 130 (1962).

[107] R. Poet, *J. Phys. B: At. Mol. Opt. Phys* **11**, 3081 (1978).

[108] E. J. McGuire, *Phys. Rev. A* **3**, 267 (1971).

[109] E. J. McGuire, *Phys. Rev. A* **16**, 62 (1977).

[110] E. J. McGuire, *Phys. Rev. A* **16**, 72 (1977).

[111] E. J. McGuire, *Phys. Rev. A* **20**, 445 (1979).

[112] Wolfram math research, *http://mathworld.wolfram.com.*

[113] M. R. H. Rudge and S. B. Schwartz, *Proc. Phys. Soc.* **88**, 563 (1966).

[114] M. J. Frisch, G. W. Trucks, H. B. Schlegel, P. M. W. Gill, B. G. Johnson, M. A. Robb, J. R. Cheeseman, T. A. Keith, G. A. Petersson, J. A. Montgomery, K. Raghavachari, M. A. Al-Laham, V. G. Zakrzewski, J. V. Ortiz, J. B. Foresman, J. Cioslowski, B. B. Stefanov, A. Nanayakkara, M. Challacombe, C. Y. Peng, P. Y. Ayala, W. Chem, M. Wong, J. L. Andres, E. S. Replogle, R. Comperts, R. L. Martin, D. J. Fox, J. S. Binkley, D. J. Defrees, J. Baker, J.P.Stewart, M. Head-Gordon, C. Gonzalez, and J. Pople, *Gaussian94 (Revision A.1.)* (Gaussian Inc., Pittsburgh PA, 1995).

[115] S. M. Younger and T. D. Märk, in *Electron impact ionization*, edited by T. D. Märk and G. H. Dunn (Springer-Verlag, Wien, 1985), pp. 24–41.

[116] H. Deutsch, K. Becker, S. Matt, and T. D. Märk, *Int. J. Mass. Spectrom.* **197**, 37 (2000).

[117] P. W. Harland and C. Vallance, *Advances in Gas Phase Ion Chemistry* **3**, 319 (1998).

[118] M. Bobeldijk, W. J. van der Zande, and P. G. Kistemaker, *Chem. Phys* **179**, 125 (1994).

[119] Y.-K. Kim and M. E. Rudd, *Phys. Rev. A.* **50**, 3954 (1994).

[120] H. Deutsch, C. Cornelissen, L. Cespiva, V. Bonacic-Koutecky, D. Margreiter, and T. D. Märk, *Int. J. Mass Spectrom. Ion Processes* **129**, 43 (1993).

[121] H. Deutsch, T. D. Mär, V. Tarnovsky, K. Becker, C. Cornelissen, L. Cespiva, and V. Bonacic-Koutecky, *Int. J. Mass Spectrom. Ion Processes* **137**, 77 (1994).

[122] P. W. Harland and C. Vallance, *Int. J. Mass Spec. Ion Proc.* **171**, 173 (1997).

[123] M. Gryzinski, *Phys. Rev.* **115**, 374 (1959).

[124] M. Gryzinski, *Phys. Rev.* **138**, A305 (1965).

[125] M. Gryzinski, *Phys. Rev. Lett.* **14**, 1059 (1965).

[126] H. Deutsch and T. D. Märk, *Int. J. Mass Spectrom. Ion Proc.* **79**, R1 (1987).

[127] D. Margreiter, H. Deutsch, and T. S. Märk, *Int. J. Mass Spectrom. Ion Proc.* **139**, 127 (1994).

[128] H. Deutsch, K. Becker, and T. D. Märk, *Int. J. Mass. Spectrom.* **185/186/187**, 319 (1999).

[129] D. K. Jain and S. P. Kahare, *J. Phys. B: At. Mol. Opt. Phys* **9**, 1429 (1976).

[130] M. Inokuti, *Rev. Mod. Phys* **43**, 297 (1971).

[131] U.S. Department of Commerce, electron impact ionization database, *http://physics.nist.gov/PhysRefData/Ionization/intro.html.*

[132] W. Hwang, Y.-K. Kim, and M. E. Rudd, *J. Chem. Phys* **104**, 2956 (1996).

[133] Y-K.Kim, W. Hwang, N. M. Weinberger, M. A. Ali, and M. E. Rudd, *J. Chem. Phys.* **106**, 1026 (1997).

[134] M. A. Ali, Y.-K. Kim, W. Hwang, N. M. Weinberger, and M. E. Rudd, *J. Chem. Phys* **106**, 9026 (1997).

[135] M. Bart, J. E. Hudson, P. W. Harland, and C. Vallance, *Chem. Phys. Phys. Chem.* **3**, 800 (2001).

[136] J. E. Hudson, C. Vallance, M. Bart, and P. W. Harland, *J. Phys. B: At. Mol. Opt. Phys.* **34**, 3025 (2001).

[137] Y-K.Kim, Private Communication.

[138] R. D. Levine and R. B. Bernstien, in *Molecular reaction dynamics* (Oxford University Press, 1974), Chap. 6.

[139] M. A. D. Fluendy and K. P. Lawley, in *Chemical Applications of Molecular Beam Scattering* (John Wiley and Sons, 1973).

[140] P. Casavecchia, *Science Spectra* **6**, 56 (1996).

[141] D. R. Hershbach, in *Nobel Lectures in Chemistry (1981-1990)*, edited by T. Frängsmyr and B. G. Malmström (World Scientific, 1986), pp. 261–314.

[142] Y. T. Lee, in *Nobel Lectures in Chemistry (1981-1990)*, edited by T. Frängsmyr and B. G. Malmström (World Scientific, 1986), pp. 317–354.

[143] J. C. Polanyi, in *Nobel Lectures in Chemistry (1981-1990)*, edited by T. Frängsmyr and B. G. Malmström (World Scientific, 1986), pp. 357–407.

[144] P. J. O. Teubner, in *Electron impact ionization*, edited by T. D. Märk and G. H. Dunn (Springer-Verlag, Wien, 1985), pp. 89–135.

[145] K. T. Dolder, *Proc. Roy. Soc.* **A264**, 367 (1961).

[146] F. A. Stevie and M. J. Vasile, *J. Chem. Phys.* **74**, 5106 (1981).

[147] J. A. Syage, *Chem. Phys. Lett* **143**, 19 (1988).

[148] F. A. Baiocchi, R. C. Wetzel, and R. S. Freund, *Phys. Rev. Lett* **53**, 771 (1984).

[149] T. R. H. R. C. Wetzel, F. A. Baiocchi, , and R. S. Freund, *J. Chem. Phys.* **88**, 823 (1988).

[150] R. J. Shul, T. R. Hayes, R. C. Wetzel, F. A. Baiocchi, and R. S. Freund, *J. Chem. Phys.* **89**, 4042 (1988).

[151] T. R. Hayes, R. J. Shul, F. A. Baiocchi, R. C. Wetzel, and R. S. Freund, *J. Chem. Phys.* **89**, 4035 (1988).

[152] T. R. Hayes, R. C. Wetzel, and R. S. Freund, *Phys. Rev. A: At. Mol. Opt. Phys.* **35**, 578 (1987).

[153] R. S. Freund, R. C. Wetzel, R. J. Shul, and T. R. Hayes, *Phys. Rev. A* **41**, 3575 (1990).

[154] R. J. Shul, R. S. Freund, and R. C. Wetzel, *Phys. Rev. A* **41**, 5856 (1990).

[155] R. S. Freund, R. C. Wetzel, R. J. Schul, and T. R. Hayes, *Phys. Rev. A* **41**, 3575 (1990).

[156] I. Torres, R. Martínez, M. N. Sánchez-Rayo, and F. J. Castaño, *J. Phys. B: Opt. Mol. At. Phys.* **33**, 3615 (2000).

[157] I. Torres, R. Martínez, M. N. Sánchez-Rayo, and F. J. Castaño, *J. Chem. Phys.* **115**, 4041 (2001).

[158] G. H. Dunn, *Phys. Rev. Lett.* **8**, 62 (1962).

[159] G. Herzburg, *Molecular Spectra and Molecular Structrue: I. Spectra of Diatomic Molecules* (D van Nostrand Co., 1950).

[160] G. H. Dunn and L. J. Kieffer, *Phys. Rev.* **132**, 2109 (1963).

[161] R. N. Zare, *J. Chem. Phys.* **47**, 204 (1967).

[162] J. A. D. Stockdale and L. Deleanu, *Chem. Phys. Lett.* **22**, 204 (1973).

[163] L. J. Kieffer and R. J. van Brunt, *J. Chem. Phys.* **46**, 2728 (1967).

[164] P. H. Doolittle, R. I. Schoen, and K. E. Schuburt, *J. Chem. Phys* **49**, 5108 (1968).

[165] R. S. Freund, *J. Chem. Phys* **54**, 3125 (1971).

[166] J. Schopman and R. Locht, *Chem. Phys. Lett.* **26**, 596 (1974).

[167] R. Locht and J. Schopman, *Int. J. Mass Spec. Ion Proc.* **15**, 361 (1974).

[168] A. Matsuo, K. Furuya, and T. Ogawa, *Chem. Phys. Lett.* **287**, 653 (1998).

[169] R. J. van Brunt, G. M. Lawrence, L. J. Keiffer, and J. M. Slater, *J. Chem. Phys.* **61**, 2032 (1974).

[170] B. R. Cameron, Ph.D. thesis, University of Canterbury, Christchurch, New Zealand, 1993.

[171] D. A. Blunt, Ph.D. thesis, University of Canterbury, University of Canterbury, Christchurch, New Zealand, 1995.

[172] W. P. Hu, Ph.D. thesis, University of Canterbury, Christchurch, New Zealand, 2000.

[173] R. Campargue, *J. Phys. Chem.* **88**, 4466 (1984).

[174] W. R. Gentry and C. F. Giese, *Rev. Sci. Instrum.* **46**, 104 (1975).

[175] B. R. Cameron and P. W. Harland, *Rev. Sci. Instrum.* **65**, 108 (1993).

[176] J. J. Thomson, in *ION–MOLECULE REACTIONS, PART I, Kinetics and Dynamics*, edited by J. L. Franklin (Longman Green and Company, 1979), p. 10.

[177] A. J. Dempster, in *ION–MOLECULE REACTIONS, PART I, Kinetics and Dynamics*, edited by J. L. Franklin (Longman Green and Company, 1979), p. 17.

[178] T. R. Hogness and E. G. Lunn, in *ION–MOLECULE REACTIONS, PART I, Kinetics and Dynamics*, edited by J. L. Franklin (Longman Green and Company, 1979), p. 23.

[179] V. Aquilanti and G. G. Volpi, *J. Chem. Phys.* **44**, 2307 (1966).

[180] V. Aquilanti and G. G. Volpi, *J. Chem. Phys.* **44**, 3574 (1966).

[181] I. G. Csizamadia *et. al.*, *J. Chem. Phys.* **52**, 6205 (1970).

[182] J. A. Burt, J. L. Dunn, M. J. McEwan, M. M. Sutton, A. E. Roche, and H. I. Schiff, *J. Chem. Phys.* **52**, 6062 (1970).

[183] W. T. Huntress and M. T. Bowers, *Int. J. Mass Spectrom. Ion Phys.* **12**, 1 (1973).

[184] J. K. Kim, L. P. Thread, and W. T. Huntress, *Int. J. Mass Spectrom. Ion Phys.* **15**, 223 (1974).

[185] K. R. Ryan, *J. Chem. Phys.* **61**, 1559 (1974).

[186] A. B. Rakshit, *Int. J. Mass Spectrom. Ion Phys.* **41**, 185 (1982).

[187] D. B. Milligan, Ph.D. thesis, University of Canterbury, 2000.

[188] D. W. Chandler and P. L. Houston, *J. Chem. Phys* **87**, 1445 (1987).

[189] B. J. Whitaker, in *Resarch in Chemical Kinetics*, edited by R. G. Compton and G. Hancock (Elsevier, 1993), Vol. 1, p. 307.

[190] C. Bordas, F. Paulig, H. Helm, and D. L. Huestis, *Rev. Sci. Instrum.* **67**, 2257 (1996).

[191] D. H. Parker and A. T. J. B. Eppink, *J. Chem. Phys.* **107**, 2357 (1997).

[192] T. J. B. Eppink and D. H. Parker, *Rev. Sci. Instrum.* **68**, 3477 (1997).

[193] B.-Y. Chang, R. C. Hoetzlein, J. A. Mueller, J. D. Geiser, and P. L. Houston, *Rev. Sci. Instrum.* **69**, 1665 (1998).

[194] D. W. Chandler, J. R. Barker, A. J. R. Heck, M. H. M. Janssen, K. T. Lorenz, D. W. Neyer, W. Roeterdink, S. Stolte, and L. M. Yoder, in *Atomic and molecular beams: the state of the art 2000*, edited by R. Campargue (Springer-Verlag, 2001), p. 519.

[195] L. McDonnell and A. J. R. Heck, *Int. J. Mass Spec. Ion Prosc.* **33**, 415 (1998).

[196] A. R. Heck and D. W. Chandler, *Ann. Rev. Phys. Chem.* **46**, 335 (1995).

[197] K. Smith, *Atomic, Molecular and Optical Physics: Charged Particles* (Academic Press, 1995), Vol. 29A, p. 253.

[198] *http://micro.magnet.fsu.edu/primer/digitalimaging/index.html.*

[199] M. Levinshtein, G. Simin, and translated by Minna M. Perelman, *Transistors: from crystals to integrated circuits* (World Scientific, 1998).

[200] C. Vallance and K. Vallentine, Private Communication.

[201] M. J. J. Vrakking, *Rev. Sci. Instrum.* **72**, 4084 (2001).

[202] C. R. Gebhard, T. P. Rakizis, P. C. Samarizis, V. Ladopoulos, and T. N. Kitsopoulos, *Rev.Sci. Instrum.* **72**, 3848 (2001).

[203] M. J. Bass, M. Brouard, A. P. Clark, and C. Vallance, *J. Chem. Phys.* **117**, 8723 (2002).

[204] R. Locht and J. Momigny, *Int. J. Mass Spectrom. Ion Phys.* **7**, 121 (1971).

[205] P. W. Harland and B. McIntosh, *Int. J. Mass Spectrom. Ion Processes* **67**, 29 (1985).

[206] A. Wiki, V. Marsico, L. Kuhnke, K. Kern, L. Paratte, S. Schweizer, and P. Renaud, *Rev. Sci. Instrum.* **70**, 3562 (1999).

[207] K. Kern, B. Lindenau, R. David, and G. Cosma, *Rev. Sci. Instrum.* **56**, 52 (1985).

[208] P. W. Atkins and R. S. Friedman, in *Molecular Quantum Mechanics* (Oxford University Press, 1995), Chap. 14.

APPENDICES

A. DERIVATION OF BEER-LAMBERT LAW FOR ELECTRON IMPACT IONIZATION

The determination of electron impact ionization cross-sections uses an expression analogous to the Beer-Lambert law.

When an electron collides with an atom or molecule one or more of the electrons in the target can be promoted from one of the bound orbitals to the continuum, provided that the electron has energy greater then or equal to the ionization energy of the target.

The number of collisions that an electron undergoes, dI^-, is proportional to the thickness of the layer, dl, the number of colliding species, n, and the number of electrons in the beam, I^-:

$$\mathrm{d}I = \sigma n I^- \mathrm{d}l \tag{A.1}$$

Where σ, the total ionization cross-section, is the proportionality constant. On rearranging:

$$\int_{I_0^-}^{I^-} \frac{\mathrm{d}I^-}{I^-} = \sigma \int_0^l n \mathrm{d}l \tag{A.2}$$

Assuming that n is independent of location over the pathlength l, this equation integrates to the Beer-Lambert law.

$$\ln \frac{I^-}{I_0^-} = \sigma n l \tag{A.3}$$

Because the sum of the ion current, I^+, and the incident current, I_0^-, gives the collected

electron current I^-, this equation transforms to:

$$\frac{I_0^- + I^+}{I_0^-} = e^{\sigma n l} \tag{A.4}$$

$$\frac{I_0^-}{I_0^-} + \frac{I^+}{I_0^-} = e^{\sigma n l} \tag{A.5}$$

$$\frac{I_0^-}{I_0^-} + \frac{I^+}{I_0^-} \approx \sum_{k=0}^{k} 1 + \frac{1}{1!}(\sigma n l) + \frac{1}{2!}(\sigma n l)^2 ... \tag{A.6}$$

$$I^- \approx I_0^- \tag{A.7}$$

$$\frac{I^+}{I^-} \approx \sigma n l \tag{A.8}$$

Because the number of secondary electrons is relatively small approximation (A.7) is valid, and because $\sigma n l \sim 1 \times 10^{-3}$, taking only the first term of the Taylor expansion is valid,[a] with the second order term only contributing $\sim 0.1\% - 0.05\%$

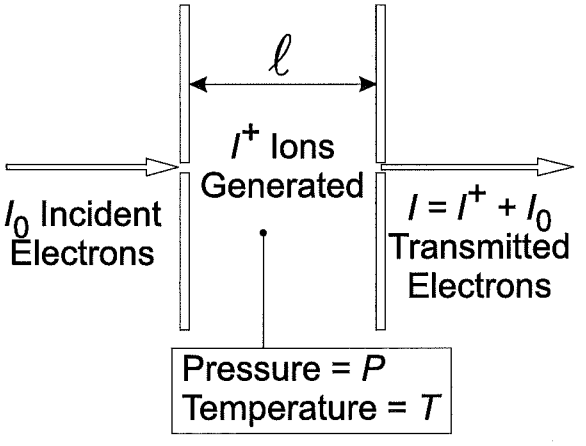

Figure A.1: Illustration of terms used in Beer-Lambert derivation of electron impact ionization cross-section.

[a] D. W. Jordan and P. Smith *Mathematical Techniques* 2nd Ed. Chapter 5

B. THE RELATIVE FLOW TECHNIQUE

Prior to the wide spread use of capacitance manometers for accurate pressure determination, McLeod gauges were generally used to measure the pressure for electron impact ionization cross-section measurements. It was realised that these measurements were inaccurate, especially for target species with a molecular mass greater then helium. Rapp and Englander-Golden[14] introduced a method which they called the relative flow technique. The absolute cross-section for H_2 was determined using a McLoed gauge. The ionization cross-sections for heavy target atoms were then normalised to the hydrogen data. Using the relative flow method a gas flows into the ionization chamber through an effusive leak valve. The flow rate of the gas through the leak valve will be inversely proportional to the molecular mass of the target gas flowing through the valve. After a period of time, t, a quasi steady state pressure will build up in the ionization tube. The pressure in the ionization tube under steady state conditios is independent of molecular mass, it is only proportional to the the gas in the reservoir and the preset opening of the leak valve.

Consider two chambers connected in series by a small aperture at $t = 0$, $Q = q$ and $p = 0$. The time rate of change in chamber p is given by;

$$Vp\frac{\mathrm{d}p}{\mathrm{d}t} = -c_2 p + c_1 Q \tag{B.1}$$

$$Vq\frac{\mathrm{d}q}{\mathrm{d}t} = -c_1 q \tag{B.2}$$

with

$$k_1 = \frac{c_1}{V_q} \tag{B.3}$$

$$k_2 = \frac{c_2}{V_p} \tag{B.4}$$

$$k_3 = \frac{c_1}{V_p} \tag{B.5}$$

Where V_p and V_q are the volumes of p and q respectively. Solving for p and q gives:

$$q = Q\exp(-k_1 t) \tag{B.6}$$

$$p = \frac{k_3 Q}{k_2 - k_1}\left[\exp(-k_1 t) - \exp(-k_2 t)\right] \tag{B.7}$$

when the quasi steady state is reached $\frac{dp}{dt} = 0$, hence

$$P_{ss}(t) = \frac{c_1}{c_2} q = \frac{c_1}{c_2} Q\exp(-k_1 t) \tag{B.8}$$

since $\frac{c_1}{c_2}$ is small, $V_p \approx V_q$ and $k_1 \ll k_2$. It follows that

$$p \approx \frac{c_1}{c_2} Q\left[\exp(-k_1 t) - \exp(-k_2 t)\right] \tag{B.9}$$

$$p(t) \approx p_{ss}(t)\left[1 - \exp(-k_2 t)\right] \tag{B.10}$$

If the leak valve c_1 is set to a preset value and the ion current is measured from when the gas sample is introduced into the collison cell, the steady state current at $t = 0$, which is proportional to the ionization cross-section, may then be determinend by extrapolation. This steady state ion current can then be compared to the steady state current of H_2 at the same valve setting.

C. PARTIAL WAVE THEORY

Assume that the interaction is described by a time-independent potential energy $V(r)$ which depends only on the separation r of the inbound electron and the target. Because the collision events are time dependent, they need to be considered in terms of the time dependent Schrödinger Equation.

$$\widehat{H}\psi(r,t) = i\hbar\frac{\partial\psi(r,t)}{\partial t} \tag{C.1}$$

$\widehat{H}$ is the Hamiltonian

$$\widehat{H} = -\frac{\hbar^2}{2\mu}\nabla^2 + V(r) \tag{C.2}$$

Because $V(r)$ is time-independent it is possible to separate out the time-dependent and time-independent energy terms.

$$\psi(r,t) = \psi(r)\mathrm{e}^{-Et/\hbar} \tag{C.3}$$

$$\widehat{H}\psi(r) = E\psi(r) \tag{C.4}$$

Writing the Laplace operator ∇^2 in spherical polar coordinates:

$$\nabla^2 = \frac{1}{r}\frac{\partial^2}{\partial r^2}r + \frac{1}{r^2}\Lambda^2 \tag{C.5}$$

where Λ is a solution to the Legendre polynomial in spherical coordinates. The partial wave theory assumes that electron impact ionization is an elastic scattering process. The angular momentum of the incident particle relative to the target partice is conserved during the collision process. The inbound electron does not apply any torque to the target. This enables the scattering amplitudes $f_k(\theta)$ and wavefunctions $\psi(r,\theta)$

to be reduced to simpler functions, each characterized by a unique value of l.[208] These two functions can be expanded to

$$f_k(\theta) = \sum_l f_l P_l(\cos\theta) \tag{C.6}$$

$$\psi(r,\theta) = \sum_l R_l(r) P_l(\cos\theta) \tag{C.7}$$

where R_l is a radial function and f_l is a constant. Both R_l and f_l are dependant on the value of l and the wave vector $\mathbf{K}$. The product $R_l P_l$, denoted ψ_l, is known as the partial wave stationary scattering state.

Combining ψ_l and equation (C.4) gives

$$\sum_l \widehat{H} R_l P_l = E \sum_l R_l P_l \tag{C.8}$$

substituting equations (C.2) and (C.5), noting that $\Lambda^2 P_l = -l(l+1)P_l$ and that the differential equation must hold for each value of l, a solution is required for the following equation:

$$\frac{\hbar^2}{2\mu r} r R_l + \frac{\hbar^2 l(l+1)}{2\mu r^2} R_l + V R_l = E R_l \tag{C.9}$$

$$\left[\frac{\hbar^2}{2\mu r} + \frac{\hbar^2 l(l+1)}{2\mu r^2} + V(r)\right] F_l(r) = E F_l(r) \tag{C.10}$$

Where $F(r) = rR_l$ is introduced to simplify the appearance of equation (C.10) in order to identify the most relevant parts of the equation.

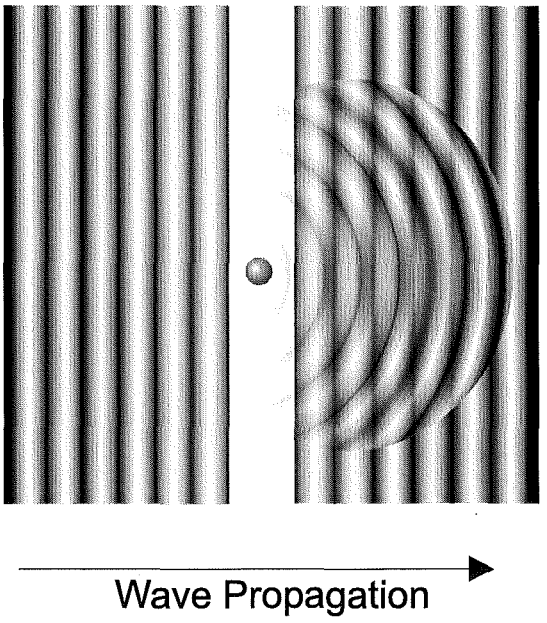

Figure C.1: Analogy for partial wave theory. The incident wave scatters off a particle to give a transmitted wave and a scattered wave

D. PERTURBATION THEORY

The perturbation due to the electric field can be examined in terms of quantum mechanical perturbation theory.

Starting from the time independent Schrödinger equation $H\psi = E\psi$, perturbation theory assumes that H, E and ψ are known for a model system which differs from the real system by a small amount. Assumed that the real system is a linear combination of a series of perturbations to the real system. H, E and ψ for the $(n+1)th$ perturbation then depends on the nth perturbation.

$$H^{(0)}\psi_0 = E_0\psi_0 \tag{D.1}$$

$$\{H^{(0)} - E_0\}\psi_0^{(1)} = \{E_0^{(1)} - H^{(1)}\}\psi_0 \tag{D.2}$$

$$\{H^{(0)} - E_0\}\psi_0^{(2)} = \{E_0^{(2)} - H^{(2)}\}\psi_0 + \{E_0^{(1)} - H^{(1)}\}\psi_0^{(1)} \tag{D.3}$$

$$\text{etc...} \tag{D.4}$$

The first order correction to the energy is written as a linear combination of the unperturbed wave functions ψ_0

$$\psi_0^{(1)} = \sum_n a_n \psi_n^{(0)} \tag{D.5}$$

where the sum is over all states n. Substitution of equation (D.5) into equation (D.2), gives, in ket notation,

$$\sum_n a_n\{H^{(0)} - E_0\}|n >= \sum_n a_n\{E_n - E_0\} = \sum_n a_n\{E_0^{(0)} - H^{(1)}\}|0 > \tag{D.6}$$

Multiplying by the bra $< 0|$ and applying the orthonormality condition

$$\sum_n a_n\{E_n - E_0\} < n|0 > \;=\; 0 \;=\; E_0^{(1)} - < 0|H^{(1)}|0 > \tag{D.7}$$

$$E_0^{(1)} \;=\; < 0|H^{(1)}|0 > \tag{D.8}$$

The same method is used to determine the second order correction to the energy

$$\psi_0^{(2)} = \sum_n b_n \psi_n^{(0)} \tag{D.9}$$

where the sum is over all states n. Substitution of equation (D.9) into equation (D.3), gives, in braket notation

$$E_0^{(2)} =< 0|H^{(2)}|0 > \tag{D.10}$$

as in the first order case, plus a second order correction to the first order energy.

$$\sum_{n=1} a_n < 0|H^{(1)}|n > \tag{D.11}$$

From equation (D.7)

$$a_n = \frac{< n|H^{(1)}|0 >}{E_0 - E_n} \tag{D.12}$$

The total energy correction for the second order perturbation is then given from equations (D.10), (D.11) and (D.12)

$$E_0^{(2)} =< 0|H^{(2)}|0 > + \sum_{n=1} \frac{< 0|H^{(1)}|n >< n|H^{(1)}|0 >}{E_0 - E_n} \tag{D.13}$$

E. THE KUHN-THOMAS RULE

The proof of the Kuhn-Thomas rule rests on the following derivation that shows that oscillator strength, f, can be written in terms of linear momentum.

$$\begin{aligned} \langle m|[H,x]|n\rangle &= \langle m|Hx|n\rangle - \langle m|xH|n\rangle && \text{(E.1)} \\ &= (E_m - E_n)\langle m|x|n\rangle && \text{(E.2)} \\ &= \hbar\omega_{mn}x_{mn} && \text{(E.3)} \end{aligned}$$

where $[H,x]$ is the Hamiltonian and position operator commutator, which may also be written as

$$\begin{aligned} [H,x] &= -\frac{\hbar^2}{2m_e}\left[\frac{\mathrm{d}^2}{\mathrm{d}x^2},x\right] + [V(x),x] && \text{(E.4)} \\ &= -\frac{\hbar^2}{2m_e}\left(\frac{\mathrm{d}^2}{\mathrm{d}x^2} - x\frac{\mathrm{d}^2}{\mathrm{d}x^2}\right) && \text{(E.5)} \\ &= -\frac{\hbar^2}{2m_e}\left(2\frac{\mathrm{d}}{\mathrm{d}x} + x\frac{\mathrm{d}^2}{\mathrm{d}x^2} - x\frac{\mathrm{d}^2}{\mathrm{d}x^2}\right) && \text{(E.6)} \\ &= -\frac{\hbar^2}{m_2} = \frac{\hbar}{\mathrm{i}m_e}p_{x,mn} && \text{(E.7)} \end{aligned}$$

therefore

$$\hbar\omega_{mn}x_{mn} = \frac{\hbar}{\mathrm{i}m_e}p_{x,mn} \tag{E.8}$$

$$p_{x,mn} = \mathrm{i}m_e\omega_{mn}x_m n \tag{E.9}$$

because, for a one electron atom $\mu_x = -ex$

$$p_{x,mn} = -\mathrm{i}\left(\frac{m_e\omega_{mn}}{e}\right)\mu_{x,mn} \tag{E.10}$$

or, over all Cartesian coordinates

$$\mathbf{p}_{mn} = -\mathrm{i}\left(\frac{m_e\omega_{mn}}{e}\right)\boldsymbol{\mu}_{mn} \tag{E.11}$$

Equation (E.11) is known as the velocity dipole relation.

Now that an equation has been established that links linear momentum, p with μ, the oscillator strength[a] can be written in terms of p and $\omega_{n0} = 2\pi\nu_{n0}$

$$f_{n0} = \frac{4\pi m_e\nu_{n0}|\mu_{n0}|^2}{3e^2\hbar} \tag{E.12}$$

$$= \frac{m_e\omega_{n0}}{3e^2\hbar}(\boldsymbol{\mu}_{0n}\cdot\boldsymbol{\mu}_{n0} + \boldsymbol{\mu}_{0n}\boldsymbol{\mu}_{n0}) \tag{E.13}$$

$$= \frac{m_e}{3e^2\hbar}\left(\frac{\mathrm{i}}{m_e}\right)(\boldsymbol{\mu}_{0n}\cdot\boldsymbol{p}_{n0} - \boldsymbol{p}_{0n}\cdot\boldsymbol{\mu}_{n0}) \tag{E.14}$$

(E.15)

Summing over all n and incorporating $\boldsymbol{\mu} = -e\mathbf{r}$

$$\sum_n f_{n0} = -\left(\frac{\mathrm{i}}{3\hbar}\right)\langle 0|\mathbf{r}\cdot\mathbf{p} - \mathbf{p}\cdot\mathbf{r}|0\rangle \tag{E.16}$$

for each of the three Cartesian coordinates x, y and z the scalar product of the $[\mathbf{r},\mathbf{p}]$

[a] equation (E.12) is the definition of oscillator strength - a dimensionless quantity

commutator is $i\hbar$, so finally, for a one-electron target

$$\sum_n f_{n0} = -\left(\frac{i}{3\hbar}\right)(3i\hbar)\langle 0|0\rangle = 1 \tag{E.17}$$

for a many electron target each electron gives a contribution of one to the oscillator strength.

$$\sum_n f_{n0} = N_e \tag{E.18}$$

which is equation (5.50).

F. DESCRIPTION OF MOLECULAR BEAM MACHINE COMPONENTS

A diagram of the outside of the molecular beam machine is shown in Figures 7.1, 7.2 and 7.3 on pages 155, 156 and 157 respectively. The molecular beam machine consists of six stainless steel vacuum chambers. Each vacuum chamber is pumped with either an oil diffusion pump or a turbomolecular pump, and is also fitted with a liquid nitrogen cryogenic pump. The turbomolecular pumps and the oil diffusion pumps can be individually isolated from the machine by either a pneumatic gate valve or hand operated gate valve. Internally each vacuum chamber that forms the main section of the beam machine is separated from the two vacuum chambers on either side of it by a stainless steel shim with three apertures. One aperture along the molecular beam axis for transmission of the beam and two apertures for the hexapole and nozzle alignment rods. All of the vacuum ports are of the Con-Flat type except the lid of the scattering chamber and the C-cell, which are sealed with a Viton type 'O'-ring.

The main frame that supports the vacuum chamber and pumps is made from 3 mm box section steel. There are two 50 mm $\times$ 80 mm beams that run the full 4100 mm length of the machine with a separation of 420 mm. Along the top of one of the beams there are two 6 mm $\times$ 12 mm steel strips held in place with pop rivets. The strips are separated by 14 mm, thus forming a guide for the carriages which support the vacuum chambers and pumps to move along. These carriages are supported by roller bearings. The two main beams are supported at a height of 1210 mm from the ground by twelve 25 mm $\times$ 50 mm beams, six on each side, resulting in a trapezoidal shape, flaring out at an angle of approximately 9 degrees from the vertical to give a foot-print of 1010 mm. The base of each trapezoid is tied together with a 25 mm $\times$ 50 mm beam. The ion gun chamber is supported by a triangular cantilever coming off the main support.

The liquid nitrogen cryogenic pumping system is operated from two 75 l dewars that are pressurized to 6 psi. One of the dewars fills the buffer chamber, nozzle chamber and mobile diffusion pump liquid nitrogen traps. The other fills the scattering chamber, electron gun, hexapole and c-cell chamber liquid nitrogen traps. The filling is controlled by an electric solenoid valve on each dewar. The pressure is provided from an in-house nitrogen supply. The liquid nitrogen flows through 3/8″ copper tubing that is insulated with Centurylon 15 mm I.D. × 13 mm wall thickness foam insulation. Total liquid nitrogen use is of the order of 100 l per day.

The vacuum protection system consists of a range of monitoring devices. Each diffusion pump has a thermocouple for temperature measurement and a type 531 thermocouple for foreline pressure measurement. The ion gauges on the vacuum system also form part of the vacuum protection system. The temperature monitoring thermocouples and the foreline pressure monitoring thermocouples are linked into a main vacuum protection unit. If the temperature exceeds a certain preset value, typically 38°C, on any one of the diffusion pumps then the power to that pump is switched of and an audio alarm is activated. The type 531 thermocouples are monitored using 2 channel MKS type 286 controllers. If the pressure exceeds a preset value on any channel of the controllers, typically 0.1 Torr, then the power to the corresponding diffusion pump or turbomolecular pump is switched off. In addition the turbomolecular pumps also have built-in thermal protection.

There are six ion gauges on the molecular beam machine, one on the nozzle chamber, buffer chamber, hexapole chamber, scattering chamber, electron gun chamber and quadrupole mass spectrometer chamber. The bulk of the ion gauges are Dunniway Stockroom Corp. type T-100K tungsten filament ion gauges. All of the ion gauges are monitored by an MKS instruments type 290 ion gauge controller, except the scattering chamber, which is monitored by an MKS instruments type 919 ion gauge controller. Any one of the type 290 ion gauge controllers can be used as part of the vacuum protection system. If the ion gauge exceeds a predetermined set point, typically 1×10^{-5} Torr then the vacuum system may be shut down, including the closing of the pneumatic

gate valves and the shutting down of other critical electronics such as the nozzle, microchannel plate power supplies and the quadrupole mass spectrometer.

There are two 150 mm O.D. PVC pipes that run underneath the length of the machine, to supply and drain the cooling water to the diffusion pumps and turbomolecular pumps. The cooling water flows from the water main into the PVC pipes where it is distributed to the diffusion pumps and turbomolecular pumps *via* 10 mm PressureFlex reinforced plastic tubing. Each pump has a valve on the supply and drain side of the main cooling coil so that it can be isolated for servicing. Initially some of the pumps were suffering from corrosion of the cooling coils, so a refrigeration unit and and air cooled heat exchanger were installed so that ethylene glycol could be recirculated through the system. The use of an air cooled system was also considered to be a good option because it would save an enormous amount of water per year. A design floor however had the air from the cooling system being discharged into the laboratory. This caused the temperature of the laboratory to rise rapidly so that the laboratory air conditioner shut down because it could not cope with the sudden rise in temperature. This in turn caused the heat exchange unit to overheat and shut down. The vacuum protection system responded by opening two solenoids allowing city water to flow around the pumps to prevent them from overheating. This had the unfortunate side effect of dumping the glycol into the drain. A water cooled heat exchanger was then added to prevent this problem, however this had the effect negating the saving of city water. Several other problems arose after the installation of the water cooled heat exchanger causing the cooling system to shut down regularly, including a potentially serious fire in one of the electro-mechanical relays and an ongoing problem with the refrigeration feed-back heat regulator solenoids. In the end the refrigeration unit suffered from serious internal corrosion such that the entire unit had to be disposed of. The beam machine is now back to being cooled by city water.

F.1 The vacuum system

In this section each of the vacuum chambers, their primary function and associated vacuum pumps will be discussed in detail.

F.1.1 The scattering chamber

To simplify the description of the scattering chamber, the direction of molecular beam propagation down the length of the machine axis is defined as north. The scattering chamber is an irregular octagonal shape. The north, east, south and west sides of the scattering chamber are longer than the remaining four sides, as shown in Figure 7.1. The scattering chamber is constructed from 1″ thick stainless steel. The north, east, south, west and northwest faces each have a 8″ Con-Flat type vacuum port, whereas the northeast, southeast and southwest faces each have a 2.75″ Con-Flat vacuum port. The vacuum in the scattering chamber varies with the experimental conditions and ranges from 2×10^{-8} to 2×10^{-6} Torr.

The north facing Con-Flat vacuum port has another vacuum chamber attached that houses the quadrupole mass spectrometer, which is used to detect the molecular beam. The quadrupole mass spectrometer chamber is separated from the scattering chamber by a three sided rectangular shaped 1 mm stainless steel shim. The fourth side of the rectangle is the northern wall of the scattering chamber. A 20 mm aperture is drilled in the center of the shim to allow the molecular beam to pass through it. The shim is held in place by four M5 screws in the northern face of the scattering chamber.

The ion/electron gun chamber is bolted to the 8″ Con-Flat vacuum port on the eastern face of the scattering chamber. It is separated from the scattering chamber by an "L" shaped stainless steel shim for differential pumping, which extends from the northern face of the scattering chamber to the northern side of the southeast face. The shim is screwed to the northern and eastern walls of the scattering chamber using four M5 screws and has a 12 mm aperture in it to allow the ion/electron beam to pass

through. In addition to the 8″ vacuum port on the eastern face there are two 2.75″ Con-Flat vacuum ports, one above the other. The lower one is blanked off, and the upper one is fitted with a 1/4″ stainless steel gas feed through, isolated with a Nupro 4HK valve. This feed through is used to pump out the gas from the ion gun as needed.

The 2.75″ Con-Flat vacuum port on the southeastern face of the scattering chamber has a Varian type 951-5106 variable leak valve. This valve can be used to introduce a scattering gas into the scattering chamber.

The southern face of the scattering chamber has a spring-loaded shim which clips into the inside of the 8″ vacuum port. The shim has an iris aperture to allow the molecular beam to pass through the center of it. This vacuum port goes through to the second hexapole chamber.

The 2.75″ Con-Flat vacuum port on the southwestern face of the scattering chamber is fitted with a Huntington four way high voltage electrical feed through. These four feed throughs lead from the high voltage fast pulsing unit to the extractor and repeller plates as discussed below.

The western face of the scattering chamber is blanked off with an 8″ Con-Flat flange when the electron gun is installed. When the ion gun is installed however, a Vacuum Generators SXP-300 quadrupole mass spectrometer is bolted to this port to monitor the ion beam component distribution alignment, and intensity. No additional ion source is required on the mass spectrometer for this purpose.

The northwestern face of the scattering chamber has a liquid nitrogen and a liquid helium trap installed for cryogenic pumping. Primarily the liquid helium trap is used as a liquid nitrogen trap, and forms a part of the serial liquid nitrogen filling system. However for some experiments, when a particularly low background pressure is required, the trap is filled with liquid helium, which is generated in the Physics Department. The boil-off from the liquid helium is re-compressed and liquefied. The liquid helium trap itself has a capacity of approximately 1L and has ridges machined all the way around it to maximize the available surface area. The liquid helium trap

may reduce the pressure by an order of magnitude.

The lid of the scattering chamber is machined out of a single piece of 1″ stainless steel. There is a 100 mm × 200 mm rectangular slot cut into the lid. This slot is covered by a second piece of 1″ stainless steel that is movable in the $x-y$ direction so that the microchannel plate–flight tube assembly can be centered along the ion product center of mass axis, as shown in Figure 7.5. A Viton 'O'-ring forms the interface between the movable section and the main part of the lid. There is a 6″ vacuum port machined into the movable section for the flight tube and microchannel plate assembly. The fiber optic bundle that forms the vacuum–camera interface is also supported by this flange. There are a further three Con-Flat vacuum ports along the northern end of the lid. Two of these are 2.75″ ports and the other is a 4.5″ port. These ports have been used for a variety of purposes including ion gauges, electrical feed throughs to the electron or ion gun, and associated detectors.

The base of the scattering chamber is also machined from a single piece of 1″ stainless steel. There is an 8″ Con-Flat vacuum port in directly below the crossing region to which an Alcatel CFV-900 880 ls^{-1} turbomolecular pump is attached. The pump is water cooled and is able to be isolated from the scattering chamber with a VAT pneumatic gate valve that can be controlled using electric solenoid valves from the main electronics rack. The turbomolecular pump is backed with a Varian SD700 mechanical pump, with a pumping speed of 726 $l\text{min}^{-1}$. There are two 2.75″ Con-Flat flanges along the western face of the base, which are used for electrical or gas feed throughs as required. There is also a 2″ liquid nitrogen vertical cold finger in the base, which is positioned just to the north of the pumping port, under the beam axis for additional cryopumping.

F.1.2 The quadrupole mass spectrometer chamber

The main purpose of the quadrupole mass spectrometer is to monitor the arrival time distribution of the supersonic molecular beam, but it has also been used for leak testing.

The chamber itself is a straight through 6″ OD stainless steel pipe with 8″ Con-Flat type vacuum seals on each end. There is a 3″ stainless steel pipe welded into the 6″ pipe at right angles to it, to which an an Alcatel 5150CP 140 ls^{-1} turbomolecular pump is attached. The turbomolecular pump uses an Alcatel CFF450 turbomolecular pump controller. The backing pump for the turbomolecular pump is an Alcatel 2008A rotary vane mechanical pump with a pumping speed of 130 $l\text{min}^{-1}$. A Dunniway Stockroom Corp. T-100K ion gauge is used to monitor the pressure, which is typically between 2×10^{-8} Torr and 5×10^{-7} depending on the experiment. The chamber can be isolated from the turbomolecular pump using a VAT pneumatic gate valve. The gate valve can be controlled from the main electronics / vacuum protection rack using electrically controlled solenoid valves. The quadrupole mass spectrometer chamber houses an Extranuclear Laboratories 4-270-9 mass spectrometer coupled to an Extranuclear Laboratories 041-1 axial beam ionizer. The voltages on the lens elements and filament are controlled from a custom built 6-channel power supply, and the filament emission is provided by a Dick Smith Electronics Q1760 general purpose power supply. The current from the channeltron multiplier is amplified by a Stanford Research Systems model SR570 fast current preamplifier. The typical operating conditions are shown in Table F.1.

F.1.3 The ion/electron gun chamber

The ion/electron gun chamber is a square box construction fabricated from 1″ stainless steel. It has an 8″ Con-Flat type vacuum port on the southern and western faces, as well as on the base and the top of the box. The northern face has four 2.75″ Con-Flat vacuum ports, one of which supports an ion gauge, one of which supports the ion gun gas feed through, and two of which are blanked off. The eastern face has a Huntington Laboratories PM-600 $x-y-z-$ translator, which also includes six 1.25″ Con-Flat electrical feed throughs that are used for powering the ion and electron gun. The Huntington translator has a 1/2″ spigot with a tapered male end, the final 10mm which is threaded. The ion and electron guns are also mounted on spigots

Table F.1: Extranuclear mass spectrometer operating conditions

Operating Parameter	Value
Filament Current	2.5A
Lens 1	-136V
Lens 2	-208V
Lens 3	+24V
Cathode	-95V
Ion energy	12V
Filament current	3.04A
Multiplier	1.8kV
SR570 gain	500nA $Volt^{-1}$
Time base (background)	2ms
Time base (ATD)	1ms
Mass resolution	1 - 8 as required
ΔM	0 - 15% as required

with threaded female sections at the ends. In order to change between the ion gun and electron gun all that is required is a disconnection of the electrical connections and an unscrewing of the gun. The top 8″ Con-Flat flange supports a disk-shaped liquid nitrogen trap which is approximately 6″ in diameter and 1″ thick. The Con-Flat flange on the southern side of the box has been blanked off. The eastern side of the box leads to the scattering chamber. The pumping requirements of this chamber are satisfied by a Varian VHS-6 6″ diffusion pump, backed by a the same Varian SD700, 726 $l\text{min}^{-1}$ mechanical pump that backs the scattering chamber turbomolecular pump. A 6″ lever-operated gate valve separates the diffusion pump from the vacuum chamber when required. An additional custom-built liquid nitrogen trap separates the diffusion pump from the gate valve.

F.1.4 The hexapole chamber

The hexapole chamber consists of a six way stainless steel 6″ cross with 8″ Con-Flat vacuum ports on each face, fabricated in the Departmental Machine Shop. On the top face there are two Huntington Laboratories high voltage feed throughs that provide

the vacuum interface for the high voltage supply to the hexapole rods. On the western side of the cross there is a flange with two 2.75″ Con-Flat vacuum ports. One of these supports an ion gauge and the other is blanked off. The eastern side of the cross has been used as a vacuum port to the mobile diffusion pump. When the mobile diffusion pump is connected to another one of the vacuum chambers, this side is blanked off. The southern side of the hexapole chamber is connected to the C-cell and is separated from it by a three-sided box, to allow differential pumping of the C-cell and hexapole chambers. The box is made from 1 mm thick stainless steel shim, which splits in two along the $y-$ axis. The fourth side of the box is formed by the northern wall of the C-cell. The box has a 12 mm aperture along the molecular beam axis to allow the beam to pass through it. The pumping requirements for the hexapole chamber are met by a Varian 1200 ls^{-1} VHS-4 oil diffusion pump. The foreline vacuum to this diffusion pump is maintained by an Alcatel 2008A rotary vane mechanical pump with a pumping speed of 130 $l\text{min}^{-1}$. The diffusion pump may be isolated from the main vacuum chamber by means of a rotary hand operated gate valve.

F.1.5 The C-cell

The molecular beam electronic resonance (MBER) spectroscopy cell, or C-cell, is a box construction similar to the ion source chamber, but has the important feature of having a removable lid. The northern face links to the hexapole chamber *via* an 8″ Con-Flat. The eastern face has an 8″ Con-Flat vacuum port, which either has the mobile diffusion pump connected to it or is blanked off, depending on the particular experiment that is being conducted. The southern 8″ Con-Flat vacuum port on the C-cell has connected to it a four way cross similar in construction to that of the hexapole chamber. There is no differential pumping barrier between this cross and the C-cell. On the western face of the C-cell there is an 8″ Con-Flat vacuum port, to which is bolted a flange with four 2.75″ vacuum ports. One of these ports provides the electrical signal to the supersonic nozzle, another supports a nude ion gauge, the third has an MKS Baratron model 622A13TAE 1000 Torr absolute capacitance manometer. This manometer is

used to monitor the pressure during venting and rough pumping of the machine. The final 2.75″ vacuum port provides the vacuum interface for the electrical feed throughs that control the electric resonance spectroscopy RF and DC fields. No molecular beam electric resonance spectroscopy was carried out in the present work, and the interested reader is refereed to Vallance[88] or Hu[172] for a full description of this technique. In the present work the C-cell was used to house the molecular beam source, in order to obtain stronger molecular beam signals. At the base of the C-cell there is an Airco 5010 hand operated rotary gate valve to separate the liquid nitrogen trap and a Varian VHS-6 oil diffusion pump from the main vacuum chamber. The diffusion pump has a pumping speed of 2400 ls^{-1} to maintain the vacuum in the C-cell. The foreline vacuum is maintained by an Alcatel 2010 rotary vane mechanical pump with a pumping speed of 160 $l$min−1.

F.1.6 The remaining vacuum chambers

The chamber immediately to the south of the C-cell is a four way cross similar in construction to that of the hexapole chamber, and was also fabricated in the Departmental Machine Shop. The upper face of the cross supports an Alcatel TMP5400 turbomolecular pump, separated from the cross by a VAT CF-150 pneumatic gate valve. The gate valve is operated from the main electronics/vacuum rack *via* electric solenoid valves. Both the western and eastern faces have two 2.75″ ports each. One of the ports on the eastern face provides a gas feed through for the nozzle and one of the ports on the western face has a type 531 thermocouple gauge for calibration of the MKS 290 foreline monitors. The remaining port on each of the faces is blanked off. The bottom face of the cross supports a Varian VHS-4 diffusion pump and a liquid nitrogen trap. The vacuum chamber is separated from the liquid nitrogen trap and diffusion pump with a hand operated rotary gate valve. The foreline vacuum for this diffusion pump is maintained by an Alcatel 2008 130 $l$min^{-1} rotary vane mechanical pump.

Bolted to the southern vacuum port of this chamber is an 8″ Con-Flat flange that

supports the alignment rods running the length of the machine and an adapter flange that connects the support flange to a Huntington Laboratories 10″ OD Con-Flat six way cross. The vacuum in this cross is maintained by a 5300 ls^{-1} Varian VHS-10 oil diffusion pump, which is backed by an Alcatel model 2063C two stage rotary vane mechanical pump with a pumping speed of 1080 $lmin^{-1}$. The top face of this cross supports a disk-shaped liquid nitrogen trap, which is approximately 6 inches in diameter and 1″ thick. The eastern side of the cross is blanked off with a glass window. The southern side of the cross has a Huntington Laboratories linear motion feed through attached to it, which is used to adjust the nozzle-skimmer distance. This side also has a 1/4″ tube gas feed through for venting of the machine with dry nitrogen. The western side has a Huntington Laboratories ES-150 bellows valve with a tube that runs through to the Alcatel mechanical pump, for rough pumping of the beam machine.

F.2 Internal components of the molecular beam machine

The internal components of the molecular beam machine are shown in Figure 7.4 on page 158.

F.2.1 Crossing region and flight tube

The repeller plate is made from 1 mm thick stainless steel and is approximately 50 mm × 200 mm. It forms the bottom of a rectangular box assembly, with open northern and southern ends. This box assembly also incorporates the extractor plate, which forms the top of the box. The extractor has a similar construction to the repeller plate but has a 25 mm aperture in the top of it centered above the molecular beam – electron/ion beam crossing region to allow the product ions to be directed upward into the time-of-flight tube and onto the microchannel plate detector. The other two walls of the box assembly form the orienting field plates. The box assembly is screwed to the southern end of the scattering chamber and has a adjustable support that sits on the base of the scattering chamber at the northern end of the box assembly.

The flight tube is constructed from perspex tube with an internal diameter of 70 mm. There are four lens elements along the length of it. The first lens element is is usually maintained at ground potential and the remaining three elements may be used as an Einzel lens system to focus the ion trajectories onto the microchannel plate. The Einzel lens elements are controlled from a custom built 6 channel ±0-300 V power supply. The total length of the flight tube, from the crossing region to the microchannel plate assembly is 231 mm.

F.2.2 Alignment rods

The alignment rods are supported by a stainless steel disk at each end of the machine with holes drilled into them to support the rods, as shown in the diagram. There are two additional supports in the C-cell for the alignment rods. The alignment rods support the nozzle and hexapole assembly.

F.2.3 Hexapole

The hexapole assembly itself consists of six 1/4″ diameter ground stainless steel rods, which are mounted in two perspex yokes, one at each end of the rods. The center of the rods inscribe an imaginary circle with 4.74 mm radius. The perspex yoke rests on the alignment rods that run down the length of the beam machine. The perspex yoke has key holes cut into it between the rods to minimize tracking across the perspex surface. Each rod has a screw that runs through the perspex to hold it in place. The voltage to the hexapoles are provided by two Glassman High Voltage EH 10 kV power supplies, one for the three positive rods and one for the three negative rods. The EH supplies were computer controlled, initially using an 33MHz 386 PC and more recently a 2.4 GHz Pentium 4 PC equipped with a LabCard PCL-1711 multifunction ADDA converter coupled to a LabCard PCLD-8710 terminal board. The supplies require a 0-10 V analogue input to provide the 0-10 kV output.

G. EQUATIONS OF MOTION FOR PARTICLE IN UNIFORM EXTRACTION FIELD

G.1 Euler angles

Figure G.1 is a reproduction of Figure 10.2 on page 202 for ease of reference. This Figure defines the angles for the following derivation.

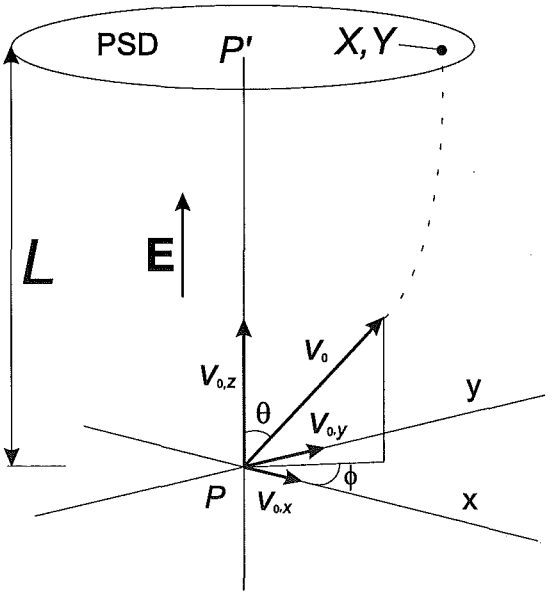

Figure G.1: Euler angle for particle in uniform extraction field

G.2 Derivation of equations of motion

With reference to Figure G.1, the velocity components are:

$$\mathbf{v}_{0,x} = \mathbf{v}_0 \sin\theta \cos\phi \tag{G.1}$$

$$\mathbf{v}_{0,y} = \mathbf{v}_0 \cos\phi \tag{G.2}$$

$$\mathbf{v}_{0,z} = \mathbf{v}_0 \sin\theta \sin\phi \tag{G.3}$$

therefore the location components on the position sensitive detector are

$$X = \mathbf{v}_{0,x} t \tag{G.4}$$

$$Y = \mathbf{v}_{0,y} t \tag{G.5}$$

$$Z = L = \mathbf{v}_{0,z} t + \frac{1}{2}\mathbf{a}t^2 \tag{G.6}$$

for a particle in a static homogeneous field $\mathbf{E}$

$$\mathbf{F} = q\mathbf{E} \tag{G.7}$$

$$= m\mathbf{a} \tag{G.8}$$

substitution of equations (G.7) and (G.8) into (G.6) gives the following expression

$$L = \mathbf{v}_{0,z} t + \frac{q\mathbf{E}}{2m} t^2 \tag{G.9}$$

the objective now is to solve equation (G.9) for t and substitute into equations (G.4) and (G.5) by applying the quadratic formula.

$$t = \left(-\mathbf{v}_{0,z} \pm \sqrt{\mathbf{v}_{0,z}^2 + \frac{2q\mathbf{E}L}{m}} \right) \frac{m}{q\mathbf{E}} \tag{G.10}$$

$$= \left(-\mathbf{v}_0 \sin\theta \sin\phi \pm \sqrt{\mathbf{v}_0^2 \sin^2\theta \sin^2\phi + \frac{2q\mathbf{E}L}{m}} \right) \frac{m}{q\mathbf{E}} \tag{G.11}$$

This equation may then be substituted into equation (G.4) but prior to this ρ is defined as follows for simplification:

$$\rho = \frac{q\mathbf{E}L}{E_k} \tag{G.12}$$

$$= \frac{2q\mathbf{E}L}{mv^2} \tag{G.13}$$

thus

$$t = \frac{2L}{\mathbf{v}_0\rho}\left(-\sin\theta\sin\phi \pm \sqrt{\sin^2\theta\sin^2\phi + \rho}\right) \tag{G.14}$$

only the addition of the root of the determinant needs to be considered because otherwise solution will lead to the physically unreasonable result of negative time or negative kinetic energy. Substitution of equation (G.14) into equation (G.4) is shown by the following:

$$X = (\mathbf{v}_0\sin\theta\cos\phi)t \tag{G.15}$$

$$= (\mathbf{v}_0\sin\theta\cos\phi)\frac{2L}{\mathbf{v}_0\rho}\left(-\sin\theta\sin\phi + \sqrt{\sin^2\theta\sin^2\phi + \rho}\right) \tag{G.16}$$

$$= \frac{2L\sin\theta\cos\phi}{\rho}\left(-\sin\theta\sin\phi + \sqrt{\sin^2\theta\sin^2\phi + \rho}\right) \tag{G.17}$$

similarly

$$Y = (\mathbf{v}_0\cos\theta)t \tag{G.18}$$

$$= (\mathbf{v}_0\cos\theta)\frac{2L}{\mathbf{v}_0\rho}\left(-\sin\theta\sin\phi + \sqrt{\sin^2\theta\sin^2\phi + \rho}\right) \tag{G.19}$$

$$= \frac{2L\cos\theta}{\rho}\left(-\sin\theta\sin\phi + \sqrt{\sin^2\theta\sin^2\phi + \rho}\right) \tag{G.20}$$

H. IMAGE SMOOTHING METHODS

General Fourier filtering methods that are applicable to one dimensional data are equally applicable to two dimensional image data. There are various approaches to smoothing and filtering of the images. The software used in the present work has several types of smoothing and filtering functions capabilities. Images may be smoothed by a simple floating average smoothing algorithm. This method only has a small effect on the data, but multiple smoothing operations may be carried out.

In image processing, filters are mainly used to suppress either the high frequencies or the low frequencies in the image. The suppression of high frequency components results in smoothing, while the suppression of low frequencies enhances sharp features and is often used for edge detection.

An image can be filtered either in the frequency or in the spatial domain. Filtering in the frequency domain involves transforming the image into the frequency domain, multiplying it with the frequency filter function and re-transforming the result into the spatial domain. The filter function is shaped so as to attenuate some frequencies and (consequently) enhance others. For example, a simple low–pass filter function is $h(i,j) = 1$ for frequencies smaller than some cut-off frequency and 0 for all other frequencies. The corresponding process in the spatial domain is to convolve the input image $f(i,j)$ with the filter function $h(i,j)$ to produce a resultant filtered image $g(i,j)$:

$$g(i,j) = h(i,j) * f(i,j) \tag{H.1}$$

The mathematical operation of convolution in the spatial domain is identical to

multiplication in the frequency domain. Computationally filtering in the frequency domain is performed by taking the Fourier transform of the image, multiplying the transformed image by the filtering function and re-transforming the image back into the spatial domain.

A variety of different low–pass filter functions may be applied to the collected ion images, each with slightly different characteristics with respect to high frequency components and attenuation. The some of the windowing functions that may be applied are as follows:

Hamming window The Hamming window is given by the expression:

$$H(x,\tau,\alpha) = \begin{cases} \alpha + (1-\alpha)\cos\left(\frac{\pi x}{\tau}\right) & |x| < \tau \\ 0 & \text{otherwise} \end{cases}, \tag{H.2}$$

with $\alpha = 0.54$. The Hamming window has the slight disadvantage of being discontinuous at the edges (and has therefore a slight bump above π), which can lead to artifacts in the smoothed image. However, the Hamming filter generally yields good results and is often a good first choice of filtering function.

Rectangular window The rectangular window is given by the expression:

$$H(x,\tau) = \begin{cases} 1 & |x| < \tau \\ 0 & \text{otherwise} \end{cases} \tag{H.3}$$

Unlike the Hamming window, the rectangular window has a very sharp cut-off at $x = \tau$. This sharp cut-off can produce undesirable ringing effects in the resultant filtered image, and for this reason the rectangular window should be used with care.

Blackman–Harris windows Both 67dB and 92dB Blackman–Harris windows have been applied to collected images. The 67dB windowing function is given by the following expression:

$$H(x,\tau) = \begin{cases} \alpha_0 + \alpha_1 \cos\left(\frac{\pi x}{\tau}\right) + \alpha_2 \cos\left(\frac{2\pi x}{\tau}\right) & |x| < \tau \\ 0 & \text{otherwise} \end{cases} \tag{H.4}$$

$$\alpha_0 = 0.42323$$
$$\alpha_1 = 0.49755$$
$$\alpha_2 = 0.07922,$$

and the 92dB Blackman–Harris windowing function is given by the expression:

$$H(x,\tau) = \begin{cases} \alpha_0 + \alpha_1 \cos\left(\frac{\pi x}{\tau}\right) + \alpha_2 \cos\left(\frac{2\pi x}{\tau}\right) + \alpha_3 \cos\left(\frac{3\pi x}{2\tau}\right) & |x| < \tau \\ 0 & \text{otherwise} \end{cases} \tag{H.5}$$

$$\alpha_0 = 0.35875$$
$$\alpha_1 = 0.48829$$
$$\alpha_2 = 0.14128$$
$$\alpha_3 = 0.01168$$

The Blackman–Harris windows have similar characteristics to the Hamming window, although the attenuation is somewhat smoother. The 92dB window will provide a greater attenuation of high frequency components than the 67dB window, but is more likely to result in a significant loss of resolution if it is not applied with due care.

Gaussian window The shape of the Gaussian function lends itself well to providing a gradual attenuation up to some cut-off frequency, however the performance of the Gaussian window is generally not as good as that obtained using either a Hamming or a Blackman–Harris window. The form of the Gaussian window is described by the following expression:

$$H(x,\tau,\sigma) = \begin{cases} \mathrm{e}{-x^2/2\sigma^2} & |x| < \tau \\ 0 & \text{otherwise} \end{cases} \tag{H.6}$$